STABILITY OF TUBES UNDER EXTERNAL PRESSURE AND STRUCTURAL LOADS

By

Spyros A. Karamanos and John L. Tassoulas

1993
NSF # CDR-8721512

OFFSHORE
TECHNOLOGY
RESEARCH
CENTER

A National Science Foundation Engineering Research Center

11/93-B51100

For more information contact:

Offshore Technology Research Center
Texas A&M University
1200 Mariner Drive
College Station, TX 77845-3400
(409) 845-6000

or,

Center for Offshore Technology
The University of Texas at Austin
2901 North IH 35, Suite 101
Austin, Texas 78722
(512) 471-3753

STABILITY OF TUBES UNDER EXTERNAL PRESSURE AND STRUCTURAL LOADS

by

Spyros A. Karamanos and John L. Tassoulas

Acknowledgments

This study was made possible by a grant to The University of Texas at Austin from Shell Oil Company. The comments and suggestions of Drs. P.W. Marshall, C.D. Edwards and D.G. Morrison are gratefully acknowledged. Computing resources were provided by The University of Texas System Center for High-Performance Computing and the Center for Offshore Technology of The University of Texas at Austin.

STABILITY OF TUBES UNDER EXTERNAL PRESSURE AND STRUCTURAL LOADS

by

Spyros A. Karamanos and John L. Tassoulas

ABSTRACT

The present work investigates the ultimate capacity of inelastic tubes under combined external pressure, bending and axial force. A geometrically and materially nonlinear finite element technique is adopted. Some special features of tube response such as the effects of initial imperfections, residual stresses and localized deformation, are taken into account. Particular emphasis is placed on the analysis of ring-stiffened tubes under combined loading. The numerical results are compared with the available experimental data, as well as with design formulas, and are of immediate significance in the design of tubular members of deep-water structures.

Table of Contents

List of Figures

Chapter 1

Introduction

Offshore compliant towers have been considered for use in moderately deep water ($2000 - 3000\,ft$) and their design constitutes an important problem of Offshore Structural Engineering. This type of construction makes use of tubular members which are subjected to a combination of structural loads and external pressure. Under such loading conditions, tubular members may buckle with catastrophic consequences for the structure. The present work is motivated by the need for accurate prediction of unstiffened and ring-stiffened tubular member capacity under combined loads consisting of bending, axial force and external pressure, and is of particular importance in offshore structural design.

1.1 Literature Review

The stability of tubular beam-columns is a challenging problem of Applied Mechanics with great significance in Offshore Structural Engineering. Both experimental and analytical investigations have been conducted during the last two decades and have led to better understanding of the phenomena involved.

1.1.1 Unstiffened Tubes

The bending instability of elastic tubes due to extensive ovalization was first analyzed by Brazier [9]. This type of instability is usually referred to as the "Brazier effect" and is described in detail in [30]. Ades [1] through a numerical technique included inelastic effects, whereas Reissner [48] was the first to examine the case of pressurized bending.

Extensive experimental results were reported in the 70's. The bending behavior of tubes was investigated by Jirsa et al. [27]. Moment-curvature diagrams for values of the diameter-to-thickness (D/t) ratio from about 30 to 80 were reported. Measurements of the increase in ovalization during bending were also obtained. Bouwkamp [8] examined the buckling and post-buckling behavior of tubes under axial loading. The columns tested had a slenderness ratio varying from 40 to 120 and a D/t ratio of 40 to 50. Pure bending tests on tubes were performed by Sherman [50]. Later, Sherman [52], [53] extended his work to the case of combined bending and axial loading. In addition, the need for safe deep-water pipeline installation urged Shell Oil Company and Battelle Colombus Laboratories to conduct experimental as well as analytical research, which gave rise to the well-known Shell and Battelle formulas for pressure-bending interaction [41], [28].

The influence of bending-tension-pressure interaction on tube stability was investigated by Kyriakides and Shaw [32] and Corona and Kyriakides [18], [19] through a series of small-scale tests and a semi-analytical procedure. Tubes were made of aluminum and stainless steel, having a D/t ratio of 18, 24 and 35. Recently, Ju and Kyriakides [33], [29] extended their experimental and analytical research on the phenomenon of local buckling due to bending. Predictions were found to be in good agreement with experiments.

Interesting experimental work concerning the stability of fabricated tubes under axial loading was published by Chen and Ross [14]. The tubes had D/t ratios of 48 and 70 and a slenderness ratio varying from 39 to 83. The most important contribution of this study was the measurement of residual stresses in fabricated tubes.

The beam-column behavior of tubular members was investigated by Erzurumlu et al. [22], [65]. First the moment-curvature curves for different values of axial load ($M - P - \phi$ curves) were obtained from a cross-sectional analysis. The analysis assumed circular cross-section throughout the deformation history and accounted for inelastic effects. Then, the nonlinear beam-column equation was solved using a finite-difference technique. However, this work did not account for the effects of external pressure or the possibility of local buckling.

Extensive analytical work was reported in the 80's by Chen and his associates [54], [55], [61], [62], [63], [64], [13], [11], [12]. Due to the large number of published papers, a summary of the basic features is given below:

- The classical beam-column equation was used:

$$\frac{d^2M}{dx^2} + P\frac{d^2w}{dx^2} = q \tag{1.1}$$

- The moment was related to deformation through $M - P - \phi$ curves (the Tresca yield criterion was employed).
- Several methods of analysis were employed:

  - Newmark's method [61]
  - Collocation method [62]
  - Newton-Raphson's method [24]
  - second-order slope-deflection method [11]

- To account for local buckling, $M - P - \phi$ relationships were revised through a simple kinematic model for cross-sectional deformation [54].
- To account for pressure [64], an initial cross-sectional radial deformation was assumed of the form:

$$w_i = w_o cos2\theta \tag{1.2}$$

Upon application of pressure, this deformation was amplified as follows

$$w = w_i \frac{1}{1 - p/p_e} \tag{1.3}$$

Using the above cross-sectional shape, the $M - P - \phi - p$ relationships were derived.

In 1985, a series of large-scale test programs began, in order to determine the ultimate capacity of unstiffened fabricated tubes which were candidates for use in offshore applications. The loading conditions included compression - bending - pressure interaction. More specifically:

- Stub Column Tests were performed by CBI [17]. 66 specimens made of ASTM A315 (ERW) material, having D/t of 41, 58 and 74, were tested. The purpose of this work was to determine the strength interaction curve (cross-sectional behavior).

- Long Column Tests were performed by CBI [15] and SwRI [57]. 36 specimens made of ASTM A315 (ERW) and API 5L Grade X42 were tested. They had D/t ratios of 42 and 63 and slenderness ratios of 50 and 72. The tubes were first pressurized, then subjected to a radial sequence of compression and bending increments. No measurements of the residual stress distribution were taken.

1.1.2 Stiffened Tubes

The use of stiffened tubes was motivated by the needs of the oil industry for deep-water tower construction. Stiffeners are in the form of rings and their main purpose is the increase of member capacity under external pressure.

So far, the research work on stiffened tubes has been experimental. More specifically, fabricated tubes that are candidates for deep-water applications have been tested by CBI and SwRI [38], [39], [16]. The tubes had a diameter-to-thickness ratio ranging from 31 to 96 and they were subjected to a combination of external pressure and axial load. The materials of the specimens were A36, A633 and A572 steel. These experiments were used to develop the API formulas for stiffened tubes under external pressure and axial force.

According to the specification rules [5], the presence of stiffeners affects only the capacity against pressure. For a given tube under combined loading of pressure, axial load and bending, the ultimate pressure is affected by the stiffener spacing, whereas the ultimate axial force and moment depend primarily on the characteristics of the unstiffened tube. However, it has been recognized [30] that an important factor affecting the bending capacity of tubes is cross-sectional ovalization. Therefore, it is believed that the presence of stiffeners will increase the ultimate moment, by restraining cross-section ovalization. This increase is expected to be more significant in the case of pressurized bending. Unfortunately, there are no experimental data on the bending response of stiffened tubes.

The available experimental data are based on *externally* stiffened tubes. On the other hand, the tubes which are candidates for deep-water applications will be *internally* stiffened. Apparently, internal stiffeners are stiffer than external stiffeners of the same radial dimension because they have a smaller average diameter (the in-plane stiffness of a ring against ovalization depends on the third power of the diameter-to-thickness ratio [60]). Therefore, they are expected to have a more beneficial effect on the member ultimate capacity than external stiffeners.

1.2 Scope of Present Work

The present work is aimed at developing a rigorous analytical technique in order to investigate the stability of tubular unstiffened and stiffened beam-columns under structural loads and external pressure. The first goal is to establish the validity of the technique by comparison with the experimental data of CBI and SwRI. A point of particular interest in this study is the effect of residual stresses and initial imperfections on member stability.

A tube element, which combines the cross-sectional ovalization with the longitudinal deformation, has been developed for the purposes of this analysis. In addition, the nine-node isoparametric shell element, introduced elsewhere [31], [56] for nonlinear analysis, is also used in this study.

A very important contribution of this research is the development and use of an analytical technique for the ultimate capacity prediction of ring-stiffened tubes under combined loading. The available literature on this topic is entirely experimental and limited to the case of pressure-axial load interaction. For the rigorous analysis of such tubes, a special element, referred to as stiffener element, has been developed as an additional layer of the tube element. The basic ideas concerning the implementation of the finite element technique are presented in the next chapter.

Finally, this work examines the accuracy of the existing design formulas. Analytical results and experimental data are compared with the new API-LRFD Draft specification [5], as well as with several other design equations from Refs. [3], [35] and [21]. Particular emphasis is given to the effects of pressure on the ultimate capacity of tubular beam-columns. It is believed that the present research effort will contribute to safer and more efficient design of offshore compliant towers.

Chapter 2

Technique

In this chapter, the implementation of the finite element procedure for the purposes of the present study is described. Two types of element are employed: a shell element formulated as a degenerated solid element and used extensively in previous work on stability of pipelines [31], [56], [30] and a tube element which has been developed for the purposes of this research. In addition, a variant of the tube element, referred to as stiffener element, is implemented for the rigorous implementation of ring stiffeners. This element is a variation of the tube element, capable of simulating both internal and external stiffeners. For the development of the finite element technique, basic ideas of tensor analysis and continuum mechanics are necessary. These are summarized in Ref. [30]. A complete treatment of continuum mechanics can be found in the books of Gurtin [23] and Malvern [36].

2.1 Basics of Finite Element Implementation

The formulation adopts a Lagrangian description of the tube using the convected-coordinate formulation presented by Needleman [42]. Nonlinear kinematics (large displacements and strains) can be modeled in this approach. The material behavior is described through a J_2-flow theory of plasticity for large deformations with isotropic hardening. The choice of hardening rule is based on the monotonic nature of the loading path. The constitutive equations relate the convected rate of the Kirchhoff stress tensor $\overset{\circ}{\boldsymbol{\tau}}$ to the rate-of-deformation tensor $\boldsymbol{d}$ through the relationship

$$\overset{\circ}{\boldsymbol{\tau}} = \boldsymbol{\mathcal{R}}\boldsymbol{d} = (\boldsymbol{\mathcal{D}} - \boldsymbol{\mathcal{L}})\boldsymbol{d} \tag{2.1}$$

where $\boldsymbol{\mathcal{D}}$ is the elastoplastic rigidity and $\boldsymbol{\mathcal{L}}$ is the geometric rigidity. The basic requirement of shell theory that the traction component normal to any lamina be zero is imposed on the constitutive equations.

The implementation is based on the principle of virtual work. Assume a deformable body and let $\boldsymbol{x}$ be the position vector of an arbitrary point in a certain equilibrium configuration. If ξ^1, ξ^2, ξ^3 are the convected material coordinates, then the base vectors are defined as

$$\boldsymbol{g}_k = \frac{\partial \boldsymbol{x}}{\partial \xi^k} \tag{2.2}$$

Let $\boldsymbol{x}'$ be the position vector in a nearby configuration. Then the incremental displacement field is

$$\boldsymbol{\Delta u} = \boldsymbol{x}' - \boldsymbol{x} \tag{2.3}$$

Let $\boldsymbol{\delta u}$ be the virtual displacement field, $\boldsymbol{t}'$ the traction on the surface B of the body in the nearby configuration and V_o the volume of the body in a reference (undeformed) configuration. Then, the linearized equation of virtual work may be stated as [31]

$$\begin{aligned} &\int_{V_o} \delta U_{i|j} S^{ijkl} \Delta U_{k|l} \, dV_o \\ = &\int_B \boldsymbol{\delta u} \cdot \boldsymbol{t}' \, dB - \int_{V_o} \delta U_{i|j} \hat{\sigma}^{ji} \, dV_o \end{aligned} \tag{2.4}$$

where $\hat{\sigma}^{ij}$ are the components of the referential (nominal) stress tensor, $\boldsymbol{G}_k$ are the base vectors in the reference configuration, tensor $\boldsymbol{S}$ is defined as

$$S^{ijkl} = (\boldsymbol{G}^i \cdot \boldsymbol{g}_n) R^{njml} (\boldsymbol{G}^k \cdot \boldsymbol{g}_m) + \tau^{jl} G^{ik} \tag{2.5}$$

τ^{ij} are the components of the Kirchhoff stress tensor with respect to the $\boldsymbol{g}_i \otimes \boldsymbol{g}_j$ (current) basis and

$$\delta U_{k|j} = \frac{\partial(\delta \boldsymbol{u})}{\partial \xi^j} \cdot \boldsymbol{G}_k \tag{2.6}$$

$$\Delta U_{k|j} = \frac{\partial(\Delta \boldsymbol{u})}{\partial \xi^j} \cdot \boldsymbol{G}_k \tag{2.7}$$

Using a finite element discretization and adopting matrix notation, the displacement field can be written as

$$\boldsymbol{\Delta}\mathbf{u} = \mathbf{N}\,\boldsymbol{\Delta}\mathbf{U} \tag{2.8}$$

in which $\mathbf{N}$ is the interpolation matrix and $\boldsymbol{\Delta}\mathbf{U}$ contains the increments of nodal degrees of freedom. Differentiating the incremental displacement field and taking components on the reference base vectors, one finds

$$grad(\boldsymbol{\Delta}\mathbf{u}) = \mathbf{B}\,\boldsymbol{\Delta}\mathbf{U} \tag{2.9}$$

where $\mathbf{B}$ contains the derivatives of the elements of the interpolation matrix. Likewise,

$$\delta\mathbf{u} = \mathbf{N}\,\delta\mathbf{U} \tag{2.10}$$

and

$$grad(\delta\mathbf{u}) = \mathbf{B}\,\delta\mathbf{U} \tag{2.11}$$

In matrix form, Equation 2.5 becomes

$$\mathbf{S} = \mathbf{W}^T\mathbf{R}\mathbf{W} + \mathbf{C} \tag{2.12}$$

Thus, the basic Equation 2.4 provides the element stiffness matrix

$$\mathbf{K} = \int_{V_o^e} \mathbf{B}^T\mathbf{S}\mathbf{B}\; dV_o^e \tag{2.13}$$

and the element external and internal load vectors:

$$\mathbf{P}_{ext} = \int_{B^e} \mathbf{N}^T \mathbf{t}' \, dB^e \tag{2.14}$$

and

$$\mathbf{P}_{int} = \int_{V_o^e} \mathbf{B}^T \mathbf{W}^T \tau \, dV_o^e \tag{2.15}$$

2.2 Pressure Effects on Stiffness Matrix

Consider the deformable body at the nearby configuration $\boldsymbol{x}'$ specified by Equation 2.3. The body is subjected to uniform external pressure p'. The traction due to pressure can be written as

$$\boldsymbol{t}' = -p'\boldsymbol{n}' \tag{2.16}$$

and the corresponding term on the virtual work equation becomes

$$-p' \int_{B'} \delta\boldsymbol{u} \cdot \boldsymbol{n}' \, dB' \tag{2.17}$$

It is possible to obtain first order approximations of the integral over B'. However, these terms are not considered in the present formulation because they disturb the desirable symmetry of the stiffness matrix. In order to preserve the symmetry, the following approximation is made

$$\boldsymbol{t}' \simeq -p'\boldsymbol{n} \tag{2.18}$$

and the integral 2.17 over B' is transformed to an integral over B.

Using the above approximation, the contribution of external pressure to the stiffness matrix is totally neglected. However, it has been observed

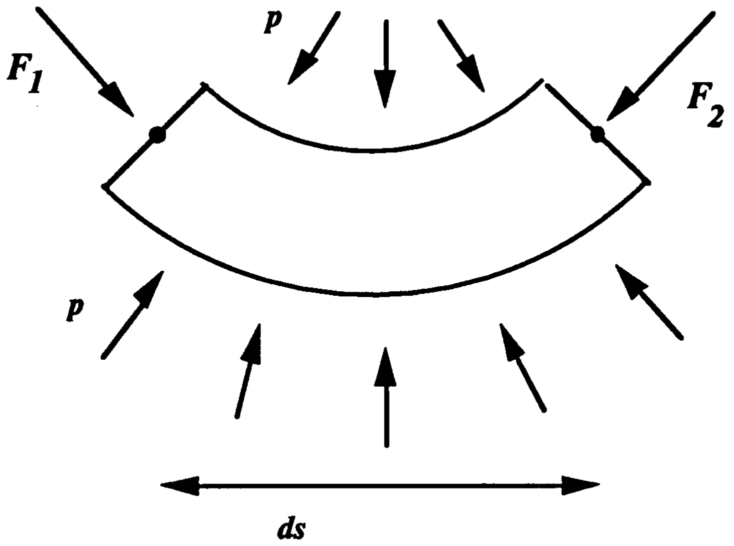

Figure 2.1: Longitudinal portion of tube subjected to external pressure.

elsewhere [26], that this contribution is very important in order to achieve numerical convergence in analyzing slender tubes under high levels of pressure. It is possible to account for the pressure effects on the stiffness matrix through an "indirect" method outlined below for the particular case of a tubular member.

Consider the longitudinal tube portion shown in Figure 2.1 at the nearby configuration $\boldsymbol{x}'$. The tube is subjected to hydrostatic pressure with capped-end forces $\boldsymbol{F}_1$ and $\boldsymbol{F}_2$, which can be expressed as follows

$$\boldsymbol{F}_1 = (pA)\,\boldsymbol{s} \tag{2.19}$$

and

$$\boldsymbol{F}_2 = -\,(pA)\,(\boldsymbol{s} + d\boldsymbol{s}) \tag{2.20}$$

where $\boldsymbol{s}$ is the unit vector tangent to the longitudinal tube axis

$$\boldsymbol{s} = \frac{d\boldsymbol{x}'}{ds} \tag{2.21}$$

A is the tube cross-sectional area and s is the longitudinal tube coordinate. For the sake of simplicity, the cross section is assumed to remain undeformed. From equilibrium,

$$d\boldsymbol{F}_l + \boldsymbol{F}_1 + \boldsymbol{F}_2 = 0 \tag{2.22}$$

and, hence, the lateral force is equal to

$$d\boldsymbol{F}_l = (pA)\, d\boldsymbol{s} \tag{2.23}$$

Consequently, the contribution of pressure to the principle of virtual work is

$$\delta W = \left[\int_0^L (pA)\, \delta\boldsymbol{u} \cdot d\boldsymbol{s}\right] + (pA)(\boldsymbol{s}_0 \cdot \delta\boldsymbol{u}_0) - (pA)(\boldsymbol{s}_L \cdot \delta\boldsymbol{u}_L) \tag{2.24}$$

where L is the tube length and $\boldsymbol{s}_0$, $\boldsymbol{s}_L$ are the tangent unit vectors at the two tube ends. Integrating by parts the above expression, one obtains

$$\delta W = -(pA) \int_0^L \frac{d(\delta\boldsymbol{u})}{ds} \cdot \frac{d(\boldsymbol{x} + \Delta\boldsymbol{u})}{ds}\, ds \tag{2.25}$$

Using a finite-element dicretization and adopting matrix notation (see Equations 2.8 - 2.11), it can be easily shown that the contribution of pressure to the element stiffness matrix is

$$\mathbf{K}_p = (pA) \int_{-1}^{1} \left(\frac{d\mathbf{N}}{d\zeta}\right)^T \left(\frac{d\mathbf{N}}{d\zeta}\right) \left(\frac{d\zeta}{ds}\right) d\zeta \tag{2.26}$$

where $\mathbf{N}$ is the interpolation matrix and ζ is the natural longitudinal coordinate. Note that, for the case of external pressure, this matrix is always non-negative and, when added to the stiffness matrix, it is expected to accelerate convergence in slender-tube analysis problems.

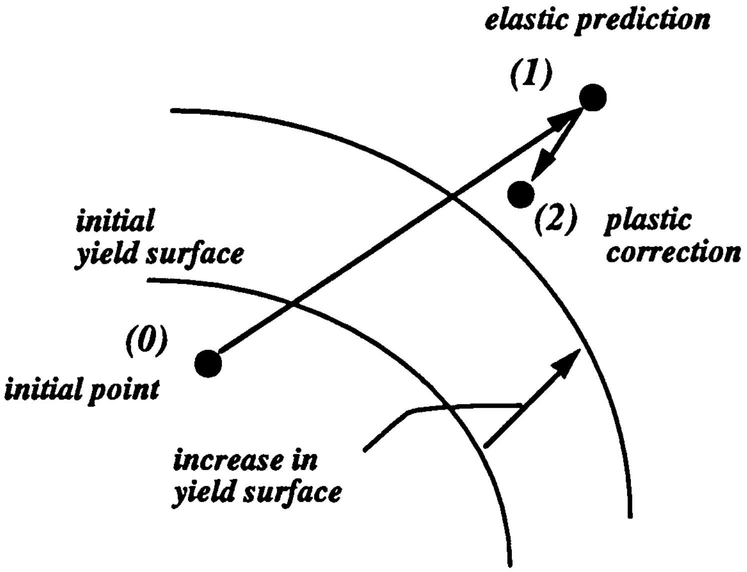

Figure 2.2: Schematic representation of integration of plasticity equations.

2.3 Integration of Constitutive Equations

For the integration of the constitutive equations two methods have been employed. The first is the Euler-backward substitution method described in detail in Ref. [31] and is a generalization of the well-known radial-return method for large strain plasticity. The second method, an elastic predictor-plastic corrector scheme, is aimed at reducing the high computational cost of the radial-return method. First, the method is outlined for small strain plasticity. Then the algorithm equations as adapted for large strains and zero radial stress (in agreement with shell theory) are presented. A detailed account of this method with proof of the algorithm equations can be found in Ref. [43].

2.3.1 Small-Strain Plasticity

It is assumed that the material follows a J_2 flow rule (von Mises) with isotropic hardening. The yield surface is given by

$$F = Y - \sigma_y(\hat{\epsilon}_p) = \sqrt{\frac{3}{2}\mathbf{s}\cdot\mathbf{s}} - \sigma_y(\hat{\epsilon}_p) = 0 \tag{2.27}$$

where $\mathbf{s}$ is the deviatoric stress tensor and $\hat{\epsilon}_p$ is a measure of the total plastic deformation:

$$\hat{\epsilon}_p = \int_0^t \sqrt{\frac{2}{3}d\epsilon^p \cdot d\epsilon^p} \tag{2.28}$$

Suppose that, at the beginning of the step, state parameters correspond to point (0) (see Figure 2.2). We want to calculate the new state parameters for a given strain increment $\Delta\epsilon^{(0)}$. The algorithm starts with the elastic prediction of stresses:

$$\sigma^{(1)} = \sigma^{(0)} + \mathcal{E}\,\Delta\epsilon^{(0)} \tag{2.29}$$

where $\mathcal{E}$ is the elastic rigidity tensor. State (1) will be the final one if point (1) is within the yield surface. If not, then an elasto-plastic correction $\Delta\sigma$ is necessary so that the corrected point (2) falls onto the yield surface:

$$\sigma^{(2)} = \sigma^{(1)} + \Delta\sigma \tag{2.30}$$

$$\hat{\epsilon}_p^{(2)} = \hat{\epsilon}_p^{(1)} + \Delta\hat{\epsilon}_p \tag{2.31}$$

In this method, the stress correction $\Delta\sigma$ is assumed to occur under zero total strain increment. Therefore,

$$\Delta\sigma = \mathcal{E}\,(\Delta\epsilon - \Delta\epsilon^p) = -\mathcal{E}\,\Delta\epsilon^p \tag{2.32}$$

Using the normality rule imposed by Drucker's postulate,

$$\Delta\epsilon^p = \Delta\lambda\;\mathbf{s}^{(1)} \tag{2.33}$$

and thus,

$$\Delta\hat{\epsilon}_p = \Delta\lambda \sqrt{\frac{2}{3}\mathbf{s}^{(1)} \cdot \mathbf{s}^{(1)}} \tag{2.34}$$

In order for state (2) to be on the yield surface, it must satisfy the yield criterion 2.27. Expanding Equation 2.27 about state (1) and keeping only linear terms one finds

$$F(1) + \left(\frac{\partial F}{\partial \sigma}\right)_{(1)} \cdot \Delta\sigma + \left(\frac{\partial F}{\partial \hat{\epsilon}_p}\right)_{(1)} \cdot \Delta\hat{\epsilon}_p = 0 \tag{2.35}$$

It is easily shown that

$$\frac{\partial F}{\partial \sigma} = \frac{3}{2Y}\mathbf{s} \tag{2.36}$$

and

$$\frac{\partial F}{\partial \hat{\epsilon}_p} = -\frac{d\sigma_y}{d\hat{\epsilon}_p} \tag{2.37}$$

Note that Equation 2.35 is a linear equation in terms of $\Delta\lambda$. Therefore, solving for $\Delta\lambda$, the state parameters at point (2) can be calculated through 2.32, 2.34 and 2.30, 2.31. A check is then made as to whether state (2) satisfies the yield criterion. If the criterion is satisfied, then state (2) is the final state. If not, iteration is necessary by setting state (2) equal to state (1), until state (2) falls on the yield surface.

2.3.2 Algorithm for Large Strains and Zero Radial Stress

Consider initial point (0) of state parameters. Assume that $\tau^{(0)^{ij}}$ are the components of the Kirchhoff stress tensor and $d^{p^{(0)}}$ the effective plastic strain at the initial stress state (0) at the beginning of the step. Moreover, $\boldsymbol{g}_k^{(0)}$ $(k = 1, 2, 3)$ are the corresponding base vectors. Given the base vectors $\boldsymbol{g}_k$ $(k = 1, 2, 3)$ at the current configuration (end of the step), the components of the Kirchhoff stress tensor and the effective plastic strain are calculated at the end of the step. The algorithm starts with the elastic prediction of stresses. More specifically,

$$\tau^{(1)^{ij}} = \tau^{(0)^{ij}} + (\mathcal{E}^{(1)^{ijkl}} - \mathcal{L}^{(1)^{ijkl}})\Delta E^{(0)}_{kl} \tag{2.38}$$

where

$$\Delta E^{(0)}_{kl} = \frac{1}{2}\left(g_{kl} - g^{(0)}_{kl}\right) \tag{2.39}$$

are the components of the increment of Lagrangian strain tensor

$$\mathcal{E}^{ijkl} = G\left(g^{ik}g^{jl} + g^{il}g^{jk}\right) + \lambda g^{ij}g^{kl}$$

$$\mathcal{L}^{ijkl} = \frac{1}{2}\left(g^{ik}\tau^{jl} + g^{jk}\tau^{il} + g^{il}\tau^{jk} + g^{jl}\tau^{ik}\right)$$

are the components of the elastic rigidity and $\Delta E^{(0)}_{33}$ is considered unknown so that $\Delta\tau^{(0)}_{33} = 0$. Having obtained the stresses at the "trial" state (1) the point is checked to determine if it is within or outside the yield surface. The effective trial stress is

$$Y_{(1)} = \left(\frac{3}{2}\, g_{ik}\, g_{jl}\, s^{(1)^{ij}} s^{(1)^{kl}}\right)^{1/2} \tag{2.40}$$

where

$$s^{(1)^{ij}} = \tau^{(1)^{ij}} - \frac{1}{3}g^{ij}g_{kl}\,\tau^{(1)^{kl}} \tag{2.41}$$

Therefore, if $Y_{(1)} \leq Y_{max}(d^{p(0)})$ then elastic behavior was correctly assumed and the final state is indeed state (1). If this inequality is not satisfied, an elastoplastic correction $\Delta\tau^{ij}$ and Δd^{p} of the state parameters is required so that the final point falls on the yield surface. Extending the idea presented in the previous section, the correction is performed under the condition that states (1) and (2) have the same base vectors $\boldsymbol{g}_k$.

After some manipulations, it can be shown that

$$\Delta\tau^{ij} = \frac{3G}{Y_{(1)}}\left(\mathcal{D}^{(e)ij33}_{(1)}\frac{s^{(1)^{33}}}{\mathcal{D}^{(e)3333}_{(1)}} - s^{(1)^{ij}}\right)\Delta d^p \tag{2.42}$$

and

$$\Delta d^p = \frac{Y_{(1)} - Y_{max}}{H_{(1)} + A} \tag{2.43}$$

where

$$A = 3G\left[1 - \frac{3G}{\mathcal{D}^{(e)3333}_{(1)}}\left(\frac{s^{(1)^{33}}}{Y_{(1)}}\right)^2\right]$$

$\mathcal{D}^{(e)ijkl}_{(1)}$ is the elastic rigidity tensor components at state (1) and

$$H_{(1)} = \left(\frac{dY_{max}}{dd^p}\right)_{(1)}$$

is the plastic modulus evaluated at state (1). Consequently,

$$\tau^{ij(2)} = \tau^{ij(1)} + \Delta\tau^{ij} \tag{2.44}$$

$$d^{p(2)} = d^{p(1)} + \Delta d^p \tag{2.45}$$

are the state parameters at stage (2). If state (2) does not satisfy the yield criterion, the procedure is repeated by setting state (2) equal to state (1).

2.4 Residual Stresses

The forming process of fabricated tubes clearly introduces circumferential residual stresses which vary along the thickness of the pipe, while the longitudinal seam is responsible for longitudinal residual stresses. It is well known that residual stresses have an important effect on member stability [58]. The present formulation has the capability to account for residual stresses and examine their effect on tube stability. Residual stress distributions in both the circumferential and the longitudinal directions have been proposed by Chen and Ross [14]. These distributions are based on actual measurements and are depicted in Figure 2.3. The circumferential distribution implies a variation of residual stresses through the thickness but not along the circumference, and the maximum residual stress is equal to 35% of the yield stress. On the other hand, the longitudinal stress distribution has a maximum value equal to the yield stress at the position of the seam and implies a variation along the circumference. For the longitudinal residual stresses, another distribution shown in Figure 2.4 has been proposed by Sherman et al. [51] with a maximum value of 80% of the yield stress. The two distributions for longitudinal residual stresses are compared in terms of their net force and moment in Table 2.1. The net force and moment are normalized by the yield force P_y and the plastic moment M_p respectively.

	net norm. thrust	net norm. moment
Chen and Ross [14]	0.000	-0.011
Sherman et al. [51]	0.050	0.058

Table 2.1: Comparison between the two residual stress distributions.

It can be seen that the distribution by Chen and Ross [14] has significantly lower values of net stress resultants and will be used almost exclusively in the present study.

Finally, it should be mentioned that in the recently published work of Prion and Birkemoe [45], longitudinal residual strain measurements on fabricated tubes are reported. These residual strains, when multiplied by Young's

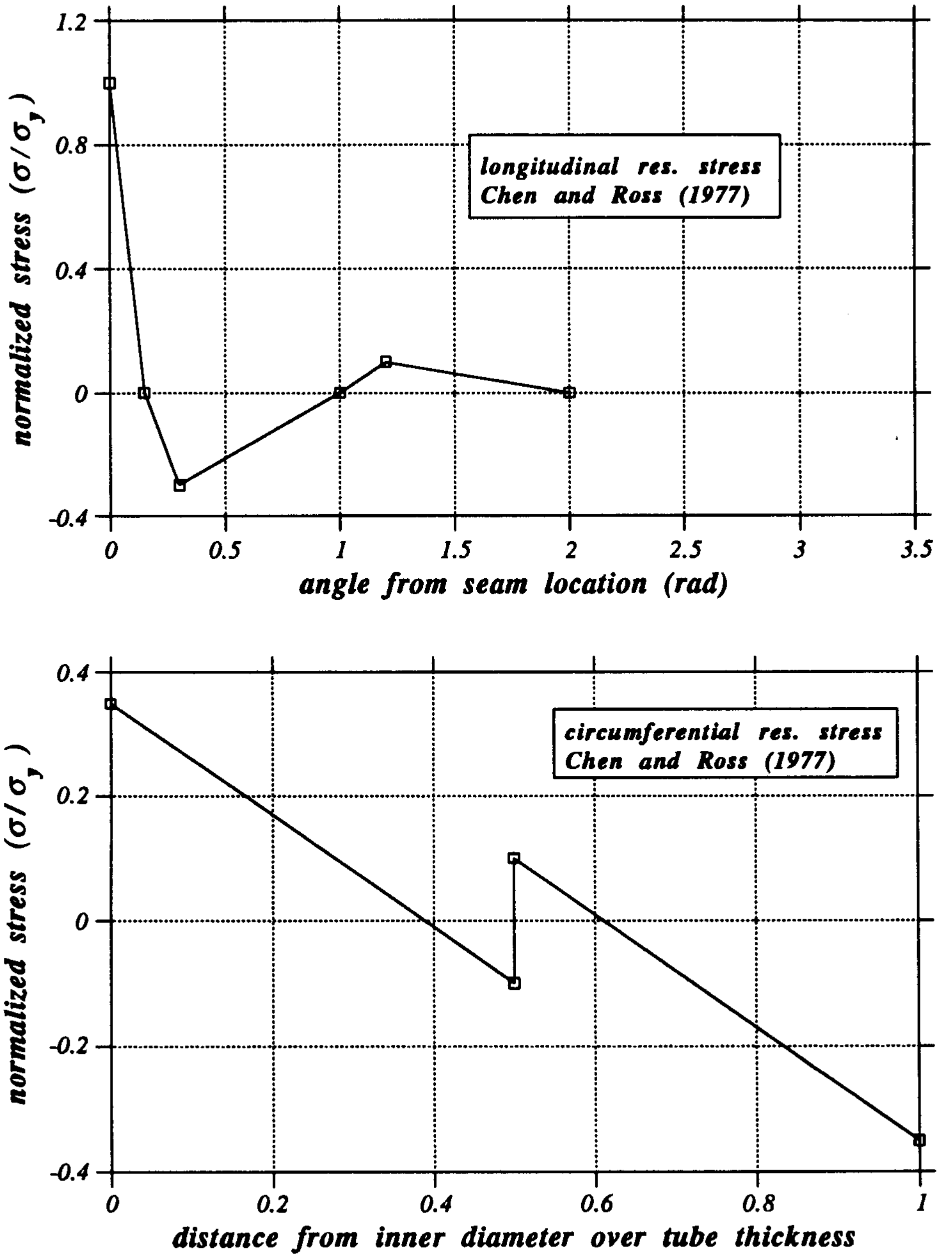

Figure 2.3: Residual stress distributions proposed by Chen and Ross.

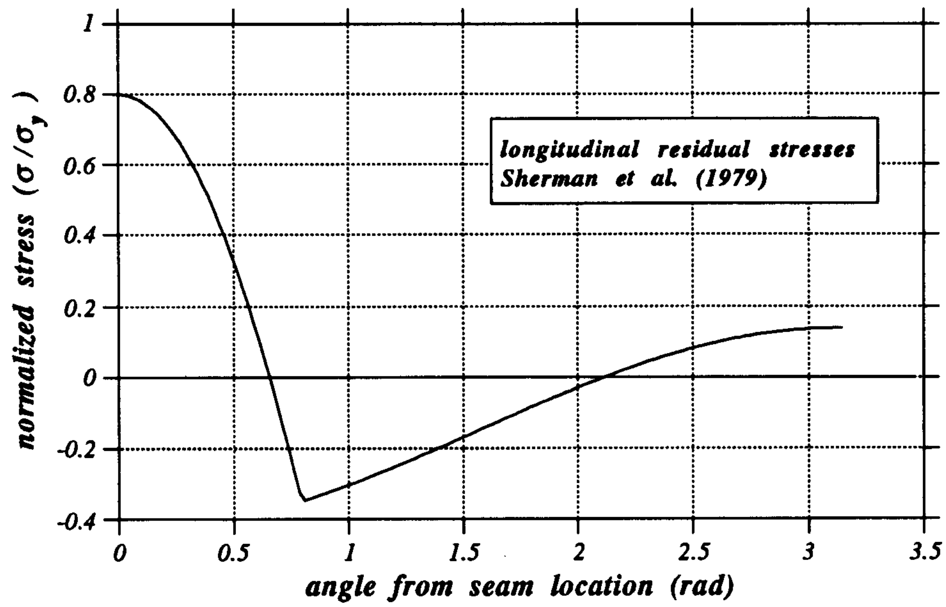

Figure 2.4: Longitudinal residual stress distribution proposed by Sherman et al.

modulus, provide a residual stress distribution very similar to the one measured by Chen and Ross [14].

2.5 Shell Finite Element

The shell element used in this study has been applied to problems of pipeline stability in Refs. [31], [56] and [30]. It is a nine-node isoparametric degenerated shell element with Lagrangian quadratic interpolation. Figure 2.5 shows the original element and a multilayered version which is used to simulate tubes of arbitrary thickness, as well as ring stiffeners. Each node has a triplet of orthonormal vectors $\boldsymbol{q}_1$, $\boldsymbol{q}_2$ and $\boldsymbol{q}_3$, so that $\boldsymbol{q}_3$ is directed through the thickness and

$$\boldsymbol{q}_3 = \boldsymbol{q}_1 \times \boldsymbol{q}_2 \tag{2.46}$$

There are five degrees of freedom associated with every node: three translational and two rotational about vectors $\boldsymbol{q}_1$ and $\boldsymbol{q}_2$. Therefore, the element has 45 degrees of freedom.

The geometry of the element is expressed as

$$\boldsymbol{x}(\xi^1, \xi^2, \xi^3) = \sum_{k=1}^{9} [(\boldsymbol{x}^{(k)} + \xi^3 t \boldsymbol{q}_3^{(k)}) N^{(k)}(\xi^1, \xi^2)] \tag{2.47}$$

where t denotes the shell thickness and $N^{(k)}$, $k = 1, \cdots, 9$, are the nodal Lagrangian shape functions (see the book by Zienkiewicz [66]).

The numerical integration is performed using a 2×2 underintegration scheme in the $\xi^1 - \xi^2$ plane and 5 Gauss points through the thickness (ξ^3-direction). Coordinate directions ξ^1, ξ^2, ξ^3 are shown in Figure 2.6.

The details of the formulation for this element can be found in Ref. [30].

2.6 Tube Finite Element

This element was developed as an alternative to the shell element and is based on the idea of combining longitudinal and cross-sectional deformation as shown in Figure 2.7.

The concept of isoparametric finite element is used to describe the longitudinal deformation. Nodes are defined along the tube and the geometry and displacements are interpolated using quadratic polynomials. Symmetry of the tube is assumed with respect to the x_2-x_3 plane (uniaxial bending), and therefore, the position and orientation of every node (k) is defined through three degrees of freedom (see Figure 2.8): two translational ($u_2^{(k)}$ and $u_3^{(k)}$ in

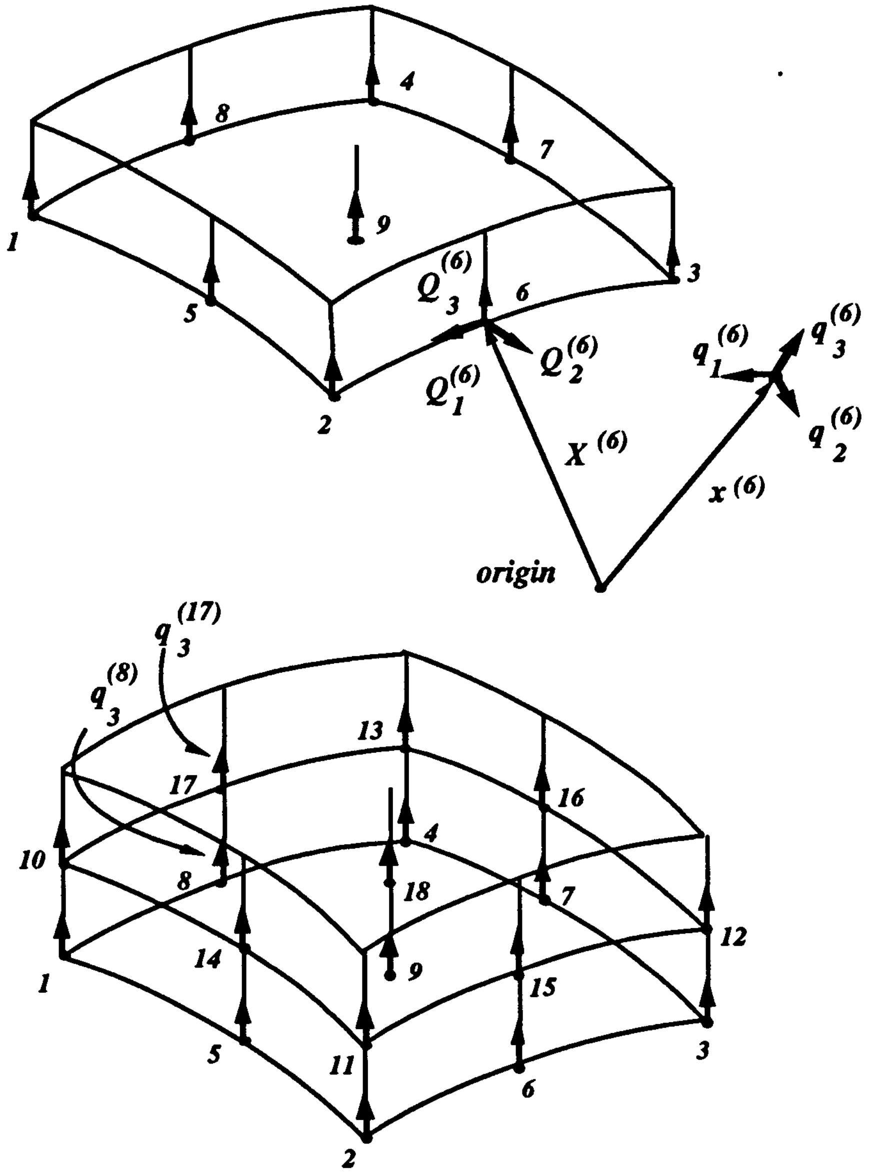

Figure 2.5: Nine-node shell element and multilayered shell element.

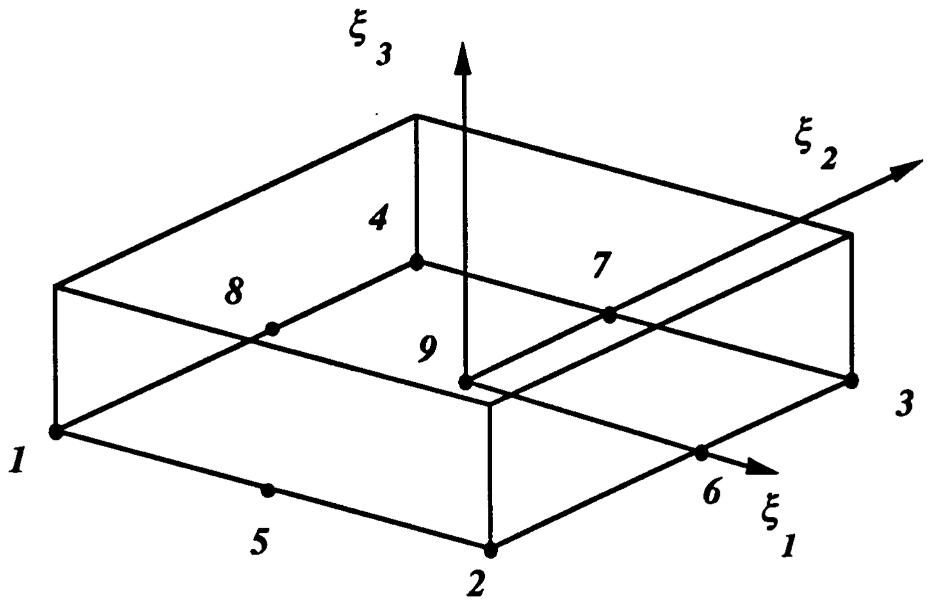

Figure 2.6: Local coordinates for shell element.

the direction of x_2 and x_3 axes respectively) and one rotational ($\theta_1^{(k)}$ about x_1 axis). Three-node elements with quadratic interpolation functions are used in this analysis. The deformed centerline of the tube (tube axis), which contains the element nodes, is defined by

$$\boldsymbol{x}_c(\zeta) = \sum_{k=1}^{3} \boldsymbol{x}^{(k)} N^{(k)}(\zeta) \tag{2.48}$$

where ζ is the longitudinal material coordinate and $N^{(k)}(\zeta)$ are the Lagrangian quadratic polynomial functions.

To describe the cross-sectional deformation:

- a reference line is chosen within the cross-section.
- the thickness is assumed to remain constant.

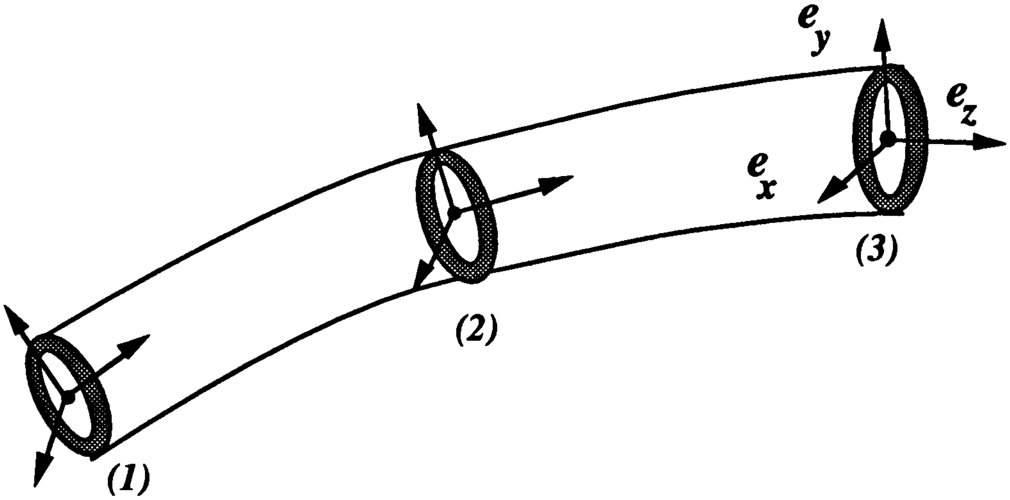

Figure 2.7: Tube finite element.

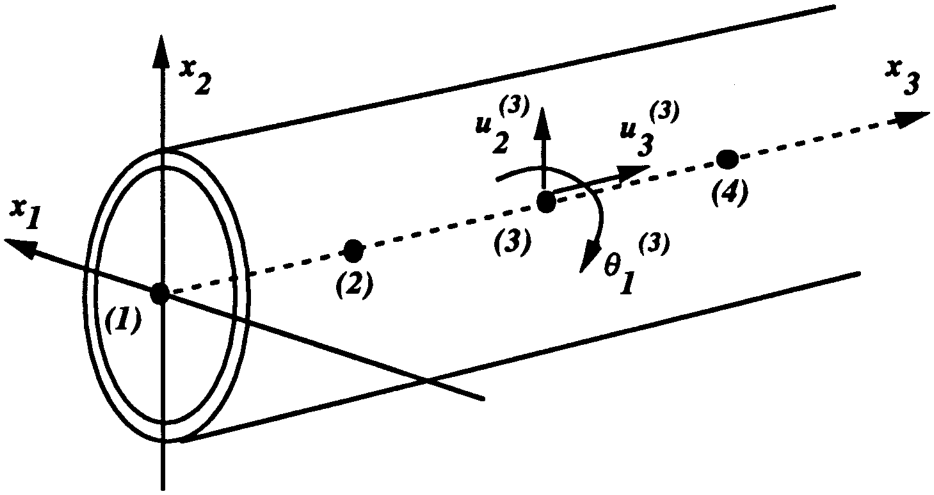

Figure 2.8: Node arrangement using tube elements.

- sections which are plane in the undeformed configuration remain plane throughout the deformation history, but are free to deform within their plane (this assumption will be revised to include warping of the cross sections)
- while a cross section deforms, fibers initially normal to the reference line remain normal to the reference line.
- ρ is the variable (material coordinate) and w the corresponding displacement through the thickness.
- θ is the variable (material coordinate) along the circumference and v the corresponding displacement.

Consider the cross-section which corresponds to node k. The position of the reference line of the pipe in this cross-section is defined as:

$$\boldsymbol{x}^{(k)} + \boldsymbol{r}^{(k)}(\theta) \tag{2.49}$$

where $\boldsymbol{x}^{(k)}$ is the position vector of node (k) and $\boldsymbol{r}^{(k)}(\theta)$ is the vector from node (k) to the arbitrary point on the reference surface. Note that $\boldsymbol{r}^{(k)}(\theta)$ is always on the cross-sectional plane. From Figure 2.9, we can write

$$\boldsymbol{r}^{(k)}(\theta) = x_r(\theta)\boldsymbol{e}_x^{(k)} + y_r(\theta)\boldsymbol{e}_y^{(k)} \tag{2.50}$$

where $\boldsymbol{e}_x^{(k)}$ and $\boldsymbol{e}_y^{(k)}$ are the unit vectors along the local axes x and y at node (k).

Let $\boldsymbol{n}^{(k)}$ be the outward unit normal vector of the pipe surface at node (k). Then, the geometry is defined as follows:

$$\boldsymbol{x}(\theta, \zeta, \rho) = \sum_{k=1}^{3} [(\boldsymbol{x}^{(k)} + \boldsymbol{r}^{(k)} + \rho\boldsymbol{n}^{(k)})N^{(k)}(\zeta)] \tag{2.51}$$

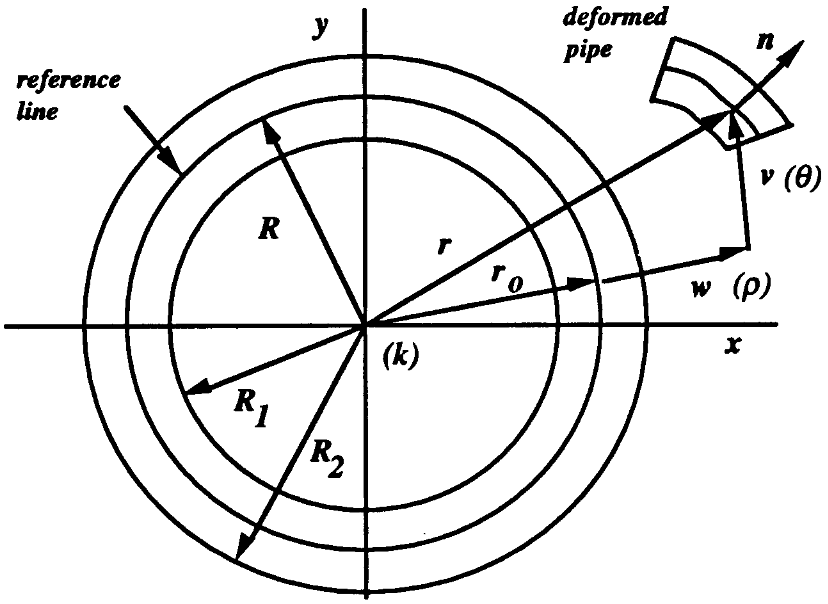

Figure 2.9: Cross-sectional ovalization parameters.

Following the formulation by Brush and Almroth [10], the position vector of the reference line at the current configuration can be expressed in terms of the radial and tangential displacements as follows:

$$\begin{aligned} x_r = & \quad (R+w)cos\theta - vsin\theta \\ y_r = & \quad (R+w)sin\theta + vcos\theta \end{aligned} \tag{2.52}$$

The outward unit normal can be written in terms of the position vector of the reference line:

$$n_x = \frac{(dy_r/d\theta)}{(ds_r/d\theta)} \tag{2.53}$$

$$n_y = -\frac{(dx_r/d\theta)}{(ds_r/d\theta)} \tag{2.54}$$

where n_x and n_y are the components of the unit normal vector with respect to the local axes x and y and

$$ds_r = \sqrt{dx_r^2 + dy_r^2} \tag{2.55}$$

It is now easy to write the components of $\boldsymbol{n}$ in terms of the radial and tangential displacements of the reference line:

$$\frac{dy_r}{d\theta} = -(R + w + v^{'})sin\theta + (w^{'} - v)cos\theta \tag{2.56}$$

$$\frac{dx_r}{d\theta} = -(R + w + v^{'})cos\theta - (w^{'} - v)sin\theta \tag{2.57}$$

$$\frac{ds_r}{d\theta} = \sqrt{R^2 + 2R(v' + w) + (v' + w)^2 + (w' - v)^2} \tag{2.58}$$

The basic Equation 2.51 can be rewritten as:

$$\boldsymbol{x}(\theta, \zeta, \rho) = \sum_{k=1}^{3}[(\boldsymbol{x}^{(k)} + (x_r + \rho n_x)\boldsymbol{e}_x^{(k)} + (y_r + \rho n_y)\boldsymbol{e}_y^{(k)})N^{(k)}(\zeta)] \tag{2.59}$$

The base vectors are computed by differentiating the above expression with respect to the material coordinates θ, ζ and ρ:

$$\boldsymbol{g}_\theta = \frac{\partial \boldsymbol{x}}{\partial \theta} = \sum_{k=1}^{3}[((x_r^{'} + \rho n_x^{'})\boldsymbol{e}_x^{(k)} + (y_r^{'} + \rho n_y^{'})\boldsymbol{e}_y^{(k)})N^{(k)}(\zeta)] \tag{2.60}$$

$$\boldsymbol{g}_\zeta = \frac{\partial \boldsymbol{x}}{\partial \zeta} = \sum_{k=1}^{3}[(\boldsymbol{x}^{(k)} + (x_r + \rho n_x)\boldsymbol{e}_x^{(k)} + (y_r + \rho n_y)\boldsymbol{e}_y^{(k)})\frac{dN^{(k)}(\zeta)}{d\zeta}] \tag{2.61}$$

$$\boldsymbol{g}_\rho = \frac{\partial \boldsymbol{x}}{\partial \rho} = \sum_{k=1}^{3}[(n_x\boldsymbol{e}_x^{(k)} + n_y\boldsymbol{e}_y^{(k)})N^{(k)}(\zeta)] \tag{2.62}$$

Assume a Fourier series expansion of the radial and tangential displacements such that

$$w = a_o + a_1\, sin\theta + \sum_{n=2,4,6,\ldots} a_n\, cosn\theta + \sum_{n=3,5,7,\ldots} a_n\, sinn\theta \tag{2.63}$$

$$v = -a_1\, cos\theta + \sum_{n=2,4,6,\ldots} b_n\, sinn\theta + \sum_{n=3,5,7,\ldots} b_n\, cosn\theta \tag{2.64}$$

Because of the symmetry with respect to the $x_2 - x_3$ plane, the non-symmetric terms are omitted from the above expressions. Quantities a_n and b_n are the degrees of freedom for the cross-sectional deformation and will be referred to as *ovalization parameters.*

To form the incremental equilibrium equations, it is necessary to write the velocity vector which is easily obtained by differentiating Equation 2.59 with respect to the time variable. The result of the differentiation is

$$\dot{\boldsymbol{x}} = \sum_{k=1}^{3}[(\dot{\boldsymbol{x}}^{(k)} + (\dot{x}_r + \rho\dot{n}_x)\boldsymbol{e}_x^{(k)} + (\dot{y}_r + \rho\dot{n}_y)\boldsymbol{e}_y^{(k)} + (y_r + \rho n_y)\dot{\boldsymbol{e}}_y^{(k)})N^{(k)}(\zeta)] \tag{2.65}$$

Note that the quantities x_r, y_r, n_x and n_y are functions of the degrees of freedom a_n and b_n. Therefore their time derivatives will be linear functions of $\dot{a}_n$ and $\dot{b}_n$.

It is customary to rewrite Equation 2.65 in terms of the incremental displacements:

$$\Delta\boldsymbol{u} = \sum_{k=1}^{3}[(\Delta\boldsymbol{u}^{(k)} + (\Delta x_r + \rho\Delta n_x)\boldsymbol{e}_x + (\Delta y_r + \rho\Delta n_y)\boldsymbol{e}_y + (y_r + \rho n_y)\Delta\boldsymbol{e}_y)N^{(k)}(\zeta)] \tag{2.66}$$

where

$$\Delta \boldsymbol{u}^{(k)} = \Delta u_2^{(k)} \hat{\boldsymbol{x}}_2 + \Delta u_3^{(k)} \hat{\boldsymbol{x}}_3 \tag{2.67}$$

and

$$\Delta \boldsymbol{e}_y^{(k)} = \Delta \theta_1^{(k)} \boldsymbol{e}_z \tag{2.68}$$

Note that Δx_r,Δy_r, Δn_x and Δn_y are linear functions of Δa_n and Δb_n. If $\mathbf{\Delta U}$ is a column vector containing all the increments of the element degrees of freedom, then Equation 2.66 can be written in matrix form as follows

$$\mathbf{\Delta u}(\theta, \zeta, \rho) = \mathbf{N}\,\mathbf{\Delta U} \tag{2.69}$$

Differentiating the above equations with respect to the material coordinates and taking components with respect to the reference base vectors we obtain

$$grad(\mathbf{\Delta u}) = \mathbf{B}\,\mathbf{\Delta U} \tag{2.70}$$

Having obtained matrices $\mathbf{B}$, $\mathbf{N}$ and the base vectors, we can proceed as in the case of the shell element described in detail in Ref. [31].

With the above formulation, the element does not have the capability of warping deformation, which is important when nonuniform cross-sectional deformation occurs. In order to include warping, the shape functions must be transformed accordingly. The following assumptions are made:

- warping has two components:
    - fiber rotation about the reference line of the cross-section.
    - warping of the reference line itself.

- warping displacements and rotations are assumed to be small (this avoids unnecessary complications in the element formulation).

The position of the reference line is again defined by Equation 2.49 where

$$\boldsymbol{r}^{(k)}(\theta) = x_r(\theta)\boldsymbol{e}_x^{(k)} + y_r(\theta)\boldsymbol{e}_y^{(k)} + z_r(\theta)\boldsymbol{e}_z^{(k)} \tag{2.71}$$

In the above equation x_r and y_r are defined as before and z_r is equal to the out-of-plane displacement $u(\theta)$ shown in Figure 2.10. Furthermore, each fiber is subjected to a rotation $\gamma(\theta)$, about unit vector $\boldsymbol{s}$ which is tangent to the deformed reference line. Then, for small rotations, the tube geometry can be written as

$$\boldsymbol{x}(\theta,\zeta,\rho) = \sum_{k=1}^{3}[(\boldsymbol{x}^{(k)} + \boldsymbol{r}^{(k)}(\theta) + \rho\boldsymbol{n}^{(k)}(\theta) + \rho\gamma\boldsymbol{m}^{(k)}(\theta))N^{(k)}(\zeta)] \tag{2.72}$$

where $\boldsymbol{n}$ is the outward unit normal vector to the non-warped surface ($z_r = 0$) and its components are defined according to Equations 2.52. Also,

$$\boldsymbol{m} = \boldsymbol{n} \times \boldsymbol{s} \tag{2.73}$$

where $\boldsymbol{s}$ is the unit vector in the direction of

$$\frac{\partial \boldsymbol{r}}{\partial \theta} = x_r^{'}\boldsymbol{e}_x + y_r^{'}\boldsymbol{e}_y + z_r^{'}\boldsymbol{e}_z \tag{2.74}$$

Note that by inserting $\gamma = u = 0$ into the above equations, the previous (non-warping) formulation is recovered. A simplification of the formulation is possible by considering small out-of-plane displacements. Then, vector $\boldsymbol{m}$ is taken equal to $\boldsymbol{e}_z$ and the geometry equation can be written in the following form:

$$\boldsymbol{x}(\theta,\zeta,\rho) = \sum_{k=1}^{3}[(\boldsymbol{x}^{(k)} + \boldsymbol{r}(\theta) + \rho\boldsymbol{n}(\theta) + \rho\gamma\boldsymbol{e}_z)N^{(k)}(\zeta)] \tag{2.75}$$

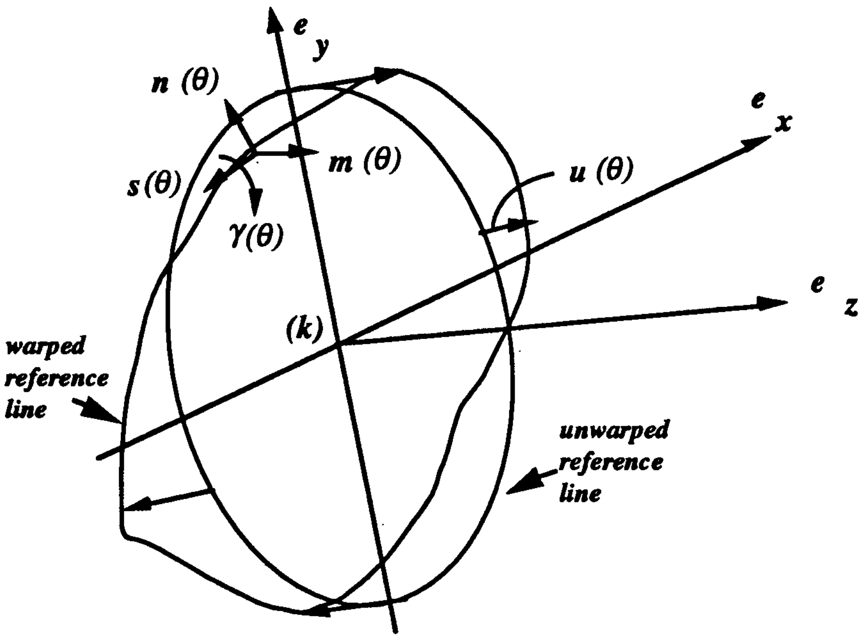

Figure 2.10: Warping parameters.

and

$$\boldsymbol{x}(\theta,\zeta,\rho)=\sum_{k=1}^{3}[(\boldsymbol{x}^{(k)}+(x_r+\rho n_x)\boldsymbol{e}_x^{(k)}+(y_r+\rho n_y)\boldsymbol{e}_y^{(k)}+(z_r+\rho\gamma)\boldsymbol{e}_z^{(k)})N^{(k)}(\zeta)] \tag{2.76}$$

Assume a Fourier series expansion for the warping functions $u(\theta)$ and $\gamma(\theta)$ as follows:

$$u=\sum_{n=2,4,6,\ldots} c_n \cos n\theta+\sum_{n=3,5,7,\ldots} c_n \sin n\theta \tag{2.77}$$

$$\gamma=\gamma_o+\gamma_1 \cos\theta+\sum_{n=2,4,6,\ldots}\gamma_n \cos n\theta+\sum_{n=3,5,7,\ldots}\gamma_n \sin n\theta \tag{2.78}$$

Fourier coefficients c_n and γ_n are the degrees of freedom for warping deformation and will be referred to as the *warping parameters*.

Having obtained Equation 2.76 the formulation follows the steps described in detail in Ref. [31].

An important consideration is the minimum number of integration points required for the evaluation of the integrals in Equations 2.13 and 2.15. Suppose that trigonometric expansions up to degree n are used. This means that the stiffness matrix will contain terms up to degree $2n$. Therefore, for elastic response, it can be shown that $2n + 1$ equally spaced integration points around the full circumference are necessary. Of course, more integration points are needed in the case of inelastic behavior. The highest order expansion considered in this research was up to eighth degree and, for this case, 15 points around the half-circumference were found to be sufficient. It is noted that only half-circumference is analyzed because of the symmetry of cross-sectional deformation.

Linear interpolation is assumed in the radial direction and, therefore, for the case of elastic behavior, exact integration requires two integration points. In this work, because of inelastic response three to five points were found to be sufficient. Note that the thinner the tube, the fewer the integration points that are necessary.

Finally, two integration points were used exclusively in the longitudinal direction with very good results.

2.7 Tracing of Unstable Equilibrium Paths

For the tracing of unstable equilibrium paths, it is necessary to implement a technique which permits calculation of equilibrium states beyond the limit (instability) point.

In this research, the well-known arc-length method is employed. The details concerning the implementation of the method in a finite-element environment are extensively presented in Refs. [20] and [47]. However, some basic ideas are presented herein for the sake of completeness. According to this method, the step-by-step numerical procedure is controlled by a parameter, referred to as "arc-length parameter", which is a combination of the load increment magnitude with the increment magnitude of some "selected" degrees of freedom. More specifically, this parameter can be written as

$$\Delta l = \sqrt{\left(\frac{\Delta P}{\Delta P_o}\right)^2 + \frac{\Delta \boldsymbol{u}^T \cdot \Delta \boldsymbol{u}}{\Delta u_o^2}} \tag{2.79}$$

where ΔP is the load increment, $\Delta \boldsymbol{u}$ is a vector which contains the increment of the "selected" degrees of freedom, and ΔP_o and Δu_o are normalization parameters. From Figure 2.11, parameter Δl can be regarded as the length increment of the equilibrium path in the P-$\boldsymbol{u}$ space. Starting from point (1) on the path, the method provides point (2) as the intersection of the path with an "arc" of radius Δl about point (1).

It has been recognized that the success of the method depends on the appropriate selection of degrees of freedom in vector $\Delta \boldsymbol{u}$. In general, convergence near and beyond the limit point is facilitated when monotonically increasing degrees of freedom are included in vector $\Delta \boldsymbol{u}$. In this work, for cases where instability was due to structural loads, nodal displacements and rotations were considered in $\Delta \boldsymbol{u}$. In the special case of pressurized bending for high levels of pressure, which is a difficult case for obtaining post-buckling configurations, the tube end-rotation was found to provide the best results.

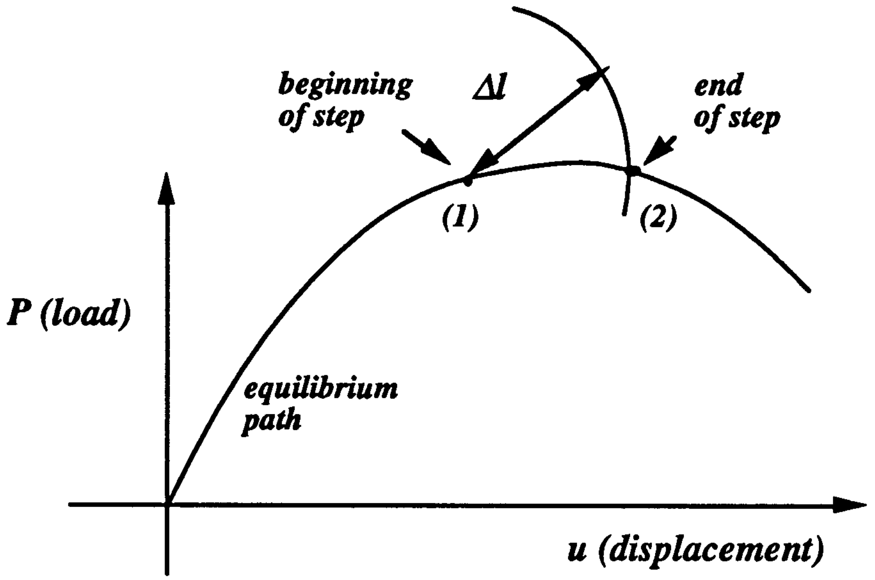

Figure 2.11: Schematic representation of arc-length method.

On the other hand, for cases with pressure-load instabilities the ovalization parameter a_2 was used successfully.

2.8 Stiffener Finite Element

The formulation of this element is based on kinematics of the tube element and simulates rigorously both external and internal stiffeners. Figure 2.12 shows a longitudinal cut of the stiffened pipe with the characteristic stiffener dimensions. It is worth noting that for fabricated tubes, the stiffener longitudinal dimension h is usually of the order of magnitude of the tube thickness t, whereas the radial dimension t' is five to eight times larger. The stiffener may be external or internal (see Figure 2.13) and is welded to the outer (or inner) pipe surface. Furthermore, the distance between two stiffeners ranges from one to four tube diameters.

2.8.1 External Stiffener

In this case, the stiffener element is assumed to be "welded" to the outer tube surface (Figure 2.14). Therefore, the stiffener inner surface must coincide with the outer tube surface. For computational convenience, the stiffener position along the longitudinal axis is assumed to correspond to a tube node, say (k). Thus, the position vector at any point of the tube outer surface that corresponds to node (k) is given by the following equation

$$\boldsymbol{x}_{out}(\theta,\zeta,\rho_o) = \boldsymbol{x}^{(k)} + (x_r + \rho_o n_x)\boldsymbol{e}_x^{(k)} + (y_r + \rho_o n_y)\boldsymbol{e}_y^{(k)} + (z_r + \rho_o \gamma)\boldsymbol{e}_z^{(k)} \tag{2.80}$$

where ρ_o is the radial coordinate of the tube outer surface. The stiffener motion with respect to the tube can be described by the following functions:

- in-plane (shear) rotation $\phi(\theta)$
- out-of-plane (warping) rotation $\psi(\theta)$

The position vector of any point of the stiffener is given by

$$\boldsymbol{x}(\theta,\zeta,\rho) = \boldsymbol{x}_{out} + \rho\boldsymbol{n}(\theta) + \rho\phi(\theta)\boldsymbol{s}(\theta) + \rho\psi(\theta)\boldsymbol{e}_z + \zeta\boldsymbol{e}_z \tag{2.81}$$

It is clear that the stiffener shape functions imply no change in deformation in the longitudinal direction.

The base vectors along the orthogonal coordinate directions are

$$\begin{aligned} \boldsymbol{g}_\theta = \partial\boldsymbol{x}/\partial\theta = \ & [x_r' + (\rho_o + \rho)n_x' - \rho\phi n_y' - \rho\phi' n_y]\boldsymbol{e}_x^{(k)} + \\ & [y_r' + (\rho_o + \rho)n_y' + \rho\phi n_x' + \rho\phi' n_x]\boldsymbol{e}_y^{(k)} + \\ & [u' + \rho_o\gamma' + \rho\psi']\boldsymbol{e}_z^{(k)} \end{aligned} \tag{2.82}$$

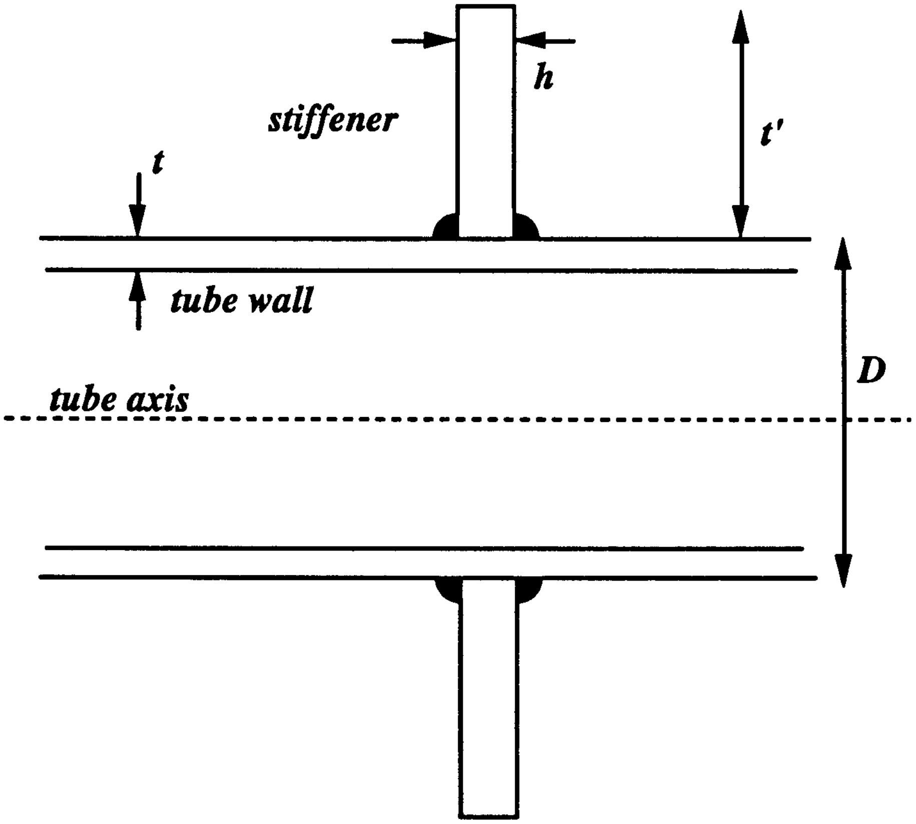

Figure 2.12: Stiffener characteristic dimensions (longitudinal view - external case).

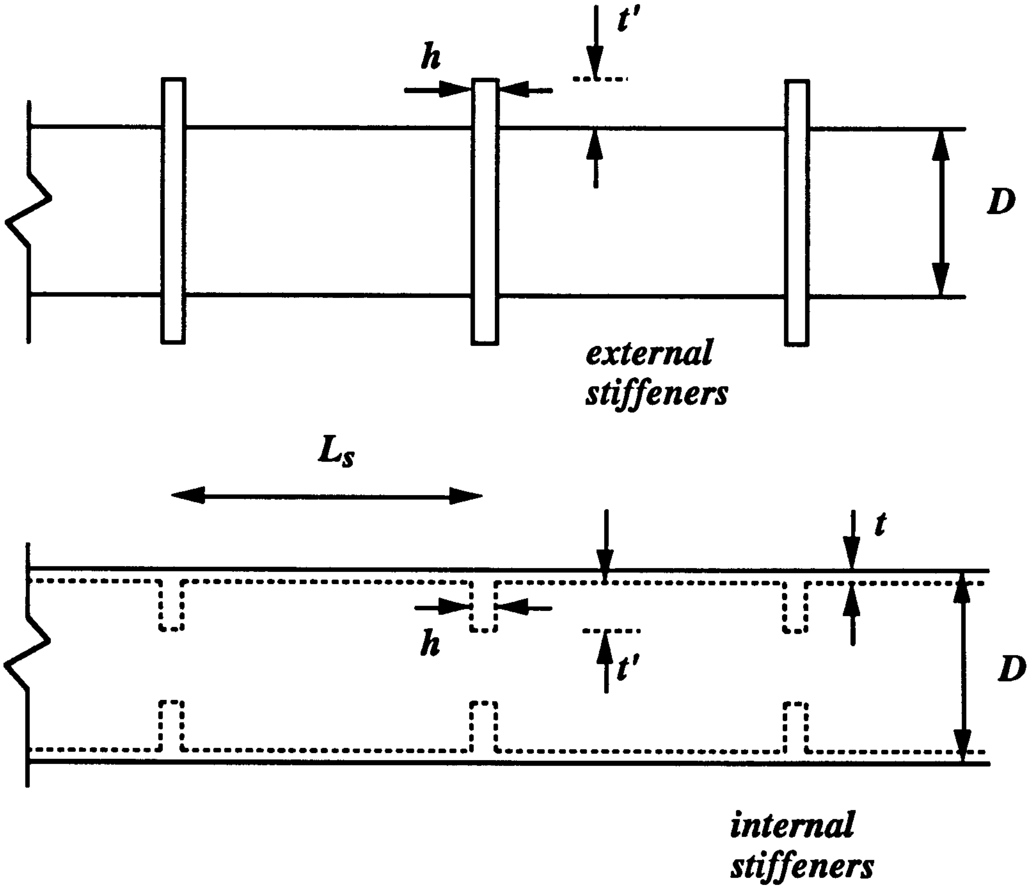

Figure 2.13: Externally and internally stiffened tubes.

$$g_\zeta = \frac{\partial \boldsymbol{x}}{\partial \zeta} = h\boldsymbol{e}_z^{(k)} \tag{2.83}$$

$$\boldsymbol{g}_\rho = \frac{\partial \boldsymbol{x}}{\partial \rho} = (n_x - \phi n_y)\boldsymbol{e}_x^{(k)} + (n_y + \phi n_x)\boldsymbol{e}_y^{(k)} + \psi \boldsymbol{e}_z^{(k)} \tag{2.84}$$

The velocity vector can be written as follows

$$\begin{aligned} \dot{\boldsymbol{x}} \ = \ & \dot{\boldsymbol{x}}^{(k)} + [\dot{x}_r + (\rho_o + \rho)\dot{n}_x - \rho\phi\dot{n}_y - \rho n_y\dot{\phi}]\boldsymbol{e}_x^{(k)} + \\ & [\dot{y}_r + (\rho_o + \rho)\dot{n}_y + \rho\phi\dot{n}_x + \rho n_x\dot{\phi}]\boldsymbol{e}_y^{(k)} + \\ & (y_r + (\rho_o + \rho)n_y + \rho\phi n_x)\dot{\theta}^{(k)}\boldsymbol{e}_z^{(k)} + \\ & \rho\dot{\psi}\boldsymbol{e}_z^{(k)} + (u + \rho_o\gamma + \rho\psi + \zeta h)\dot{\theta}^{(k)}\boldsymbol{e}_y^{(k)} \end{aligned} \tag{2.85}$$

To discretize the rotational parameters $\phi(\theta)$ and $\psi(\theta)$, we consider their Fourier expansion:

$$\psi = \psi_o + \sum_{n=2,4,6,\ldots} \psi_n \, cos n\theta + \sum_{n=1,3,5,\ldots} \psi_n \, sin n\theta \tag{2.86}$$

$$\phi = \sum_{n=2,4,6,\ldots} \phi_n \, sin n\theta + \sum_{n=1,3,5,\ldots} \phi_n \, cos n\theta \tag{2.87}$$

Fourier coefficients ψ_n and ϕ_n are the degrees of freedom for stiffener deformation and will be referred to as *stiffener parameters.*

2.8.2 Internal Stiffener

When the stiffener is internal (see Figure 2.13) the stiffener outer surface coincides with the tube inner surface, which is given by the following equation:

$$\boldsymbol{x}_{in}(\theta, \zeta, \rho) = \boldsymbol{x}^{(k)} + (x_r + \rho_i n_x)\boldsymbol{e}_x^{(k)} + (y_r + \rho_i n_y)\boldsymbol{e}_y^{(k)} + (z_r + \rho_i\gamma)\boldsymbol{e}_z^{(k)} \tag{2.88}$$

where ρ_i is the radial coordinate of the inner pipe surface at node (k). The implementation follows the aforementioned steps of the external stiffener case.

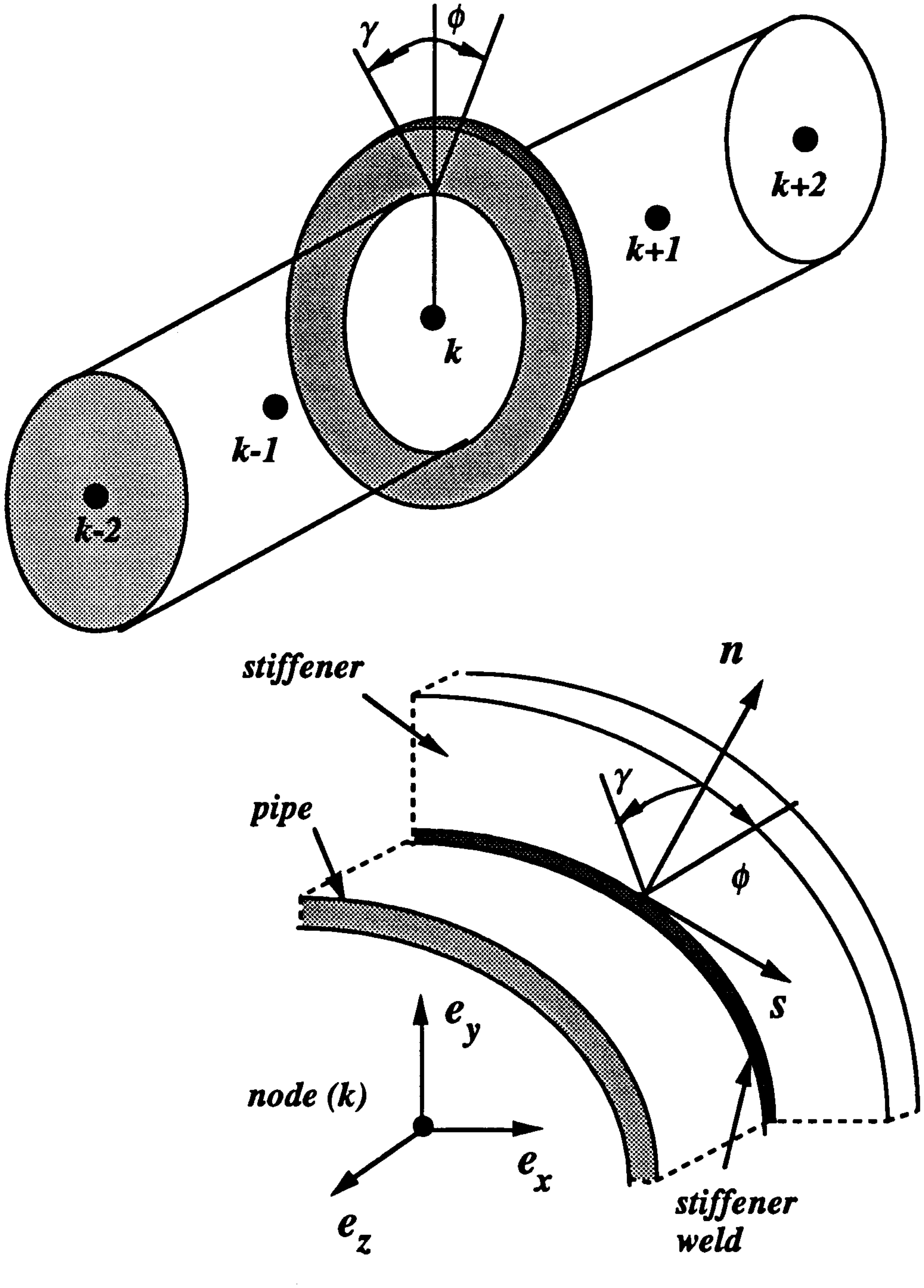

Figure 2.14: External stiffener element.

Chapter 3

Results for Unstiffened Tubes

In this chapter, extensive results are obtained for unstiffened tubes. Included are results for simple cases which are easily verified by comparison with closed-form solutions, cases studied previously using shell elements (Ref. [30]), and several beam-column interaction curves which are compared with the AISC and API specification curves [3], [5]. Furthermore, some aspects of localized deformation under bending are presented. Particular emphasis is given to the effects of pressure on member stability. In all graphs presented in this Chapter, the values of pressure, moment, axial force, curvature and ovalization amplitude are normalized by the yield pressure $p_y = 2\sigma_y t/D$, the fully plastic moment $M_p = \sigma_y Z$, the yield axial force $P_y = \sigma_y A$, the curvature parameter $k_I = t/D^2$ and the tube radius R respectively, except for the cases of *elastic* tube behavior where the values of pressure and moment are normalized by the elastic buckling pressure $p_e = 2E(t/D)^3/(1-\nu^2)$, and the elastic moment parameter $M_e = ERt^2/\sqrt{1-\nu^2}$ respectively. Finally, it should be pointed out that for deriving the following results, tube elements are used, unless otherwise specified.

3.1 Preliminary Cases

Consider a tube segment having outer diameter of 6.625 in, thickness of 0.157 in and length of 5.4 in. The material stress-strain curve is shown in Figure 3.1. The yield stress is $\sigma_y = 56.24\,ksi$, the proportional limit is $\sigma_p = 50.80\,ksi$ and Young's modulus is $E = 29.56 \cdot 10^3\,ksi$. A specimen, designated as C22J1 with these characteristics was tested by CBI [15] in pure bending. The geometric properties of the section are:

- mean diameter $D_m = 6.468\,in$
- cross-sectional area $A = 3.19\,in^2$
- moment of inertia $I = 16.68\,in^4$
- radius of gyration $r = 2.287\,in$
- elastic section modulus $S = 5.159\,in^3$
- plastic section modulus $Z = 6.567\,in^3$

Therefore, the characteristic loads for the tube are the following:

- yield compressive force $P_y = 179.4\,kips$
- API ultimate moment [4] $M_n = 341.2\,k - in$
- fully plastic moment (using D_m) $M_p = 369.4\,k - in$
- API buckling pressure [5] $p_{hc} = 692.3\,psi$
- Shell buckling pressure [41] $p_{cs} = 879.6\,psi$
- yield radial pressure (using D_m) $p_y = 2730.6\,psi$

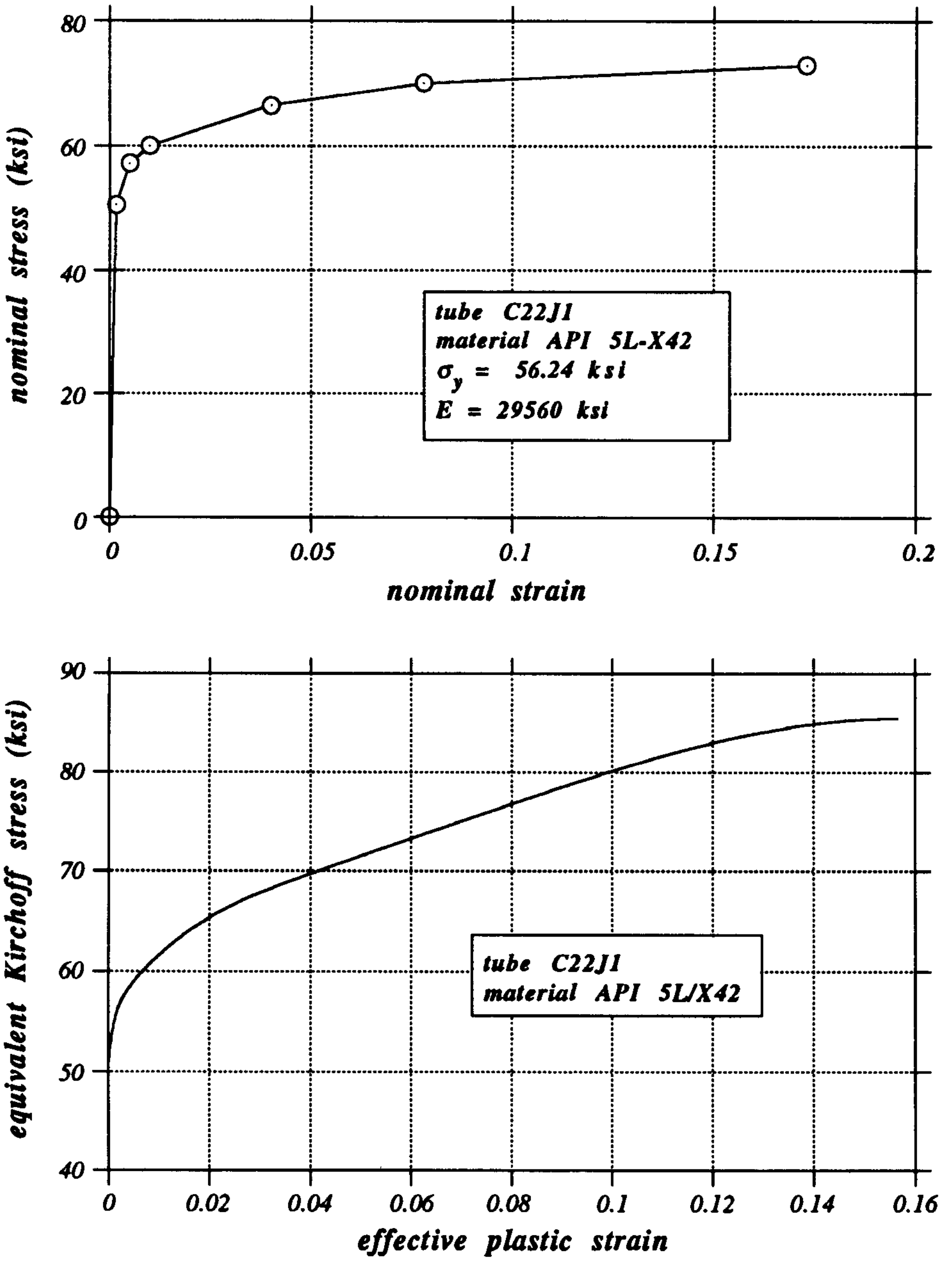

Figure 3.1: Material curve for tube C22J1.

The specimen is subjected to a moment of $3 \cdot 10^4\, lb - in$, a compressive force of $2 \cdot 10^4\, lb$ or a tensile force of $2 \cdot 10^4\, lb$ and hydrostatic pressure of $100\, psi$. In all these cases, the behavior is elastic and there exists a closed-form solution.

The numerical results are reported along with the closed-form solutions in Tables 3.1, 3.2 and 3.3 and the agreement is excellent. Note that for the cases of axial load, tension gives a larger displacement than compression. This is because the numerical method takes into account the nonlinear behavior of the tube. Indeed, compression tends to increase the cross-sectional area and the tube becomes "stiffer", whereas tension decreases the cross-sectional area.

	closed-form	numerical
deflection (in)	$0.8871 \cdot 10^{-3}$	$0.8864 \cdot 10^{-3}$
rotation (in)	$0.3286 \cdot 10^{-3}$	$0.3283 \cdot 10^{-3}$
a_2 (in)	N/A	$0.4823 \cdot 10^{-3}$
b_2 (in)	N/A	$-0.2415 \cdot 10^{-3}$

Table 3.1: Response of tube C22J1 under moment of $3 \cdot 10^4\, lb - in$.

	closed-form	compression (num.)	tension (num.)
axial displ. (in)	$0.1145 \cdot 10^{-3}$	$0.1144 \cdot 10^{-3}$	$-0.1146 \cdot 10^{-3}$
expansion a_o (in)	$0.2058 \cdot 10^{-3}$	$0.2056 \cdot 10^{-3}$	$-0.2058 \cdot 10^{-3}$

Table 3.2: Response of tube C22J1 under axial force of $2 \cdot 10^4\, lb$.

	closed-form	numerical
axial displ. (in)	$0.8178 \cdot 10^{-4}$	$0.8178 \cdot 10^{-4}$
contraction a_o (in)	$-1.9525 \cdot 10^{-3}$	$-1.9525 \cdot 10^{-3}$

Table 3.3: Response of tube C22J1 under hydrostatic pressure of $100\, psi$.

The bending case is more carefully investigated in order to examine the influence of cross-sectional ovalization parameters. Note that the warping parameters are of no interest in these analyses because the cross-sectional deformation is uniform along the tube length.

	case 1	case 2	case 3	case 4	case 5	case 6
deflection ($10^{-3}in$)	0.80666	0.80666	0.88642	0.88644	0.88644	0.88644
rotation ($10^{-3}rad$)	0.29876	0.29876	0.32830	0.32831	0.32831	0.32831
a_o ($10^{-6}in$)	0.0	-0.10811	-0.11317	-0.11357	-0.11358	-0.11358
a_1 ($10^{-4}in$)	0.0	0.0	0.95398	0.95400	0.95400	0.95400
a_2 ($10^{-4}in$)	0.0	0.0	0.0	0.48231	0.48231	0.48231
b_2 ($10^{-4}in$)	0.0	0.0	0.0	-0.24152	-0.24152	-0.24152
a_3 ($10^{-8}in$)	0.0	0.0	0.0	0.0	0.70269	0.70237
b_3 ($10^{-8}in$)	0.0	0.0	0.0	0.0	0.14030	0.14019
a_4 ($10^{-10}in$)	0.0	0.0	0.0	0.0	0.0	0.30445
b_4 ($10^{-10}in$)	0.0	0.0	0.0	0.0	0.0	0.93782

Table 3.4: Influence of ovalization parameters on the elastic pure bending response of tube C22J1 under a moment of $3 \cdot 10^4\ lb - in$.

In case 1, all ovalization degrees are constrained and in each consecutive case an additional Fourier coefficient is released. It is observed (Table 3.4) that if the linear term (a_1) is included, the deflection and rotation are in complete agreement with the classical beam theory. Additional terms do not affect the deflection and the rotation. Note that terms a_2 and b_2 are related by

$$b_2 \simeq -\frac{a_2}{2} \tag{3.1}$$

and this shows that ovalization deformation is "inextensional". It must be pointed out that, in this case, the behavior of the tube is linear elastic due

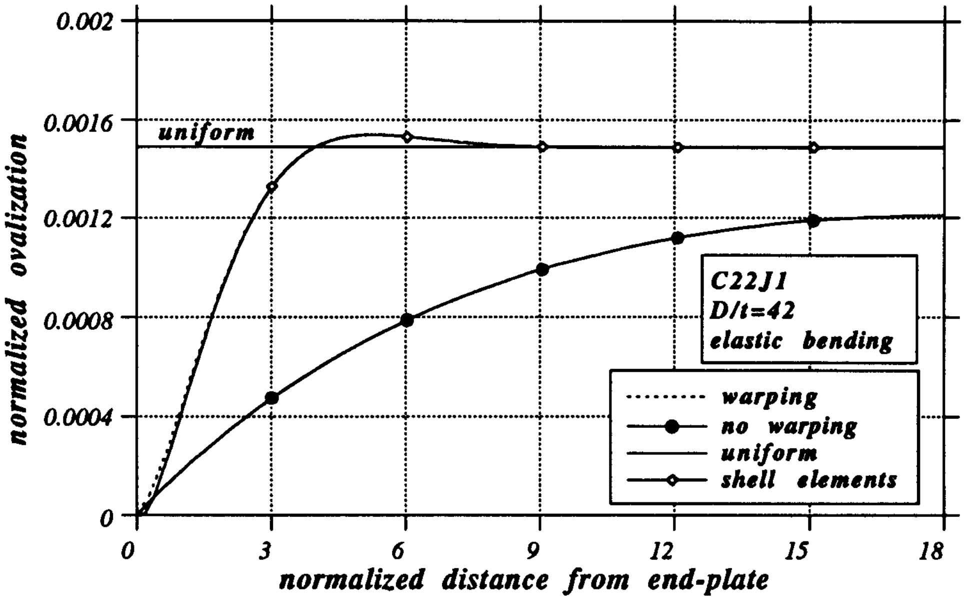

Figure 3.2: Effects of boundary conditions on elastic bending response.

to the low level of loading. The influence of ovalization parameters on the ultimate capacity is investigated later on.

The necessity of warping deformation for the cases of non-uniform cross-sectional deformation along the tube is worthy of investigation. The tube segment is assumed to have the same cross-sectional and material characteristics as before. Its length is taken equal to 120 *in* (about 18 diameters long). The end section is restrained from ovalizing and is subjected to a small moment of $3 \cdot 10^4\, lb - in$ which is about 11% of the first yield moment. The variation of ovalization along the tube is shown in Figure 3.2, where the section with zero coordinate is the end section. In this graph, the values of ovalization and distance from the end are normalized by the tube radius R and diameter D respectively. The behavior of warping and non-warping elements is compared with the uniform ovalization solution. It is clear that the non-warping element exhibits very stiff behavior whereas the warping element with 4 rotational and 2 translational warping parameters behaves very well. Note that about 4 diameters away from the end section, the end effects become negligible and disappear completely beyond about 9 diameters. The warping elements also give the same results when compared with the shell elements.

3.2 Pure Bending

In order to investigate the ultimate bending capacity of tubes, the influence of ovalization parameters on the pure-bending response of the tube is examined. The moment-curvature curve of tube C22J1 is obtained for different trigonometric expansions. The results are shown in the first graph of Figure 3.3. Clearly, not all curves exhibit a limit-point type of instability. More precisely, a limit point is obtained when up to at least fourth degree terms are included. The basic ideas about this instability phenomenon, referred to as "Brazier effect", are presented in detail in Ref. [30].

The second graph of Figure 3.3 shows a detail of the previous region where the limit point occurs. Apparently, the fourth term in the trigonometric expansion is the *key parameter* in order to obtain the limit moment, whereas additional terms do not significantly affect the tube response. The limit points are shown in the following table:

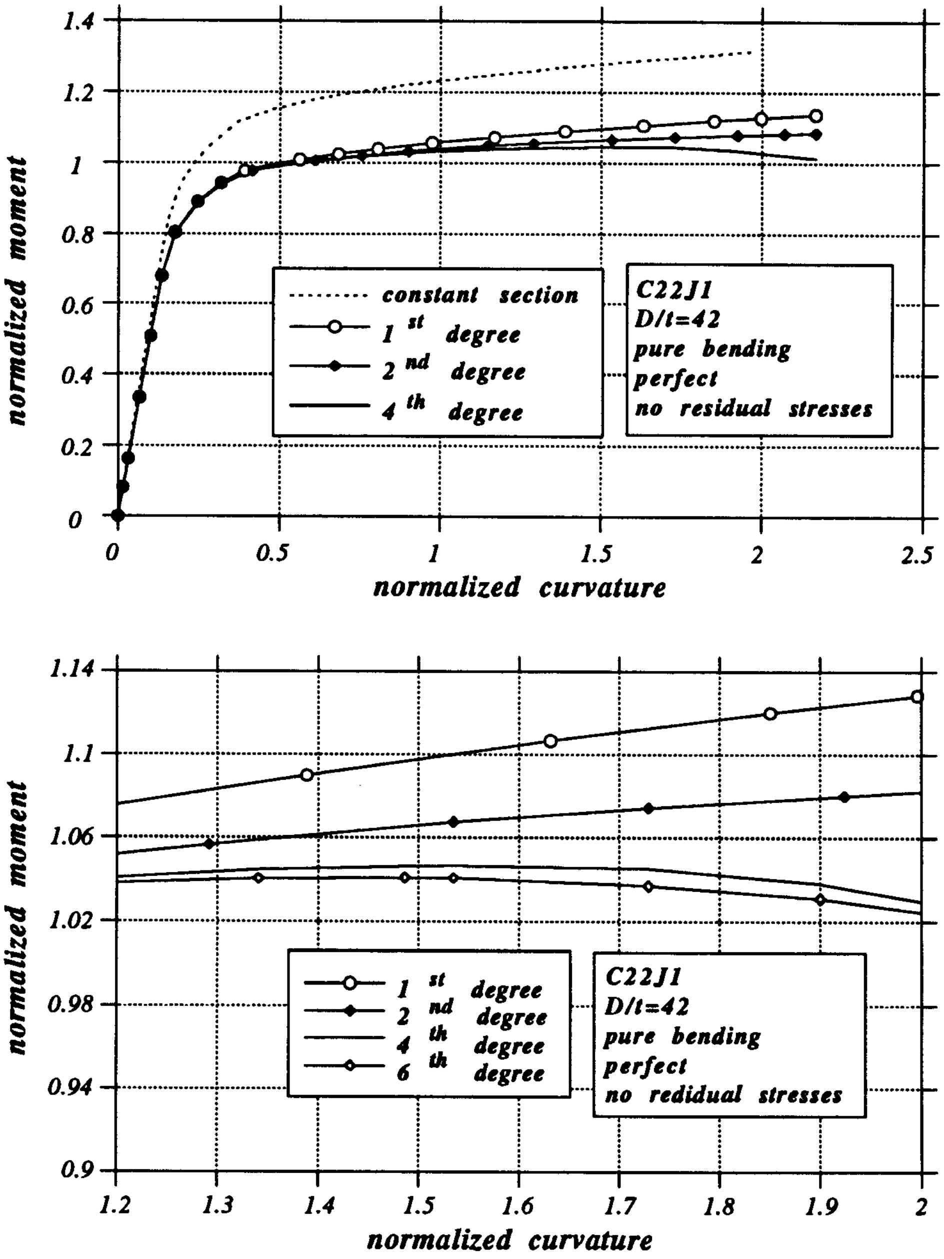

Figure 3.3: Pure bending of tube C22J1.

	limit moment ($k - in$)	limit curvature (in^{-1})
up to 3^{rd} degree	–	–
4^{th} degree	386.568	$5.756 \cdot 10^{-3}$
5^{th} degree	386.550	$5.756 \cdot 10^{-3}$
6^{th} degree	384.513	$5.483 \cdot 10^{-3}$

Table 3.5: Ultimate capacity of tube C22J1 under pure bending.

Figure 3.3 indicates that the shape function found by Brazier [9], which includes trigonometric terms up to the second degree, is not satisfactory for inelastic pure bending of tubes for this range of D/t values, and that trigonometric terms up to the fourth degree should be used. Figure 3.4, shows cross-sectional ovalization in terms of bending curvature. Note that, around the limit point, ovalization amplitude is less than 5% of the tube radius.

The pure bending behavior of a relatively thin inelastic tube, referred to as tube C6J5, is shown in Figure 3.5. The tube has a diameter-to-thickness ratio of about 63 and its material follows the stress-strain curve depicted in Figure 3.6. A tube with the same geometric and material characteristics was tested by CBI under pure pressure during the experimental program reported in Ref. [15]. It is interesting to note that both tubes C22J1 and C6J5 have an ultimate moment capacity above the plastic moment M_p. Obviously, the presence of strain-hardening is responsible for this phenomenon.

Extensive numerical results for pure bending of tubes were reported in Ref. [30] for a thick tube made of X-52 steel using shell elements. The same tube is analyzed herein using tube elements, in order to compare with the previous results. Of course, a first comparison between the tube and the shell elements was reported previously for the case of nonuniform ovalization

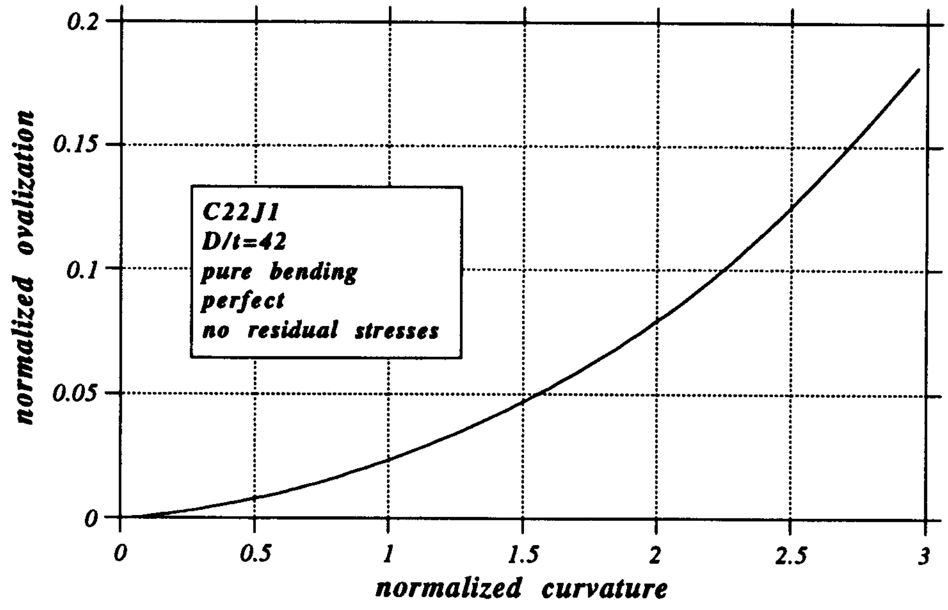

Figure 3.4: Pure bending of tube C22J1; cross-sectional ovalization.

under pure bending and it was found that the elements had identical behavior. However, the level of loading was almost seven times below the yield limit. Therefore, it is interesting to compare the two elements with regard to their ultimate bending capacity. The tube under consideration has outside diameter and thickness of $12.75\,in$ and $0.59\,in$ respectively, which imply a D/t ratio of about 21. The stress-strain curve of the material is depicted in Figure 3.7.

The influence of the number of ovalization parameters on the pure bending behavior for the X-52 tube is summarized in Table 3.6.

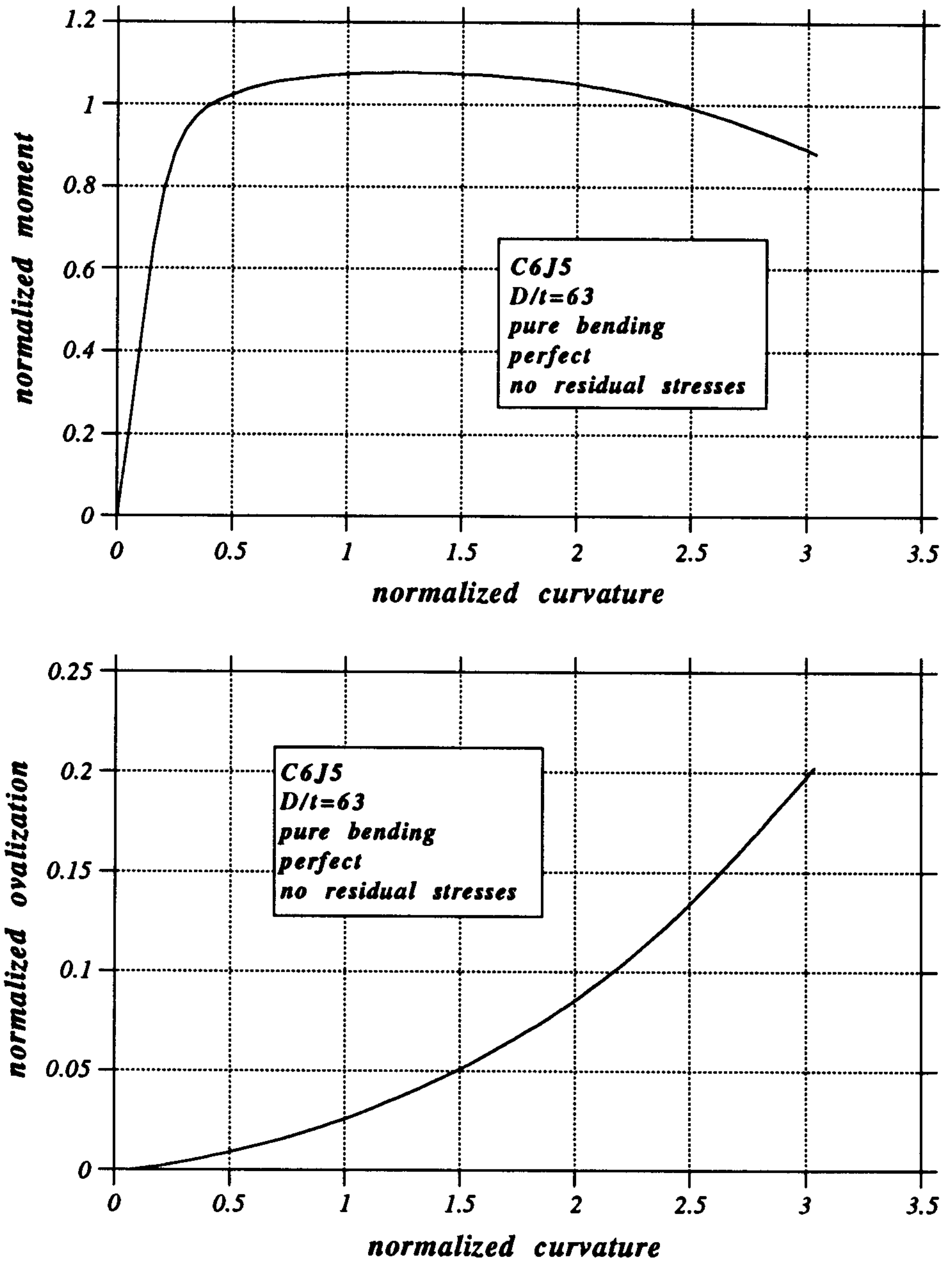

Figure 3.5: Pure bending of tube C6J5.

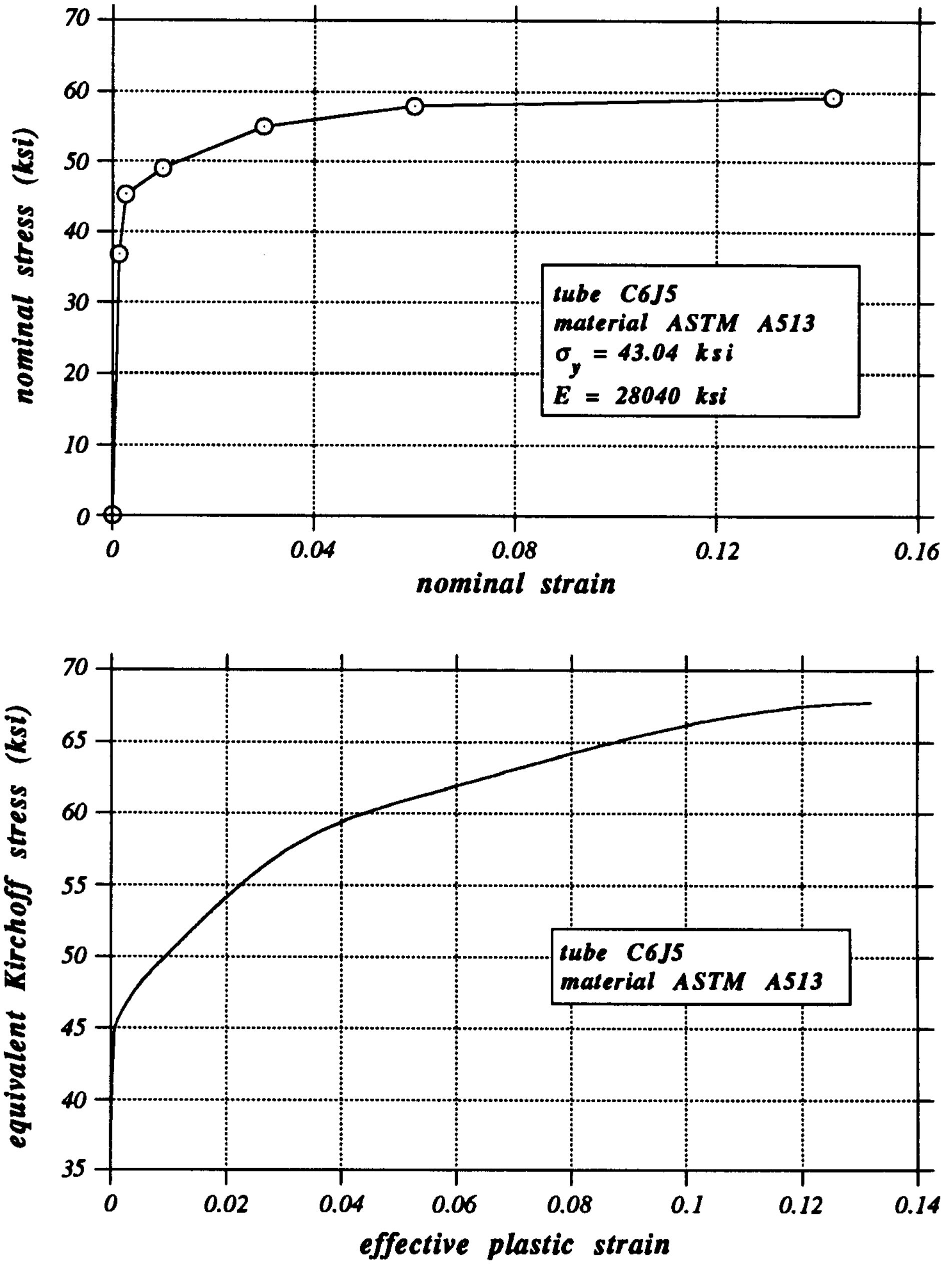

Figure 3.6: Material curve for tube C6J5.

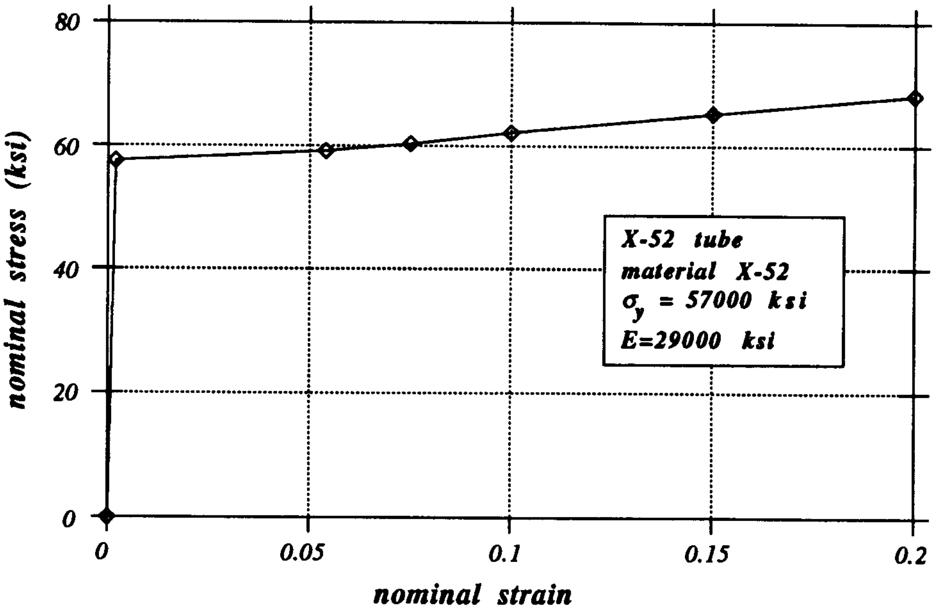

Figure 3.7: Material curve for tube X-52.

	limit moment ($k - in$)	limit curvature (in^{-1})
up to 1^{st} degree	–	–
2^{nd} degree	5099.50	$3.5094 \cdot 10^{-3}$
4^{th} degree	5086.34	$2.6836 \cdot 10^{-3}$
6^{th} degree	5085.03	$2.6011 \cdot 10^{-3}$
8^{th} degree	5085.03	$2.6011 \cdot 10^{-3}$
shell elements	5095.80	$2.6667 \cdot 10^{-3}$

Table 3.6: Ultimate capacity of tube X-52 under pure bending.

It is clear that the limit point is obtained using terms up to the second degree and that the ultimate moment is very close to the shell-element solution. A graphical representation of these results are shown in Figure 3.8. This implies a different response from the previous tube because of the difference in thickness. More specifically, thicker tubes undergo smaller cross-sectional ovaliza-

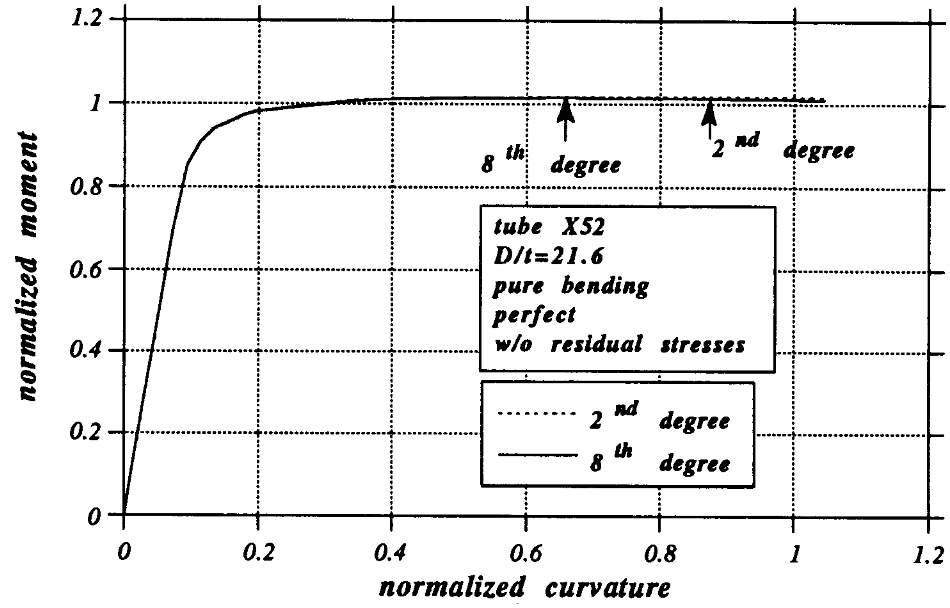

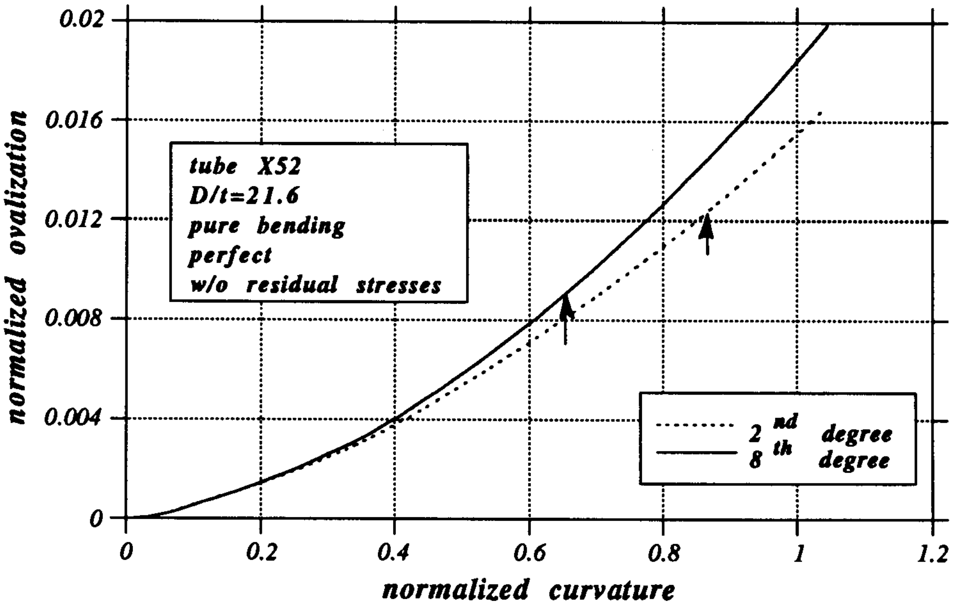

Figure 3.8: Pure bending of tube X-52.

tion and, therefore, less cross-sectional parameters are necessary for obtaining limit point. However, in order to obtain the corresponding curvature close to the shell-element solution, terms up to the fourth degree must be included. Nevertheless, the value of the curvature where ultimate moment occurs is of no particular importance because the post-yielding part of the moment-curvature curve is nearly flat.

During bending of inelastic tubes (such as C22J1, C6J5 and X-52) the cross-section ovalization amplitude is less than 10% of the tube radius. In fact, plasticity effects rather than geometric nonlinearities are mainly responsible for the nonlinear tube behavior. In order to investigate the geometric effects on bending response, a parametric study has been conducted for a thin elastic tube with a diameter-to-thickness ratio of 200. This tube will be referred to as tube 200. The Young's Modulus and Poisson's ratio have been assumed equal to 29000 ksi and 0.32 respectively. The first graph of Figure 3.9 shows the moment-curvature curves for increasing number of cross-sectional deformation parameters. Note that expansions of order six and eight provide essentially the same result. On the other hand, it is impossible to obtain a limit point using a fourth-order expansion. This is because such an expansion underestimates cross-sectional ovalization which is the most important factor for limit-point instability (see the second graph of Figure 3.9).

As mentioned before, the ovalization instability of thin elastic tubes was first analytically investigated by Brazier [9], through a simplified ring model. More specifically, Brazier extended the Saint Venant solution for pure bending to include nonlinear ovalization effects. By minimization of the potential energy, he obtained the cross-sectional deformation shape as a sum of trigonometric functions up to the second degree and the moment-curvature curve in closed form. Figure 3.10 shows Brazier's curve in comparison with the tube element results. The ultimate moment as well as the corresponding curvature are very close. On the other hand, Brazier's solution is not satisfactory for the unstable part of the equilibrium path beyond the limit point. By examining the second graph of Figure 3.10 it appears that Brazier's model overestimates cross-sectional deformation and, therefore, underestimates bending stiffness. Similar results are obtained in Ref. [44], where eight-node shell finite element results are compared with Brazier's analytical solution.

3.3 External Pressure

In order to examine the effects of external pressure on tubular members, some theoretical background is necessary. The buckling of thin elastic tubes under pressure has been investigated by Timoshenko [60]. For long perfect tubes, the bifurcation buckling pressure is equal to

$$p_e = \frac{2E}{1-\nu^2}\left(\frac{t}{D}\right)^3 \tag{3.2}$$

This pressure controls instability in the absence of initial imperfections and residual stresses provided that stresses remain within the elastic range. Assuming a bilinear stress-strain curve, the minimum external pressure that causes inelastic effects depends on the constraint imposed in the longitudinal direction. More specifically, using the von Mises yield criterion,

- for longitudinally free tube

$$p_y = 2\,\sigma_y\left(\frac{t}{D}\right)$$

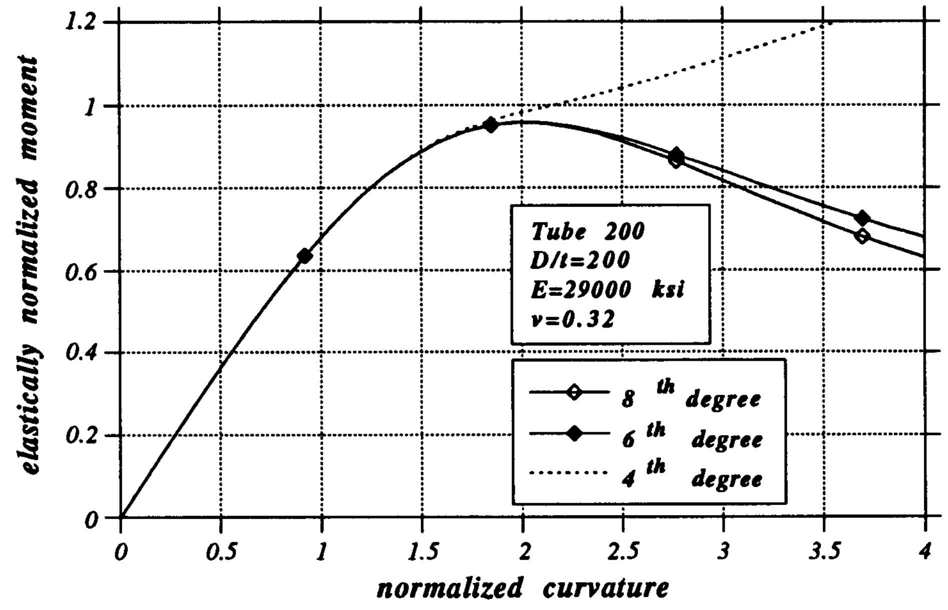

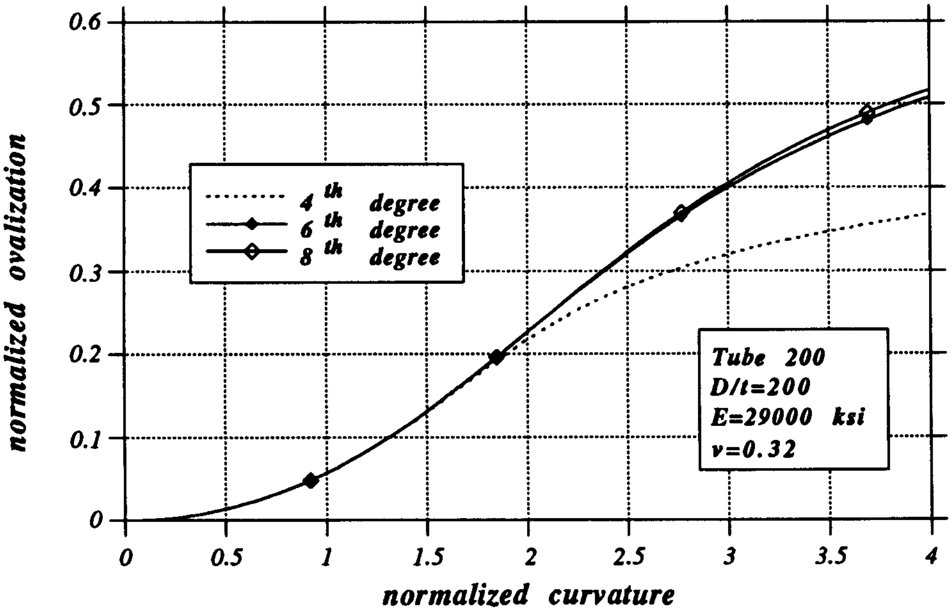

Figure 3.9: Pure bending of tube 200.

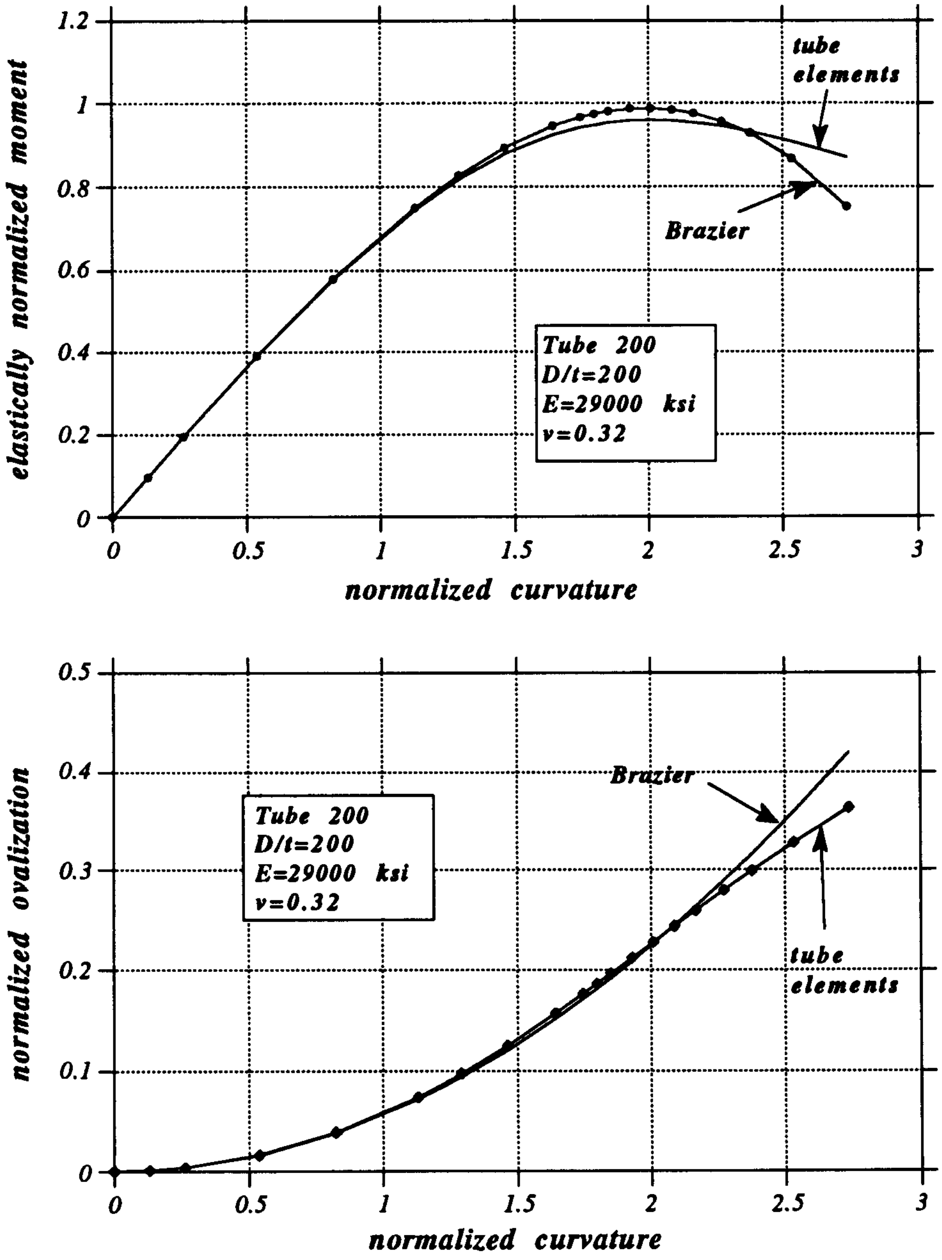

Figure 3.10: Comparison of Brazier's solution with numerical results (elastic tube 200).

- for longitudinally restrained tube (plane strain)

$$p_{y1} = \frac{2}{1+\nu^2-\nu}\sigma_y\left(\frac{t}{D}\right)$$

- for tube with capped-end compressive force

$$p_{y2} = \frac{4}{\sqrt{3}}\sigma_y\left(\frac{t}{D}\right)$$

Note that the case of capped-end compression is most likely to occur in actual applications. By equating p_{y2} and p_e the limit between elastic and inelastic buckling is obtained:

$$\left(\frac{D}{t}\right)_{lim} = 0.931\sqrt{\frac{E}{(1-\nu^2)\,\sigma_y}} \simeq \frac{166}{\sqrt{\sigma_y}} \tag{3.3}$$

where Young's modulus and Poisson's ratio are assumed equal to 29000 ksi and 0.30 respectively, and σ_y is the yield stress in ksi. Clearly, for regular steel material and D/t greater than 30, elastic buckling governs.

Another interesting point is the nature of the elastic post-buckling equilibrium path. It has been shown [10] that for elastic buckling, the post-buckling path is stable. This is verified in Figure 3.11, where tube 200 is assumed to have a very small initial out-of-roundness of the form

$$w_i = w_o \cos 2\theta \tag{3.4}$$

where the ovalization amplitude w_o is taken equal to 0.002% of the tube radius R, which is a very small value. Note that according to API rules [5], imperfections are measured in terms of the out-of-roundness parameter e:

$$e = \frac{D_{max} - D_{min}}{D} = \frac{2\,w_o}{R} \tag{3.5}$$

In this Figure, the value of pressure is normalized by the elastic buckling pressure given by Equation 3.2 and the result is referred to as "elastically normalized pressure". The pressure level at which extensive ovalization starts is almost identical to the prediction obtained from Equation 3.2 and the increasing pressure along the postbuckling path indicates stable postbuckling behavior.

Figure 3.12, shows the pressure-ovalization curve for a tube of D/t equal to 48, referred to as tube 5A. A specimen with the same diameter, thickness and material was tested by CBI [39] under pure pressure. The tube has a diameter-to-thickness ratio equal to 48 and a yield stress equal to 42.1 *ksi*. A bilinear stress-strain curve with a post-yielding modulus of $E/400$ is employed. In this analysis, the tube is assumed to have a very small initial out-of-roundness ($e = 0.45 \cdot 10^{-4}$) and no residual stresses. Extensive ovalization starts at a pressure very close to the bifurcation pressure predicted by Equation 3.2 and the initial post-buckling path is increasing. However, when plasticity occurs, the stiffness is immediately reduced and instability occurs. This is indicated by the descending path beyond the limit point.

The above tubes are assumed to have a very small value of initial imperfection and zero residual stresses. In addition, they have a large value of D/t ratio ($D/t > 40$). Therefore, they are expected to buckle in the elastic range. Nevertheless, the distinction between elastic and inelastic buckling is not obvious for imperfect tubes and becomes even more complicated for the case of residual stresses, which are always present in actual offshore applications.

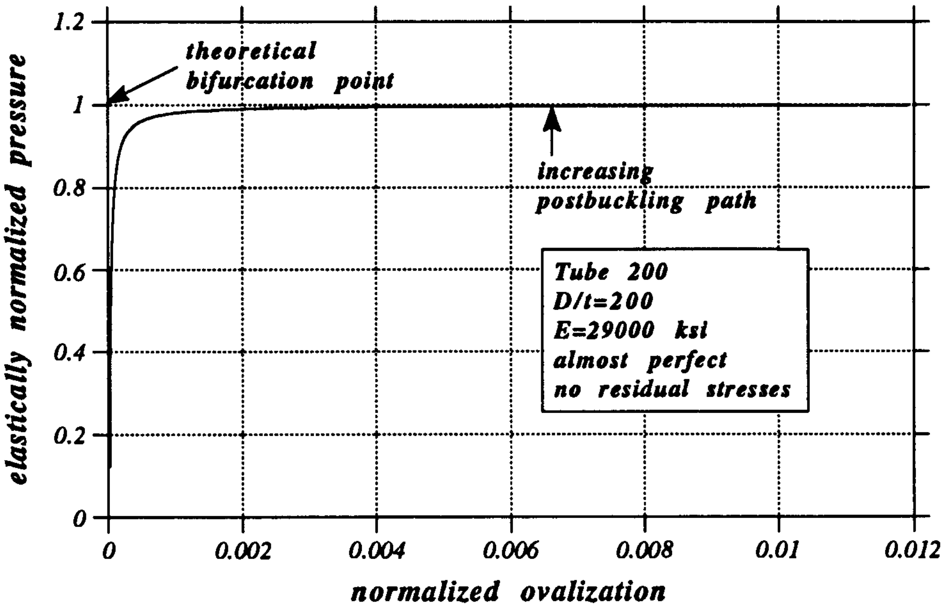

Figure 3.11: Hydrostatic pressure loading of tube 200.

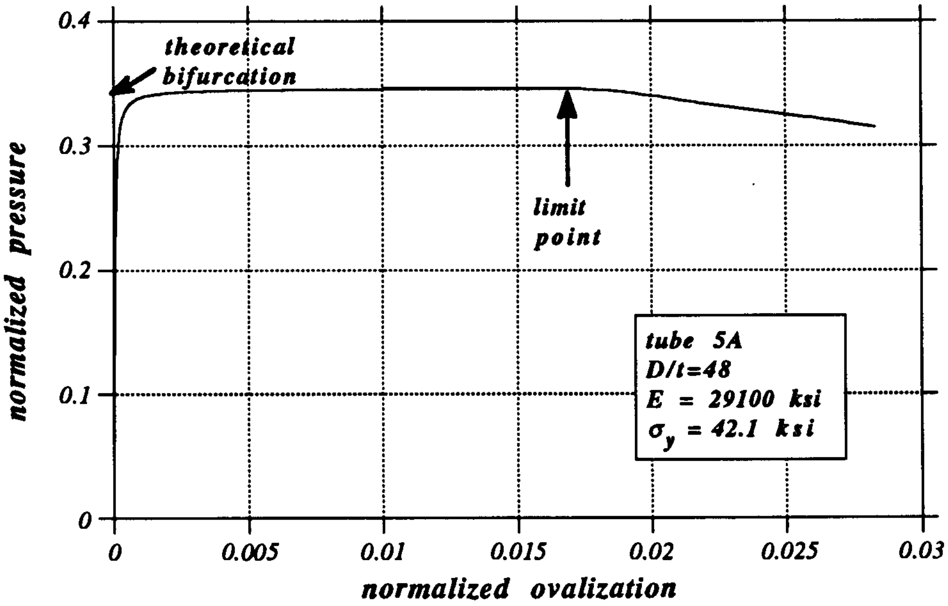

Figure 3.12: Hydrostatic pressure loading of tube 5A.

The effects of initial out-of-roundness on pure pressure collapse of tube C22J1 are shown in Figure 3.13. Clearly, initial out-of-roundness is very important for the ultimate pressure capacity of tubes. For initial out-of-roundness equal to the API requirements, there is a 20% reduction in pressure capacity from the "perfect" case. These results are summarized in Figure 3.14 where the effects of residual stresses in overall capacity are depicted as well. For very small imperfection (e less than 0.0002) buckling is elastic and, therefore, the inclusion of circumferential residual stresses ($\sigma_{circ,max} = 0.35\sigma_y$), does not affect the ultimate capacity. However, when longitudinal residual stresses are included ($\sigma_{long,max} = \sigma_y$), pressure capacity is reduced even for the perfect case.

It is interesting to compare the analytical results shown in Figure 3.14 with the predictions of Shell pipeline [41] and API [5] formulas. In this graph, the out-of-roundness imperfection is normalized so that the API allowable value corresponds to unity. The Shell formula, using the mean diameter $D_m = 6.468\,in$, gives $p_{cs} = 879\,psi$ whereas the API formula predicts $p_{hc} = 692\,psi$. These values correspond to normalized pressures of 0.322 and 0.253 respectively. It is clear that the Shell formula provides a high value of ultimate capacity, because it is based on the elastic buckling pressure of perfect tubes (i.e. Equation 3.2). On the other hand, the API formula gives a very reasonable (somewhat conservative) prediction.

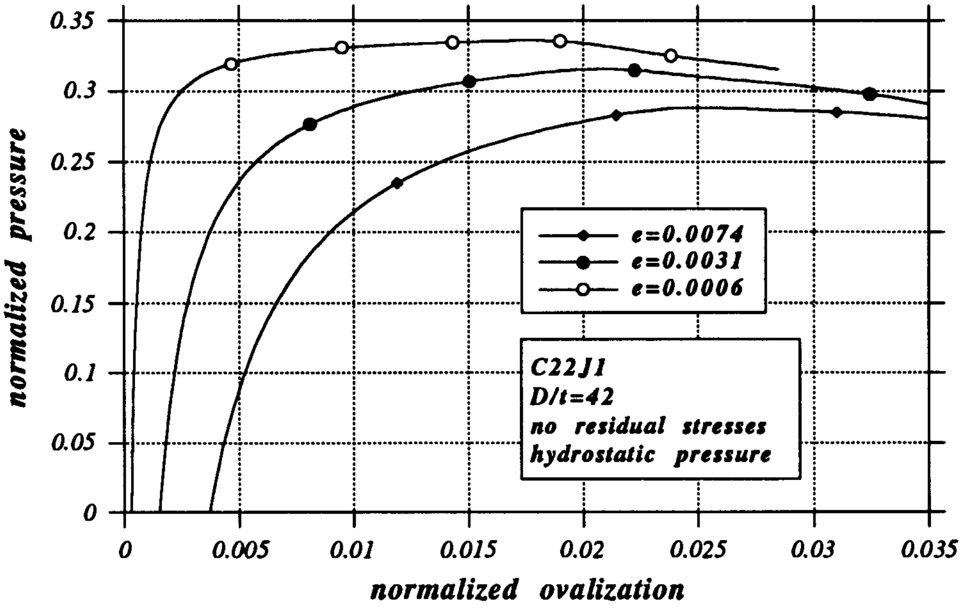

Figure 3.13: Hydrostatic pressure loading of tube C22J1 for different values of initial out-of-roundness.

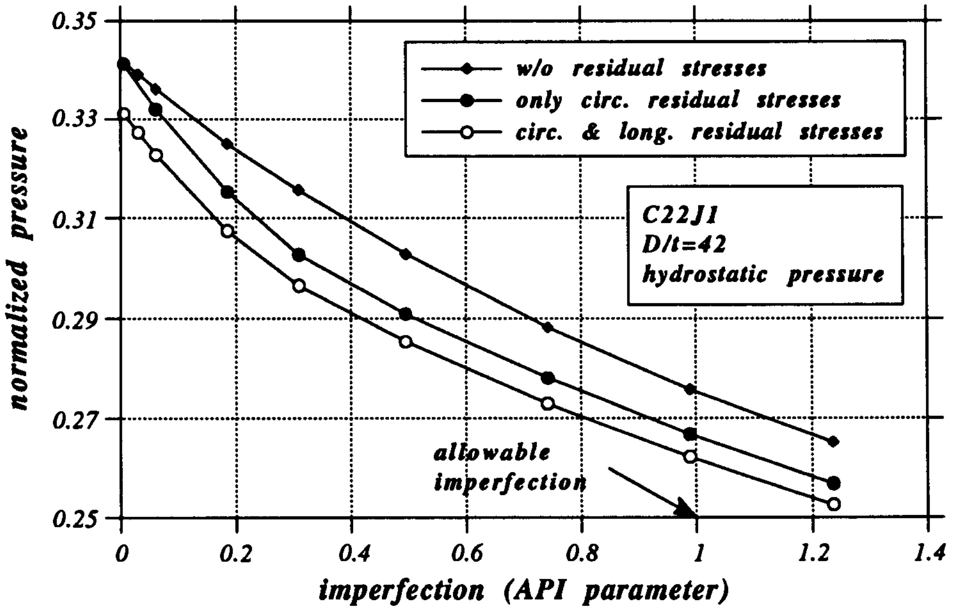

Figure 3.14: Effects of residual stresses and initial imperfections on pure pressure capacity.

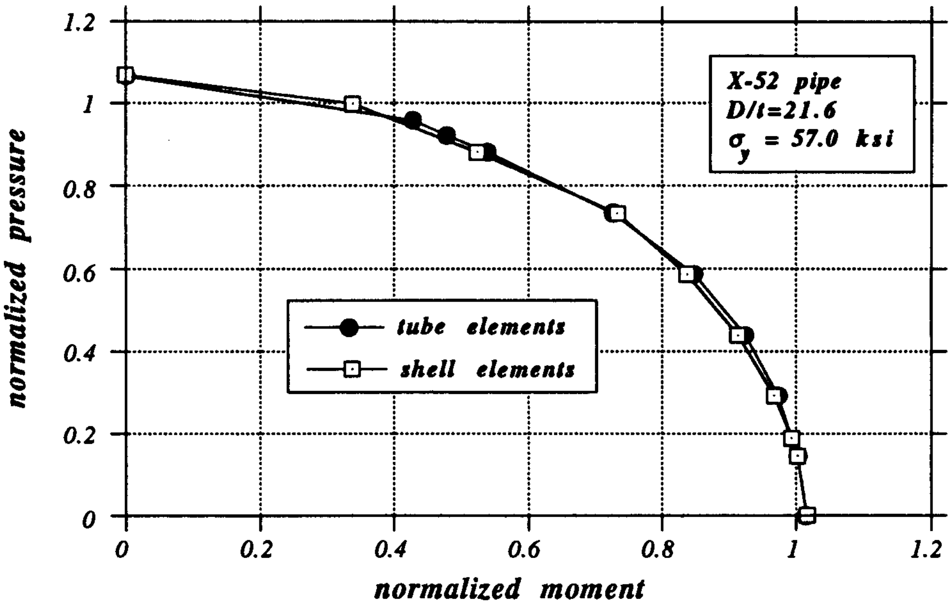

Figure 3.15: Comparison between shell and tube elements for pressurized bending for pressurized bending of tube X-52.

3.4 Pressurized bending

In Ref. [30], the case of pressurized bending was investigated for the X-52 tube using shell finite elements. The main result was the reduction of bending capacity in the presence of pressure. The same interaction is rederived for the X-52 tube using tube elements and the results are depicted in Figure 3.15. It can be seen clearly that the two curves are in excellent agreement.

The influence of the number of ovalization parameters on the pressurized bending case of X-52 tube is also examined. The pressure is taken equal to 4872.50 *psi* which is about 80% of the collapse pressure of the perfect pipe. Table 3.7 summarizes the results.

	limit moment $(k - in)$	limit curvature (in^{-1})
2^{nd} degree	2710	$2.4621 \cdot 10^{-4}$
3^{rd} degree	2717	$2.5012 \cdot 10^{-4}$
4^{th} degree	2634	$2.3581 \cdot 10^{-4}$
5^{th} degree	2636	$2.3576 \cdot 10^{-4}$
6^{th} degree	2624	$2.3502 \cdot 10^{-4}$
7^{th} degree	2618	$2.3228 \cdot 10^{-4}$
shell element	2627	$2.3467 \cdot 10^{-4}$

Table 3.7: Ultimate capacity of tube X-52 under pressurized bending.

It can be concluded that an expansion up to the fourth degree gives satisfactory results for pressurized bending of tubes with D/t ratio of about 20.

Figure 3.16 shows the pressure-bending interaction for tube C22J1 extensively analyzed earlier for other loading cases. Recall that, for both X-52 and C22J1 tubes, the instability that occurs during pressurized bending is due to extensive cross-sectional ovalization (Brazier effect). The pressure-moment $(p - M)$ interaction of tube C22J1 is presented for zero residual stresses and two values of initial imperfection $(e = 0.0, 0.002)$. The tube is first pressurized and, subsequently, keeping the pressure constant, it is subjected to bending until a limit moment is reached. Note that the two curves are very close.

The effects of initial imperfections and residual stresses are depicted in Figure 3.17. Initial out-of-roundness is taken equal to the maximum allowable by the API specification [5] $(e = 0.01)$. Apparently, for low levels of pressure the ultimate capacity is slightly affected, whereas there is a significant reduction of the interaction capacity for high values of pressure.

In Figure 3.18 the interaction curve for maximum allowable out-of-roundness $(e = 0.01)$ and nonzero residual stresses is compared with the API

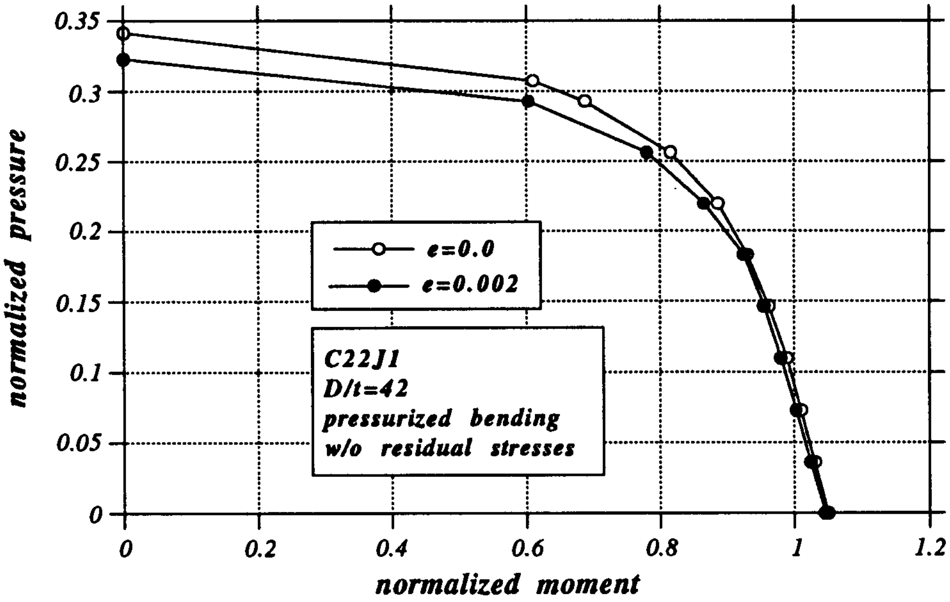

Figure 3.16: Pressure-moment interaction for tube C22J1 (without residual stresses).

interaction formula:

$$A^2 + B^{2\eta} + 2\nu AB = 1.0 \tag{3.6}$$

where

$$A = \frac{M + \sigma_{ce} S}{M_n} \tag{3.7}$$

$$B = \frac{p}{p_{hc}} \tag{3.8}$$

where σ_{ce} is the axial stress due to pressure (capped-end stress), p_{hc} is the ultimate pressure for zero axial stress

$$p_{hc} = 1.76E\left(\frac{t}{D}\right)^3 \tag{3.9}$$

and M_n is the ultimate moment in the absence of pressure:

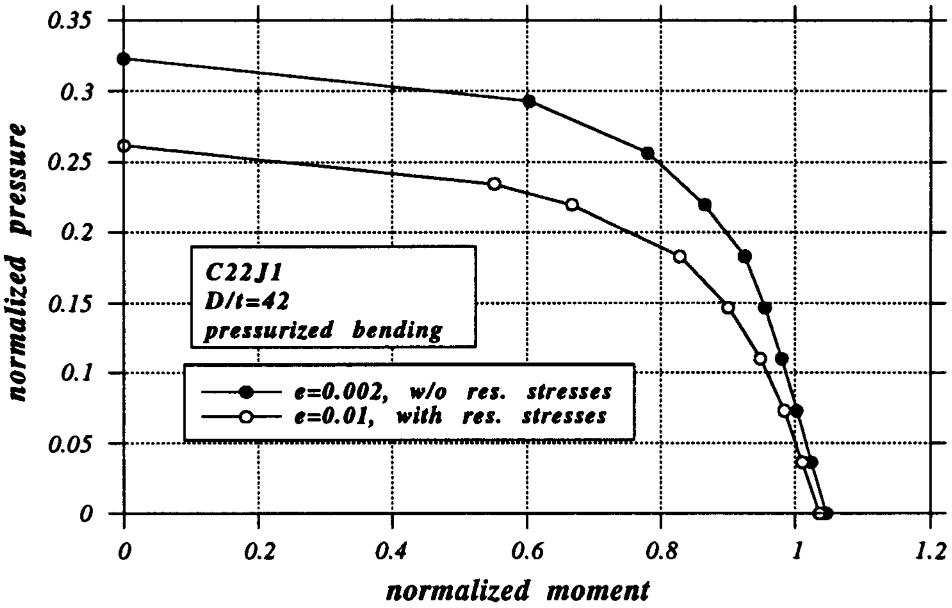

Figure 3.17: Pressure-moment interaction for tube C22J1 (with and without residual stresses).

- for $D/t \leq 1500/\sigma_y$

$$M_n = M_p$$

- for $1500/\sigma_y < D/t \leq 3000/\sigma_y$

$$M_n = M_p \left(1.13 - 2.58\frac{\sigma_y D}{E t}\right) \tag{3.10}$$

- for $3000/\sigma_y < D/t \leq 300$

$$M_n = M_p \left(0.94 - 0.76\frac{\sigma_y D}{E t}\right)$$

There is generally good agreement between the two curves. The difference in bending capacity between the curves for low values of pressure is due to strain-hardening which is neglected in the specification equation.

The pressure-curvature envelope for an imperfect tube including the effects of residual stresses is shown in the second graph of Figure 3.18 compared with the well-known Shell pipeline formula, widely used in pipeline design:

$$\frac{p}{p_{cs}} + \frac{k}{k_I} = 1 \tag{3.11}$$

where p_{cs} and k_I are defined in [41]. The comparison appears to be fairly satisfactory.

It is interesting to note the concave shape of the $p - k$ envelope as opposed to the convex $p - M$ envelope. Even for large values of pressure (50 - 60 % of the collapse pressure), the drop in moment is not dramatic. However, the ductility reduction is quite pronounced. This trend, also reported in Ref. [30], can be observed when comparing the moment-curvature curves for three levels of pressure shown in Figure 3.19.

3.5 Aspects of Localized Buckling under Bending

In previous Sections, tube instability due to extensive bending ovalization was examined. This phenomenon, referred to as "Brazier effect" characterizes the response of relatively thick tubes and results in a very smooth type of instability. However, it has been observed experimentally that tubes fail catastrophically because of buckling of the compression tube side. This type of failure may occur before or after the ovalization limit point and reduces significantly the tube bending capacity.

The bending buckling of elastic thin tubes ($D/t > 100$) was investigated by Seide and Weingarten [49] using a nonlinear shell theory and a

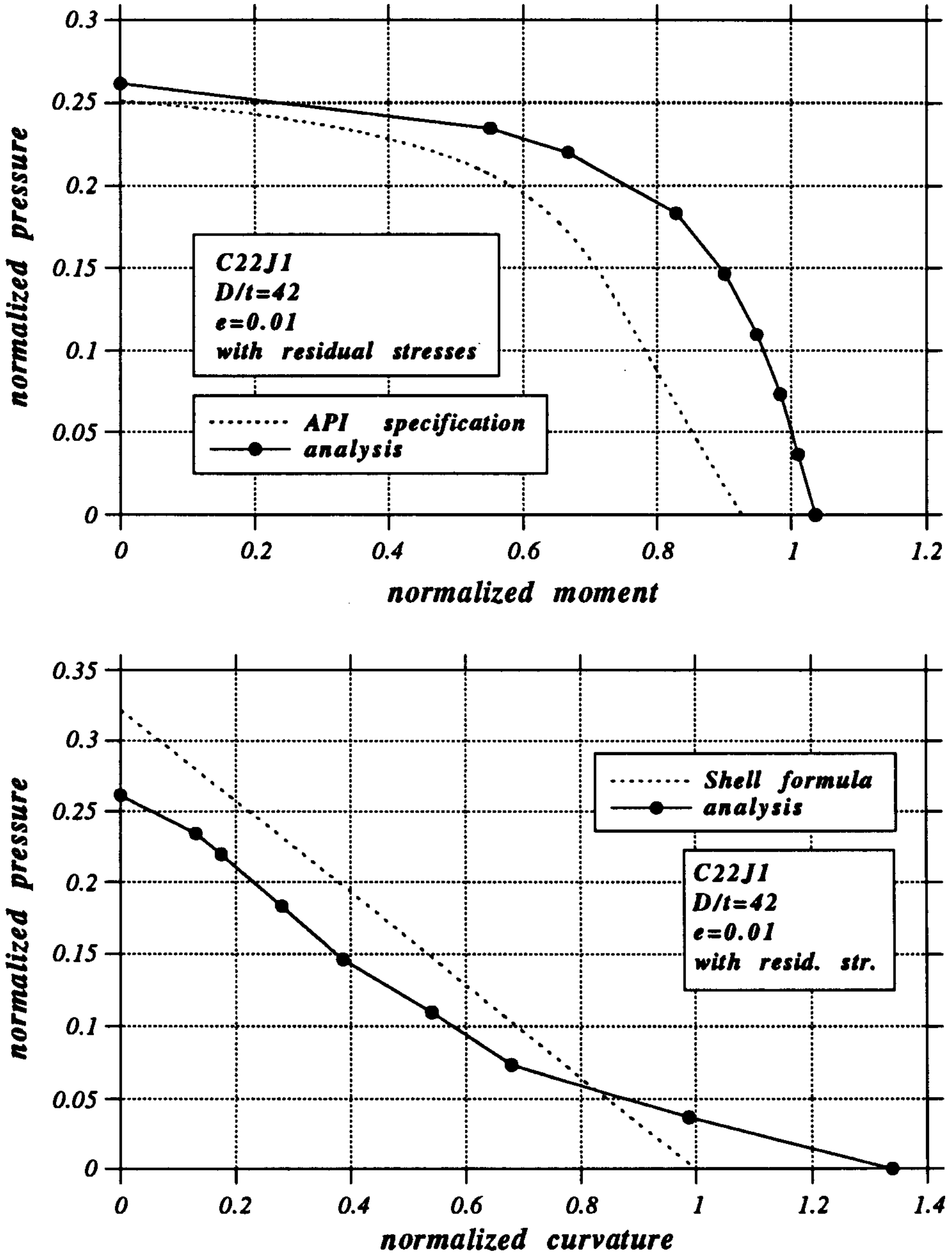

Figure 3.18: Pressure-moment interaction for tube C22J1 comparison with design formulas.

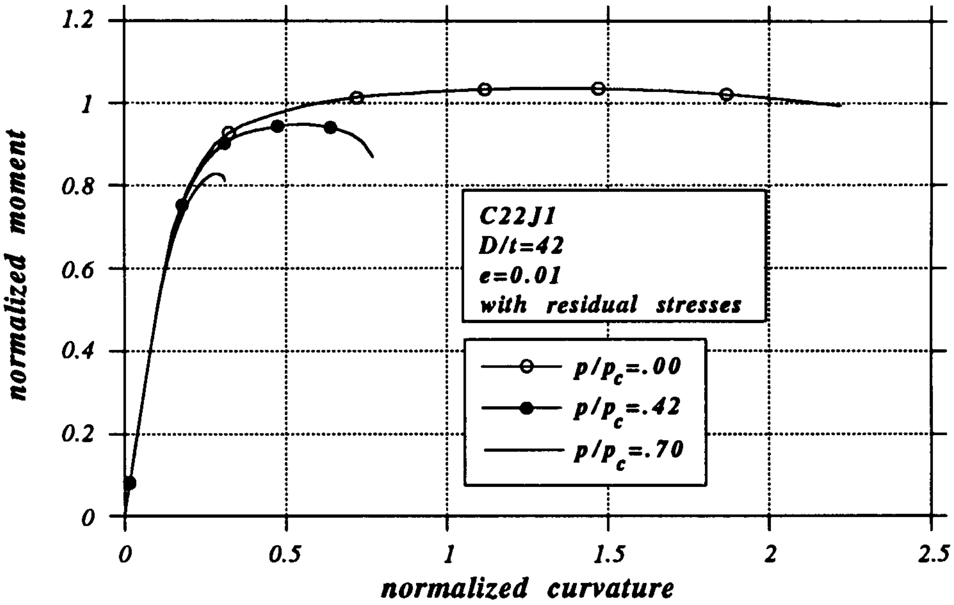

Figure 3.19: Bending curves of tube C22J1 for three different levels of pressure.

Galerkin method. It was found that the buckling moment depends on D/t but, in all cases, corresponds to a stress which is within 1.5% of the buckling stress due to uniform axial compression. More specifically, the buckling stress due to axial compression is given by the following formula (see Ref. [10]):

$$\sigma_{cr} = 0.577 \frac{Et}{R\sqrt{1-\nu^2}} \tag{3.12}$$

According to Seide and Weingarten [49], the buckling moment is approximately equal to

$$M_{cr} = 1.813 \frac{ERt^2}{\sqrt{1-\nu^2}} \tag{3.13}$$

On the other hand, Brazier's solution [9] suggests that ovalization instability occurs at

$$M_{lim} = 0.987 \frac{ERt^2}{\sqrt{1-\nu^2}} \tag{3.14}$$

which is almost 50% of M_{cr}. However, experimental evidence shows that catastrophic localized buckling occurs *prior* to the limit point. This inconsistency is due to the fact that the numerical procedure in Ref. [49] does not account for the cross-sectional ovalization of the pre-buckling configuration. Ovalization flatens the section and increases the maximum bending stress. Figures 3.20 and 3.21 show the response of three thin elastic tubes under pure bending. In all three cases, bending buckling occurs *just before* the limit point and the post-buckling configuration is a wavy pattern.

By normalizing the moment and the curvature, the three pipes have an identical response as shown in Table 3.8. Note that the moment is normalized by the elastic moment parameter M_e and the normalized value is referred to as "elastically normalized moment". Furthermore, the half wavelength of the post-buckling configuration, when normalized by $\sqrt{Dt}$, appears to be the same for all three tubes. The results are summarized below and are in excellent agreement with those reported by Ju and Kyriakides [29].

tube	elast. normalized moment M_b	normalized curvature k_b	normalized half wavelength
100	0.9428	1.760	1.700
200	0.9432	1.764	1.694
400	0.9438	1.770	1.700
200 [29]	0.9240	1.740	1.693

Table 3.8: Elastic buckling of thin tubes under bending; comparison with Ju and Kyriakides [29].

An interesting computational aspect of this problem concerns the tube length required to obtain the wavy deformation pattern. Clearly, the tube must be

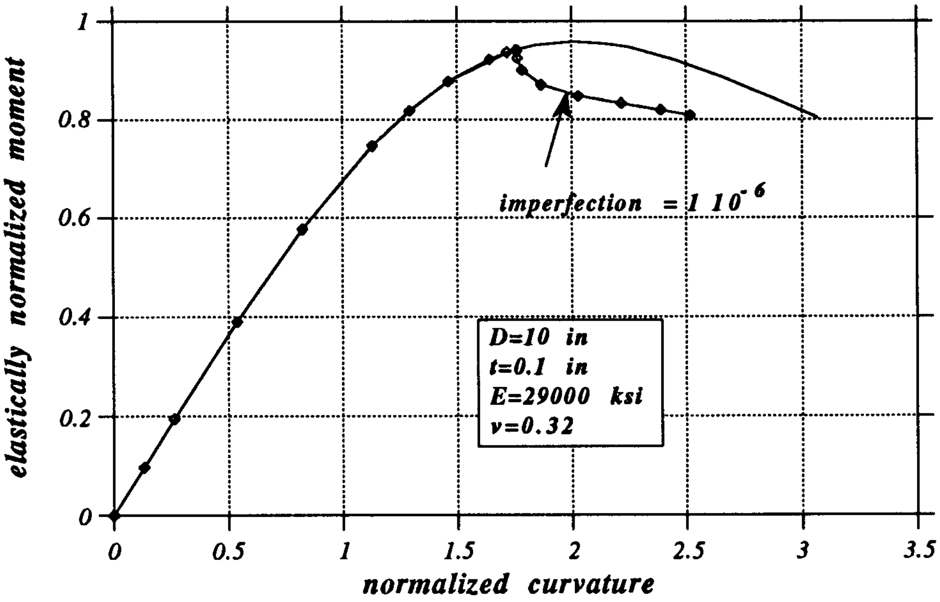

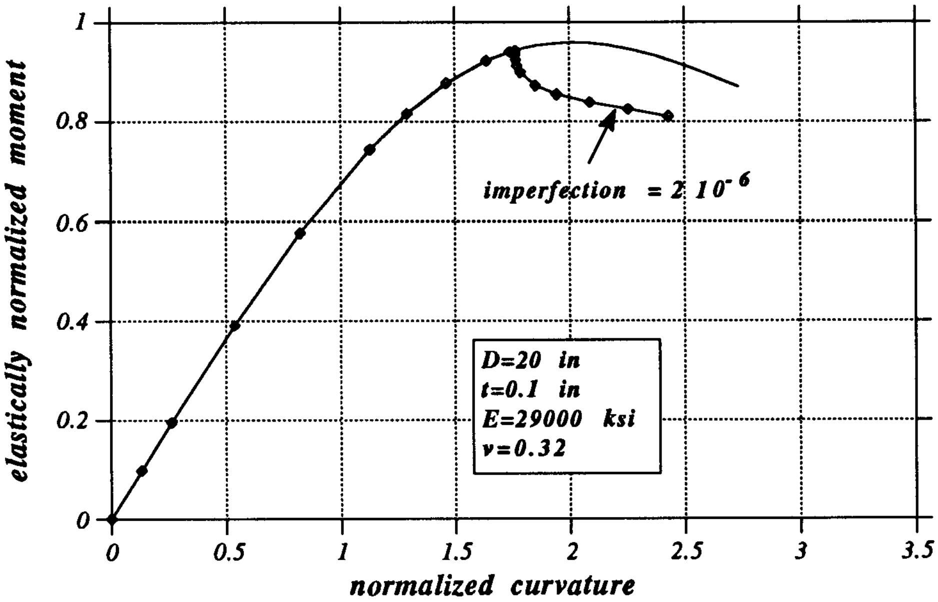

Figure 3.20: Bending buckling of tubes 100 and 200.

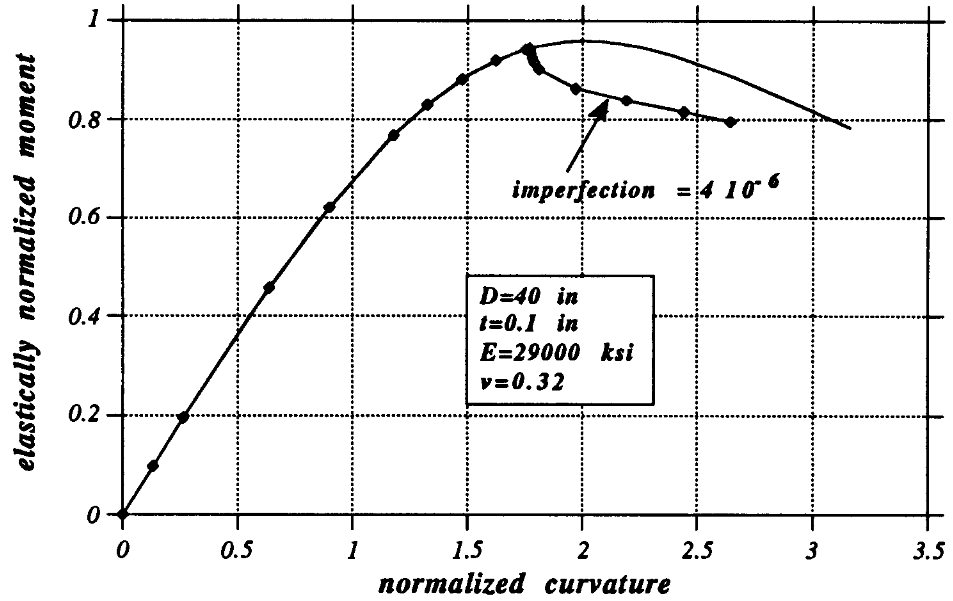

Figure 3.21: Bending buckling of tube 400.

several diameters long so that the response is independent of the end conditions. However, it is possible to avoid such a computationally expensive analysis by considering the symmetry of the problem. Assuming that the tube is infinitely long, only a half-wavelength-long segment needs to be analyzed, with zero warping conditions at the two ends. Of course, the wavelength is not known a priori and, therefore, several trial values must be considered. The value that corresponds to the minimum moment capacity is equal to the actual half wavelength. Nevertheless, it was found that small variations (within 10%) of the assumed value of wavelength do not have significant effects on the response. Five tube elements were employed for this analysis with very good results. Moreover, an eighth-order expansion of the cross-sectional deformation was found to give excellent results.

The bifurcation instability of thin elastic tubes under bending into a wavy pattern, although an interesting issue of solid mechanics, is of no particular importance for practical offshore considerations. Tubes which are candidates for deep-water applications have a diameter-to-thickness ratio between 35 and 60 and exhibit inelastic response. In addition, end sections are usually constrained against ovalization and, therefore, maximum cross-sectional deformation occurs at the middle section of the tube. As a consequence, deformation localizes at the middle section in the form of a sharp "kink". This type of buckling has been observed in previous experimental works [33], [46], [15] and results in a sudden and catastrophic drop in bending capacity.

First, a ten-diameter long segment of a tube which has the cross-sectional and material characteristics of C22J1 is analyzed in pure bending. The tube is assumed to have both longitudinal and circumferential residual stresses and a uniform initial out-of-roundness equal to the API allowable value ($e = 0.01$). The specimen ends are restrained against cross-sectional deformation. These conditions result in maximum cross-sectional deformation at the middle section and, consequently, this is the section where localized deformation is expected to occur. An eighth-order expansion is assumed for cross-sectional deformation and the element size about the middle section is taken equal to 8.5% of the tube diameter. The moment-curvature curve is shown in Figure 3.22. A sharp drop in moment capacity occurs at $k_b/k_I = 1.57$ indicating local buckling instability. However, this "buckling" point is located after the limit point ($k_{lim}/k_I = 1.19$) and does not affect the value of the maximum moment. In the same figure, the moment-curvature curve derived from two-dimensional analysis is also shown. Recall that the two-dimensional

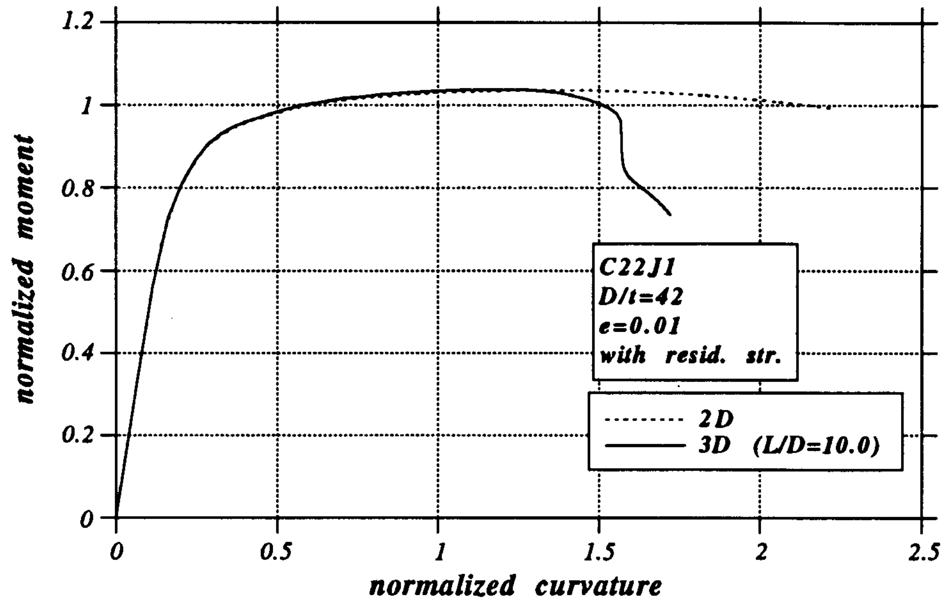

Figure 3.22: Bending response of tube C22J1.

analysis assumes uniform deformation along the tube and, consequently, the only possible mode of instability is the "Brazier effect". The two curves begin to deviate at a value of normalized curvature equal to 1.3 which is after the limit point.

The post-buckling configuration of the tube is shown in Figure 3.23. Obviously, the sharp "kink" at the middle cross-section is responsible for the sudden drop in moment capacity. The symmetry of tube geometry and boundary conditions implies that the deformation should be symmetric about the middle-section. Therefore, it would be reasonable to analyze half the tube, imposing symmetry conditions (i.e., zero warping) at the middle section, thus reducing the computational cost. The results from such an analysis of tube C22J1 are shown in Figure 3.24. Apparently, the two curves are considerably different after the limit point. This indicates that the post-buckling configuration is not symmetric about the middle section and, in order to obtain the exact shape analytically, the *entire tube* must be analyzed. This argument is further justified by observing the tube deformation around the local buckle shown in Figure 3.25 obtained from half-tube analysis. This shape has not been encountered in previous bending experiments [17].

The effects of pressure on a ten-diameter tube segment under bending are shown in Figure 3.26. The bending response for a pressure level equal to 55% of the collapse pressure of the unstiffened tube ($p = 400\,psi$ and $p_c = 714\,psi$) is compared with the response obtained from a cross-sectional analysis. The value of the maximum moment is the same for the two analyses. However, the three-dimensional analysis indicates a sudden drop in moment capacity just after the limit point.

The bending curves for the two pressure levels are compared in the second graph of Figure 3.26. Clearly, the presence of external pressure reduces the ductility of the member significantly. Recall that a similar effect was observed in the previous section using cross-sectional analysis. In Figure 3.27, some results derived from three-dimensional analysis are compared with the interaction curve derived in the previous section. The points are in very good agreement with the interaction curve. This implies that, although the tube loses substantial ductility, the ultimate moment is not affected by the presence of localized phenomena.

Localization of deformation is also detected in the bending response of a ten-diameter-long tube which has the cross-sectional and material charac-

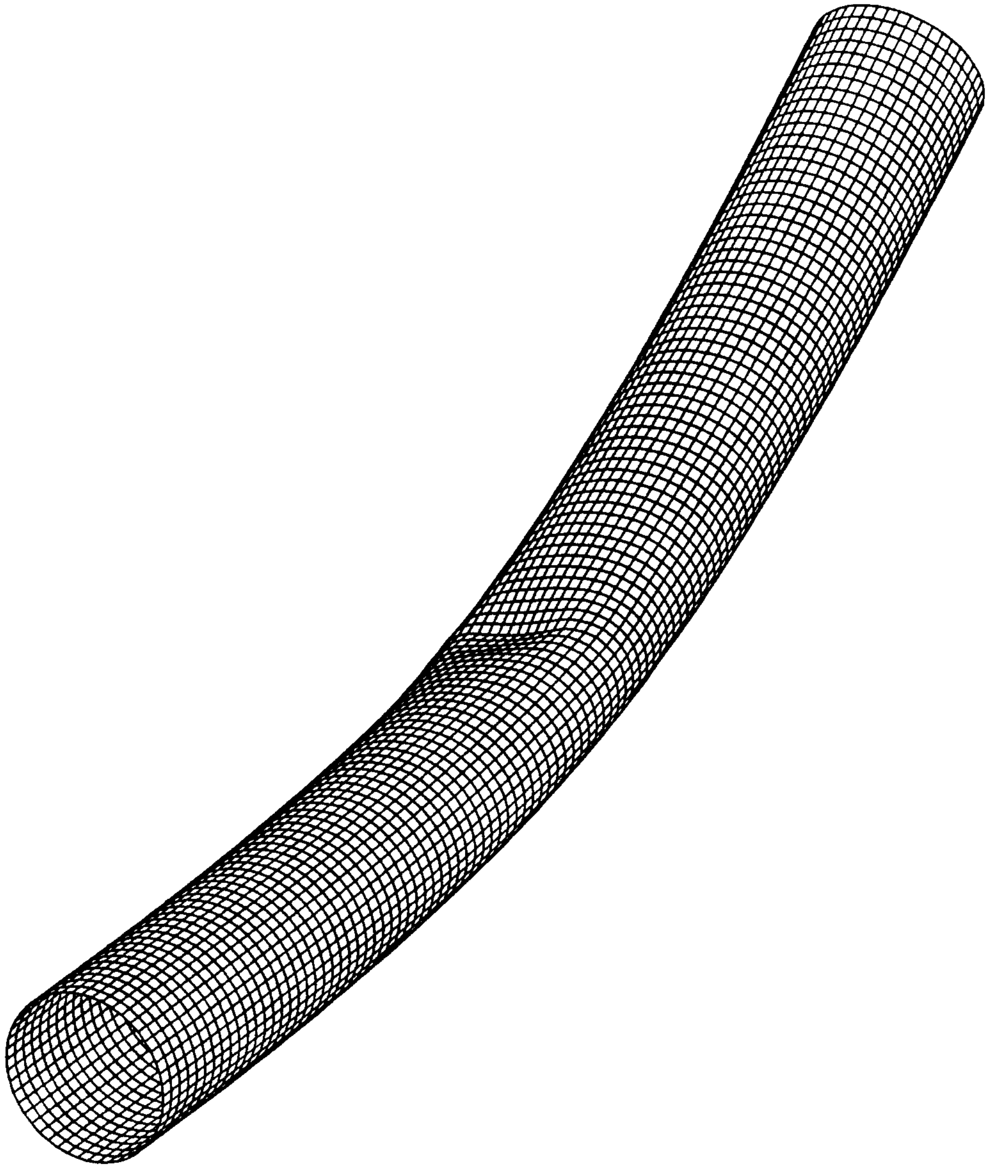

Figure 3.23: Deformed shape of tube C22J1 after local buckling.

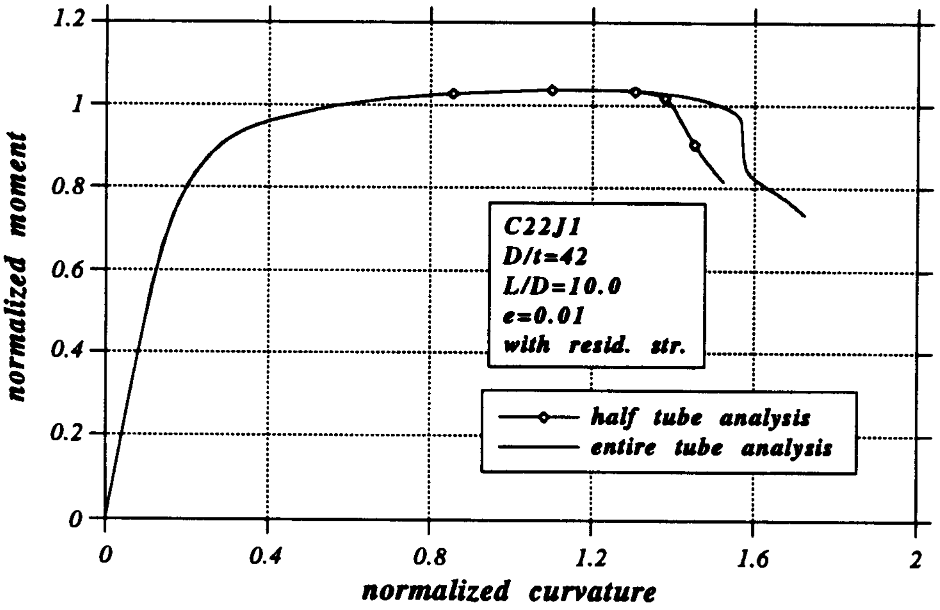

Figure 3.24: Bending responses of tube C22J1 for entire and half tube analysis.

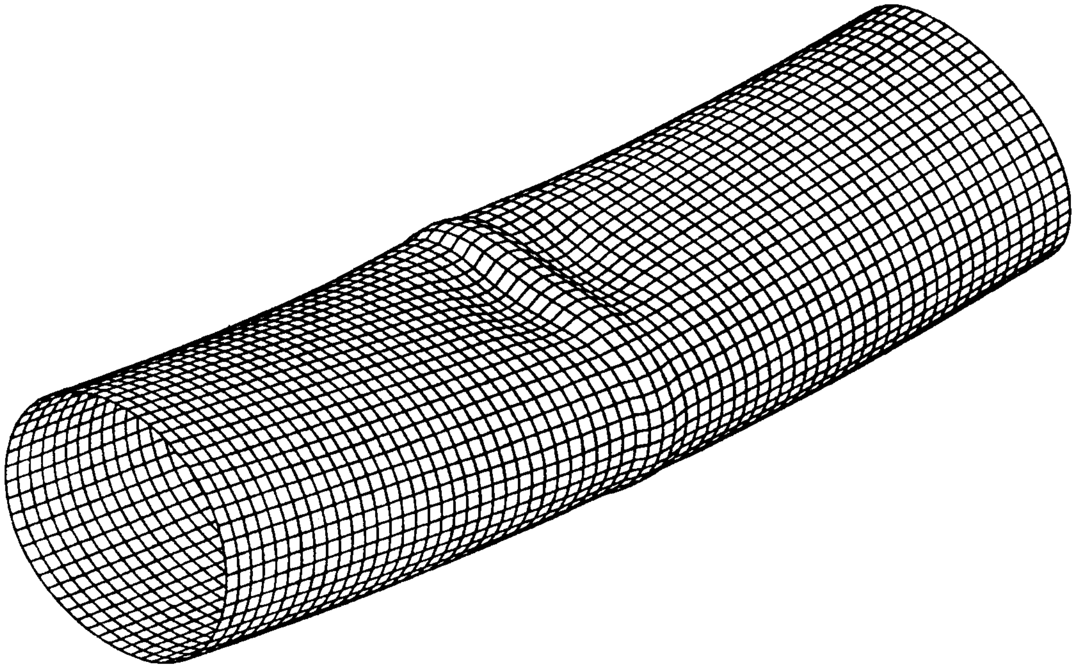

Figure 3.25: Buckling shape of tube C22J1 obtained from half-tube analysis (central portion of tube).

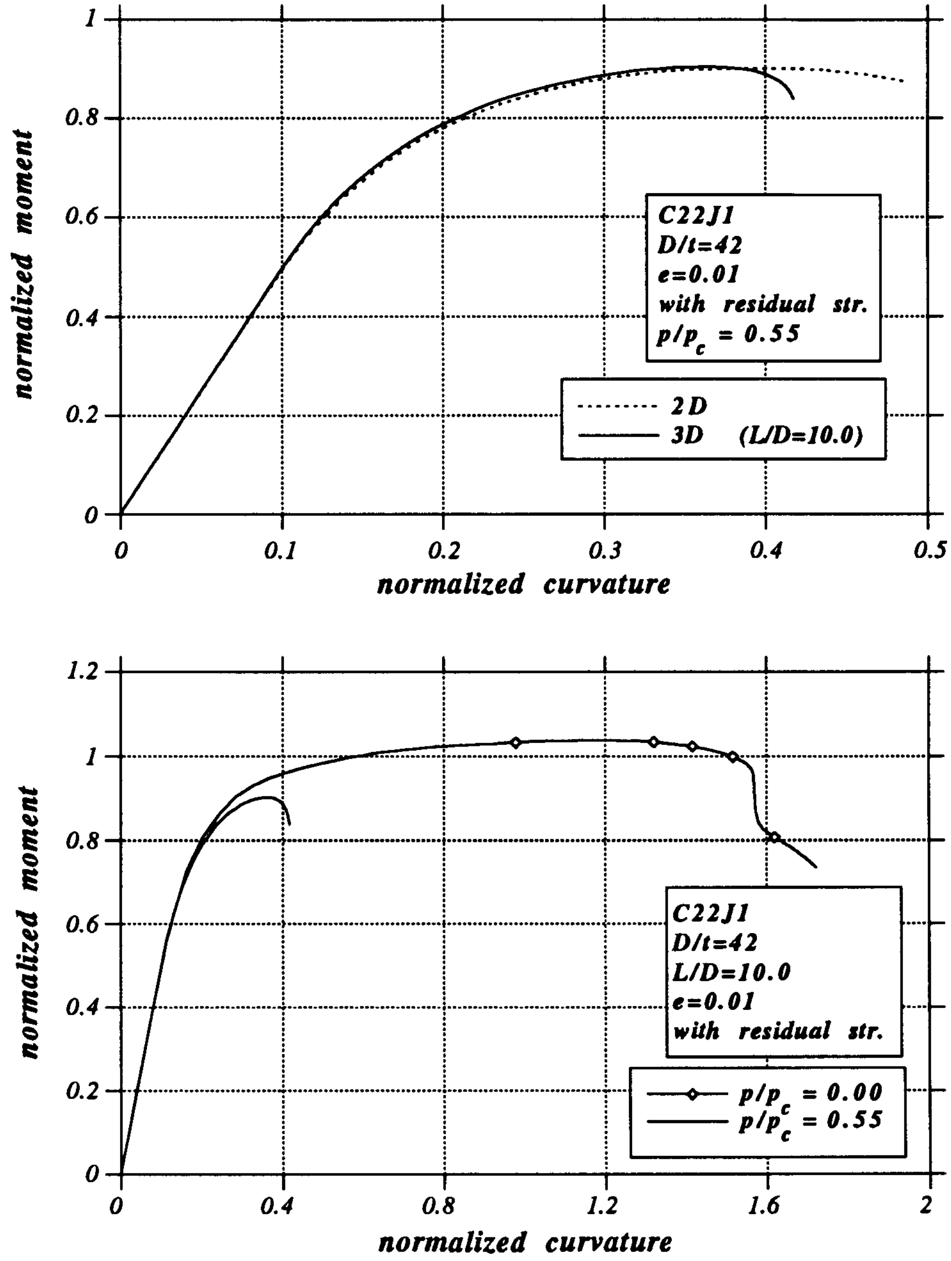

Figure 3.26: Bending response of tube C22J1 under pressure ($p_c = 714\,psi$).

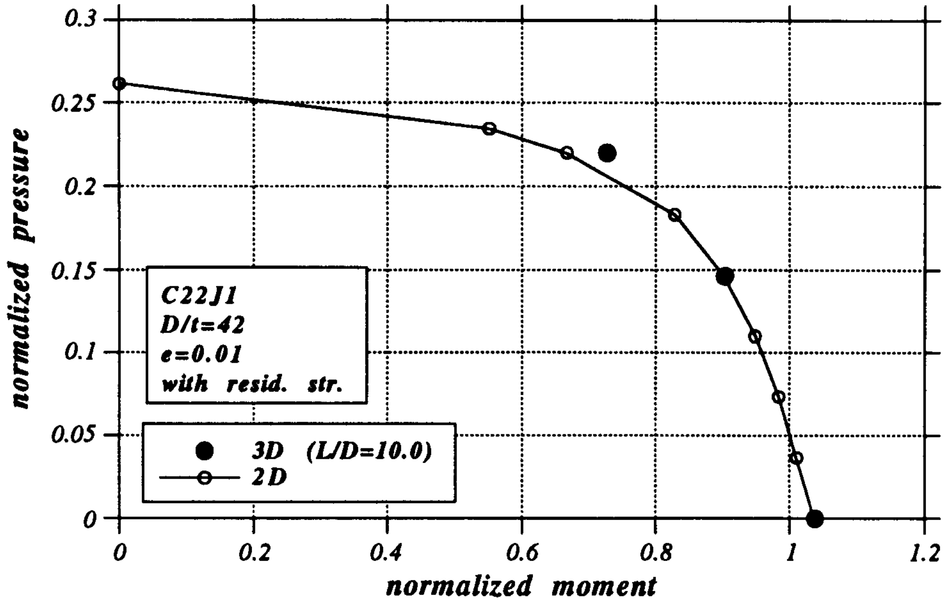

Figure 3.27: Comparison of $3D$ results with $2D$ interaction curve for pressurized bending (tube C22J1).

teristics of C6J5. The element size and order of expansion used for tube C22J1 are adopted for this tube as well. The tube is assumed to have nonzero residual stresses and an initial ovalization equal to the API allowable value. In addition, the end sections remain undeformed and, therefore, the maximum cross-sectional deformation occurs in the middle section. In Figure 3.28, the bending curve from three-dimensional analysis is compared with the corresponding curve derived from cross-sectional analysis. Their comparison suggests that deformation starts to localize at a value of normalized curvature equal to 1.45. However, as in the case of tube C22J1, localization does not affect the value of the ultimate moment.

It is also worth investigating the effects of tube length on the bending response. Consider tube C22J1 with a uniform initial ovalization e equal to

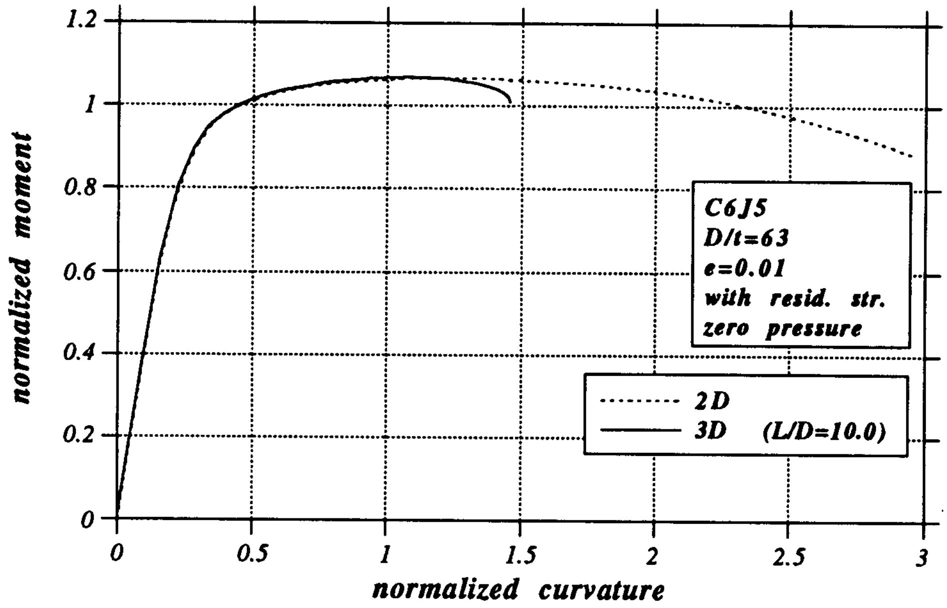

Figure 3.28: Bending response of tube C6J5.

0.01 and nonzero residual stresses. The tube end sections are held undeformed in order to ensure that localization occurs in the middle section. Results are plotted in Figure 3.29 whereas Figure 3.30 shows the post-buckling configuration for the cases where tube length is equal to three and five diameters. Apparently, ductility is significantly increased when the length is reduced, but the value of maximum moment is not substantially affected. These results are of particular importance for the design of stiffened tubes. In the present case, the undeformed end sections may be regarded as sections which carry very heavy stiffeners. The effects of stiffeners on tubular member capacity will be further investigated in Chapters 5 and 6.

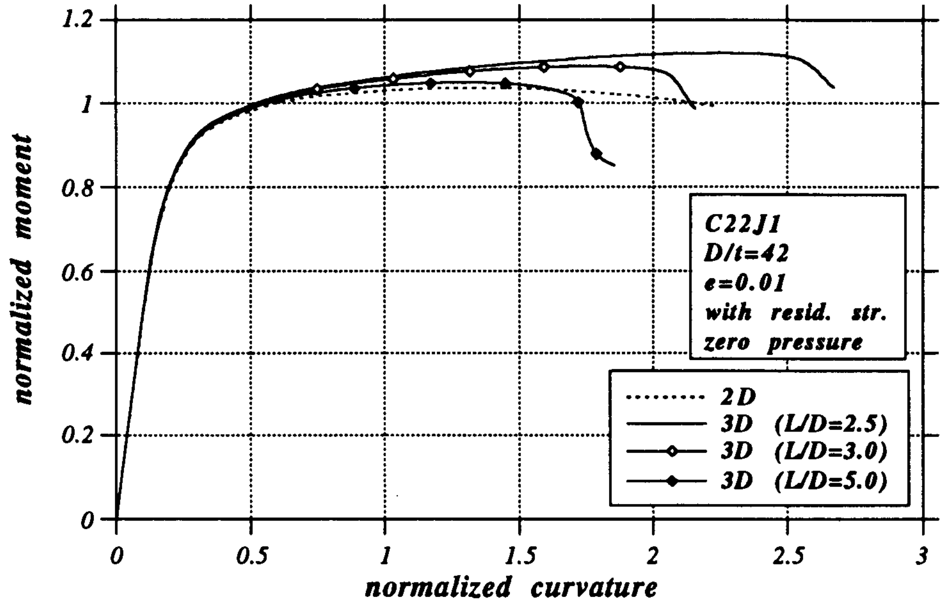

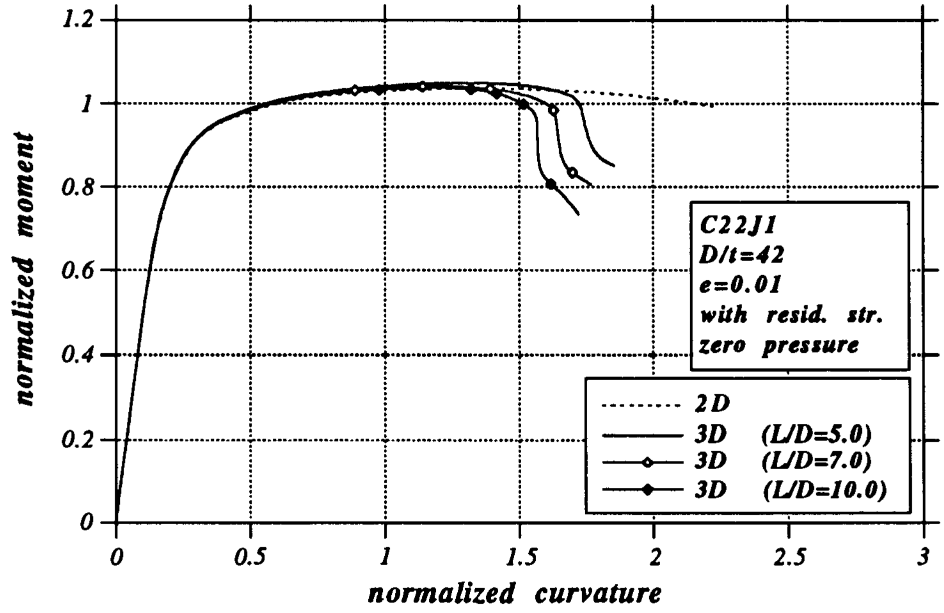

Figure 3.29: Effects of tube length on bending response of C22J1 (undeformed end sections).

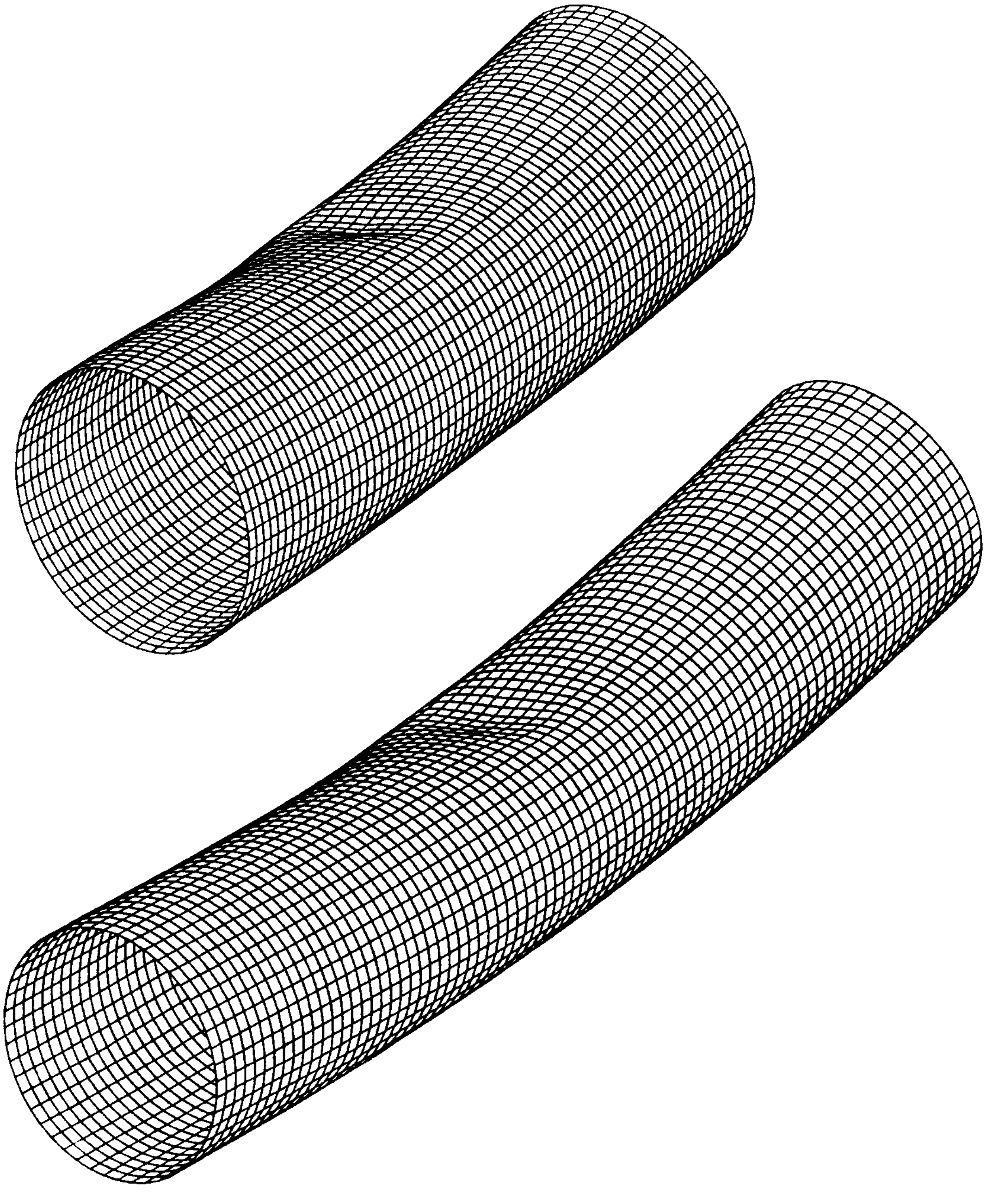

Figure 3.30: Post-buckling shapes of tube C22J1 for L/D = 3.0 and $L/D = 5.0$.

3.6 Beam-Column Stability in the Absence of Pressure

In this section, the beam-column stability is considered. The tube is assumed to have the cross-sectional and mechanical properties of tube C22J1 extensively analyzed in the previous sections. The first goal is to obtain the buckling curve (i.e., buckling load for different values of the slenderness ratio). Figure 3.31 shows the buckling curves for two typical values of initial out-of-straightness using tube elements in the absence of initial out-of-roundness and residual stresses. The initial out-of-straightness imperfection is assumed to be of sinusoidal form in the plane of bending. The initial lateral displacement of the tube axis, denoted by $y_i(x_3)$, can be written as

$$y_i(x_3) = \delta_o \, sin\left(\frac{\pi x_3}{L}\right) \tag{3.15}$$

The measure of out-of-straightness is then

$$\Delta = \frac{\delta_o}{L} \tag{3.16}$$

The tube is considered to be simply supported. The predictions are successfully compared with the parabolic buckling curve adopted by API.

Next, the interaction between compressive force and bending moment is presented for the same tube and for two values of the slenderness ratio. The tube is assumed to be simply supported and subjected to axial load and two end moments of equal magnitude and opposite direction. The external pressure is assumed to be zero in all cases. The solid line in Figure 3.32 shows the thrust-end moment $P-M$ interaction derived using tube elements. These cases are analyzed with zero initial out-of-straightness, except for the zero moment case, where a maximum longitudinal imperfection $\Delta = 1/4000$ is

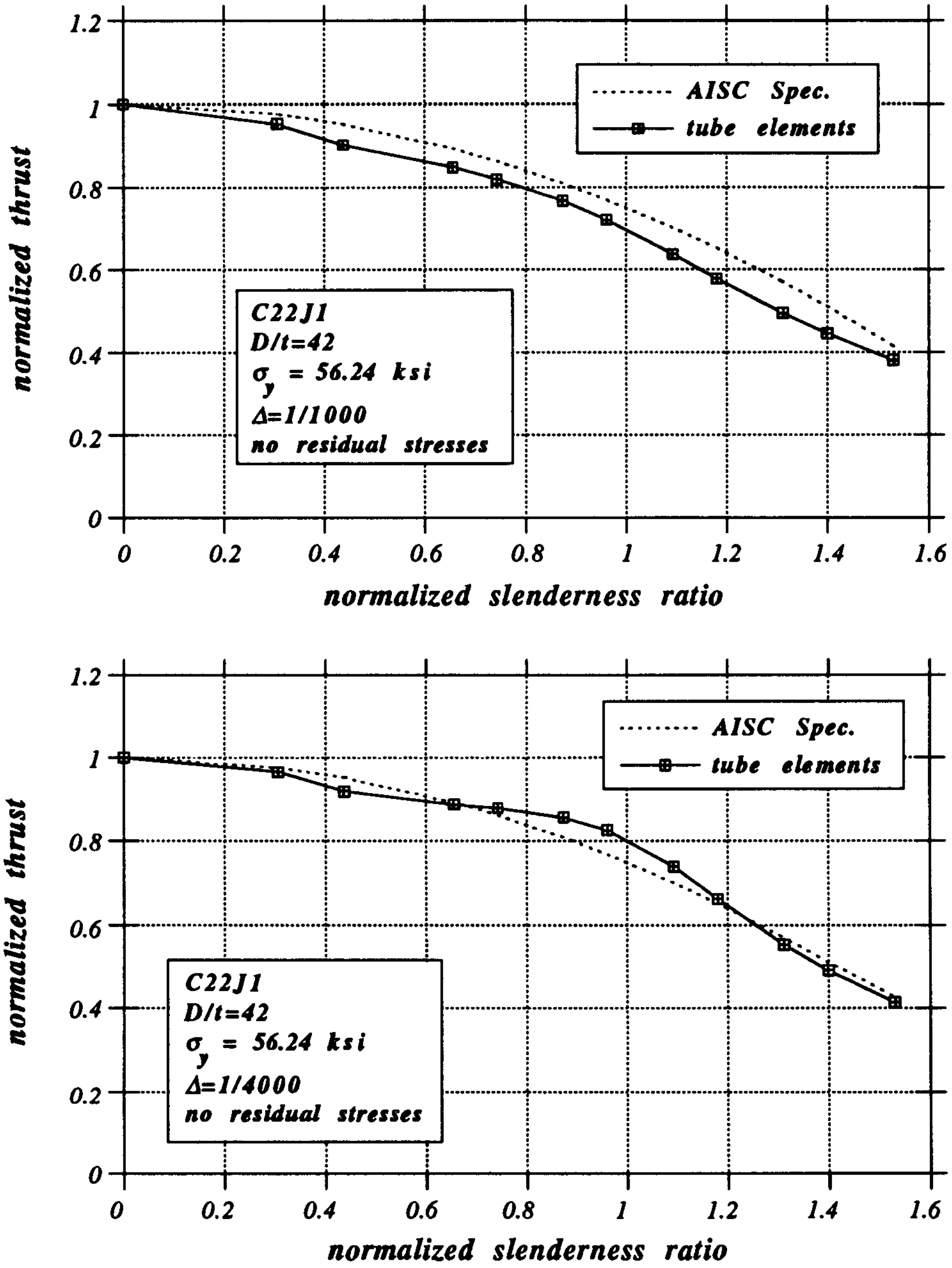

Figure 3.31: Axial capacity of tube C22J1 for two values of initial out-of-straightness.

assumed. The curve is compared with the well-known beam-column equation with amplification factor, adopted by API:

$$\frac{P}{P_{cr}} + \frac{M}{(1 - P/P_e)M_n} = 1 \qquad (3.17)$$

and the results are very satisfactory. For this analysis, the element size is assumed equal to 70% of the tube diameter and a fourth-order expansion is employed for the cross-sectional deformation. The above mesh appears to be quite coarse. However, it will be shown in the last section of this Chapter, as well as in Chapter 6, that the ultimate capacity of slender columns is not affected when a finer mesh is used. This phenomenon implies that global instability, rather than localized buckling governs slender-column behavior.

Finally, the interaction between axial load and bending moment in the presence of residual stresses is depicted in Figure 3.33. Apparently, the ultimate capacity is affected for cases where the moment is very small, and buckling is controlled by Euler-type instability.

3.7 Cross-sectional capacity under thrust and bending

The prediction of cross-sectional capacity under the simultaneous presence of axial force and bending moment is important for the determination of the ultimate strength of tubes with small values of slenderness ratio. In fact, according to the API specification [4], the "cross-sectional strength" interaction equation

$$\frac{P}{P_y} + \frac{M}{M_n} = 1 \qquad (3.18)$$

must be satisfied in addition to the global stability interaction Equation 3.17. The linear form of Equation 3.18 was found not to agree with experimental

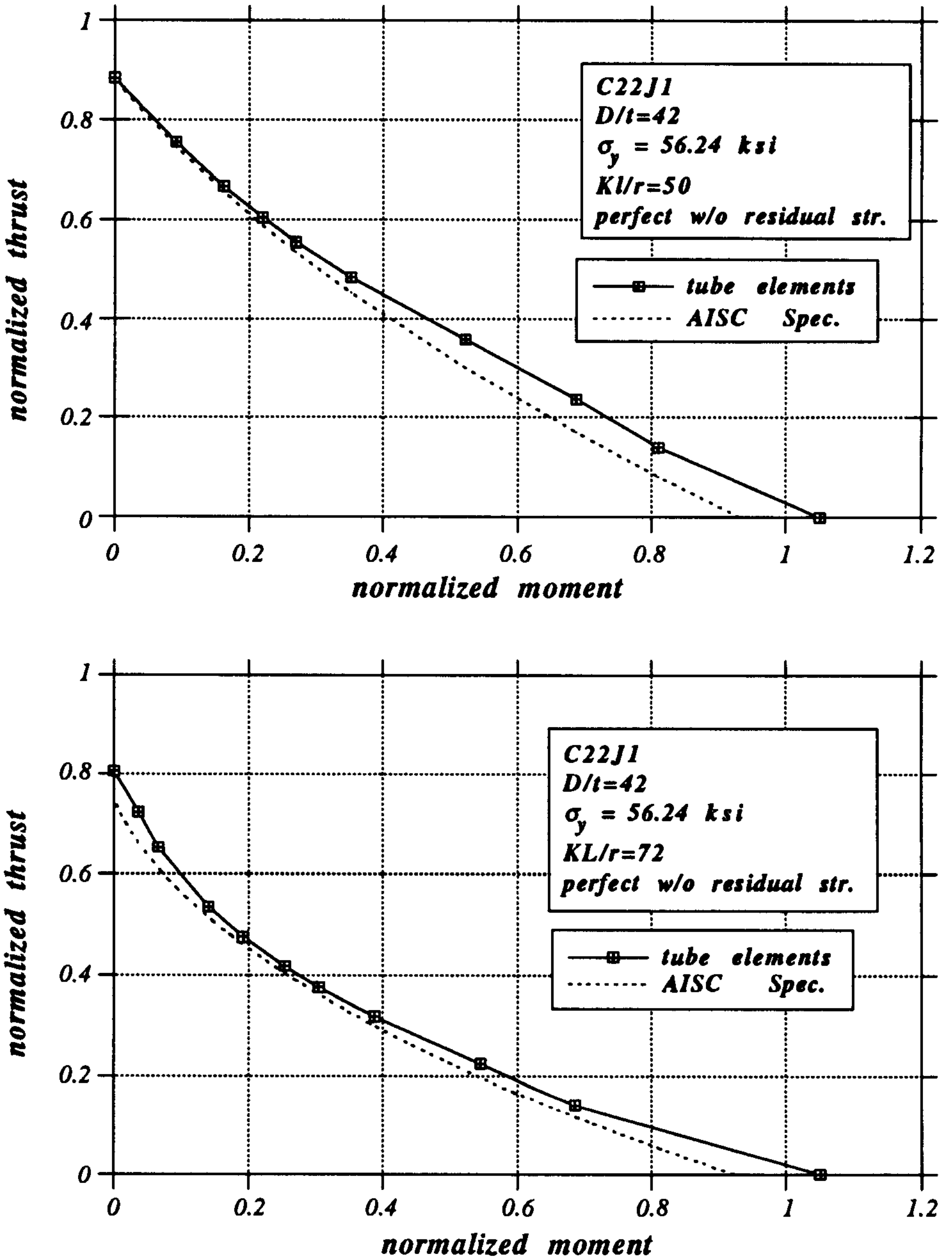

Figure 3.32: Moment-thrust envelopes of tube C22J1 for two values of slenderness ratio.

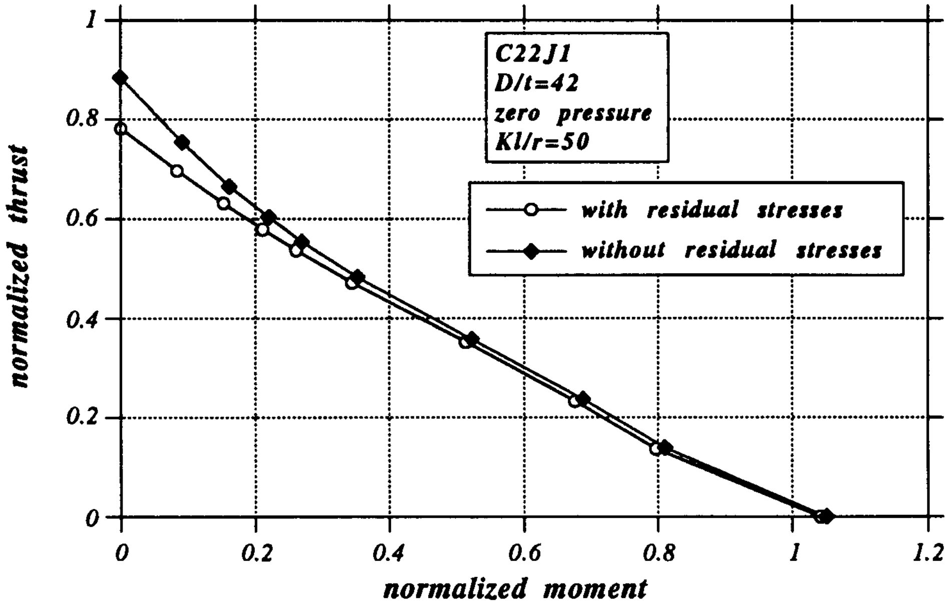

Figure 3.33: Effects of residual stresses on moment-thrust envelope of tube C22J1 for slenderness ratio $KL/r = 50$.

data [37] and was substituted by the following equation in the recent API-LRFD specification [5]:

$$cos\left(\frac{\pi}{2}\frac{P}{P_y}\right) = \frac{M}{M_n} \tag{3.19}$$

The above equation is the theoretical thrust-moment interaction for cross-sectional plastification of a tube.

The above two interaction equations are compared in Figure 3.34 with results from the present analytical technique. In these results, the axial force is assumed to be tensile. Furthermore, bending moment and axial force are simultaneously increased by the same proportion (radial loading path). The analytical results verify the "convex" shape of the interaction implied by Equation 3.19. Note that the apparent difference between analysis and pre-

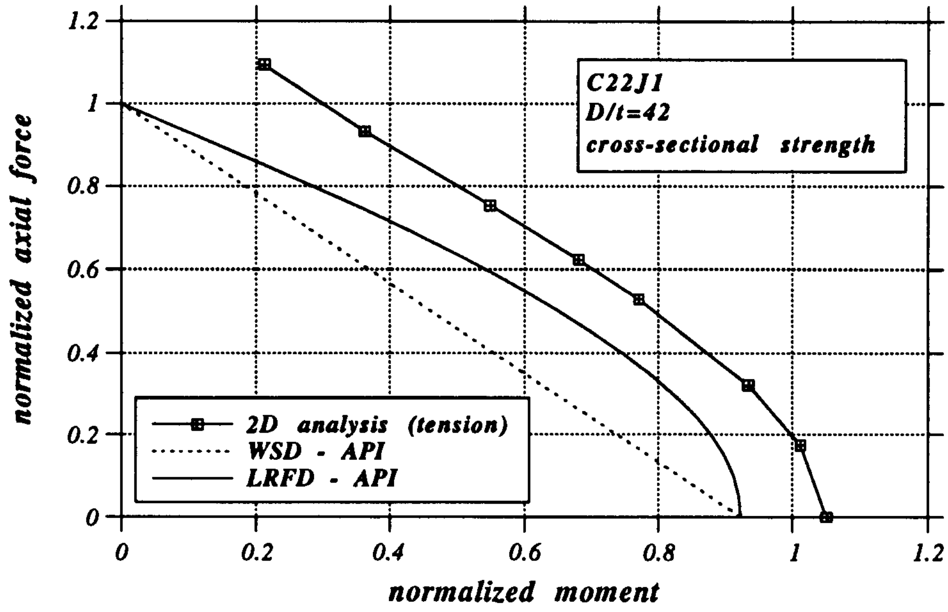

Figure 3.34: Cross-sectional capacity of tube C22J1 under axial force and bending moment (radial loading).

dictions is due to the post-yielding strength of tube C22J1 which is neglected in the specification equation.

Another interesting observation involves the difference in response when axial compression is used instead of axial tension. Figure 3.35 implies that compressive force increases the ultimate capacity. This can be explained by the fact that axial compression tends to increase the area enclosed by the tube and, thus, decreases the rate of ovalization and provides additional cross-sectional stiffness.

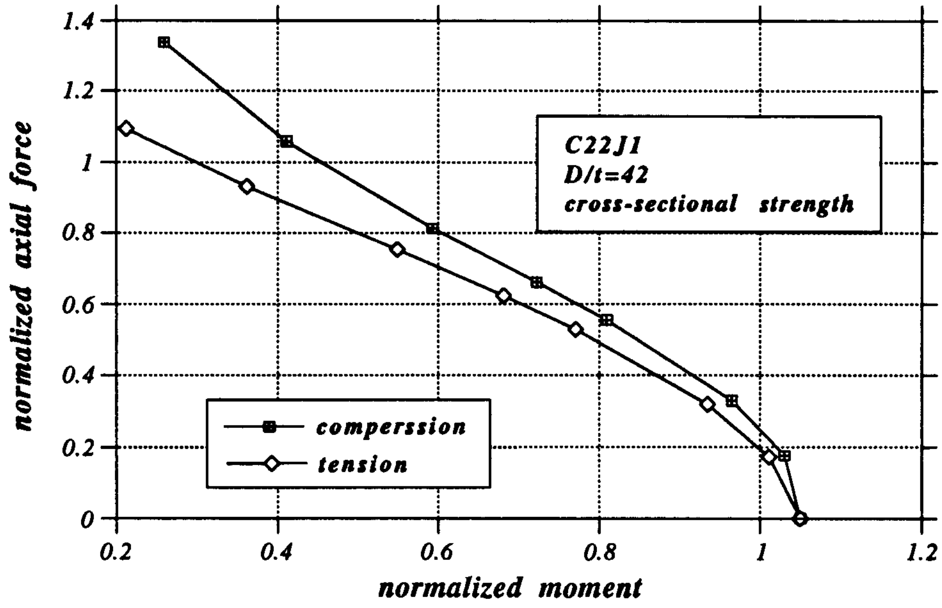

Figure 3.35: Cross-sectional capacity of tube C22J1 under bending moment and tension or compression (radial loading).

3.8 Effects of Pressure on Global Tube Stability

In a previous section, the beam-column stability was examined under zero external pressure. In this section, the effects of external pressure are considered.

It has been noted in a previous analysis [63] that for the case of elastic buckling of bars using the classical beam-column approach, pressure does not contribute to member instability. This is because the "tensile component" of the pressure, produces a curvature-dependent lateral load $-(pA)\, d^2y/dx^2$ which must be included in the equilibrium equation and apparently cancels the effect of the capped-end force pA (see Figure 3.36). Thus, the stability equation is independent of the hydrostatic pressure p.

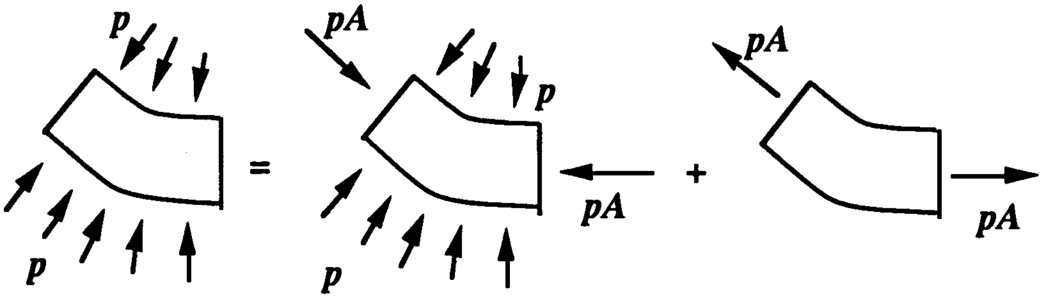

Figure 3.36: Effects of pressure on global member stability.

However, the previous argument hinges on the assumption that the cross section remains unchanged along the tube. This is not the case for high values of pressure because of possible extensive ovalization at certain tube sections. This ovalization is accentuated by initial imperfections and residual stresses. Moreover, a localized deformation may occur and further reduce axial load capacity. These effects must be investigated in order to achieve better understanding of the phenomenon. It is worth mentioning however, that specification rules [5] do not imply any interaction between pressure and axial load.

Figure 3.37 shows the effects of external pressure on member stability under axial load. The tube has the cross-sectional and material characteristics of tube C22J1 and a slenderness ratio KL/r equal to 50. The behavior of this tube under hydrostatic pressure is shown on the second graph of Figure 3.37. The initial out-of-straightness (Δ) and out-of-roundness (e) are chosen equal to 0.001 and 0.01 respectively, which are the specification limits [3]. External pressure does not have a significant effect on global instability. The effect becomes important for pressure levels above 85% of the collapse pressure. In the same graph, the axial capacity under pressure in the presence of residual stresses is also presented. Results indicate a similar reduction of axial thrust capacity.

The same trend is implied by Figure 3.38 which shows the axial capacity of tube C6J5 in the presence of external pressure. The slenderness ratio (KL/r) of the tube is taken equal to 50. The behavior of this tube under pure pressure is shown in the second graph of Figure 3.38. Apparently, for pressure levels below 85% of the collapse pressure, the ultimate capacity is almost unaffected.

All cases analyzed involve pressure levels p/p_y below 26%. In Chapter 6, the analysis of stiffened columns will show that the p/p_y ratio is the most important parameter for pressure-thrust interaction and pressure effects on thrust capacity are significant for p/p_y greater than 40%, provided, of course, that the collapse pressure is not reached. The above argument verifies that for the unstiffened cases investigated in this section, the axial capacity is affected by the presence of pressure only in the proximity of ultimate pressure level.

Finally, for the analysis of tubes under axial load and pressure, the finite element mesh is chosen to be very fine about the middle section, where $P-\Delta$ effects are maximum and instability occurs. The element size about the middle section is taken equal to 10% of the tube diameter. For both tubes considered, localized deformation occurred at the middle section, *after* the limit point is obtained. Figures 3.39 and 3.40 show the post-buckling configurations of axially loaded tube C22J1 under zero pressure and 400 *psi* respectively. For visualization purposes, deformations are magnified by a factor of 5. Note that practically all deformation occurs about the tube middle section because of the $P - \Delta$ effect. Moreover, the effects of pressure are responsible for the considerable tube ovalization about the middle section. However, these localized phenomena do not affect the value of the ultimate load. Some cases were reexamined using the coarse mesh employed in section 3.6 without significant differences in the ultimate capacity.

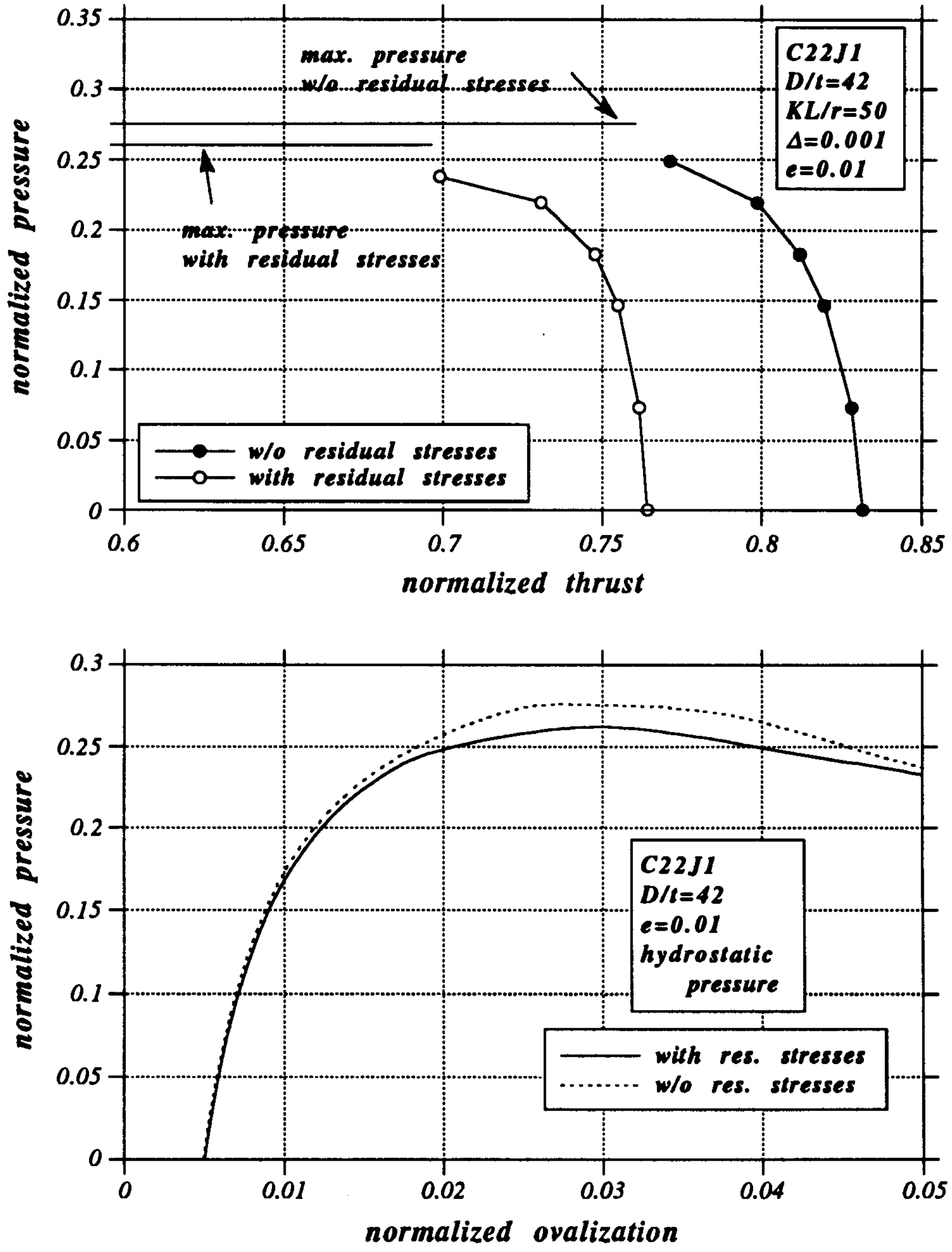

Figure 3.37: Axial force capacity under pressure for tube C22J1 (slenderness ratio $KL/r = 50$).

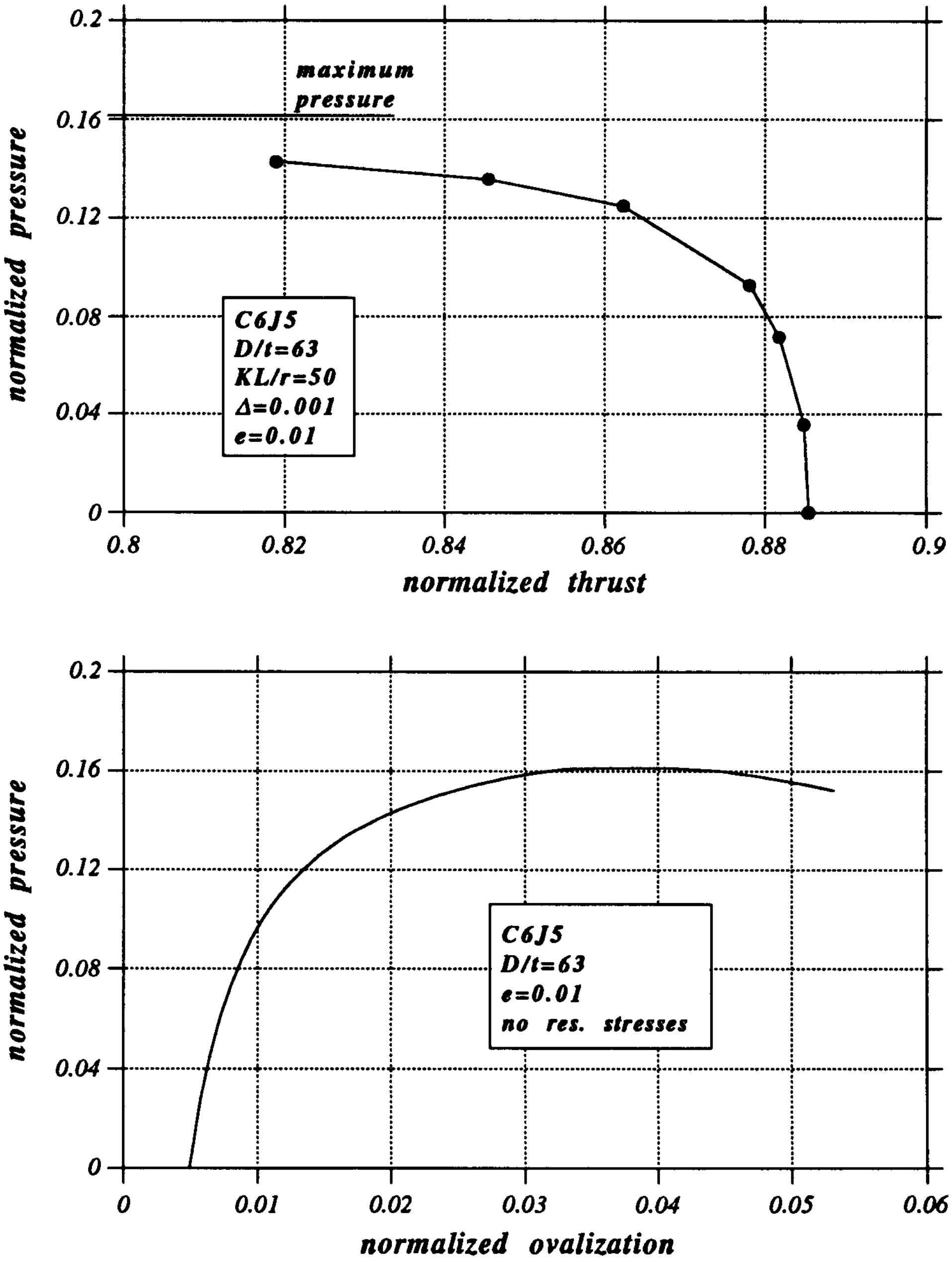

Figure 3.38: Axial force capacity under pressure for tube C6J5 (slenderness ratio $KL/r = 50$).

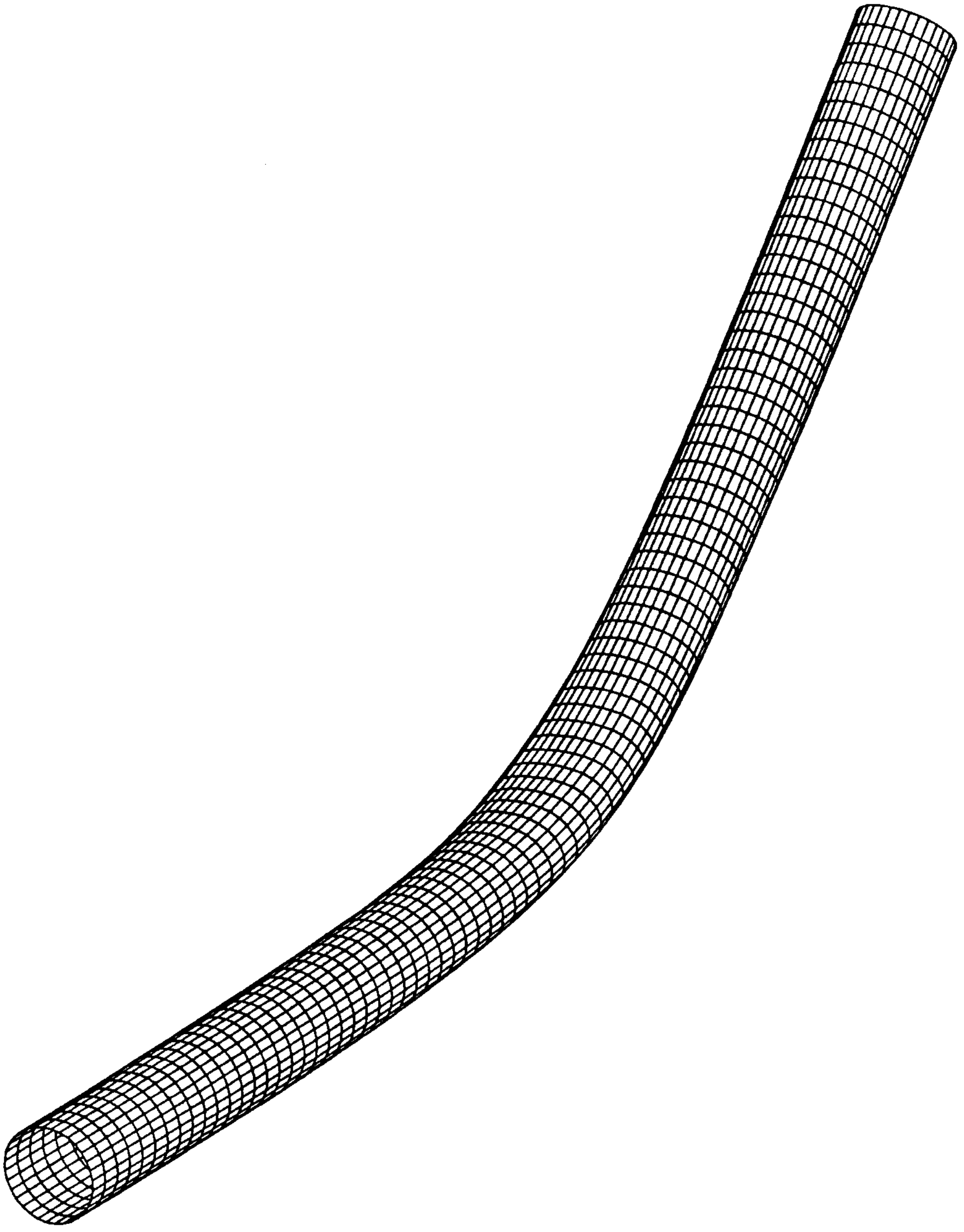

Figure 3.39: Post-buckling configuration for axially loaded tube C22J1 (zero pressure; deformations magnified by a factor of 5).

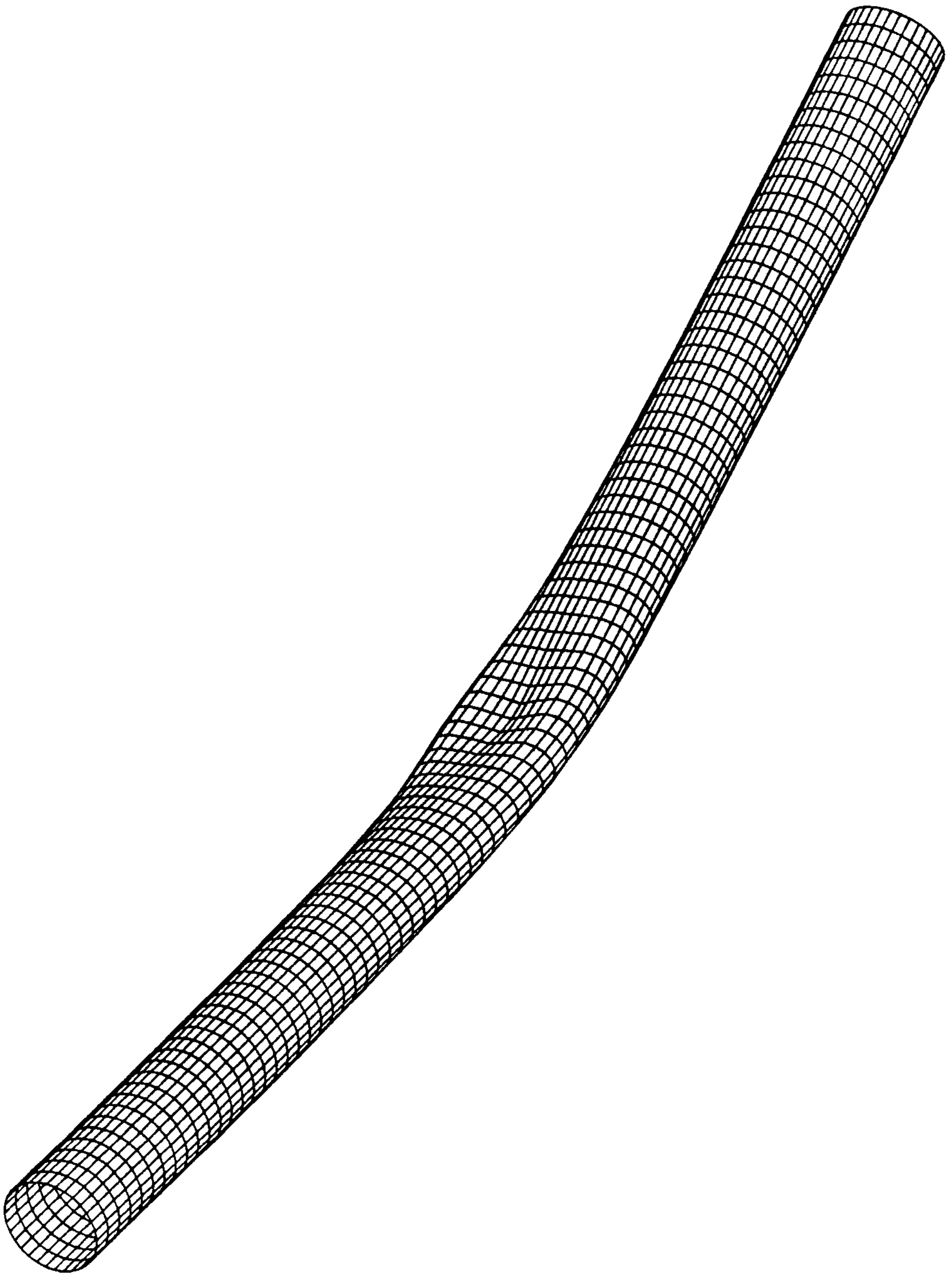

Figure 3.40: Post-buckling configuration for axially loaded tube C22J1 ($p/p_y = 0.146$; deformations magnified by a factor of 5).

Chapter 4

Comparison with Experimental Data for Unstiffened Tubes

One of the major goals of this research is to examine the analytical predictability of the experimental data reported by CBI [15] and SwRI [57] on tubular beam-columns. In this chapter, the column tests by CBI and SwRI are compared with results obtained using the analytical procedure described earlier. In all graphs, the values of pressure, moment, axial force and curvature are normalized by the yield pressure p_y, the fully plastic moment M_p, the yield axial force P_y and the curvature parameter $k_I = t/D^2$ respectively.

4.1 CBI Long Column Tests

A comparison will be made first between the CBI data [15] and numerical results. These tests were performed with fabricated tubes made of ASTM A315 (ERW) and API 5L Grade X-42 steel. The tests comprise three groups of specimens as shown in Table 4.1.

Group	KL/r	D/t
I (5 specimens)	72	42
II (10 specimens)	72	63
III (11 specimens)	50	42

Table 4.1: Experiments performed by CBI [15].

4.1.1 Groups I and III

The specimens are relatively thick tubes having D/t ratios of about 42. In all cases involving pressure and structural loads, the specimens were first pressurized up to a prescribed level and, subsequently, keeping the pressure constant, they were subjected to a proportional loading path of axial force and moment. The above loading sequence is followed in the present analysis. Moreover, the specimens are analyzed using the following assumptions:

- pressure-thrust-moment cases ($p - P - M$)
    - full three-dimensional analysis
    - only circumferential residual stresses
    - initial out-of-roundness (e) equal to 0.002
    - no initial out-of-straightness ($\Delta = 0.0$)
    - material curve given in Figure 3.1 ($\sigma_y = 56.24 ksi$)
- pressure-moment cases ($p - M$)
    - cross-sectional analysis
    - only circumferential residual stresses
    - initial out-of-roundness (e) equal to 0.002
    - no initial out-of-straightness
    - material curve given in Figure 3.1 ($\sigma_y = 56.24 ksi$)
- pressure-thrust cases ($p - P$)

  - full three-dimensional analysis
  - circumferential and longitudinal residual stresses
  - initial out-of-roundness (e) equal to the measured value [15]
  - initial out-of-straightness (Δ) equal to the measured value [15]
  - material curve given in Figure 3.1 ($\sigma_y = 56.24ksi$)

- pure pressure cases
  - cross-sectional analysis
  - circumferential and longitudinal residual stresses
  - initial out-of-roundness (e) equal to the measured value [15]
  - material curve given in Figure 3.1 ($\sigma_y = 56.24ksi$)

The assumption that longitudinal residual stresses for the "moment" cases have negligible effects is justified by the fact that the seam of the pipe during the experimental procedure was placed on the neutral axis so that the effects of residual stresses are minimized. Therefore, in this analysis, longitudinal residual stresses are omitted for the sake of keeping the symmetry with respect to the bending plane.

The value of initial out-of-roundness for the "moment" cases is assumed to be smaller than the values measured on the specimens [15]. It should be mentioned that there is not enough information on the position of the minimum and maximum diameters (D_{min} and D_{max}) with respect to the plane of bending. Here, the imperfection is assumed to be of the form:

$$w_i = w_o cos2\theta \tag{4.1}$$

Therefore, according to the out-of-roundness definition by API [5]

$$e = \frac{(D_{max} - D_{min})}{D} = 2\frac{w_o}{R} \tag{4.2}$$

This means that (for positive values of w_o) the minimum and maximum diameters are on and normal to the plane of bending respectively, which is a conservative arrangement. Thus, w_o is taken equal to 1/1000 of the radius R of the tube (i.e. $e = 0.002$), which is a small imperfection, in order to counteract the effects of this arrangement.

In addition, "moment" cases are assumed to have zero initial out-of-straightness, since initial transverse deformations are negligible when compared with bending deformations.

Cases with zero axial force are analyzed as two-dimensional (cross-sectional) problems. This simplification is quite reasonable because of the great length of the specimens (equal to 25 and 18 diameters for Groups I and III respectively). On the other hand, the actual experimental procedure is simulated for the cases with nonzero axial compressive force. It should be pointed out that the reported experimental moment M_{rep} is not the end-moment M_{end} but the moment at a certain distance from the pinned end. The two moment values are related by:

$$M_{rep} = M_{end} + P\, d\, sin\phi \tag{4.3}$$

where P is the axial force, d is the distance from the specimen end to the point where the moment is measured, and ϕ is the end rotation. In the present analysis, the exact experimental procedure described in [15] is simulated and the reported experimental moment is compared with the moment at distance d form the pinned end.

Specimens tested in axial compression and pressure combination (i.e. the "no moment" cases) are free to rotate at the ends in any direction. Therefore, the actual out-of-straightness and out-of-roundness values reported in Ref. [15] are used in this analysis.

The only available stress-strain curve for this series of results is depicted in Figure 2-2 of the CBI report [15], shown previously in Figure 3.1, and is used for all specimens of Groups I and III. Of course, for every specimen, both the yield stress and the Young's modulus are reported. The static yield stress in the longitudinal direction for these experiments ranged from 48.3 ksi to 56.2 ksi. Therefore, an attempt was made to adjust the given material curve to the yield stress and the Young's modulus of each specimen, as suggested by C. D. Edwards [37]. Nevertheless, it will be shown later that this effort did not result in better predictions.

Measurements reported by CBI [15] show that tubes for Groups I and III have an important material anisotropy. More specifically, the circumferential static yield stress is reported equal to 43.1 ksi, which is considerably lower than the corresponding longitudinal yield stresses. This anisotropy can be implemented by revising the plasticity model to account for an anisotropic yield function. Another way to introduce material anisotropy is through the circumferential residual stresses. The second approach is adopted in this work, because of its simplicity and efficiency, and the distribution proposed by Chen and Ross [14] is used.

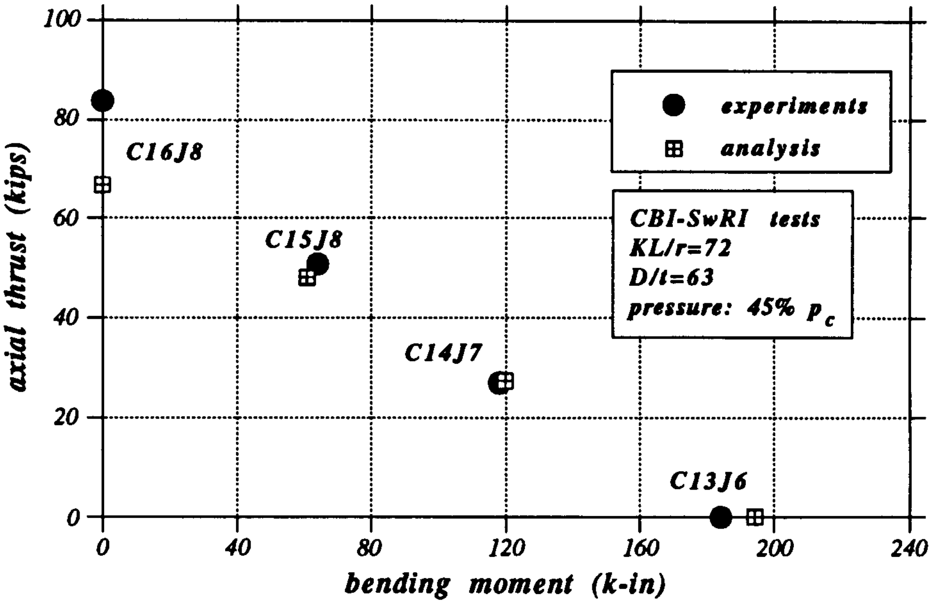

Figure 4.1: Experimental and analytical results for Group I (pressure level 45% p_c).

The results for Groups I and III are shown in Tables 4.2 and 4.3 and, in graphical form in Figures 4.1, 4.2, 4.3 and 4.4. Note that in these graphs the results from SwRI presented in another section of this Chapter are included. It can be seen from the results that the predictions are in very good agreement with the experimental data.

For the three-dimensional cases (i.e. those with nonzero axial force), the element size is taken equal to 50% of the tube diameter. Furthermore, the cases involving only axial force and pressure (i.e. those with zero end moments) are also analyzed with a finer mesh about the middle section (element size equal to 10% of the tube diameter), without significant change in ultimate capacity.

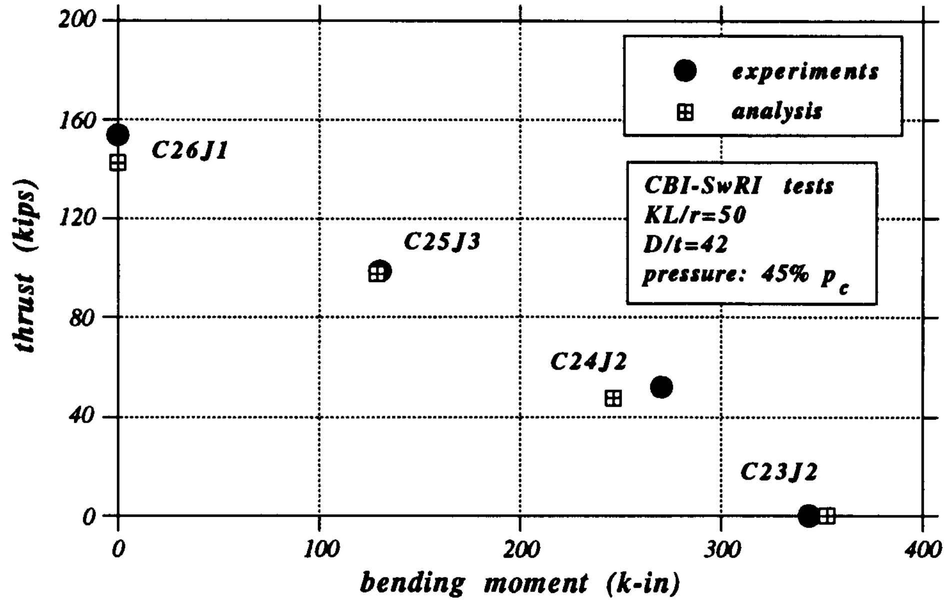

Figure 4.2: Experimental and analytical results for Group III (pressure level 45% p_c).

specimen	press. (psi)	exp-thrust ($kips$)	exp-mom. ($k-in$)	thrust ($kips$)	moment ($k-in$)
C2JB	0.0000	0.0000	362.20	0.000	381.72
C4JC	357.50	0.0000	337.00	0.000	348.73
C1JC	591.50	0.0000	266.20	0.000	286.24
C5JE	378.20	72.100	127.00	72.945	128.49
C3JD	605.90	68.600	126.50	68.552	126.41

Table 4.2: Comparison between experimental data and analytical results for Group I.

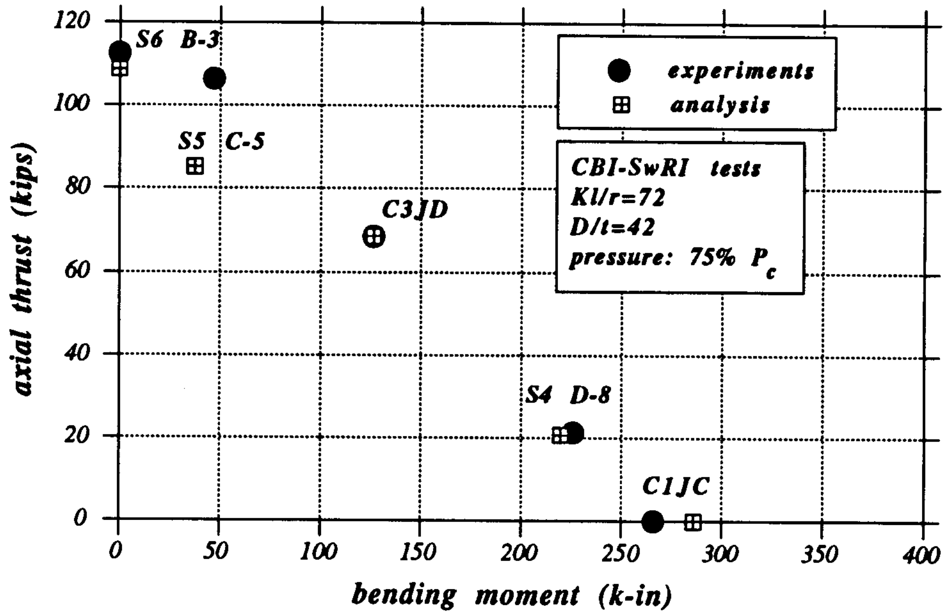

Figure 4.3: Experimental and analytical results for Group I (pressure level 75% p_c).

specimen	press. (psi)	exp-thrust $(kips)$	exp-mom. $(k - in)$	thrust $(kips)$	moment $(k - in)$
C22J1	0.000	0.0000	383.30	0.000	384.32
C23J2	349.40	0.0000	343.60	0.000	352.71
C18J1	621.40	0.0000	288.10	0.000	280.24
C25J3	359.30	98.800	130.20	97.586	128.60
C24J2	336.00	52.200	270.60	47.534	246.41
C26J1	377.40	153.80	0.0000	142.52	0.0000
C17JE	0.0000	154.30	0.0000	142.98	0.0000
C21J1	625.00	137.70	0.0000	138.95	0.0000
C19J2	585.60	47.000	246.70	45.625	239.48
C20J2	555.90	93.300	120.00	91.574	117.78
C27J3	610.00	68.300	184.50	68.251	184.37

Table 4.3: Comparison between experimental data and analytical results for Group III.

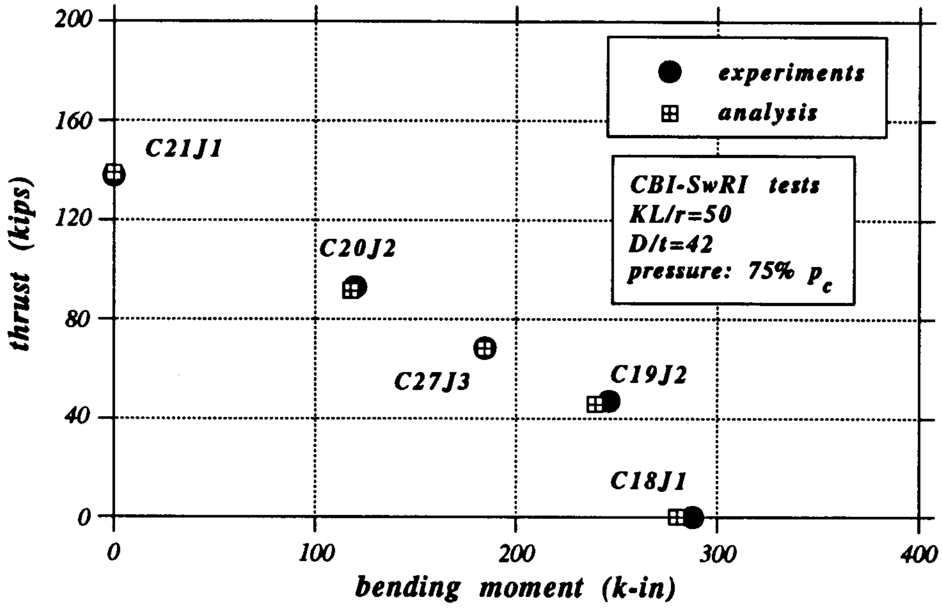

Figure 4.4: Experimental and analytical results for Group III (pressure level 75% p_c).

For the six cases of pressurized bending (C22J1, C23J2, C18J1, C2JB, C4JC and C1JC) the results indicate loss of bending capacity in the presence of external pressure. This trend, extensively investigated in Chapter 3, is shown in Figures 4.5 and 4.6 and it is in very good agreement with the experiments. For these specimens, collapse is due to extensive inelastic cross-sectional ovalization.

As mentioned earlier, it was attempted to "adjust" the available material curve to the yield stress and Young's modulus of every specimen. Table 4.4 shows the predictions for the six cases of pressurized bending using the "adjusted" curves. Clearly, the predictions based on this approach are not in better agreement with test data than those summarized above (with the stress-strain curve of Figure 3.1. This implies that the use of a "universally"

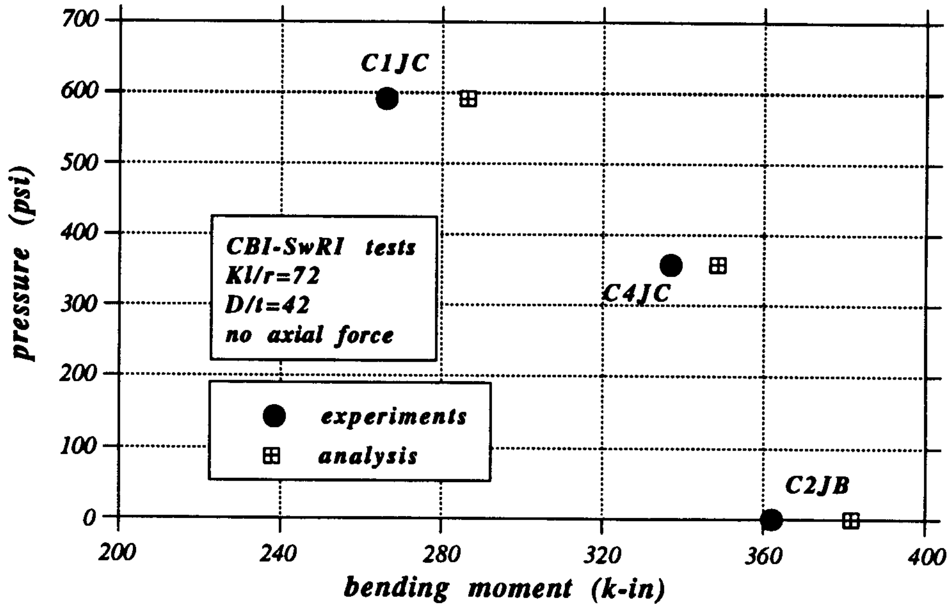

Figure 4.5: Pressurized bending tests (Group I).

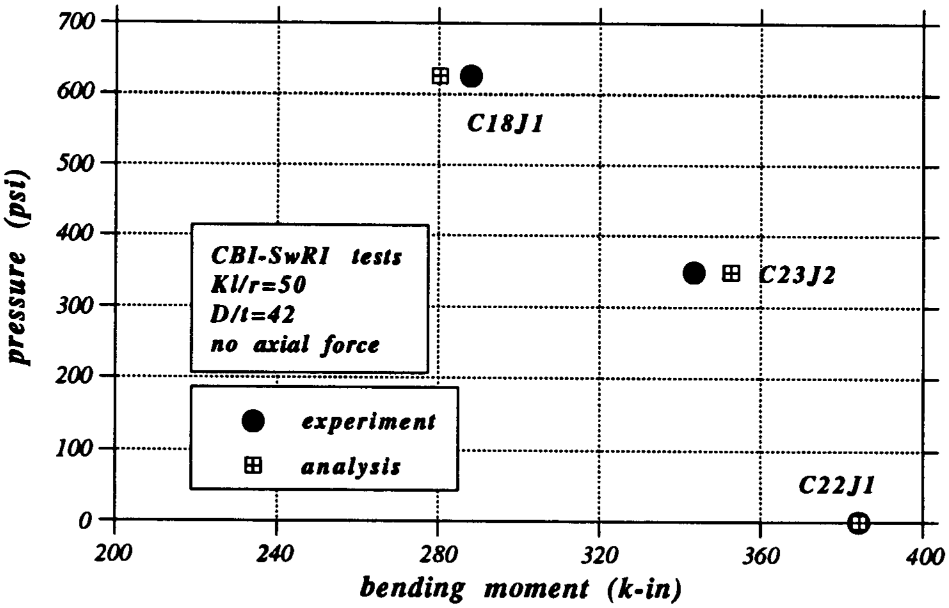

Figure 4.6: Pressurized bending tests (Group III).

normalized curve for all specimens does not provide necessarily good analytical results.

specimen	press. (psi)	exp-moment ($k - in$)	moment ($\sigma_y = 56.24\,ksi$)	moment (adjusted curve)
C22J1	0.0000	383.30	384.32	383.34
C23J2	349.40	343.60	352.71	322.00
C18J1	625.00	288.10	280.24	273.64
C2JB	0.0000	362.20	381.72	326.81
C4JC	357.50	337.00	348.73	307.58
C1JC	591.50	266.20	286.24	233.77

Table 4.4: Parametric study for the pressure-bending cases of Groups I and III.

Experiments show a significant drop in ultimate axial capacity when the external pressure is increased from 45% to 75% of the collapse pressure (Group III, specimens C17JE, C26J1 and C21J1). A similar, but not as significant, drop in strength is indicated by the numerical results. In order to investigate this trend in more detail, a parametric study was performed and is summarized in Table 4.5. The assumptions used in this parametric study are shown in Table 4.6. Note that, even for large values of circumferential residual stresses, specimen C21J1 does not exhibit the capacity reduction indicated by the experiments.

$\sigma^{(max)}_{c/res}/\sigma_y$	specimen	exper.	case No.1	case No.2	case No.3	case No.4
	C17JE	154.32				
	C26J1	153.75				
	C21J1	137.71				
	C17JE		159.75	159.74		
0.0000	C26J1		159.55	159.46		
	C21J1		155.97	155.49		
	C17JE		156.62	156.60	142.10	156.56
0.3500	C26J1		156.51	156.41	142.22	156.00
	C21J1		152.71	151.74	139.54	152.40
	C17JE		154.98	154.95	141.86	154.99
0.5000	C26J1		154.63	154.40	141.94	154.18
	C21J1		150.30	149.00	139.01	150.47
	C17JE		153.13	153.11	141.27	153.10
0.6500	C26J1		152.25	152.01	141.33	151.90
	C21J1		147.34	144.74	137.72	147.70

Table 4.5: Parametric study for pressure-thrust specimens: C17JE ($p = 0$), C26J1 ($p = 327psi$) and C21J1 ($p = 625psi$).

	case No.1	case No.2	case No.3	case No.4
circ. res. stresses	yes	yes	yes	yes
long. res. stresses	no	no	yes	no
out-of-roundness	0.002	0.004	0.002	0.002
out-of-straightness	1/6000	1/6000	1/6000	1/6000
type of element	tube	tube	tube	shell

Table 4.6: Assumptions for cases 1, 2, 3 and 4.

These results are in accordance with the analytical results shown in Figures 3.37 and 3.38 of Chapter 3. Results from cases 1 and 4 are practically the same. In fact, the only difference between the two cases is the type of element used and it can be concluded that tube elements behave almost identically to the shell elements. These results are also compared with the predictions of the AISC specification:

- working stress design (WSD):

$$P_{cr} = P_y\,(1 - 0.25\lambda^2) \tag{4.4}$$

- ultimate strength design (LRFD)

$$P_{cr} = P_y\,0.658^{\lambda^2} \tag{4.5}$$

The formulas predict 157.75 *kips* and 146.56 *kips* respectively. The analytical results are very close to the LRFD predictions, whereas experimental results fall in between the two predictions. On the other hand, the API specification [5] implies no interaction between axial thrust and external pressure.

Finally, excellent results are obtained for the case where all loading parameters (thrust, moment and pressure) are non-zero as shown in Figures 4.1, 4.3, 4.2 and 4.4. It is again noted that the reported numerical and experimental values of moment do not correspond to the end moments (see Equation 4.3)

4.1.2 Group II

The specimens of Group II have a D/t ratio equal to 63 and may be classified as relatively thin tubes. The assumptions made for the results of Groups I and III are adopted in this series as well. However, since the material of the specimens is ASTM A315 (ERW), the material curve depicted in Figure 3.6, which is very similar to the material curve shown in Figure 2-3 of Ref. [15], is used for all specimens. In fact, this is the only material curve for the specimens of Group II. However, these specimens have longitudinal static yield stresses within a narrow range ($41.3\,ksi$ - $43.5\,ksi$) and, therefore, the use of a single material curve seems quite reasonable.

Analytical predictions together with experimental data are shown in Table 4.7 and, in graphical form in Figures 4.7 and 4.8. The four cases with thrust-pressure-moment interaction (C14J7, C15J8, C9J6 and C10J7) are in very good agreement with the experimental results. This implies that, even for this value of D/t, global rather than localized instability governs the behavior. The pure pressure case (C6J5) is also very close to the experimental data.

specimen	exp-press. (psi)	exp-thrust $(kips)$	exp-mom. $(k-in)$	press. (psi)	thrust $(kips)$	moment $(k-in)$
C7AJ8	0.000	83.300	0.0000	0.0000	66.72	0.0000
C16J8	108.20	83.900	0.0000	108.20	66.71	0.0000
C11J7	172.30	76.800	0.0000	172.30	67.91	0.0000
C6J5	225.70	0.0000	0.0000	235.89	0.0000	0.0000
C12J5	0.000	0.0000	175.70	0.0000	0.0000	202.99
C13J6	105.90	0.0000	186.10	105.90	0.0000	194.17
C8J5	170.80	0.0000	178.50	170.80	0.0000	176.89
C14J7	103.60	27.000	118.10	103.60	27.415	119.91
C15J8	106.60	50.800	64.100	106.60	48.050	60.914
C9J6	174.30	25.100	112.50	174.30	24.851	111.39
C10J7	170.50	48.700	67.400	170.50	46.262	64.026

Table 4.7: Comparison between experimental data and analytical results for Group II.

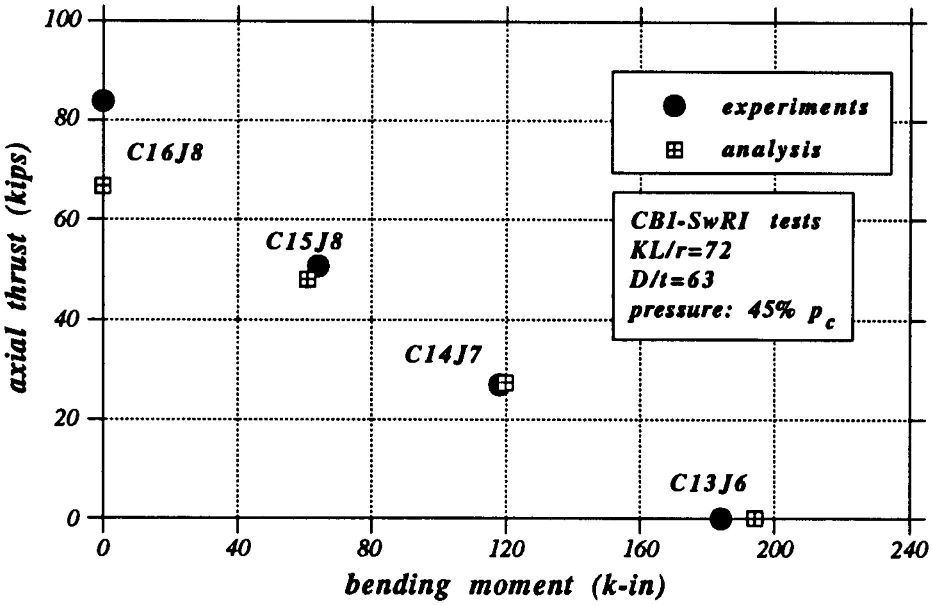

Figure 4.7: Experimental and analytical results for Group II (pressure level 45% p_c).

The analytical predictions for the three "no-moment" cases (C7AJ8, C16J8 and C11J7) fall below the experimental values. On the other hand, the predictions of the specification equations 4.4 and 4.5, are 74.82 *kips* and 66.93 *kips* respectively. Analytical predictions are in very good comparison with the LRFD formula but quite below the experimental values.

Finally, the three cases of pressurized bending (C12J5, C13J6 and C8J5) show the same trend indicated earlier in Figures 4.6 and 4.5. More specifically, bending capacity is reduced with increasing external pressure. The moment-pressure interaction for this Group is shown in Figure 4.9. Note that the comparison with the experimental results is very good for tubes C13J6 and C8J5 and poor for C12J5. In fact, the reported moment for C12J5, which has zero pressure, is lower than the ultimate moment of C8J5 which is subjected

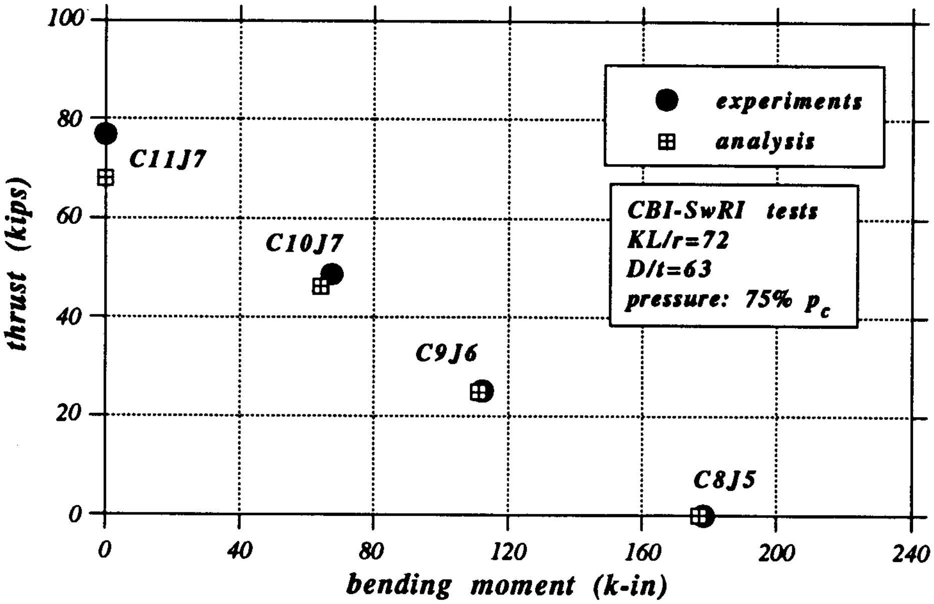

Figure 4.8: Experimental and analytical results for Group II (pressure level 75% p_c).

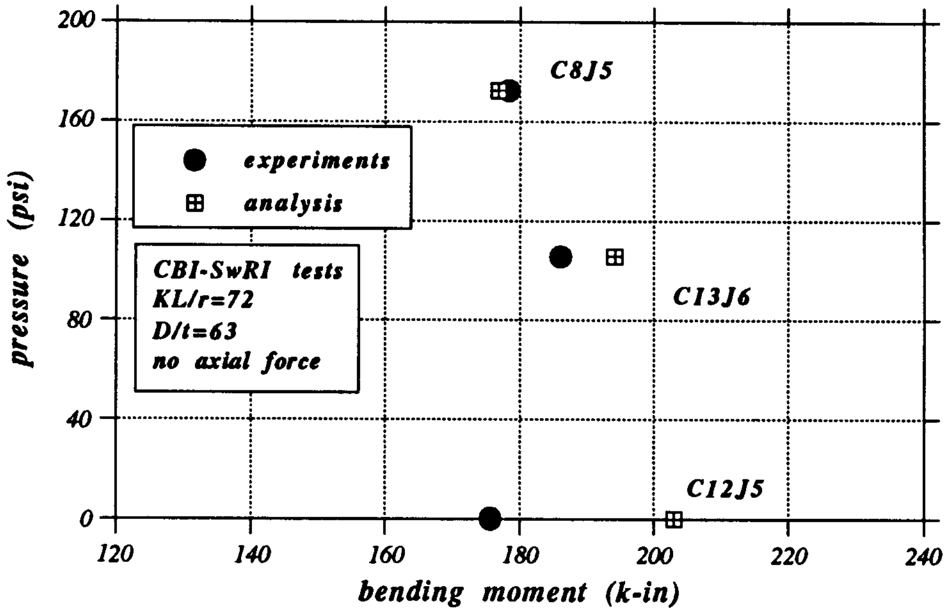

Figure 4.9: Pressurized bending tests (Group II).

to a significant amount of pressure. In order to examine any possible localized buckling that would explain the low capacity of specimen C12J5, this specimen is reanalyzed taking into account the three-dimensional geometry of the specimen in order to examine the possibility of localized phenomena. Figure 4.10 shows the comparison between two-dimensional and three-dimensional results. Points ($3D$) and ($2D$) correspond to the ultimate moment stage for the three-dimensional and two-dimensional case respectively. The value of the maximum moment is the same for the two cases. Nevertheless, for three-dimensional analysis, ultimate load occurs earlier and the equilibrium path deviates from the two-dimensional path *beyond the limit point.* This is an indication of localized phenomena which, however, do not affect the ultimate load on the specimen. Therefore, the limit moment obtained from two-dimensional analysis is a very good prediction of the specimen ultimate strength. Note that the same behavior was observed in the previous Chapter, where the bending capacity of inelastic tubes was extensively examined. In addition, similar conclusions were reported in the experimental work by Ju and Kyriakides [33], concerning pure bending strength of aluminum pipes.

4.2 SwRI experiments

The SwRI experimental program [57] includes nine tests performed on fabricated tubes made of API 5L Grade X42 steel. The nominal outside diameter of the tubes was $6.625\,in$ and the thickness about $0.157\,in$. That makes a D/t ratio of about 42. The slenderness of the tubes was about 72, except for one specimen tested under pure pressure which had a slenderness ratio KL/r of 50. These specimens have the same geometric and mechanical

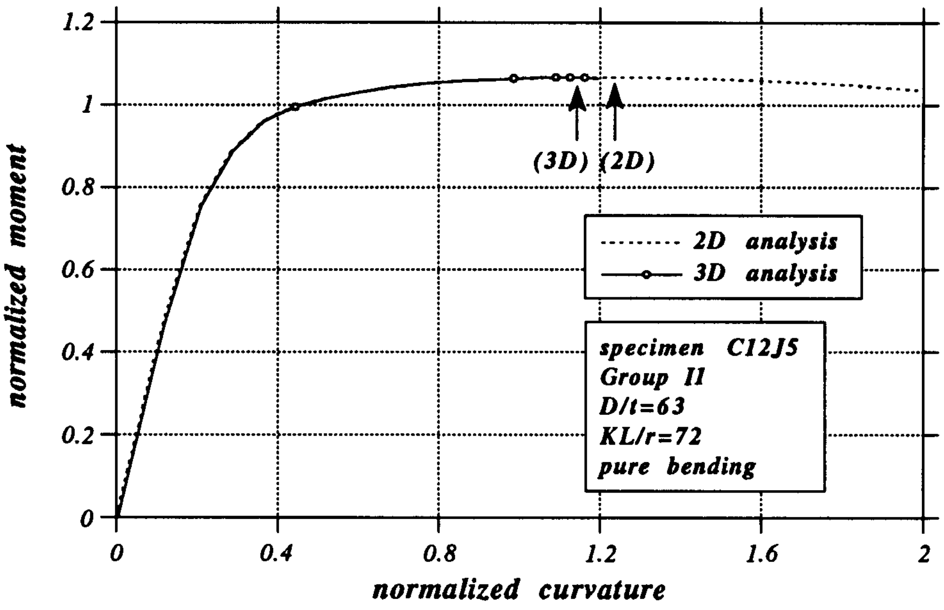

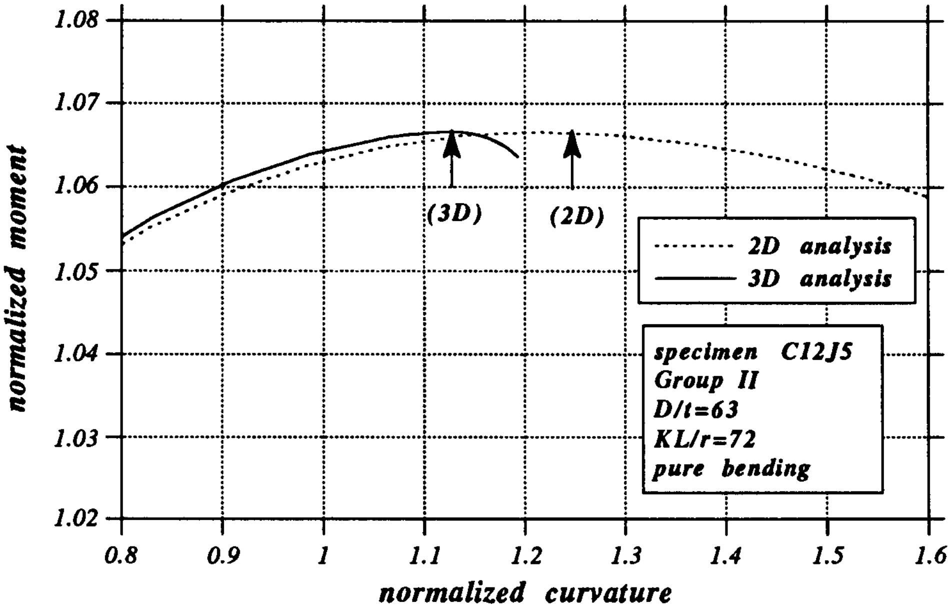

Figure 4.10: Cross-sectional and three-dimensional behavior of tube C12J5.

characteristics as those of Groups I and III.

In this study, eight of the nine experiments are analyzed. Tube S3 shows, under a high level of pressure, a limit moment capacity which is much higher than the limit moment under zero pressure of a similar tube tested by CBI [15]. The reason for this result is the presence of an axial tensile force on the specimen equal in magnitude to the capped-end force, which is applied after the specimen is pressurized and before application of the end-moments. The capped-end force is in static equilibrium with the lateral pressure and is always normal to the end-section, but on the other hand, the axial tensile force is directed along the undeformed axis of the pipe, thus causing a "beneficial" $P - \Delta$ effect which is responsible for the high value of limit moment. This experiment is not considered in the present analysis.

The basic assumptions made for the previous experiments are followed in this series as well. In addition, the element size considered in the CBI experiments is also used for these experiments. The material curve depicted in Figure 3.1 is used to analyze these tubes as well. It must be noted that stress-strain curves are reported for all specimens tested in SwRI. However, the initial modulus reported is far below the well-known value of $29,500\,ksi$ for steel material. This makes the curves rather questionable and, therefore, they are not considered in this analysis.

Another point of interest is the position of the longitudinal weld. In this series of experiments, the seam was placed near (but not exactly on) the plane of bending, whereas in the CBI tests it was placed on the neutral axis in order to minimize the effect of residual stresses. The analysis takes into account longitudinal residual stresses through the proposed distribution by Chen and Ross [14], with the seam on the plane of bending for symmetry purposes. In addition, circumferential residual stresses are assumed to be nonzero and the distribution proposed by Chen and Ross [14] is adopted.

Table 4.8 shows the analytical results in comparison with the experimental data. These results are also shown in Figures 4.1 and 4.3 together with the results from Group I. The cases of pure pressure (S1 and S10) are very well predicted, being within 6% of the experimental values. The difference in the analytical results of S1 and S10 is due to the differences in diameter, thickness and initial imperfection.

specimen	exp-press. (psi)	exp-thrust $(kips)$	exp-mom. $(k-in)$	press. (psi)	thrust $(kips)$	moment $(k-in)$
S1 B-4	760.00	0.0000	0.0000	778.88	0.0000	0.0000
S10 A-10	774.00	0.0000	0.0000	747.09	0.0000	0.0000
S2 A-2	0.0000	126.69	0.0000	0.0000	118.73	0.0000
S8 E-9	373.00	114.09	0.0000	373.00	119.40	0.0000
S6 B-3	574.00	112.50	0.0000	574.00	117.47	0.0000
S4 D-8	591.00	21.373	226.03	591.00	20.776	219.61
S5 C-5	589.00	106.45	46.822	589.00	85.191	37.472
S7 A-1	393.00	37.758	271.83	393.00	30.229	218.13

Table 4.8: Comparison between experimental data and analytical results for SwRI experiments.

The cases with nonzero axial force and moment interaction (S4, S5 and S7) show a certain difference between experiments and analysis. The largest difference occurs in specimens S5 and S7 (about 20%). It is important to note that the predicted values underestimate the capacity of the tubes.

The analytical results for the three "no-moment" tests with thrust-pressure interaction (S2, S6 and S8) are quite close to the reported experimental data. In addition, it can be easily verified that LRFD equation 4.5 predicts an ultimate axial load of 118.05 *kips* which is very close to both experiments and analysis. On the other hand, working stress design equation 4.4 gives 134.55 *kips* which is a rather unconservative prediction. Experiments show a certain drop in strength when the pressure is increased from zero to 45% of the collapse pressure and a similar behavior for cases with levels of pressure equal to 45% and 75% of the collapse pressure. This trend is different from the one indicated by CBI experiments [15], where the drop in ultimate capacity occurred when the pressure was increased from 45% to 75% of the collapse pressure. In the present analysis, all three specimens have approximately the same axial capacity. However, it should be noted that specimen S6 (with a pressure level of 75% p_c) has a smaller initial imperfection than specimens S2 and S8. Finally, the differences in diameter and thickness are responsible for the fact that specimen S2 (with zero pressure) has a lower compression capacity than specimen S8 (with a pressure level of 45% p_c).

Chapter 5

Stiffened Tubes Under External Pressure and Tension

The use of stiffened tubes has been dictated by the increasing depth of offshore operations. Nowadays, compliant towers are designed for $2000 - 3000ft$ and, in such depths, the use of unstiffened tubes becomes uneconomical. The ultimate capacity of ring-stiffened tubes under combined external pressure and axial force is investigated in this chapter. The stiffener element described in Chapter 2 is employed for both internally and externally stiffened tubes. Analytical results are compared with the experimental data reported in Refs. [38], [39] and [16]. In all graphs of this Chapter, the values of pressure and tension are normalized by the yield pressure $p_y = 2\sigma_y t/D$ and the yield tension $P_y = \sigma_y A$ respectively.

5.1 Preliminary Results

As mentioned before, stiffeners are used in order to increase the ultimate capacity of tubes under external pressure. Ring-stiffeners may be internal or external and are spaced at a distance L_s ranging between one and four tube diameters D in actual offshore members. Clearly, ultimate pressure depends on stiffener spacing as well as the diameter-to-thickness ratio D/t of the unstiffened tube. Therefore, in order to account for this interaction, the following geometric parameter is introduced:

$$M = \frac{L_s}{D}\sqrt{\frac{2D}{t}} \tag{5.1}$$

also adopted by the API specification [4]. The specification requires that

$$M \leq 1.6\frac{D}{t} \iff \frac{L_s}{D} \leq 1.13\sqrt{\frac{D}{t}} \tag{5.2}$$

in order to benefit from the presence of stiffeners. If the above criterion is not met, then the design follows the unstiffened tube rules. The validity of this spacing criterion is extensively examined in this section.

It was shown in Chapter 3 that unstiffened tubular members exhibit an ovalization type of deformation at buckling and the ultimate pressure is considerably below the yield pressure level. The use of ring-stiffeners is aimed at preventing cross-sectional ovalization, thereby increasing the collapse pressure.

An important consideration in this analysis is whether capped-end compression is present or not. It has been shown (see Chapter 3) that capped-end compression does not affect ultimate pressure capacity in the elastic range. Therefore, for unstiffened tubes having a diameter-to-thickness value greater than 35, capped-end compression has no significant effect on their behavior. However, when stiffeners are employed, buckling may occur in the inelastic range and, in this case, capped-end compression effects are important. As an example, consider the extreme case of failure due to yielding of the entire unstiffened cross-section. Then, according to the von Mises criterion, the presence of capped-end compression increases yielding capacity by 15%. In the following sections, the term "hydrostatic pressure loading" will imply that capped-end compression is present. On the other hand, "radial pressure loading" will mean zero capped-end force.

First, the ultimate pressure capacity of a tube for different stiffener sizes is investigated. It is expected that for small stiffener dimensions the ultimate capacity will be asymptotically equal to the pressure capacity of the unstiffened tube. On the other hand, for large stiffener dimensions, failure is due to the yielding of the entire cross-section. The tube considered for this study has the cross-sectional characteristics of tube C22J1. In this analysis, the pipe was assumed free of residual stresses with initial out-of-roundness (e) equal to 0.002. In addition, it is assumed to be infinitely long with equally spaced external or internal stiffeners at a distance of two tube diameters ($L_s/D = 2$) and loaded under hydrostatic pressure.

In Figures 5.1 and 5.2, the collapse pressure is plotted in terms of ovalization at section $a-a$ and the section on the stiffener for different stiffener sizes. The two sections will be referred to as "middle" section and "stiffener" section respectively. Note that because of the symmetry of the problem, only the part of the pipe between section $a-a$ and a stiffener needs to be analyzed. As expected, the difference in cross-sectional ovalization between the middle section and the stiffener section becomes more pronounced with increasing stiffener size.

The variation of ultimate pressure with increasing stiffener radial dimension t' is shown in Figure 5.3. In this graph, results for both internal and external stiffeners are reported and the stiffener radial dimension is normalized by the tube thickness. Apparently, for increasing size, ultimate pressure capac-

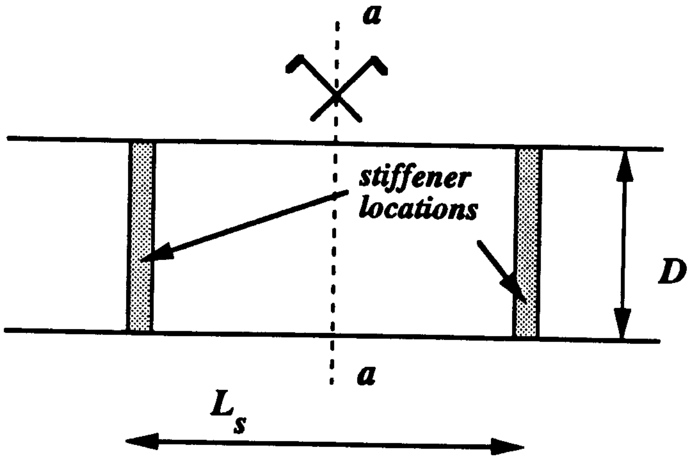

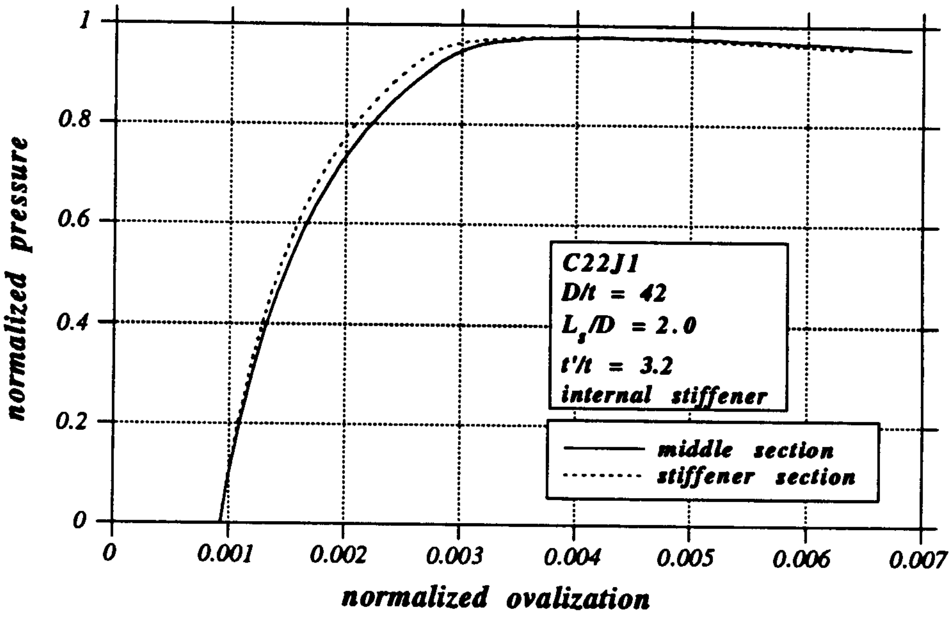

Figure 5.1: Pressure-ovalization curve for $L_s/D = 2.0$ and $t' = 0.5\,in$ (internal stiffener).

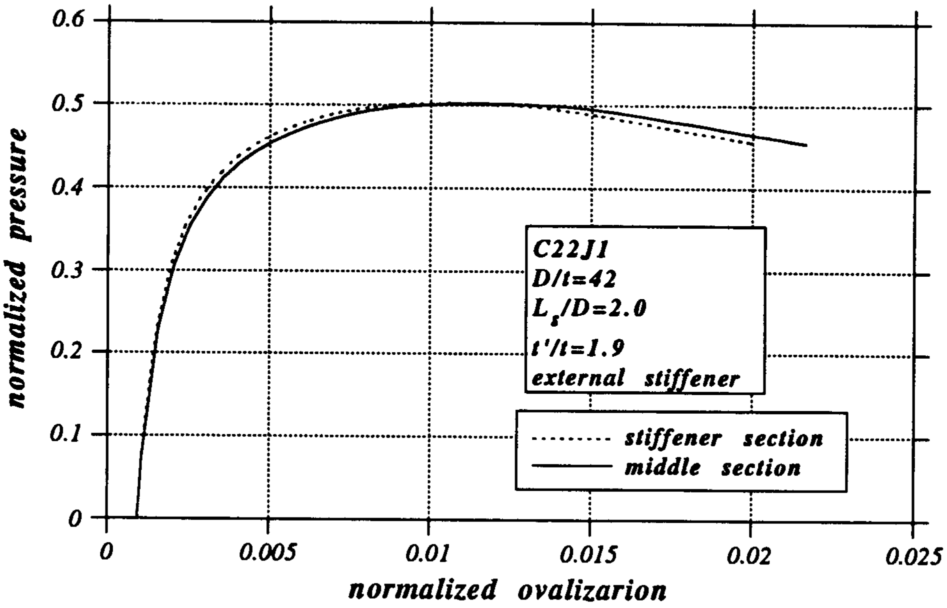

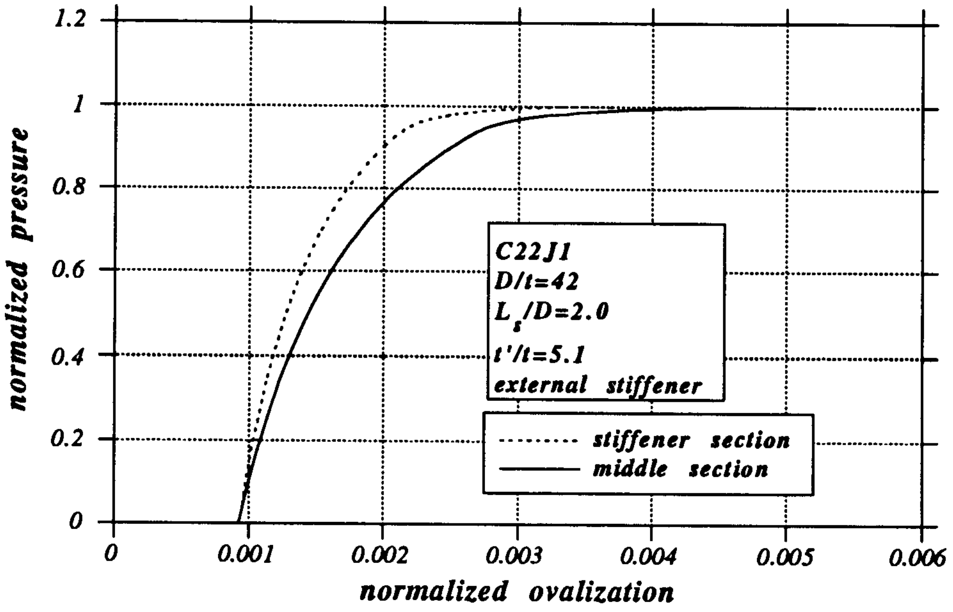

Figure 5.2: Pressure-ovalization curve for $L_s/D = 2.0$ and for two values of stiffener size (external stiffener).

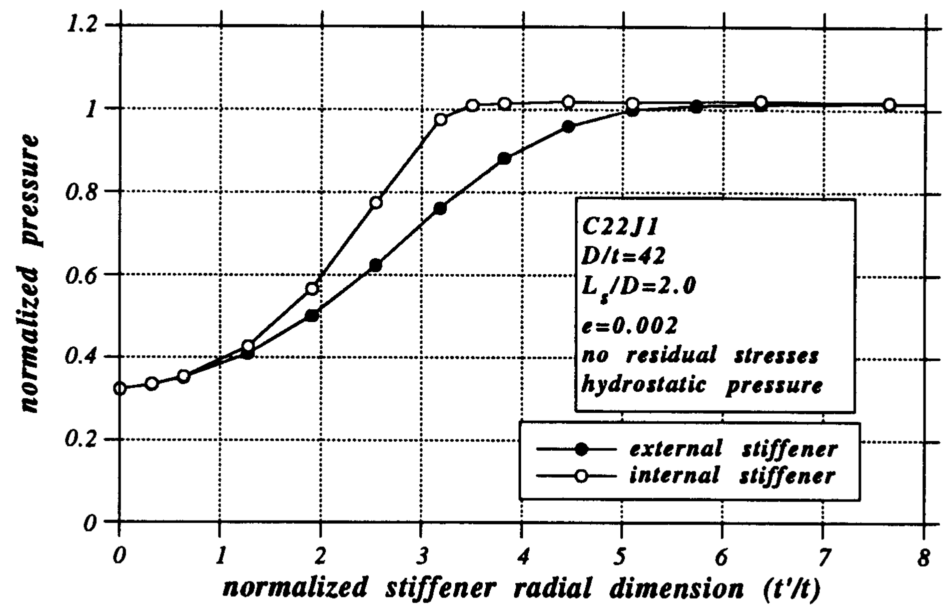

Figure 5.3: Effect of stiffener size on the ultimate pressure capacity.

ity is increased. For small values of stiffener size, ovalization-type of collapse occurs with significant deformation. On the other hand, for the cases where the size exceeds a certain value, the unstiffened cross-section will be in the plastic range and yielding failure follows. Note that for tube C22J1, the first inelastic action (i.e., the first point where the material modulus is significantly reduced) occurs at the proportional limit which is 50.8 *ksi* and corresponds to an hydrostatic pressure of about 2800 *psi* (see Figure 3.1). This value is equal to the ultimate pressure for large values of stiffener size.

A first result from this parametric study is the existence of a certain stiffener size above which there is almost no significant increase in ultimate capacity. This characteristic value of stiffener size clearly depends on the geometric parameters (L_s/D and D/t) the material behavior as well as whether

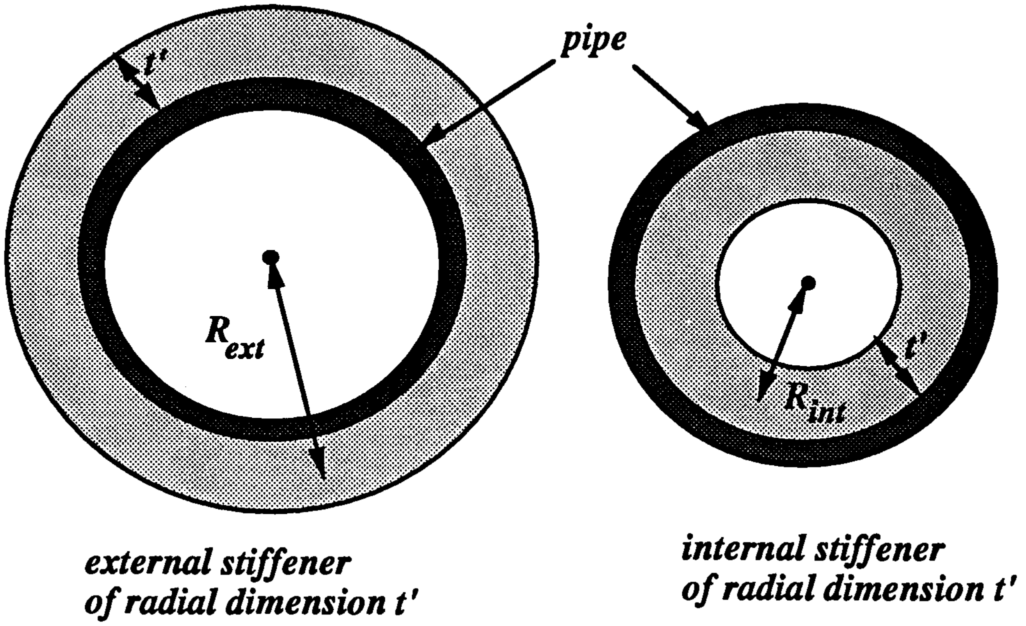

Figure 5.4: Cross-sectional views of internal and external stiffeners.

the stiffener is internal or external. In particular, the use of internal stiffeners increases cross-sectional stiffness and, therefore, a smaller stiffener size is required to achieve plastic failure. A qualitative, yet reasonable, explanation for this difference follows by approximating the in-plane stiffness of a stiffener. More specifically, consider the mean radii R_{ave} of the internal and external stiffeners depicted in Figure 5.4. According to Timoshenko [60], the in-plane ovalization stiffness of a ring is proportional to $(t'/R_{ave})^3$. Therefore, considering the geometry of tube C22J1 and assuming stiffener radial and longitudinal dimensions equal to $1.0\,in$ and $0.145\,in$ respectively, the internal stiffener is about 2.5 times stiffer than the external.

Figure 5.5 shows the behavior of a long tube when external and internal stiffeners of the same radial dimension t' are considered. For these results, stiffener radial and longitudinal dimensions are taken equal to 1.0 *in* (i.e. $t'/t \simeq 6.4$) and 0.145 *in* respectively. In addition, the tube is assumed to have a small initial out-of-roundness ($e = 0.002$) and stiffener spacing was assumed equal to two tube diameters. Clearly, internal stiffeners are stiffer than external stiffeners and result in higher pressure capacity.

Figure 5.6 shows the capacity of stiffened tubes under external hydrostatic pressure for varying stiffener spacing. As in the previous results, stiffener radial and longitudinal dimensions are taken equal to 1.0 *in* and 0.145 *in* respectively. The ultimate pressure for the unstiffened case has been calculated to be 882 *psi*. In fact, this is the value of ultimate pressure for large spacing. On the other hand, when hydrostatic pressure reaches the level of about 2800*psi*, the entire cross-section enters into the inelastic range, resulting in the sudden reduction of stiffness which is followed by yielding failure.

It is important to point out that the presence of stiffeners causes nonuniform cross-sectional ovalization along the tube. In order to account for this phenomenon, which is a major reason for instability, an eighth-order expansion of cross-sectional deformation is assumed for all cases examined in this Chapter. In addition, the stiffener in-plane deformation is expanded up to the eighth degree. Furthermore, the element size depends on the stiffener spacing. For small spacing values ($L_s/D \leq 5$), the tube buckles inelastically and, therefore, a small element size is employed (10-15% of the tube diameter). On the other hand, for larger values of spacing, the tube behavior tends to be similar to the response of the unstiffened tube. Consequently, a coarser mesh may be used.

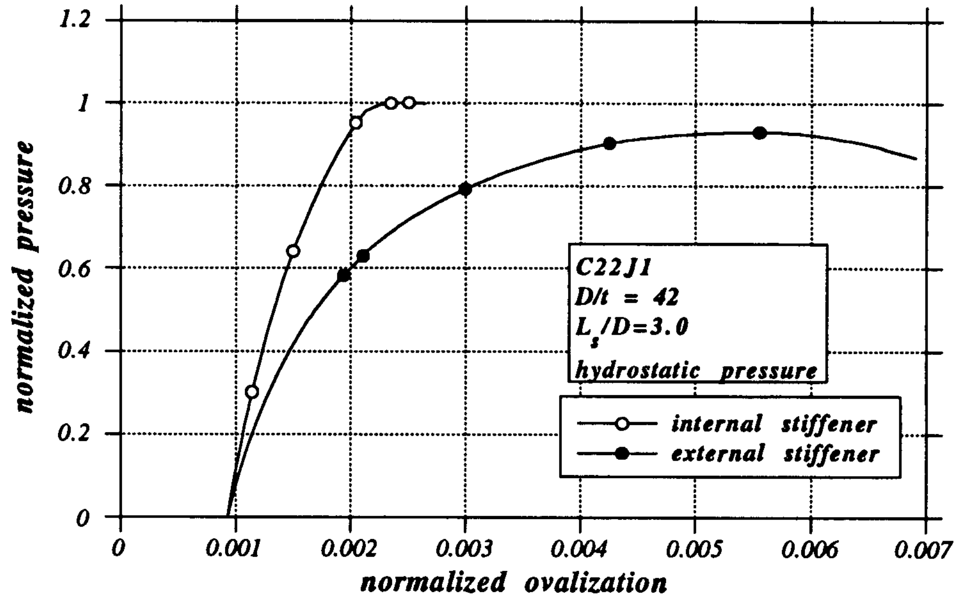

Figure 5.5: Pressure-ovalization curves for internal and external stiffeners.

For a diameter-to-thickness value equal to 42, Equation 5.2 indicates no stiffener effect for spacing greater than 7.3 tube diameters. However, Figure 5.6 implies that some benefit in ultimate capacity is achieved even for larger values of spacing. The same effect will be examined in more detail in the next section.

It is interesting to compare the ultimate pressure for internal and external stiffener for different values of spacing. The difference is clear for intermediate values of spacing ($3.5 \leq L_s/D \leq 6.0$). For smaller values of spacing, both internal and external stiffeners provide such stiffness that the entire tube cross-section yields. On the other hand, for large spacing values, the behavior tends to be similar to the unstiffened case and, therefore, it makes no difference whether the stiffener is internal or external.

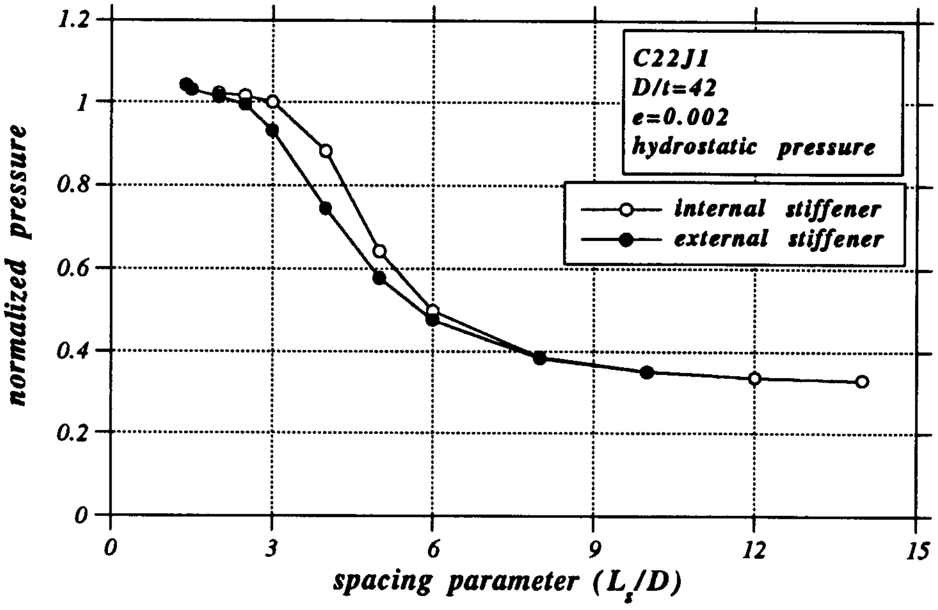

Figure 5.6: Ultimate pressure versus spacing parameter for tube C22J1.

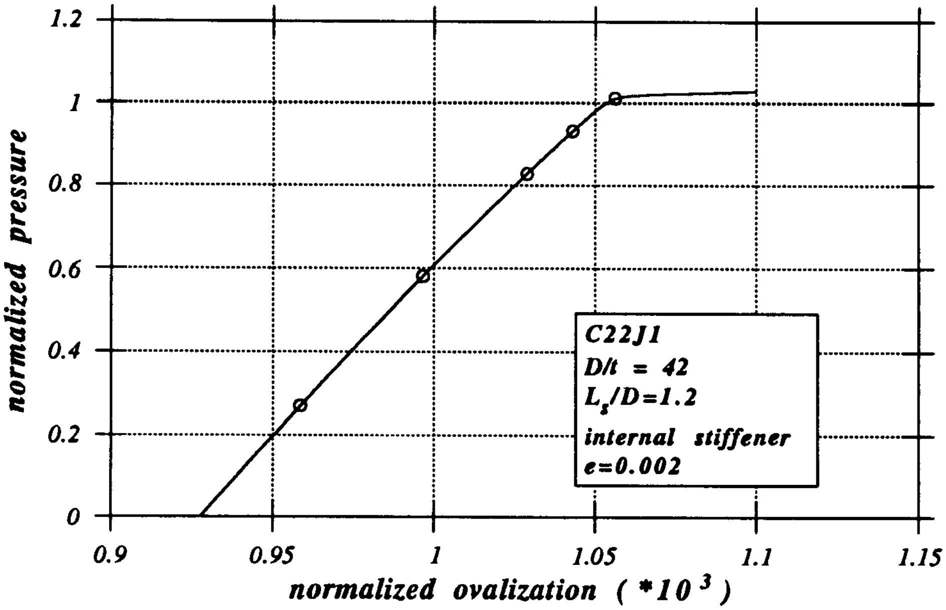

Figure 5.7: Pressure-ovalization curve of tube C22J1 for $L_s/D = 1.20$ (internal stiffener).

For very small spacing (e.g., $L_s/D \leq 1.4$) it was impossible to compute a limit point of pressure. This is shown in Figure 5.7 where pressure is plotted in terms of "middle-section" ovalization for $L_s/D = 1.2$. Clearly, beyond a certain pressure, the tube cross-section becomes entirely inelastic and the stiffness matrix almost singular. Subsequently, before a limit point occurs, the tube material enters into the strain-hardening region and the pressure starts rising again. For design purposes, the member has failed but the instability mechanism is not clearly predicted in the numerical simulation. However, the tube is assumed to be residual-stress free with a small value of initial imperfection. The ultimate capacity of the same tube under a more realistic set of assumptions will be investigated below.

The effects of capped-end compression are depicted in Figure 5.8. As expected, capped-end compression increases the ultimate capacity for small values of spacing (e.g. $L_s/D \leq 4.0$) because of inelastic behavior, which obeys the von Mises yield criterion. However, there is no significant effect for spacing parameter values above 4.0. This value is apparently the "border" between elastic and inelastic instability.

The ultimate pressure capacity of tubes under axial tensile load is of major importance in the design of stiffened tubes and is examined extensively in the next section where analytical predictions are compared with experimental data. In this section some preliminary results are depicted in Figure 5.9. The first of these graphs shows the variation of ultimate pressure in terms of the spacing parameter for hydrostatic pressure loading when axial tension is at the level of 55% of yield tension T_y. On the other hand, the second graph shows the same effect for radial pressure loading. In both cases, the presence

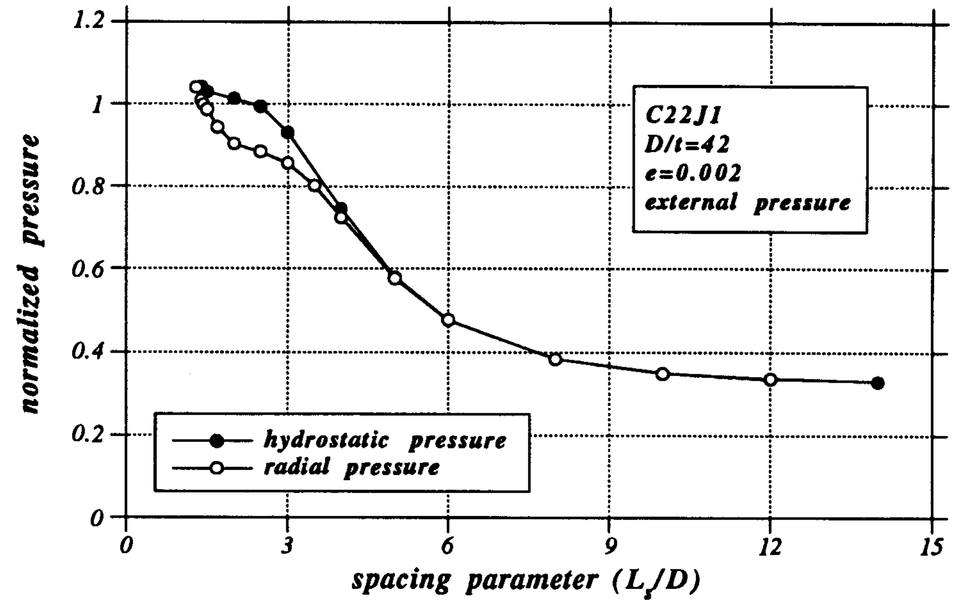

Figure 5.8: Effects of capped-end compression on ultimate pressure of tube C22J1.

of tension reduces the ultimate capacity for small spacing values. It should be noted that in the case of hydrostatic loading, the total axial force is not constant and the capped-end compression tends to "eliminate" tension effects. For the sake of completeness, the behavior under tension for hydrostatic and radial loading conditions is presented in Figure 5.10.

In all previous results, tube C22J1 was assumed to be free of residual stresses with a small value of initial imperfection ($e = 0.002$). Therefore, it is interesting to recalculate the ultimate capacity considering residual stresses and initial out-of-roundness equal to the API allowable value ($e = 0.01$). The stiffeners are assumed to be external and both longitudinal and circumferential residual stresses are assumed to be non zero. The results are shown in the first graph of Figure 5.11 and the new curve is considerably lower than the old

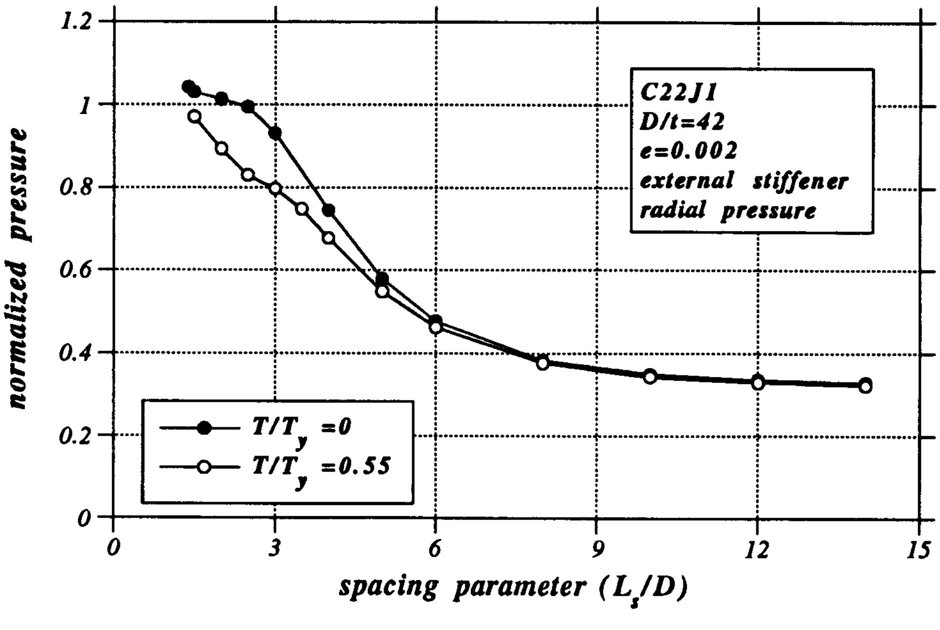

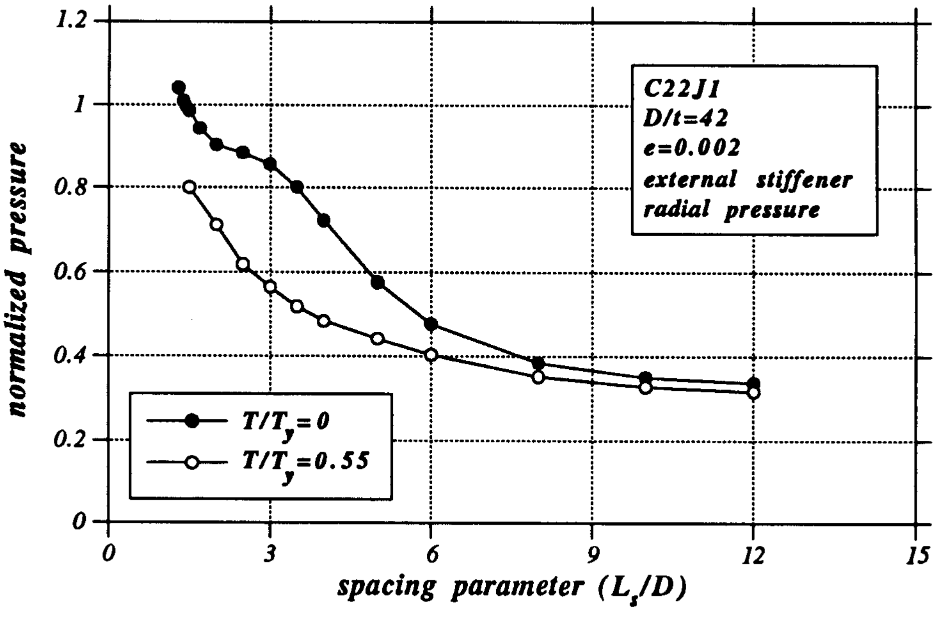

Figure 5.9: Effects of externally applied tension on ultimate pressure of tube C22J1.

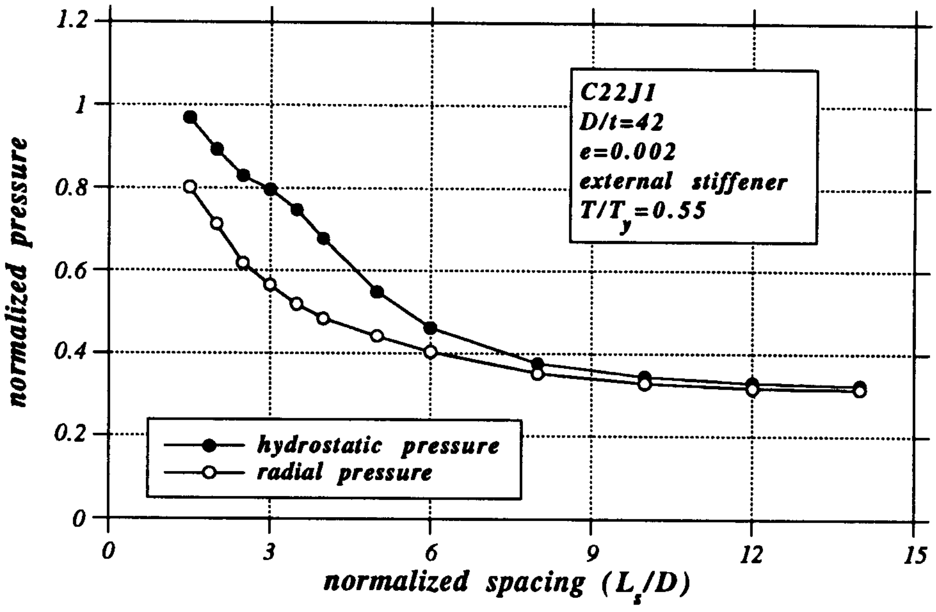

Figure 5.10: Effects of capped-end compression on ultimate pressure of tube C22J1 in the presence of axial tension.

one. In addition, with the new assumptions, it is possible to obtain a limit pressure point for small values of spacing. As mentioned above, in the absence of residual stresses and assuming a small initial out-of-roundness ($e = 0.002$) it was impossible to compute a limit point for small spacing ($L_s/D \leq 1.4$).

Finally, the results obtained with the new assumptions are compared with the API predictions [5] in the second graph of Figure 5.11. The ultimate pressure specified by API rules is

$$p_{hc} = 2\,\sigma_{hc}\left(\frac{t}{D}\right) \tag{5.3}$$

where the buckling hoop stress σ_{hc} is computed through the "elastic" buckling hoop stress

$$\sigma_{he} = 2\,C_h\,E\left(\frac{t}{D}\right) \tag{5.4}$$

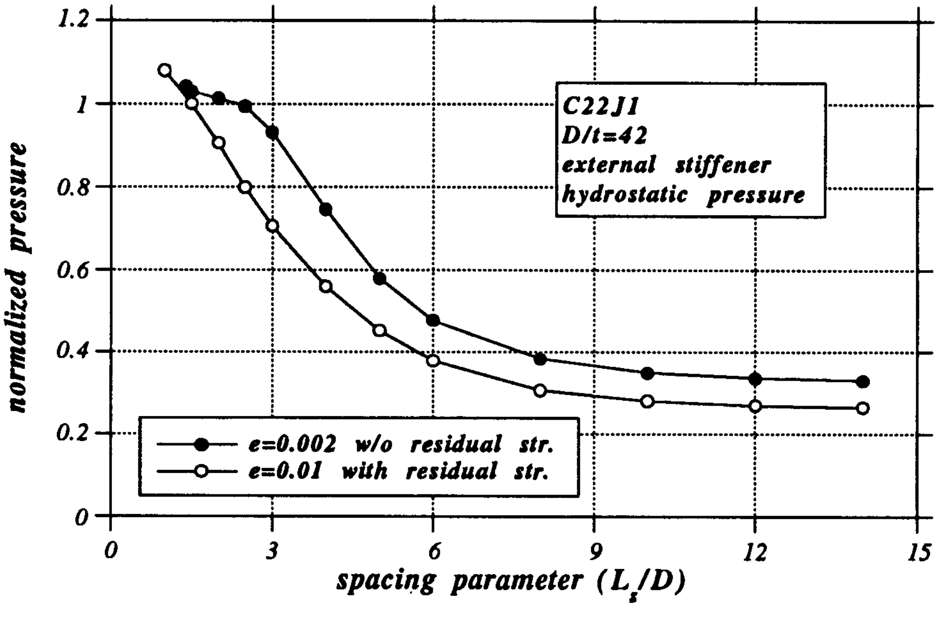

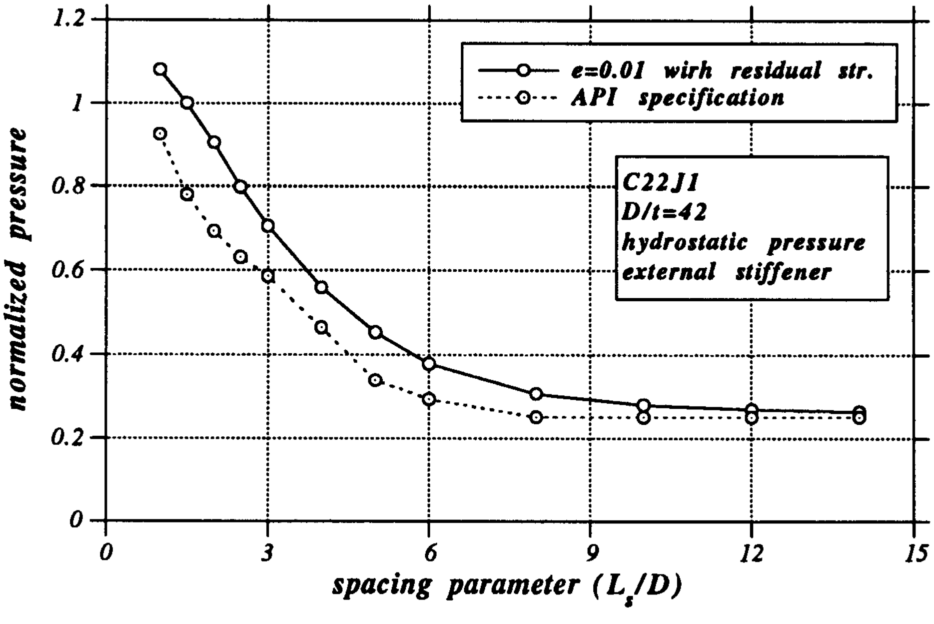

Figure 5.11: Effects of residual stresses on ultimate pressure of tube C22J1.

and C_h depends on the tube geometry. If $\sigma_{he} > 0.55\sigma_y$, the ultimate hoop stress is given by

$$\sigma_{hc} = 0.7\,\sigma_y \left(\frac{\sigma_{he}}{\sigma_y}\right)^{0.4} \tag{5.5}$$

whereas, if $\sigma_{he} \leq 0.55\sigma_y$,

$$\sigma_{hc} = \sigma_{he} \tag{5.6}$$

Apparently, both curves show a similar drop in ultimate capacity for increasing spacing. Nevertheless, the analytical results are somewhat higher than the specification predictions. Furthermore, the specification curve becomes flat at a smaller value of spacing than the analytical curve. This indicates that stiffeners increase the ultimate pressure even for spacings larger than the value proposed by API through Equation 5.2.

5.2 Comparison with Experimental Data

So far, the work on ring-stiffened tubes has been entirely experimental and is summarized in Refs. [38], [39] and [16]. In these experimental efforts, tubular specimens, having a wide range of diameter-to-thickness ratios, were subjected to a combination of external pressure and axial load until collapse. The diameter-to-thickness ratio ranged between 30 and 96, and stiffeners were spaced at a distance of 0.85 to 4 tube diameters. All specimens had *external* stiffeners. In the present work, an analytical prediction of the ultimate capacity is attempted, for those specimens having D/t values between 30 and 50, because they represent tubes which are candidates for typical deep-water applications [37].

Experiments reported in Ref. [38] were tested under hydrostatic pressure (i.e. with the presence of capped-end compression). On the other hand, tension and compression test values reported in Refs. [39] and [16] correspond to the net axial force on the specimen, which means that additional external tension was applied to "eliminate" capped-end compression. The above experimental procedures are simulated in the present analysis.

For each specimen, the yield stress σ_y and Young's modulus E, as well as the initial imperfection (e) reported in Refs. [38], [39] and [16] are used in this analysis. The material curve is assumed to be bilinear with a post-yielding modulus equal to $E/400$. In addition, because of the forming process of fabricated tubes, both longitudinal and circumferential residual stresses are considered, following the distributions of Chen and Ross [14]. It should be mentioned that the majority of the specimens do not meet the out-of-roundness requirement by API ($e_{lim} = 0.01$). In such a case, API predictions can be corrected with the following empirical factor:

$$f_p = \frac{1 - 0.2\sqrt{100\,e}}{0.8} \leq 1.0 \tag{5.7}$$

as suggested by the API commentary, for better correlation with the experimental data.

5.2.1 Specimens Under Radial Pressure and Tension

These tests were performed by SwRI and CBI, and comprised nine test groups. In the present work, Groups 1, 2, 5, 6, 7 and 9 are examined. The other groups involve thin tubes with D/t values greater than 60, which are not of immediate interest. During testing, almost all specimens were first axially loaded and, subsequently, keeping the tension constant, pressure was raised until collapse. However, four specimens (1F, 2E, 6D, 6E) were first pressurized to a level of 80% of the API predicted pressure. Then axial tension was increased up to a prescribed value and, finally, pressure was raised until collapse. These conditions are simulated in the present analysis in order to establish consistency with the experimental procedure. During the experiments, additional tension was applied to the specimens to "eliminate" the effects of the capped-end force. Therefore, in the analytical procedure, the capped-end compression is set equal to zero.

For all test groups presented in this section, experimental and numerical results are compared with the API formula for pressure-tension interaction:

$$\left(\frac{T}{T_y}\right)^2 + \left(\frac{p}{p_{hc}}\right)^{2\eta} + 2\,\nu\left(\frac{T}{T_y}\right)\left(\frac{p}{p_{hc}}\right) = 1 \qquad (5.8)$$

where

$$\eta = 5 - 4\left(\frac{\sigma_{hc}}{\sigma_y}\right) \qquad (5.9)$$

is a parameter for inelastic effects, T_y is the yield tension, p_{hc} is the ultimate pressure predicted by API for zero tension (Equation 5.3), σ_{hc} is the hoop stress corresponding to p_{hc} and ν is the Poisson's ratio, equal to 0.3 for steel material.

Table 5.1 shows the geometric and material properties for Group 1. These specimens are very stiff tubes, having a diameter-to-thickness ratio of about 35 and stiffener spacing L_s/D equal to 1.52. Experimental results are compared with numerical predictions in Table 5.2. The comparison is shown in graphical form together with the API interaction formula in the first graph of Figure 5.12. In the absence of axial force, the collapse pressure is close to the yield pressure and the presence of compressive axial force equal to half the yield force increases the pressure capacity due to the von Mises yield criterion. This is shown in both the experimental and numerical predictions. However, the specification curve does not account for this beneficial effect. In addition, experimental as well as analytical results indicate a reduction in pressure capacity with increasing tension. The analytical results are in very good agreement with the specification curve.

specimen	D/t	L_s/D	M	e	$\sigma_y\,(ksi)$	$E\,(ksi)$
1A	33.4	1.52	12.4	0.01583	34.9	29100
1B	33.2	1.51	12.3	0.02494	34.9	29100
1C	33.8	1.51	12.5	0.00711	35.6	28400
1D	33.8	1.51	12.5	0.00950	35.6	28400
1E	33.2	1.51	12.5	0.02333	35.1	29100
1F	33.3	1.57	12.8	0.01333	41.8	30300

Table 5.1: Geometrical and material properties of Group 1 ($\eta = 1.00$).

specimen	tension $(kips)$	exp-pressure (psi)	num-pressure (psi)
1A	-16.0	2100	2056.6
1B	204.0	1950	1812.2
1C	-641.0	2480	2289.0
1D	416.0	1900	1675.2
1E	699.0	1450	1176.8
1F	796.2	1920	1502.9

Table 5.2: Results for Group 1.

Table 5.4 presents the results for the second group of specimens which have diameter-to-thickness D/t and spacing L_s/D values equal to 47 and 2.3 respectively. From Equation 5.1, a value of M equal to 22.3 is obtained and, therefore, the tubes may be classified as relatively stiff. The second graph of Figure 5.12 is a graphical representation of the results. Apparently, the analytical prediction for specimen 2D is considerably lower than the corresponding experimental result. In order to examine the reason for this difference, specimen 2D was reanalyzed considering a material curve which had a post-yielding modulus equal to $E/100$. The ultimate pressure was calculated to be $457 psi$ which is quite closer to the experimental result. This shows a sensitivity of the ultimate pressure to the post-yielding modulus for large values of tension.

specimen	D/t	L_s/D	M	e	$\sigma_y\,(ksi)$	$E\,(ksi)$
2A	46.6	2.29	22.2	0.01292	33.2	30400
2B	46.6	2.31	22.3	0.01317	33.2	30400
2C	46.6	2.30	22.2	0.01383	33.2	30400
2D	47.4	2.29	22.3	0.01808	31.7	30400
2E	45.9	2.23	22.2	0.00367	34.0	30300

Table 5.3: Geometrical and material properties of Group 2 ($\eta = 1.85$).

specimen	tension $(kips)$	exp-pressure (psi)	num-pressure (psi)
2A	-385.0	1150	1130.4
2B	254.0	1000	1118.0
2C	574.0	929	908.4
2D	989.0	550	360.4
2E	664.2	1080	930.1

Table 5.4: Results for Group 2.

Specimens of Group 5 have two rigid end plates at a distance of about 8 diameters. Tube properties are shown in Table 5.5 and the analytical results are compared with experimental data in Table 5.6. These tubes do not satisfy the spacing requirement 5.2 and, therefore, they are considered as unstiffened by the API specification. In order to examine the validity of

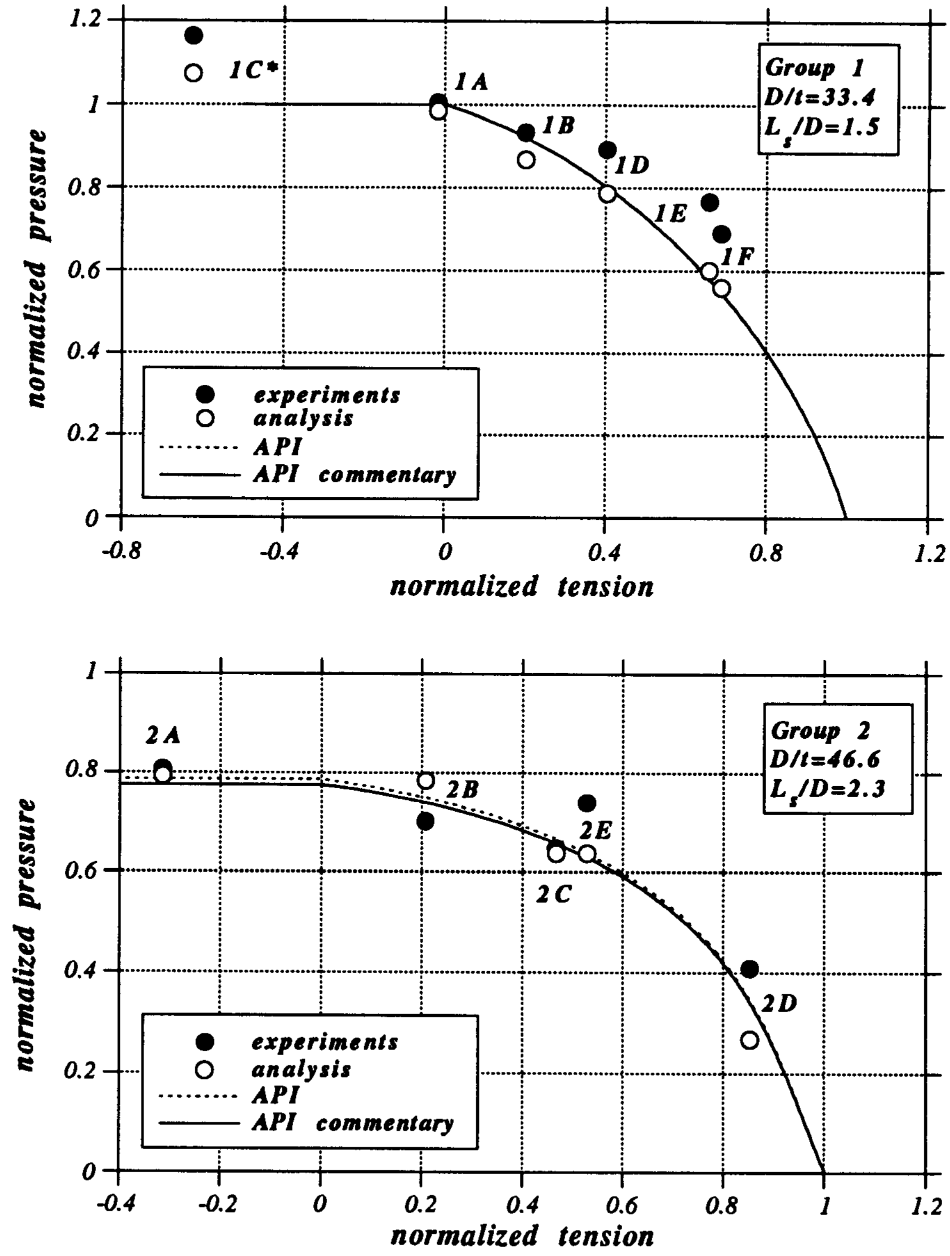

Figure 5.12: Results for Groups 1 and 2.

this statement, a cross-sectional analysis is first conducted neglecting rigid-end effects. In Figure 5.13, analytical results are in good agreement with the specification values, but much below the experimental data. For the second set of analytical results, the three-dimensional geometry of the specimen is simulated, and the end-sections are assumed to remain undeformed. Results were obtained in closer agreement with the experimental data (see the first graph of Figure 5.14). Finally, a third set of results is obtained assuming an initial out-of-roundness equal to the maximum API imperfection ($e = 0.01$). Analytical results are depicted in the second graph of Figure 5.14 and they are in excellent agreement with experiments.

A first conclusion from the above parametric study is the sensitivity of results to the value of initial out-of-roundness. Moreover, end-plates provide beneficial stiffness and increase overall capacity for spacing distance greater than the limit distance indicated by Equation 5.2.

specimen	D/t	L_s/D	M	e	$\sigma_y\,(ksi)$	$E\,(ksi)$
5A	47.0	8.02	77.7	0.02050	42.1	29100
5B	47.0	8.03	77.9	0.02350	42.1	29100
5C	46.4	8.02	77.3	0.02128	42.2	30000
5D	46.4	8.01	77.2	0.02461	42.2	30000

Table 5.5: Geometrical and material properties of Group 5 ($\eta = 3.90$).

specimen	tension ($kips$)	exp-press. (psi)	num-press. 2D (psi)	num-press. 3D (psi)	num-pressure 3D-API (psi)
5A	-12.0	600	398.96	497.50	588.75
5B	341.0	560	367.51	465.65	569.22
5C	584.0	525	372.24	441.49	526.84
5D	775.0	400	286.87	269.59	346.77

Table 5.6: Results for Group 5.

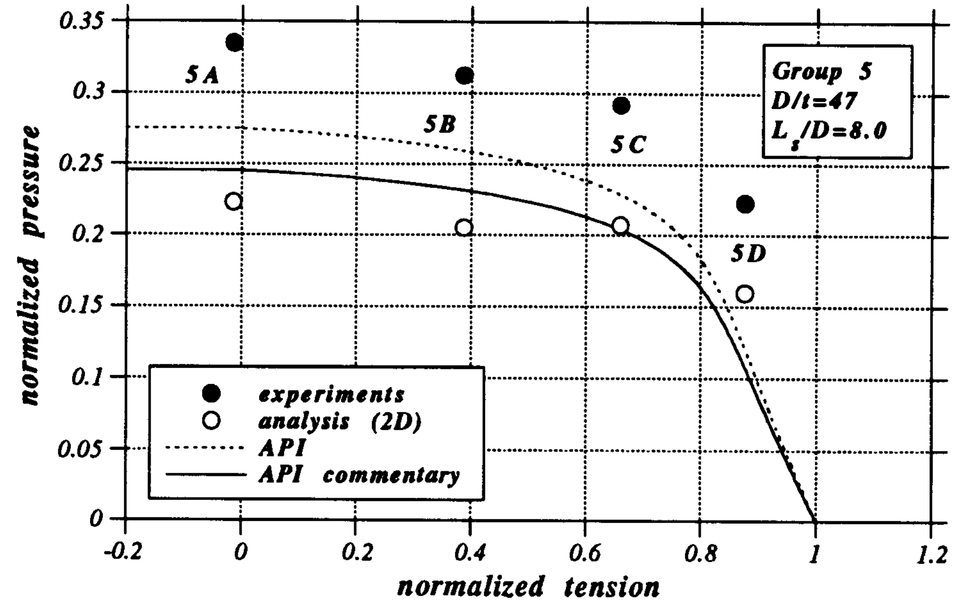

Figure 5.13: Results for Group 5 (two-dimensional analysis).

Group 6 comprises five stiff tubes, with geometric characteristics similar to the specimens of Group 1. However, the material had a higher yield stress ($\sigma_y = 54.5\,ksi$). Results are reported in Table 5.8 and Figure 5.15. During testing, specimen 6A collapsed because of stiffener weld failure. This explains the low experimental value in comparison with the numerical prediction and the API curve. The other experimental values are in very good agreement with the analytical results. However, both experimental and analytical results are below the API curve, which makes the specification predictions rather unconservative.

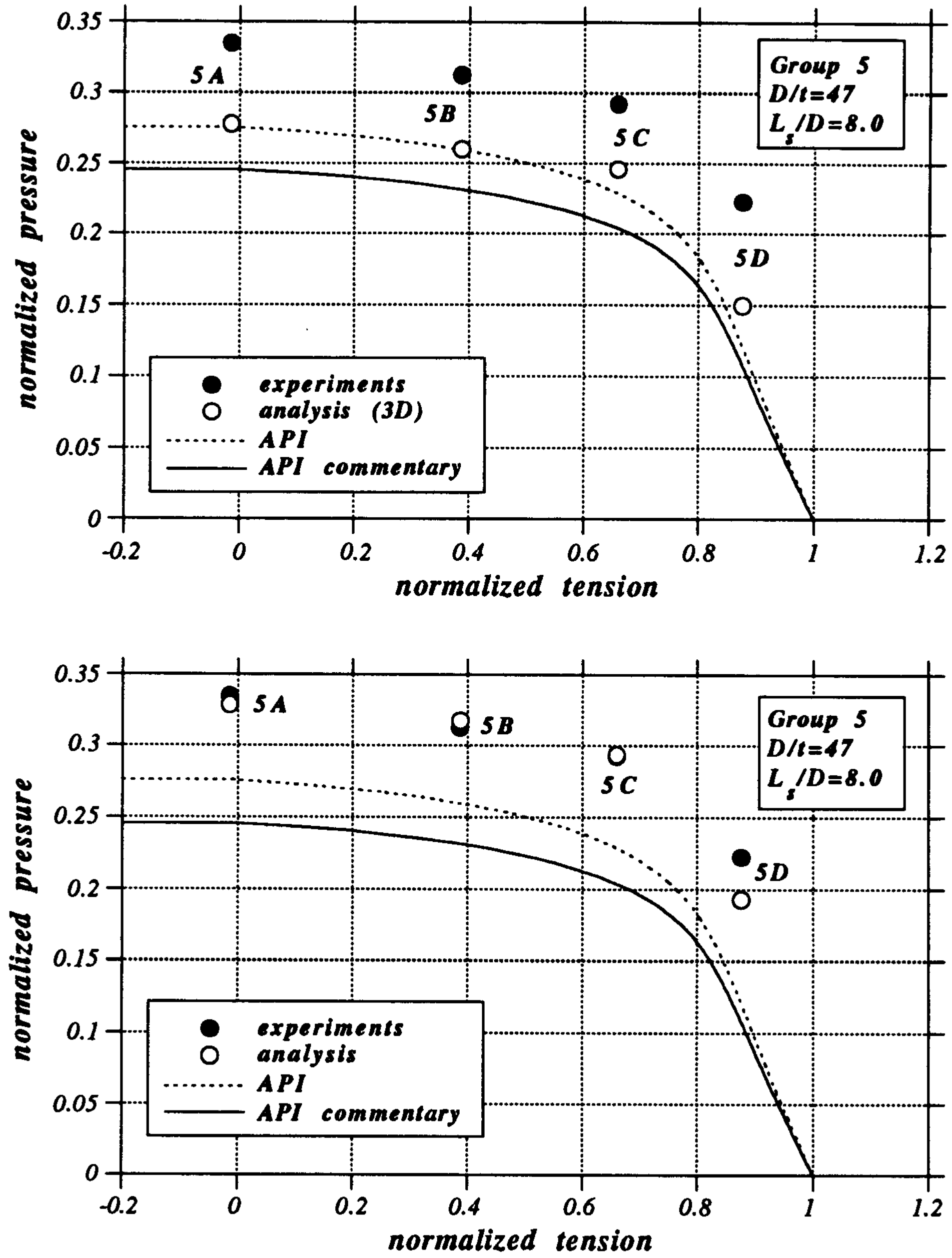

Figure 5.14: Results for Group 5; reported and API imperfection (three-dimensional analysis with end-plates).

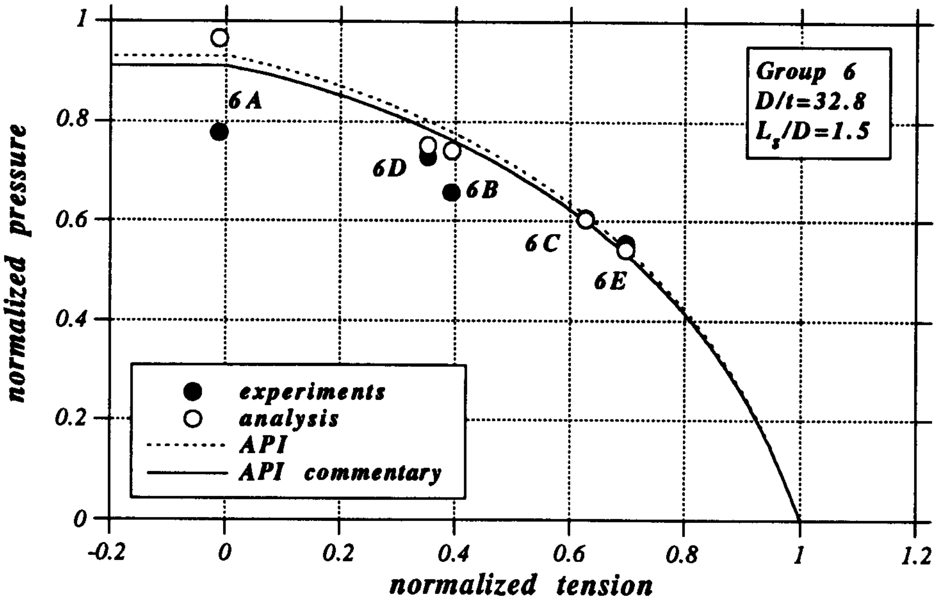

Figure 5.15: Results for Group 6.

specimen	D/t	L_s/D	M	e	$\sigma_y\,(ksi)$	$E\,(ksi)$
6A	32.8	1.53	12.4	0.01456	54.8	29400
6B	32.8	1.48	12.0	0.01994	54.8	29400
6C	32.8	1.53	12.4	0.01161	55.4	30500
6D	33.3	1.58	12.9	0.02128	53.7	29400
6E	33.5	1.58	12.9	0.00662	53.7	29400

Table 5.7: Geometrical and material properties of Group 6 ($\eta = 1.23$).

specimen	tension $(kips)$	exp-pressure (psi)	num-pressure (psi)
6A	-18.0	2600	3228.3
6B	634.0	2200	2480.8
6C	1021.0	2050	2037.4
6D	555.6	2390	2465.9
6E	1098.1	1820	1776.8

Table 5.8: Results for Group 6.

Group 7 consists of four specimens having approximately the same geometric characteristics as the specimens of Group 2 ($L_s/D = 2.3$ and $D/t = 46$). However, the material yield stress is about $52\,ksi$ and the reported initial out-of-roundness is considerably below the API maximum allowable value ($e = 0.0016 - 0.0056$). The results obtained for the reported value of initial imperfection are shown in the first graph of Figure 5.16 and are significantly above the experimental data, especially for cases 7A and 7B. A second set of results is obtained assuming initial imperfection equal to the API allowable value ($e = 0.01$). Apparently, numerical predictions get closer to the experimental data and this suggests an important sensitivity of the results to the value of initial imperfection. These results are plotted in the second graph of Figure 5.16. Recall that a similar sensitivity was observed in the parametric study of Group 5.

specimen	D/t	L_s/D	M	e	$\sigma_y\,(ksi)$	$E\,(ksi)$
7A	46.2	2.31	22.2	0.00321	52.0	30400
7B	45.6	2.32	22.2	0.00163	52.0	30400
7C	45.6	2.32	22.2	0.00563	52.0	30400
7D	46.4	2.38	23.0	0.00487	51.7	30400

Table 5.9: Geometrical and material properties of Group 7 ($\eta = 2.34$).

specimen	tension ($kips$)	exp-press. (psi)	num-press. (psi)	num-press. (API) (psi)
7A	552.5	1275	1753.6	1616.1
7B	-0.1	1500	1888.2	1696.0
7C	919.3	1280	1482.7	1440.5
7D	1027.4	1180	1330.2	1291.4

Table 5.10: Results for Group 7.

The three specimens of Group 9 have the same geometric characteristics to those of Group 5. However, they are made of high strength steel ($\sigma_y \simeq 60\,ksi$). Results are presented in Table 5.12 and it is clear that end-plates are responsible for some significant increase in the ultimate capacity. Experimental results are far off the specification curve and the results from cross-sectional analysis, as indicated by the first graph of Figure 5.17. Very good agreement is obtained by conducting three-dimensional analysis and including rigid end conditions (see the second graph of Figure 5.17).

It is important to note the failure of the API formula in predicting these tests as well as those of Group 5. The formula is very conservative because it classifies the specimens as unstiffened. However, end-effects are more important than expected and provide a "beneficial" additional stiffness. In Figure 5.18, the pressure-deformation curve is plotted for specimen 9A. The ovalization at the middle cross-section between the end-plates is taken as the deformation parameter. The analysis is not terminated just after the limit point but is continued to obtain the postbuckling path. The postbuckling configuration at point (1) is shown in Figure 5.19. Clearly, the tube is not long enough to exhibit uniform ovalization around the middle-section. Note that the unstable post-buckling path becomes stable again *before contact* of the top and bottom generators. This implies that the region around the middle cross-section is not free of end-plate effects. Therefore, the end-effects must be taken into account for spacing values larger than those specified by Equation 5.2.

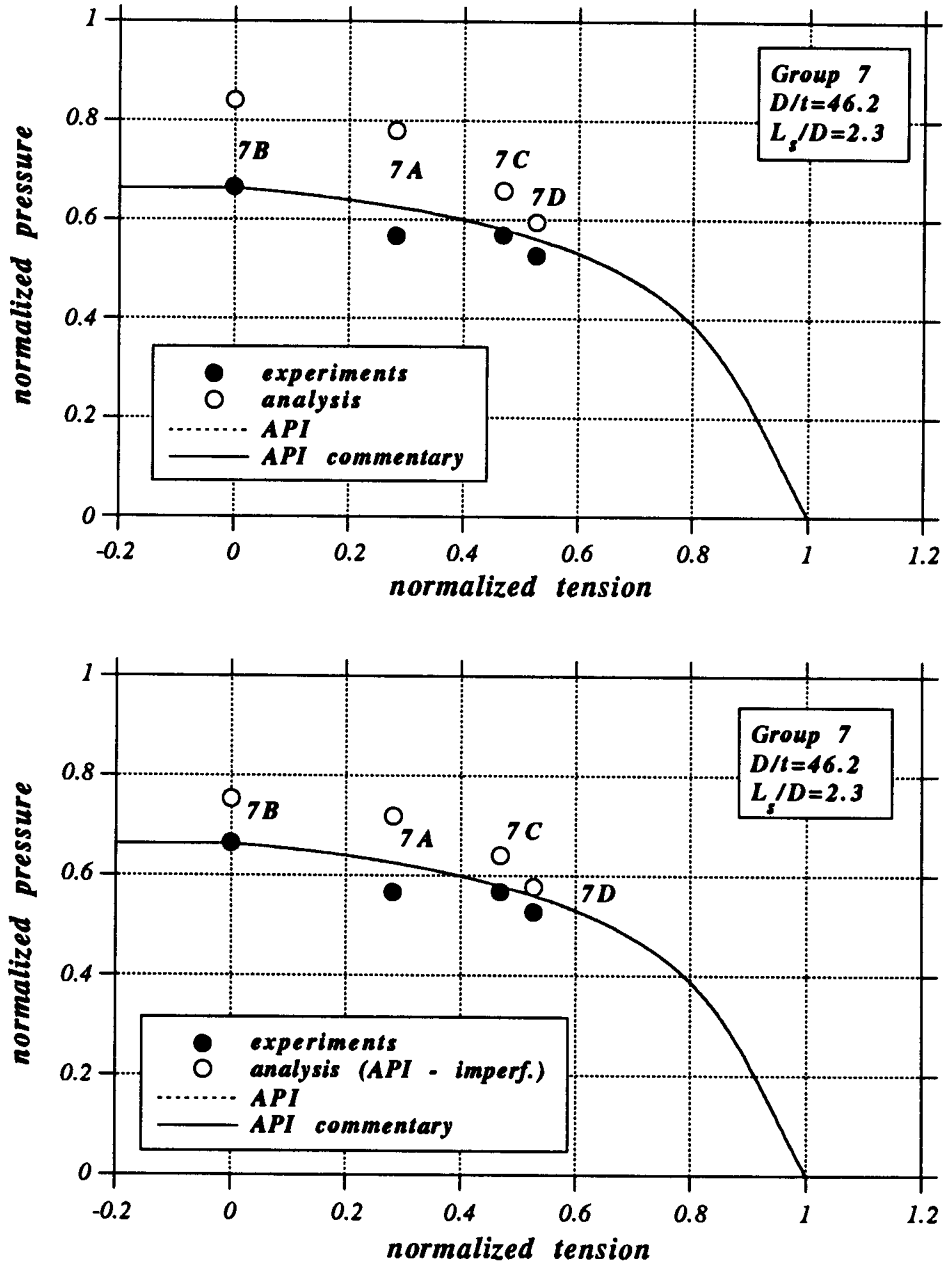

Figure 5.16: Results for Group 7 (reported and API imperfection).

specimen	D/t	L_s/D	M	e	$\sigma_y\,(ksi)$	$E\,(ksi)$
9A	45.7	8.21	78.5	0.03122	56.1	30900
9B	45.7	8.18	78.2	0.01933	56.1	30500
9C	45.5	8.18	78.0	0.02511	56.0	30100

Table 5.11: Geometrical and material properties of Group 9 ($\eta = 4.13$).

specimen	tension ($kips$)	exp-press. (psi)	num-press. 2D (psi)	num-press. 3D (psi)
9A	5.6	570	436.3	528.7
9B	620.4	580	463.1	574.8
9C	935.2	460	399.7	448.9

Table 5.12: Results for Group 9.

5.2.2 Specimens Under Hydrostatic or Radial Pressure

The experimental results for the first set of these specimens are reported in [38]. During testing, the tubes were subjected to hydrostatic pressure (i.e., capped-end compression was not eliminated) and spacing ranged from 1.5 to 4 tube diameters. Analytical results are shown in Table 5.13. The second set of this category comprises seven specimens reported in [39] as well as two specimens from [16]. In these experiments, capped-end compression was eliminated by applying a tensile force of equal magnitude, in order to keep the axial stress constant, with the exception of tube 10-B which was tested under hydrostatic pressure (including capped-end compression). The analytical results are shown in Table 5.14. Finally, the three pure pressure tests examined in Chapter 4 are included for the sake of completeness and the results are depicted in Table 5.15. Note that the actual experimental conditions are

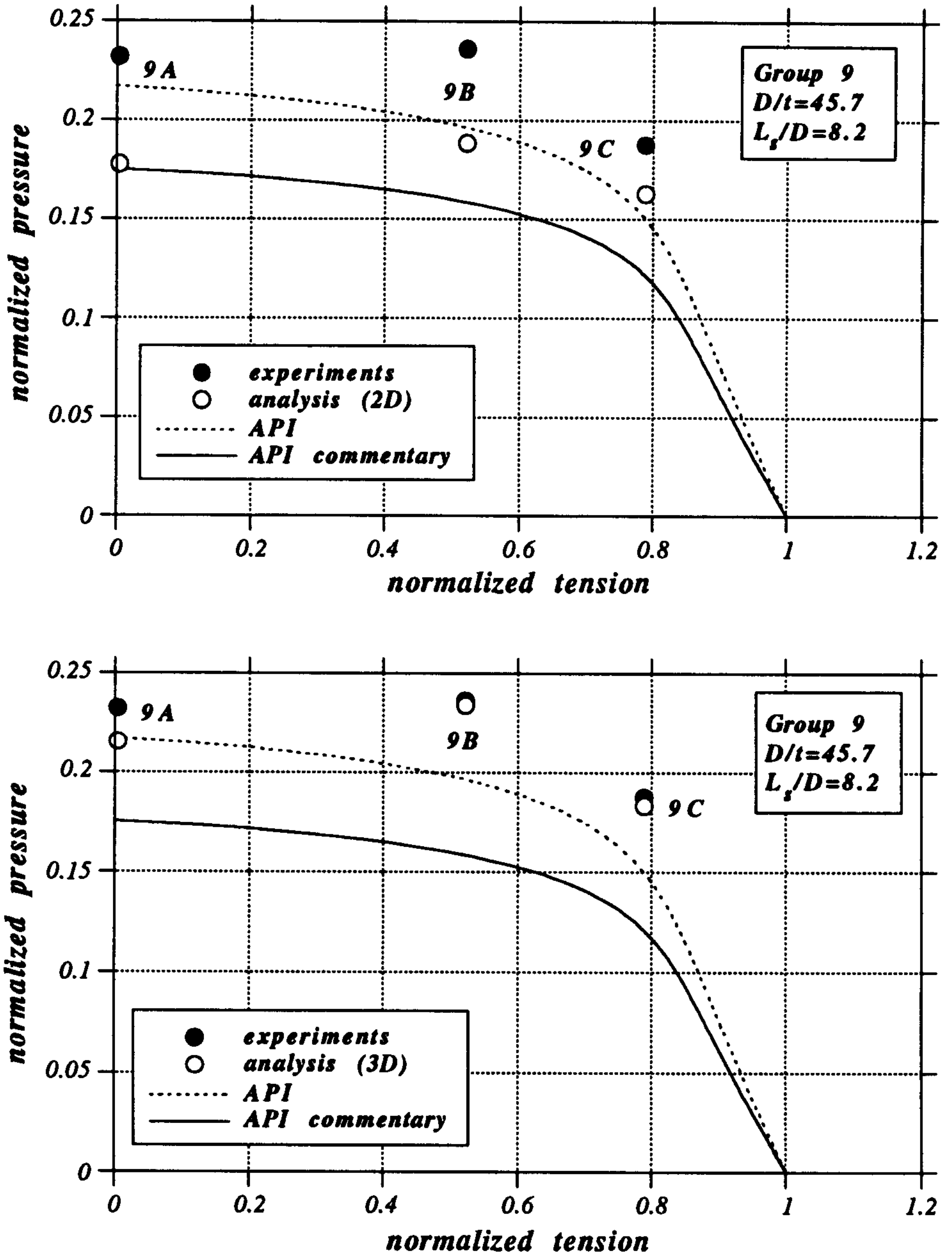

Figure 5.17: Results for Group 9 (two-dimensional and three-dimensional analysis).

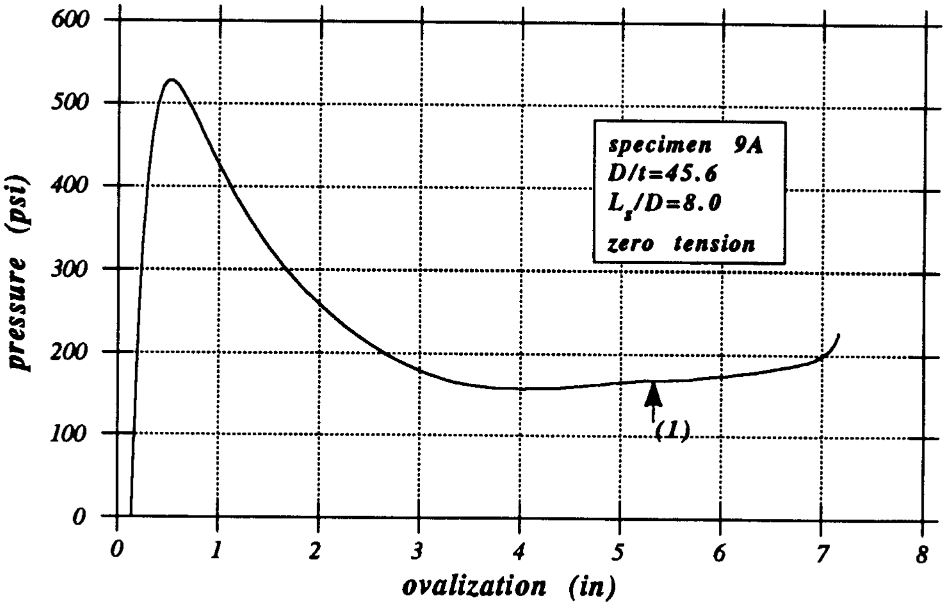

Figure 5.18: Pressure versus middle section ovalization of specimen 9A (three-dimensional analysis with end-plates).

simulated in the analysis of all tubes.

It is helpful to present the results in the graphical form of Figure 5.20 as suggested by P. W. Marshall [37]. More specifically, the collapse pressure is normalized by the yield pressure p_y of the unstiffened cross-section. In addition, the results are plotted in terms of buckling parameter σ_{he}/σ_y, where σ_{he} is the "elastic" collapse hoop stress given by the API specification 5.3, and depends on D/t, L_s/D and Young's modulus E. It must be noted that σ_{he} does not have any specific physical meaning for stiffened tubes which collapse in the inelastic range. However, it is a convenient parameter to describe the geometric properties of a stiffened tube.

In general, there is a good comparison between experimental data,

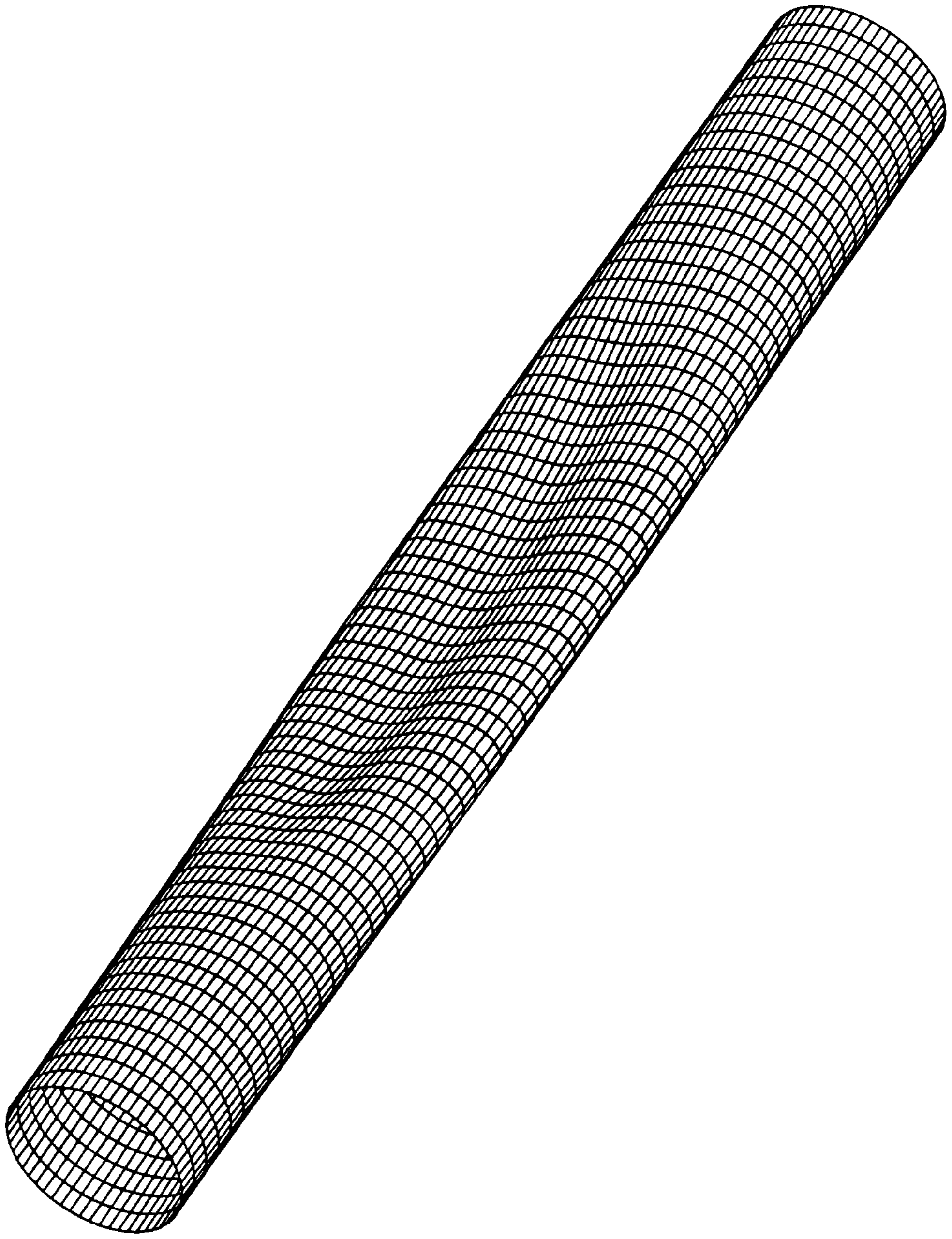

Figure 5.19: Graphical simulation of specimen 9A at point (1).

numerical results and specification predictions. Experimental and numerical results are plotted taking into account the corrected value of σ_{he} according to Eq. 5.7 when initial out-of-roundness exceeds API limits. There are four specimens whose experimental collapse pressure is below the specification predictions. Analytical results for two of these specimens (15 and 16) are in very good agreement with test data and indicate that the specification prediction is unconservative. The reason for this is the small stiffener size of these tubes. According to Ref. [38], these specimens were designed to fail because of "global" buckling and their stiffener sizes were much smaller than those of the other specimens. During testing of specimen 6A, the ultimate pressure was not reached because of stiffener weld failure and this explains the low experimental pressure. Nevertheless, no reasonable explanation was found for the low experimental value of specimen 2 [40].

Very good results were obtained for the "unstiffened" tubes located on the left part of the graph. On the other hand, analytical predictions which are quite close to the specification rules are somehow below the experimental data for heavily stiffened tubes (shown on the right side of the graph). Finally, for moderately stiffened tubes, with the exception of tubes 6A and 2, both experiments and analysis are in good agreement with the API equation.

specimen	M	e	σ_{he}	σ_y	p_{exp}	p_{num}
1A	12.4	0.01583	101.63	34.9	2100	2056.6
1C	12.5	0.00711	103.89	35.6	2480	2289.0
2A	22.2	0.01292	42.95	33.2	1150	1130.4
5A	77.7	0.02050	10.34	42.1	600	497.5
6A	12.4	0.01456	106.00	54.8	2600	3228.3
7B	22.2	0.00163	45.45	52.0	1500	1888.2
9A	78.5	0.03122	10.52	56.1	570	528.7

Table 5.13: Specimens under pure pressure (first set).

specimen	M	e	σ_{he}	σ_y	p_{exp}	p_{num}
1	16.1	0.02320	75.42	39.5	2200	2564.7
2	15.7	0.02210	82.04	59.2	2700	3811.8
3	22.1	0.02110	55.25	35.2	2120	2168.0
4	30.1	0.01290	43.88	35.2	1790	2027.0
5	33.0	0.01670	29.84	37.8	1350	1580.6
7	37.0	0.01030	27.58	33.7	1080	1300.9
8	39.9	0.01410	21.33	41.7	870	1076.6
15	24.1	0.02160	50.85	39.5	1650	1736.7
16	20.3	0.01580	39.24	41.0	780	902.8
10-A	8.57	0.00830	113.36	33.7	1620	1509.0
10-B	8.57	0.00840	112.98	56.9	2600	2686.6

Table 5.14: Specimens under pure pressure (second set).

specimen	M	e	σ_{he}	σ_y	p_{exp}	p_{num}
C6J5	230.0	0.00409	6.32	43.0	225.7	235.9
B4	230.0	0.00370	14.61	56.2	760.0	778.9
A10	175.0	0.00617	14.61	56.2	774.0	747.1

Table 5.15: Specimens under pure pressure (third set).

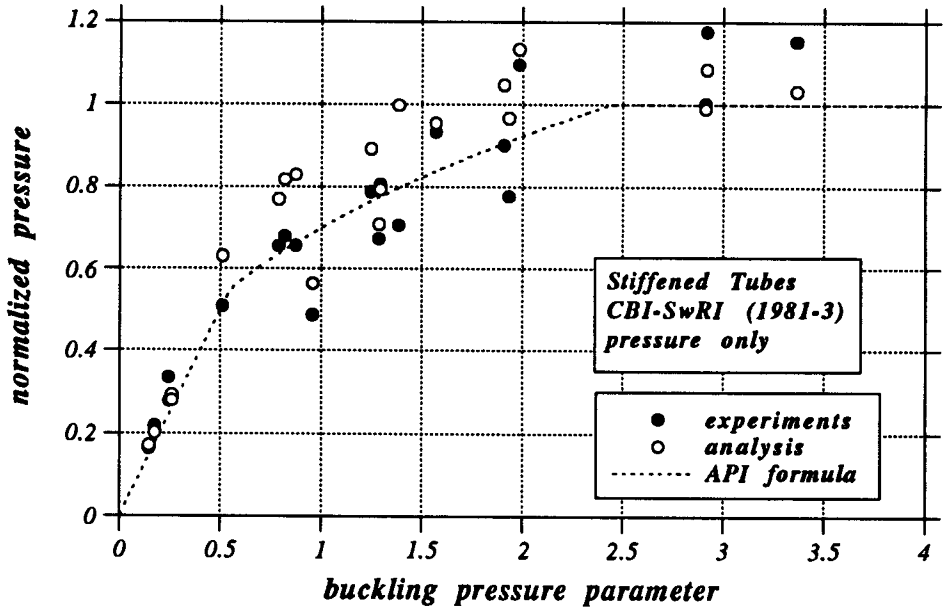

Figure 5.20: Test results for hydrostatic and radial pressure.

Chapter 6

Analysis of Stiffened Tubular Beam-Columns

In this Chapter, the ultimate capacity of stiffened tubes under thrust, bending and external pressure is examined. First, the tube response under pressurized bending in the absence of axial force is treated. Then, the effects of pressure on the axial capacity of stiffened tubes are investigated. Finally, slender stiffened beam-columns are analyzed and results are presented in the form of thrust-moment interaction diagrams. In all cases, results are compared with the AISC and API specification rules, as well as with some simplified equations proposed by Loh [35] and Dorgant [21]. Particular emphasis is given on the reduction of axial capacity due to pressure, which is an important design issue. In addition, in order to achieve better understanding of the capacity under pressurized bending, the CBI stub column test data [17] are compared with analytical results. The tested stub columns have undeformed end-sections and, therefore, each specimen may be regarded as a single panel of a heavily stiffened long tube. Nevertheless, it should be mentioned that, by the time the present research effort was completed, experimental data on the capacity of slender stiffened tubes under pressure, thrust and bending were not available. Finally, it is important to note that, in all graphs, the values of pressure, moment, axial force and curvature are normalized by the yield pressure $p_y = 2\sigma_y t/D$, the fully-plastic moment $M_p = \sigma_y Z$, the yield axial force $P_y = \sigma_y A$ and the curvature parameter $k_I = t/D^2$, respectively.

6.1 Pressurized Bending of Stiffened Tubes

The bending capacity of unstiffened tubes under external pressure was investigated extensively in Chapter 3 for tubes of various D/t values. The major conclusion from that analysis was the reduction of bending capacity for increasing level of external pressure. In this Section, the effects of ring stiffeners on pressurized bending are examined. It is expected that the presence of stiffeners would increase the capacity. More specifically, stiffeners prevent large cross-sectional ovalization, which is a very important source of instability, thus increasing the ultimate bending capacity.

6.1.1 Analytical Preliminaries

Figures 6.1 - 6.7 show the pressure-moment interaction for a tube which has the cross-sectional and material characteristics of tube C22J1, extensively analyzed in previous Chapters. The tube is subjected to hydrostatic pressure (with capped-end compression) and is assumed to be infinitely long. Therefore, only one panel needs to be analyzed. The stiffeners are ***internal*** and their spacing is taken equal to three tube diameters ($L_s/D = 3.0$).

Because of nonuniform ovalization along the tube, cross-sectional deformation parameters up to the eighth degree are included in the analysis. In addition, the stiffener size about the middle section (i.e., at the location where the buckle is expected), is taken equal to 8.5% of the tube diameter. Motivated by the local buckling results of Chapter 3, an entire panel between stiffeners is analyzed. Obviously, the analysis of a half panel with zero warping at the end sections is consistent with tube geometry and boundary conditions.

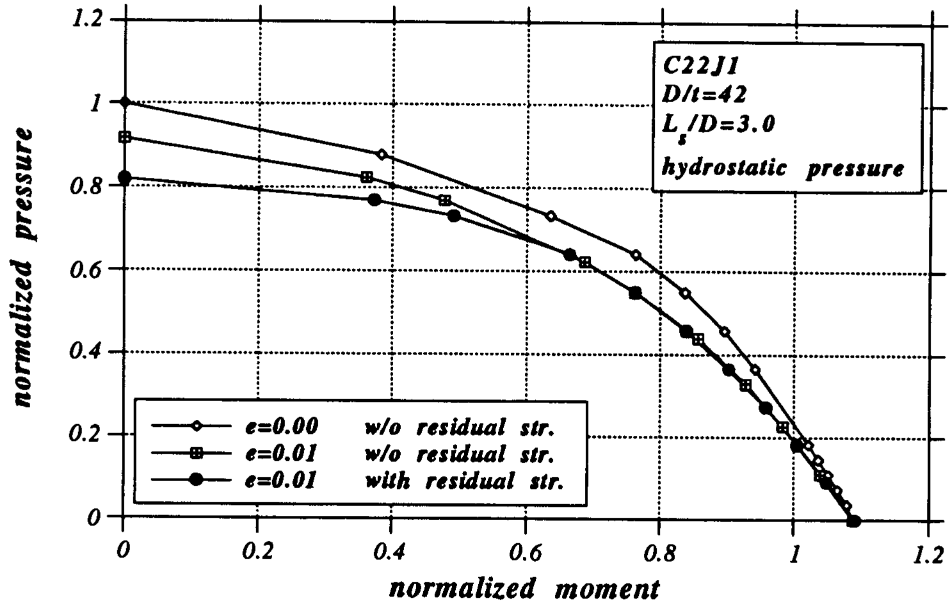

Figure 6.1: Pressure-bending interaction curves for tube C22J1 ($L_s/D = 3.0$).

However, such analysis does not provide the exact postbuckling shape, because of the nonsymmetric configuration of the buckle (see section 3.5). Nevertheless, the analysis of a few cases using half-panel conditions and element size equal to 20% of the tube diameter (i.e., a coarse mesh) did not indicate any significant change in the ultimate moment value.

Three interaction curves are shown in Figure 6.1. The first curve is derived under the assumption of zero residual stresses and zero initial out-of-roundness, except for the case of pure pressure where a small initial out-of-roundness is considered ($e = 0.002$) in order to obtain a limit point. The second curve assumes zero residual stresses and an initial out-of-roundness equal to the API allowable value ($e = 0.01$). Finally, the third curve represents the tube response in the presence of residual stresses and an initial imperfection e equal

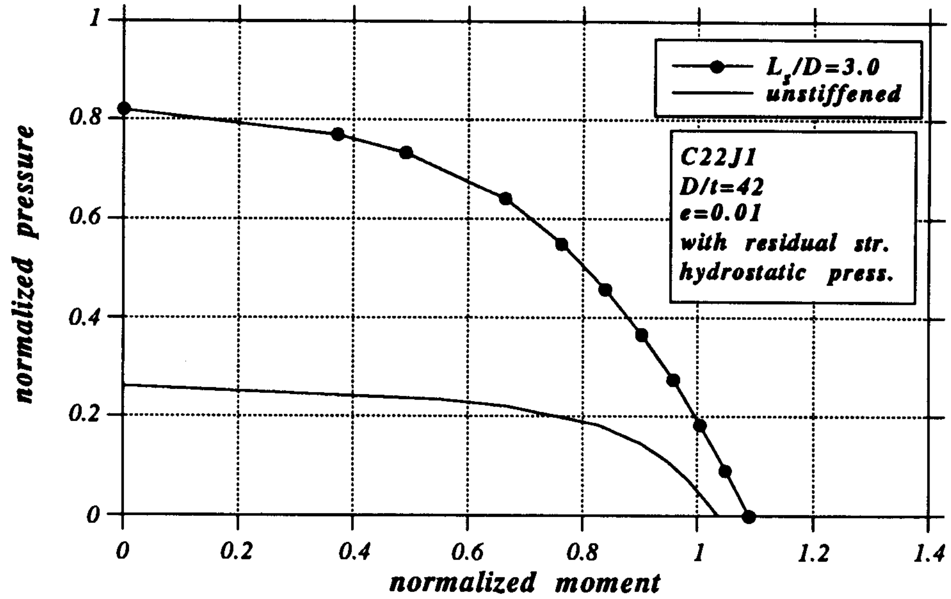

Figure 6.2: Comparison of stiffened and unstiffened cases for tube C22J1.

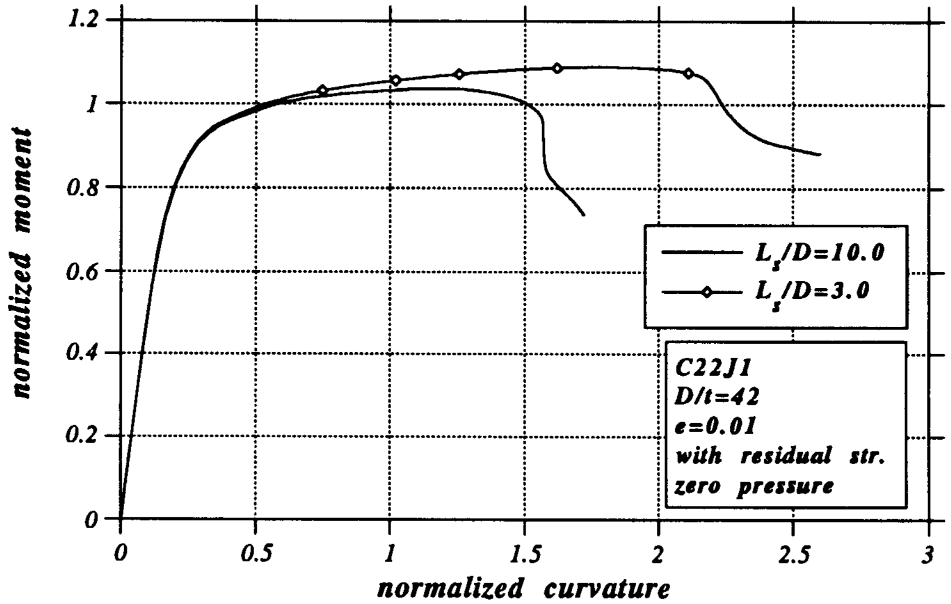

Figure 6.3: Moment-curvature curves of tube C22J1 for $L_s/D = 3.0$ and $L_s/D = 10.0$.

to 0.01. It is interesting to note that initial out-of-roundness affects bending at all pressure levels, whereas the effects of residual stresses are apparent only at high pressure levels.

In Figure 6.2, the pressure-moment interaction curve of the stiffened tube is compared with the corresponding interaction curve of the unstiffened tube, reported in Chapter 3. The difference between the two curves is very pronounced for high pressure levels. In fact, stiffeners permit the use of tube C22J1 for pressure levels above 50% of the yield pressure p_y. For this tube, the yield pressure p_y is equal to $2731\,psi$ and, therefore, approximately half of this pressure corresponds to the design pressure for $3000\,ft$. On the other hand, the use of unstiffened tubes is limited to considerably smaller depths.

Ring-stiffeners do not have an important influence on the ultimate moment capacity at low pressure levels. Recall that the value of the ultimate moment depends primarily on the properties of the unstiffened cross-section and the yield stress σ_y. However, the presence of stiffeners prevents extensive ovalization and results in more "ductile" behavior. In this case, the moment increase is about 7%. Figure 6.3 compares the moment-curvature diagram under zero pressure for L_s/D equal to 3.0 with the corresponding diagram of the "unstiffened" case ($L_s/D = 10.0$) presented in Chapter 3. Clearly, the ultimate moment for the stiffened tube occurs at a larger value of curvature and is followed by a relatively less sharp drop in capacity than for the unstiffened tube. Figures 6.4 and 6.5 show the stiffened tube shape after buckling. Apparently, the buckle about the middle cross-section is responsible for the sudden drop of the curve. Note that the buckle of the pressurized bending case is smoother and deeper than the buckle of the pure bending case, because of the presence of pressure. More specifically, external pressure flattens the cross-section, increases ovalization and contributes to an "ovalization" instability rather than a "kink-type" of buckling. It should be noted that, for a stiffened tube, the curvature is not constant along the tube and, therefore, the ratio of the relative rotation between two stiffener sections over the stiffener spacing is used as a measure of curvature. This parameter is normalized by the characteristic curvature value ($k_I = t/D^2$).

Figure 6.6 shows the response under three levels of pressure. The effects of pressure on the value of the ultimate moment are not very pronounced. However, the presence of pressure reduces the ductility of the member significantly . Recall that a similar trend was observed in Chapter 3, where the unstiffened tube was analyzed under various pressure levels (see Figure 3.17).

Finally, the derived interaction curve for nonzero residual stress and imperfection $e = 0.01$ is compared with the API interaction formula D.3.3-1 in Figure 6.7. This formula is based on the total energy failure theory and concerns the capacity of tubes under tension, bending and pressure. In the absence of tension, formula D.3.3-1 may be written as follows:

$$A^2 + B^{2\eta} + 2\nu AB = 1.0 \tag{6.1}$$

where

$$A = \frac{M_{n1} + \sigma_{ce} S}{M_n} \tag{6.2}$$

$$B = \frac{p}{p_{hc}} \tag{6.3}$$

M_{n1} is the moment capacity under pressure, σ_{ce} is the capped-end stress, S is the elastic section modulus and η is the inelastic exponent specified by

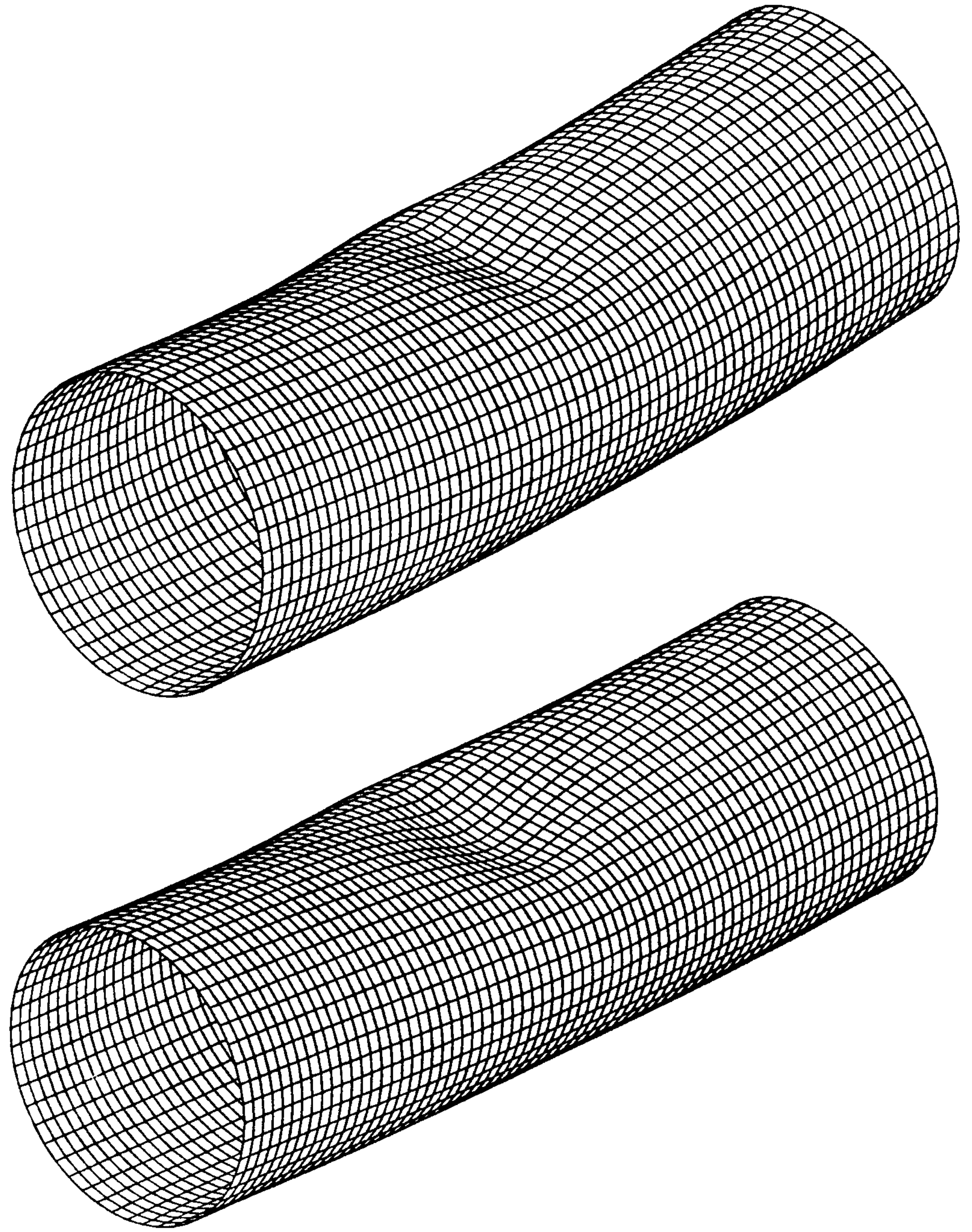

Figure 6.4: Buckled shapes of tube C22J1 ($L_s/D = 3.0$); pure bending (top) and bending with $p/p_y = 0.183$ (bottom).

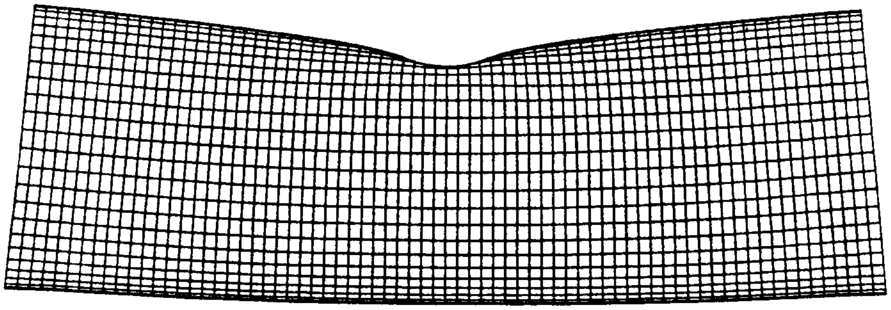

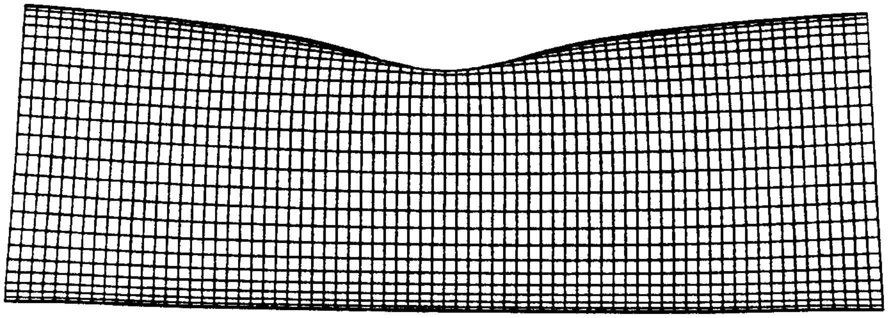

Figure 6.5: Buckled shapes of tube C22J1 ($L_s/D = 3.0$); pure bending (top) and bending with $p/p_y = 0.183$ (bottom).

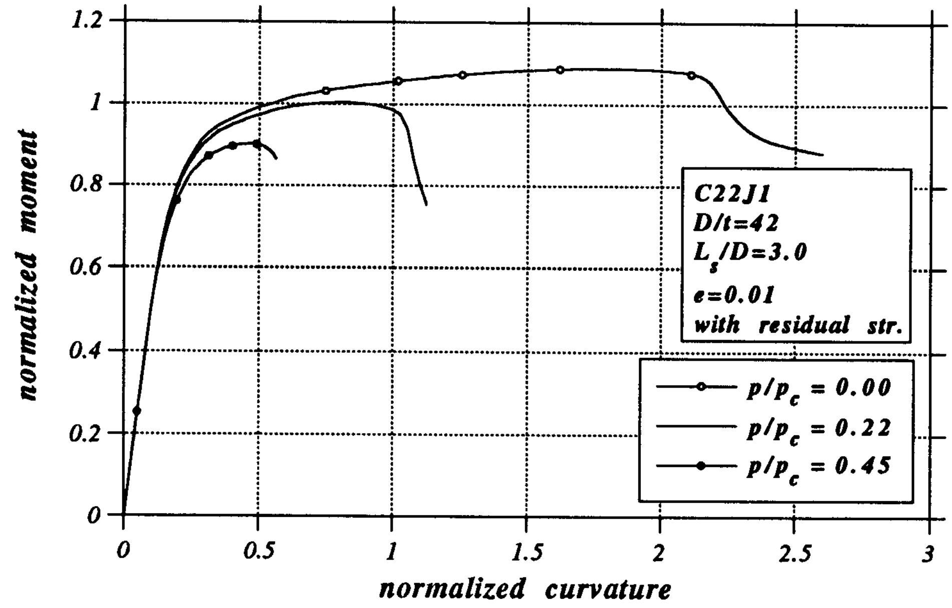

Figure 6.6: Bending-moment curves for three levels of pressure (tube C22J1, $L_s/D = 3.0$, $p_c = 2236\,psi$).

Equation 5.9. Obviously, the specification curve is rather conservative when compared with the analytical results. However, it has been shown in Chapter 3 that the ultimate moment for relatively thick tubes with significant strain hardening is usually higher than the fully-plastic moment M_p. In the case of stiffened tubes, this phenomenon is more pronounced because of the additional stiffness provided by the stiffener. It is therefore necessary that the API formula for pure bending (Equation 3.10) be revised in order to account for the beneficial effects of strain hardening and stiffeners. In Chapter 5, it was pointed out that the API equation for pure pressure, Equation 5.3, does not take into account the beneficial effects of internal stiffeners and capped-end compression and, therefore, underestimates the ultimate pressure capacity. A more accurate prediction of these two points would result in better agreement

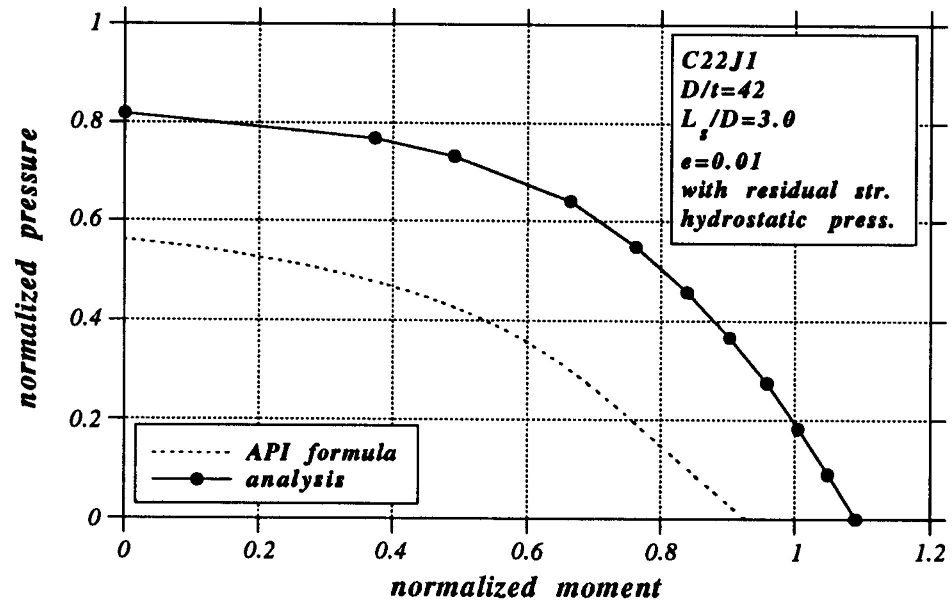

Figure 6.7: Comparison of interaction curve for C22J1 with API formula ($L_s/D = 3.0$).

between the two curves.

6.1.2 CBI Stub Column Tests

Although there are no experimental data for pressurized stiffened tubes under bending, the CBI experiments on stub columns [17] can be used towards better understanding of tube behavior. These experiments concern the capacity of short tubes ($L/D = 3.0$) under combined loading. For the purposes of the present work, the specimens under bending and external pressure are considered. In these tests, the end-sections of the specimens are welded on rigid plates. Therefore, each specimen may be regarded as a panel of a long stiffened tube, whose stiffeners remain practically undeformed.

All specimens have nominal outside diameter equal to 8 *in*, length equal to 24 *in* and they are classified in four groups according to their diameter-to-thickness ratio. Herein, tubes from Groups 1, 2 and 3, with D/t values of 32.0, 42.4 and 58.8 respectively, are analyzed. Group 4 includes very thin tubes which are not of immediate interest. The geometric and material properties of the tubes are shown in Table 6.1 and the material curves are depicted in Figures 6.8, 6.9, 6.10, 6.11 and 6.12. All tubes are assumed to have residual stresses and, for each tube, the initial out-of-roundness reported in the CBI report [17] is used.

In order to be consistent with the experimental procedure, the pressure is first raised up to a prescribed value. Then, keeping the pressure constant, the tube is subjected to bending until collapse. Specimens 1-13 and 2-13 are subjected to hydrostatic pressure. All other specimens have radial pressure. Results for Groups 1, 2 and 3 are presented in Tables 6.2, 6.3 and 6.4, together with the experimental data. In graphical form, the results are presented in Figures 6.13, 6.14 and 6.15, and compared with the predictions of the specification formula (Equation 6.1). Note that tubes 1-BC, 1-12 and 1-13 have a higher yield stress and, therefore, an average yield stress of 37.12 *ksi* is used for plotting the specification equation. In general, the experimental data are in good agreement with the numerical predictions. On the other hand, the specification predictions underestimate the ultimate capacity. It is interesting to note that for low values of pressure, the specification predictions are very conservative with respect to both experiments and analysis. It was mentioned earlier, that the API rules do not account for strain hardening or for the beneficial effects of end restraints. These two reasons explain the conservativeness of the specification formula for bending capacity.

specimen	1	2	3
D (in)	8.0	8.0	8.0
L (in)	24.0	24.0	24.0
t (in)	0.250	0.1887	0.136
D/t	32.0	42.4	58.8
M	24.4	28.0	32.8
σ_y (ksi)	34.8/40.9	37.9	41.1
E $(10^3\,ksi)$	30.6/29.0	29.7	29.0

Table 6.1: Geometric and material properties of tubes analyzed (CBI stub column tests).

specimen	exp-press. (psi)	exp-mom. $(k - in)$	num-press. (psi)	num-mom. $(k - in)$
1-BC	0	721.7	0	668.7
1-12	968	654.5	968	597.0
1-07	1704	288.6	1074	313.8
1-01	2131	0.0	2198	0.0
1-13	2344	0.0	2595	0.0

Table 6.2: Experimental data and analytical results for Group 1.

specimen	exp-press. (psi)	exp-mom. $(k - in)$	num-press. (psi)	num-mom. $(k - in)$
2-02	0	565.0	0	491.1
2-12	600	474.3	600	432.6
2-07	1199	284.9	1199	308.1
2-01	1500	0.0	1682	0.0
2-13	1649	0.0	1793	0.0

Table 6.3: Experimental data and analytical results for Group 2.

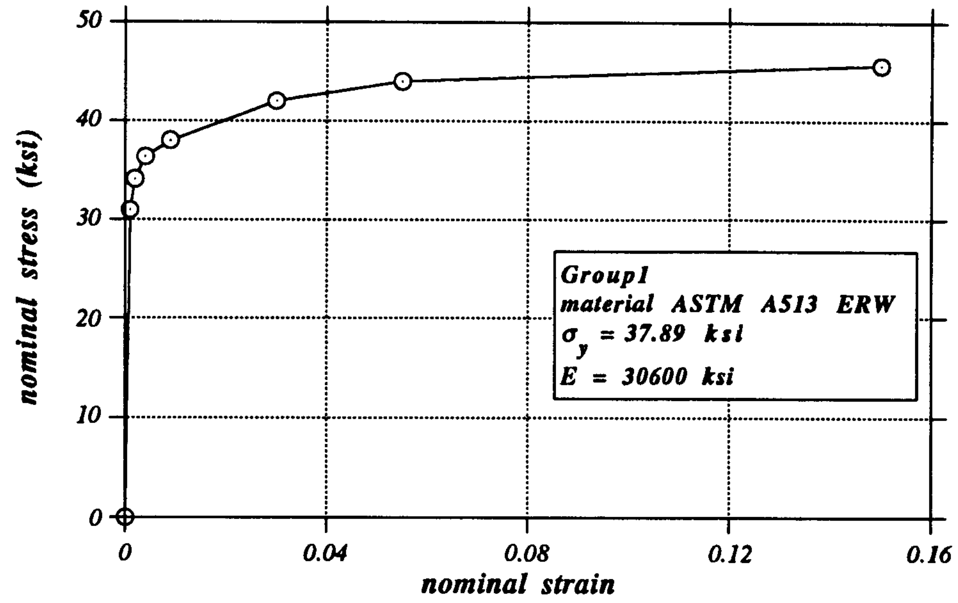

Figure 6.8: Material curve for specimens 1-01, 1-02 and 1-07 (Group 1).

specimen	exp-press. (psi)	exp-mom. ($k-in$)	num-press. (psi)	num-mom. ($k-in$)
3-02	0	391.1	0	385.0
3-12	375	362.6	375	338.6
3-07	750	250.1	750	271.2
3-01	937	0.0	1089	0.0

Table 6.4: Experimental data and analytical results for Group 3.

Figures 6.16 and 6.17 show the post-buckling shapes of specimens 2-13 and 3-12. Note that the buckle of specimen 3-12 is not as sharp as the buckles shown in previous graphs for pure bending. Clearly, the presence of external pressure is responsible for this phenomenon (see also Figures 6.4 and 6.5).

In order to investigate the effects of strain hardening, tubes of

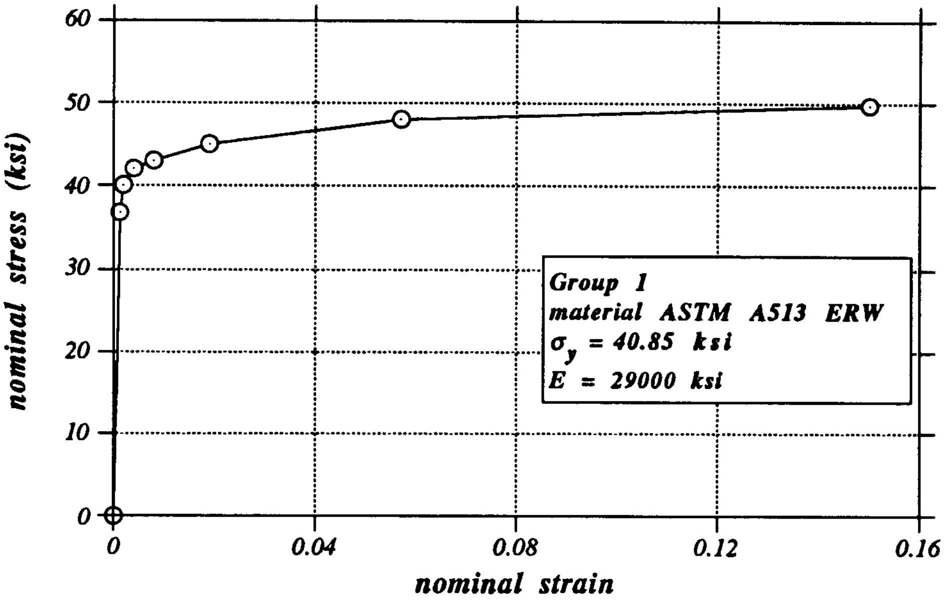

Figure 6.9: Material curve for specimens 1-12, and 1-13 (Group 1).

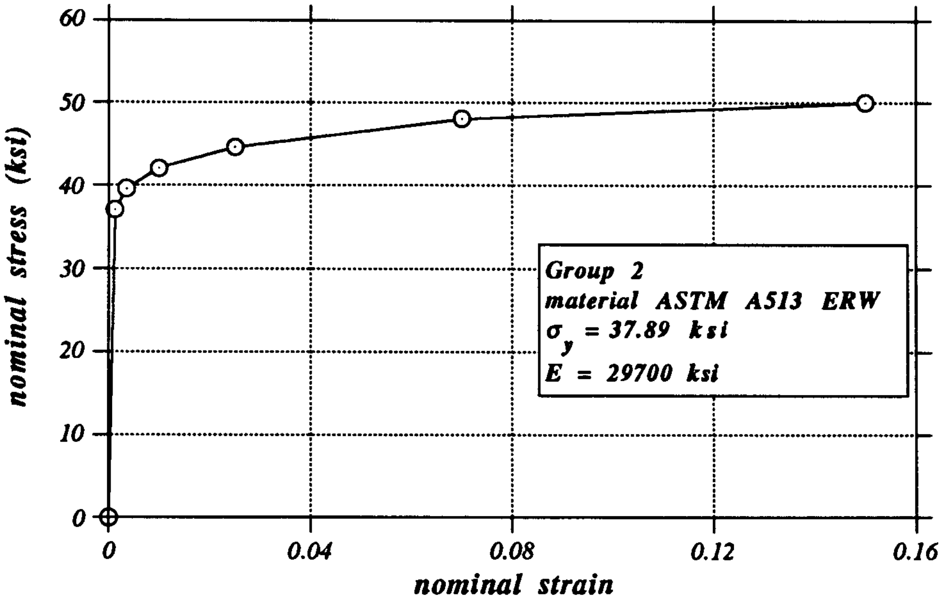

Figure 6.10: Material curve for specimens of Group 2.

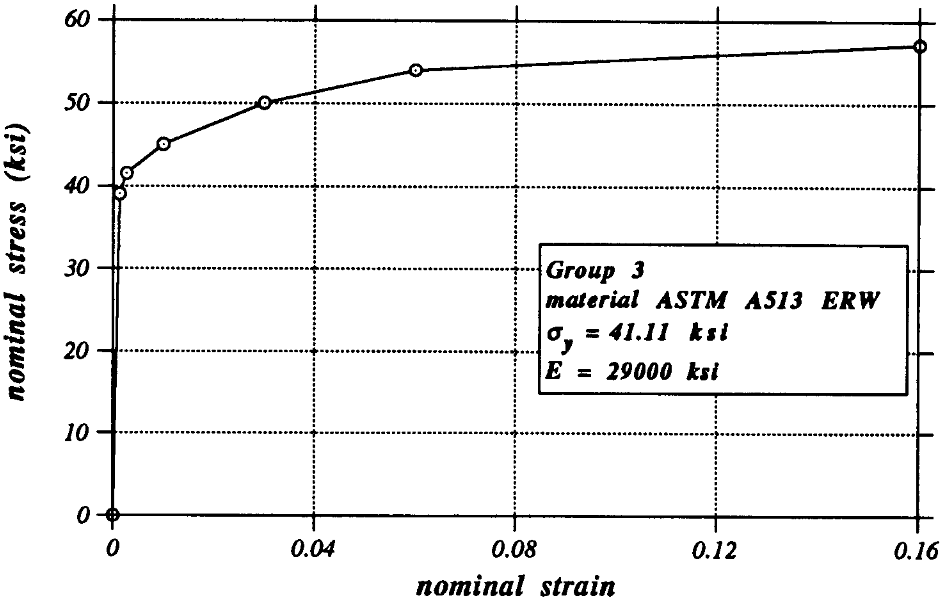

Figure 6.11: Material curve for specimens of Group 3.

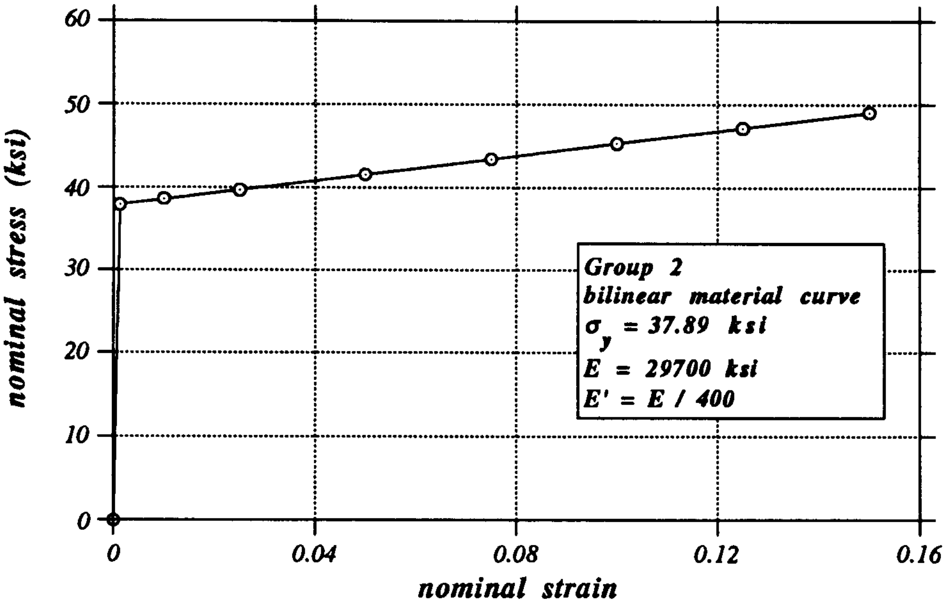

Figure 6.12: Bilinear material curve for specimens of Group 2.

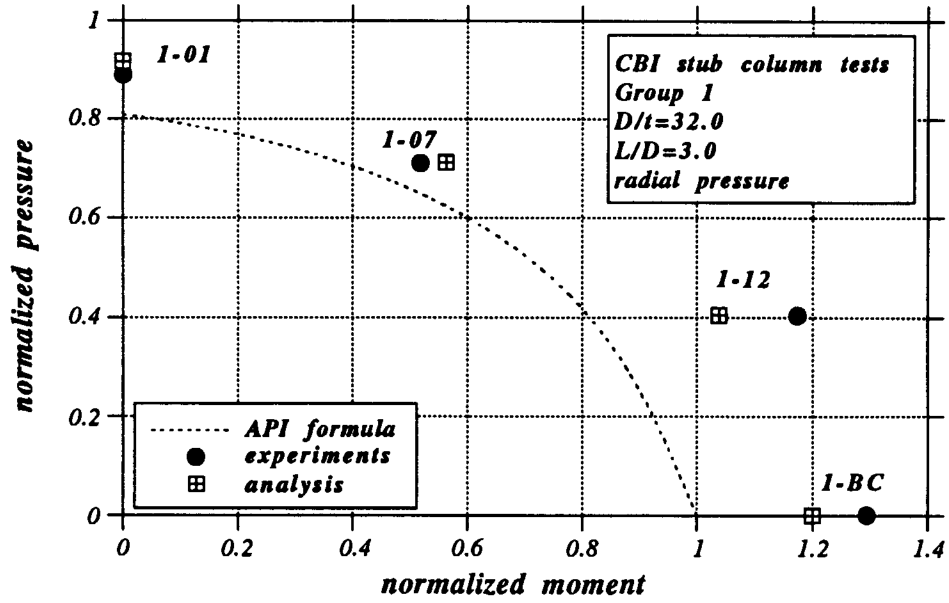

Figure 6.13: Comparison between experimental data and analytical results (Group 1).

Group 2 are reanalyzed using a bilinear material curve with a post-yielding modulus equal to $E/400$ (see Figure 6.12). In Table 6.5, the results are compared with those obtained using the material curve of Figure 6.10, which has substantial strain hardening. Apparently, there is a difference between the two sets of results which is more pronounced for small values of pressure. Recall that for low pressure levels, tubes exhibit a “ductile” bending response involving large strains and, consequently, strain hardening is an important factor in determining their ultimate capacity. On the other hand, the response is almost independent of strain hardening for hydrostatic and radial pressure loading.

The specification rules somewhat underestimate the ultimate pressure capacity. In the present experiments, the end sections are welded to rigid plates and, therefore, they provide the highest possible stiffness against oval-

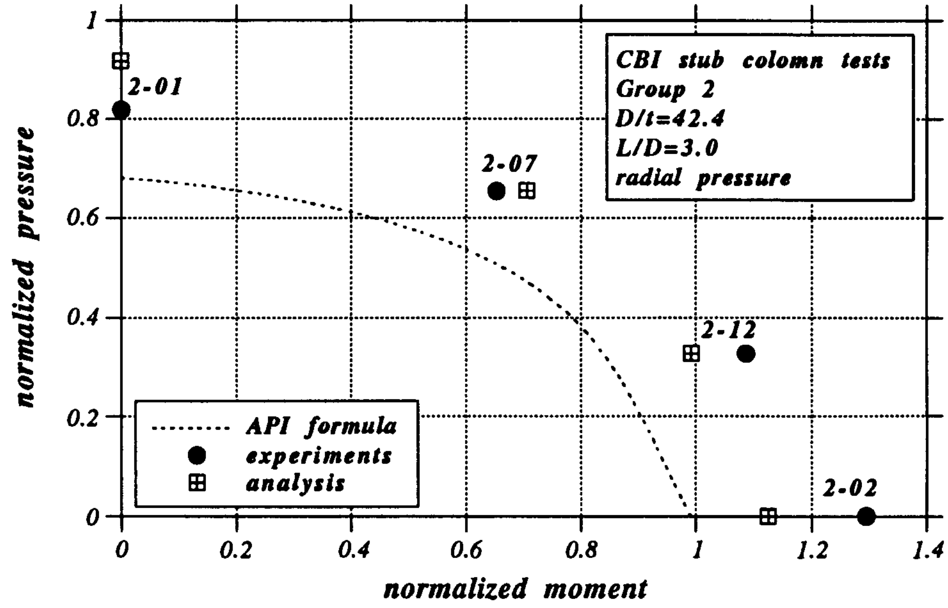

Figure 6.14: Comparison between experimental data and analytical results (Group 2).

ization. Tube 3-01 is reanalyzed, assuming that it is a single panel of a long stiffened tube. The stiffener radial and longitudinal dimensions were chosen equal to 0.75 *in* and 0.15 *in*, so that they just satisfy the stiffener-size requirement

$$I_c \geq \sigma_{he} \frac{t L_s D^2}{8E} \tag{6.4}$$

where I_c is the moment of inertia for the ring composite section. The ultimate capacity was calculated to be 883 *psi*, which is 18% below the capacity for undeformed end conditions (1089 *psi*). This result is a good reason for using the rather conservative API formula (Equation 5.3).

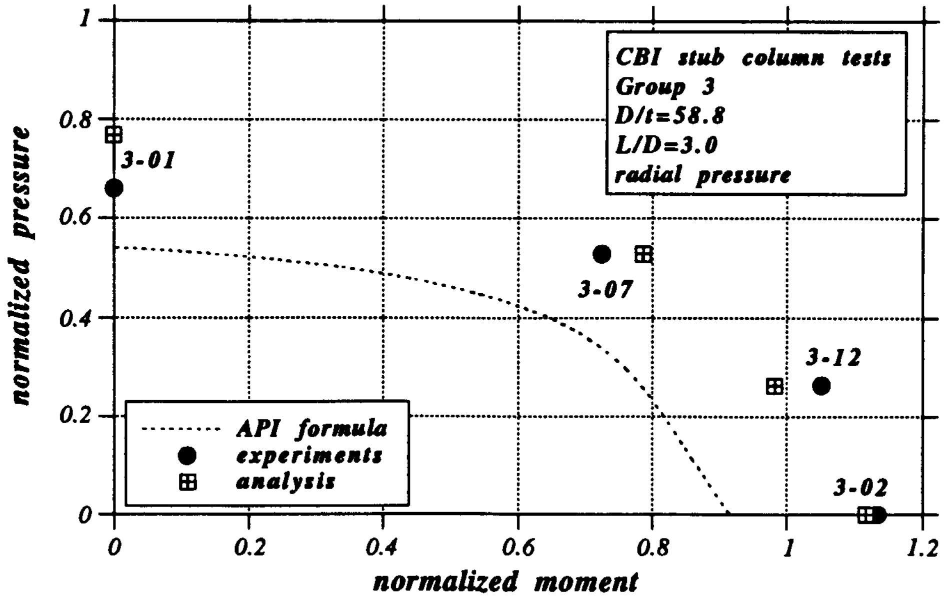

Figure 6.15: Comparison between experimental data and analytical results (Group 3).

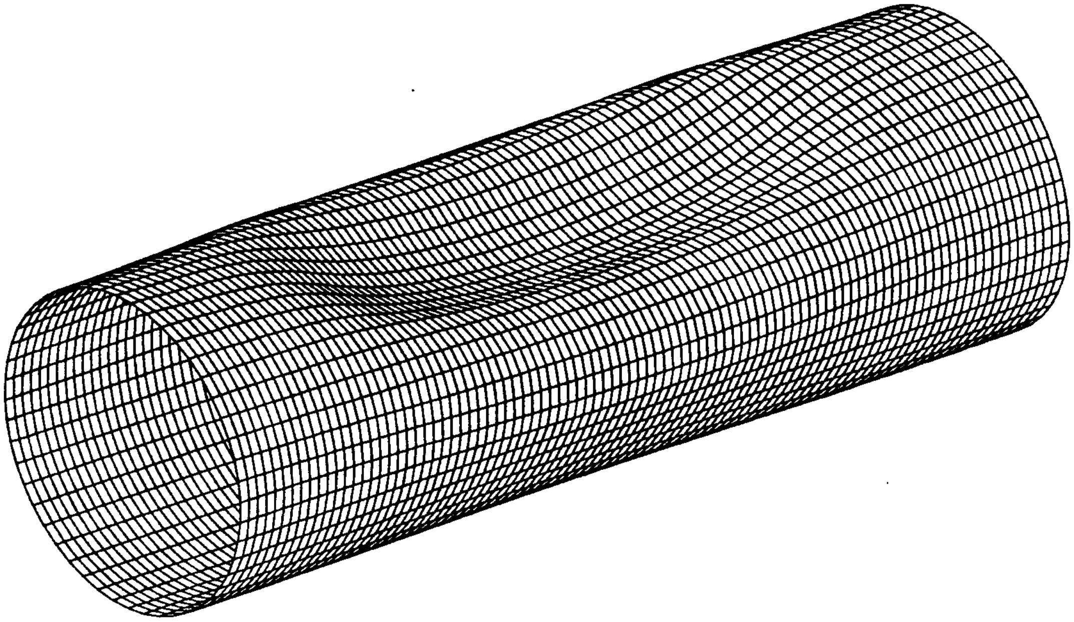

Figure 6.16: Post-buckling shape of specimen 2-13.

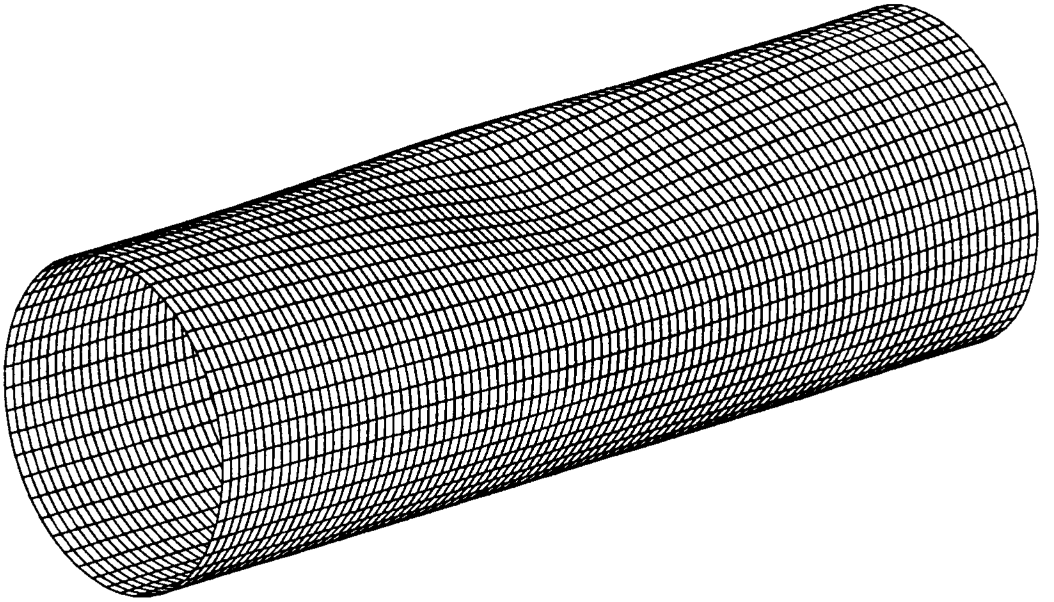

Figure 6.17: Post-buckling shape of specimen 3-12.

specimen	press. (psi)	moment $(k-in)$	press.$(E/400)$ (psi)	moment $(E/400)$ $(k-in)$
2-02	0	491.1	0	441.7
2-12	600	432.6	600	403.1
2-07	1199	308.1	1199	279.8
2-01	1682	0.0	1666	0.0
2-13	1793	0.0	1790	0.0

Table 6.5: Effects of strain hardening on ultimate capacity (Group 2 - analytical results).

Finally, both experiments and analysis indicate an increase in pressure capacity in the presence of capped-end compression and, consequently, the material behavior seems to follow the von Mises criterion rather than the Tresca yield theory. This important result was also observed in the first part of

Chapter 5 and justifies the use of the von Mises yield function in our analysis.

6.2 Axial Capacity in the Presence of Pressure

The axial capacity of tubes under external pressure is of major importance in the design of offshore platforms. Most of the vertical members of these structures are subjected to loading combinations where the uniform axial stress ranges from twice to four times the maximum bending stress [37].

The axial capacity of tubes under zero pressure is shown in Figure 6.18 for different values of the slenderness ratio. The tube is assumed to have the cross-sectional and material characteristics of tube C22J1. It should be noted that for zero pressure, the presence of stiffeners does not affect the axial capacity. Both circumferential and longitudinal residual stresses are assumed to be nonzero, whereas the initial out-of-roundness is chosen equal to the API allowable imperfection ($e_{lim} = 0.01$). For the initial out-of-straightness, a value of Δ equal to $1/4000$ is used. This value, although significantly smaller than the AISC allowable value ($\Delta_{lim} = 1/1000$), is a representative value for the specimens tested by CBI [15] and SwRI [57]. In fact, it has been reported in Ref. [58] that, generally, the initial out-of-straightness of fabricated tubes is considerably smaller than the AISC limit. In the same graph, the analytical results are compared with two specification formulas. The first formula is the well-known Bleich's parabola [7], also adopted by the API specification [5]:

$$P_{cr} = P_y \left(1 - 0.25\lambda^2\right) \tag{6.5}$$

On the other hand, the recent AISC-LRFD specification [3] proposes the following, more conservative, exponential formula:

$$P_{cr} = P_y \, 0.658^{\lambda^2} \tag{6.6}$$

The parabolic formula somewhat overestimates the capacity, whereas the exponential formula is in excellent agreement with the analytical results. A first reason for the unconservativeness of the parabolic formula might be the assumed distribution of residual stresses. Indeed, the use of a different distribution might increase the analytically computed axial capacity. However, besides the information reported in Refs. [14] and [45], there are no other measurements of residual stresses and, therefore, no attempt was made to adopt another residual stress distribution in the course of the present work. Furthermore, the estimation of the effective buckling length (KL) is, perhaps, another reason for the unconservative predictions of the parabolic formula [7], which is based on experimental data. End restraints, which may appear during testing, decrease the effective length and result in a higher experimental buckling load.

The effects of pressure on the axial capacity are not considered by the API specification rules [4] and [5]. It was pointed out in Chapter 3 that the effects of lateral pressure on the beam-column equation are canceled by the presence of capped-end compression. Of course, this argument is based on the assumption that the tube remains elastic with constant cross-section. However, stiffened tubes are designed for high levels of pressure and, therefore, inelastic behavior is expected to reduce the axial capacity.

In Refs. [21] and [35], several simplified formulas have been proposed to account for the pressure effects on the axial buckling load. However, they

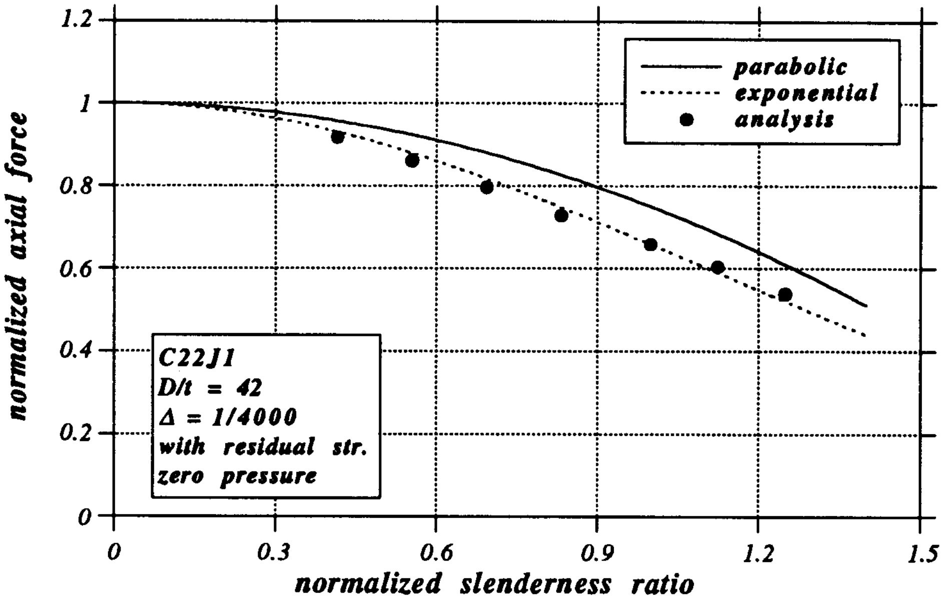

Figure 6.18: Buckling curve for tube C22J1; comparison with design equations.

have not yet been adopted by the specification. In order to present the background of these formulas, recall the general form of column-buckling equations:

$$\sigma_{cr} = \sigma_y f(\lambda) \tag{6.7}$$

where

$$\lambda = \frac{KL}{r}\sqrt{\frac{\sigma_y}{\pi^2 E}} \tag{6.8}$$

is the normalized slenderness ratio, or, equivalently,

$$\sigma_{cr} = \frac{E_T}{E}\sigma_e \tag{6.9}$$

where

$$\sigma_e = \frac{\pi^2 E}{(KL/r)^2} \tag{6.10}$$

is the stress corresponding to the Euler buckling load and E_T is the tangent modulus. A first approach to account for pressure effects would be the use of

Equation 6.7 with a modified yield stress and the method will be referred to as the "modified yield stress method". More specifically, the axial stress is equal to

$$\sigma_x = \sigma_a + \sigma_{ce} \tag{6.11}$$

where σ_a is the applied axial stress and σ_{ce} is the capped-end compressive stress. Note that from simple statics,

$$\sigma_h = \frac{pD}{2t} \tag{6.12}$$

and

$$\sigma_{ce} = \frac{pD}{4t} \tag{6.13}$$

Assume that the hoop stress is equal to $\alpha\sigma_y$ where α is a number between 0 and 1 indicating the level of external pressure with respect to the yield pressure. Then, the reduced yield stress σ_{y1} is given by

$$\sigma_y = F(\sigma_{y1} + 0.5\alpha\sigma_y, \alpha\sigma_y) \tag{6.14}$$

where $F(\sigma_x, \sigma_h)$ is the yield criterion of the material for biaxial state of stress. Using the von Mises yield criterion, the reduced yield stress is computed as follows:

$$\sigma_{y1} = \sigma_y\sqrt{1 - \frac{3\alpha^2}{4}} \tag{6.15}$$

On the other hand, the Tresca criterion results in the following equation:

$$\sigma_{y1} = \sigma_y\left(1 - \frac{\alpha}{2}\right) \tag{6.16}$$

In Ref. [21], the total energy criterion is also suggested. This criterion with a value of Poisson's ratio equal to 0.3 gives

$$\sigma_{y1} = \sigma_y\left(-0.2\alpha + \sqrt{4 - 3.76\alpha^2}\right) \tag{6.17}$$

In the general case, the reduced yield stress can be written as

$$\sigma_{y1} = m\sigma_y \tag{6.18}$$

where

$$m = m(\alpha) \tag{6.19}$$

and, hence, the modified slenderness ratio is

$$\lambda_1 = \frac{KL}{r}\sqrt{\frac{\sigma_{y1}}{\pi^2 E}} = \lambda\sqrt{m} \tag{6.20}$$

Consequently, the reduced axial capacity can be expressed as

$$\sigma_{cr1} = \sigma_{y1} f(\lambda_1) \tag{6.21}$$

Of course, the reduced buckling stress depends on the form of the function $f(\lambda)$. Using Bleich's parabola

$$\sigma_{cr1} = \sigma_{y1}(1 - 0.25{\lambda_1}^2) \tag{6.22}$$

and

$$\frac{\sigma_{cr1}}{\sigma_{cr}} = m\left(\frac{1 - 0.25m\lambda^2}{1 - 0.25\lambda^2}\right) \tag{6.23}$$

On the other hand, the exponential AISC-LRFD formula results in the following expressions

$$\sigma_{cr1} = \sigma_{y1}\, 0.658^{{\lambda_1}^2} \tag{6.24}$$

and

$$\frac{\sigma_{cr1}}{\sigma_{cr}} = m\, 0.658^{(m-1){\lambda_1}^2} \tag{6.25}$$

According to Loh [35], Equation 6.9 can also be used to account for pressure effects. Assuming Bleich's parabola, the tangent modulus at buckling can be written as follows:

$$E_T = 4\,E\,\frac{\sigma_{cr}}{\sigma_y}\left(1-\frac{\sigma_{cr}}{\sigma_y}\right) \tag{6.26}$$

In Ref. [35], Loh modifies the above expression assuming the Tresca yield criterion. Herein, Loh's idea is presented in a more general way, in order to encompass any yield criterion. More specifically, in the presence of pressure, the tangent modulus E_T is modified as follows

$$E_T = 4\,E\,\frac{\sigma_{cr}+\sigma_{ce}}{\sigma_{y1}}\left(1-\frac{\sigma_{cr}+\sigma_{ce}}{\sigma_{y1}}\right) \tag{6.27}$$

where σ_{ce} is the capped-end compressive stress and σ_{y1} is the modified yield stress due to pressure effects. The above consideration results in the following formula for the critical load in the inelastic range:

$$\sigma_{cr1} = 0.5\,\sigma_{y1}\left(A+\sqrt{A^2+4B}\right) \tag{6.28}$$

where

$$A = 1-\frac{\sigma_{y1}}{4\sigma_e}-\frac{2\sigma_{ce}}{\sigma_{y1}} \tag{6.29}$$

and

$$B = \frac{\sigma_{ce}}{\sigma_{y1}}\left(1-\frac{\sigma_{ce}}{\sigma_{y1}}\right) \tag{6.30}$$

Thus, the reduction in axial capacity can be written as

$$\frac{\sigma_{cr1}}{\sigma_{cr}} = \frac{\sigma_{y1}}{\sigma_y}\left[\frac{A+\sqrt{A^2+4B}}{2(1-0.25\lambda^2)}\right] \tag{6.31}$$

In the above equations, σ_{y1} depends on the assumed yield function. Using Tresca's criterion,

$$\sigma_{y1} = \sigma_y \tag{6.32}$$

whereas, the adoption of the von Mises criterion results in

$$\sigma_{y1} = 0.5\sigma_y \left(\alpha + \sqrt{4 - 3\alpha^2}\right) \tag{6.33}$$

where α indicates the level of the applied hoop stress with respect to the yield stress ($\alpha = \sigma_h/\sigma_y = p/p_y$).

The previous idea results in a closed-form expression for the parabolic buckling curve. However, it can be applied to any buckling curve. For example, the adoption of the exponential AISC-LRFD formula results in the following equation for the tangent modulus at buckling:

$$E_T = E(-2.724)\left(\frac{\sigma_{cr}}{\sigma_y}\right)\left[ln\left(\frac{\sigma_{cr}}{\sigma_y}\right)\right] \tag{6.34}$$

In the presence of pressure,

$$E_T = E(-2.724)\left(\frac{\sigma_{cr} + \sigma_{ce}}{\sigma_{y1}}\right)\left[ln\left(\frac{\sigma_{cr} + \sigma_{ce}}{\sigma_{y1}}\right)\right] \tag{6.35}$$

Therefore,

$$\sigma_{cr} = (-2.724)\left(\frac{\sigma_{cr} + \sigma_{ce}}{\sigma_{y1}}\right)\left[ln\left(\frac{\sigma_{cr} + \sigma_{ce}}{\sigma_{y1}}\right)\right]\sigma_e \tag{6.36}$$

where

$$\sigma_{y1} = m(\alpha)\,\sigma_y \tag{6.37}$$

and

$$\sigma_{ce} = \frac{\alpha}{2}\sigma_y \tag{6.38}$$

Equation 6.36 cannot be solved in closed form but, instead, a numerical procedure should be employed.

Two stiffened tubes with the cross-sectional and material characteristics of tube C22J1 are analyzed. The slenderness ratios (KL/r) of these tubes are chosen equal to 50 and 72 and, therefore, the tubes will be referred to as C22J1_50 and C22J1_72 respectively. Note that two similar unstiffened beam-columns were analyzed in Chapter 3. The tubes have an initial out-of-roundness e equal to 0.01 and residual stresses according to the distributions proposed by Chen and Ross [14]. The stiffeners are *internal*, their dimensions are the same as those employed in the first part of Chapter 5 ($t' = 1.00\,in$, $h = 0.145\,in$) and the stiffener spacing parameter L_s/D is equal to 1.92 and 2.77 for tubes C22J1_50 and C22J1_72 respectively. For the initial out-of-straightness, a value of Δ equal to 1/4000 is used for both tubes.

Consistently with all previous results for stiffened tubes, deformation parameters up to the eighth degree are included. In addition, the element size is assumed equal to 18% of the tube diameter D for the central panel, and 60% of D for the other panels. Obviously, the maximum deformation occurs at the central panel because of $P - \Delta$ effects. Table 6.6 shows the analytically calculated ultimate pressure for tubes C22J1_50 and C22J1_72.

tube	max. press. (psi)	yield press. (psi)
C22J1_50	2648.4	2730.6
C22J1_72	2325.8	2730.6

Table 6.6: Maximum (collapse) pressure and yield pressure for tubes C22J1_50 and C22J1_72.

In Figure 6.19, the reduction of axial load capacity for tube C22J1_50 is compared with three reduction formulas. The variable on the vertical axis is the ratio of the axial capacity P_c at a certain pressure level over the axial capacity P_{co} for zero pressure. As expected, the analytical results are in very

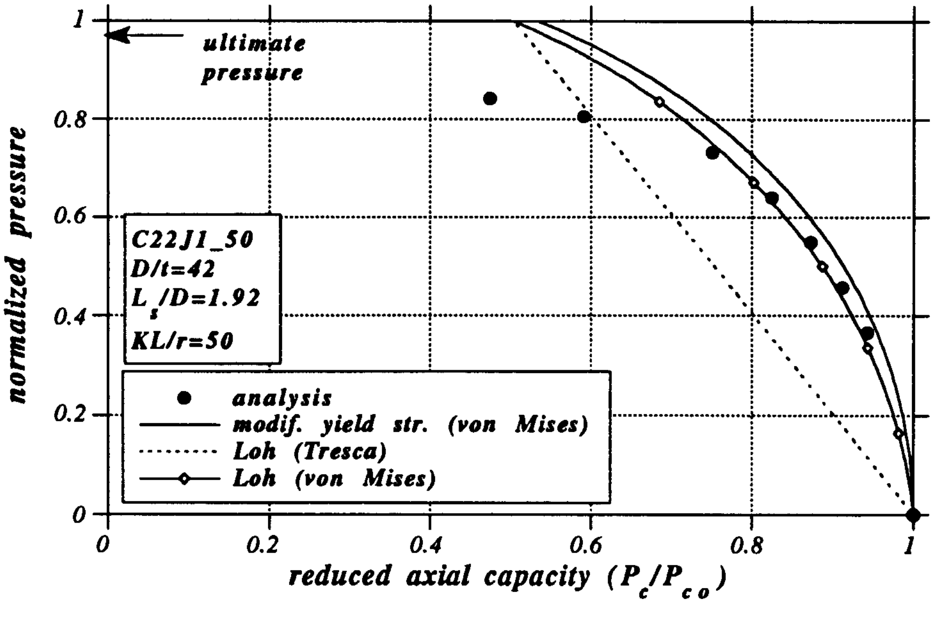

Figure 6.19: Effects of pressure on axial capacity for tube C22J1

good agreement with Loh's method employing the von Mises yield criterion. In addition, good predictions are obtained by the modified yield stress method with the von Mises equivalent stress. Recall that our analysis is also based on the von Mises yield criterion, which suggests an increase in axial yield stress in the presence of hoop compression. On the other hand, Loh's method with Tresca yield criterion predicts substantially lower axial capacity. Nevertheless, the analytical results deviate from the simplified formulas for pressure levels near the collapse pressure of the tube which is, usually, less than the yield pressure.

The same trend appears in Figure 6.20, where the analytical results for tube C22J1_72 are compared with those obtained from three simplified formulas. Again, Loh's method with the von Mises criterion is in close agreement

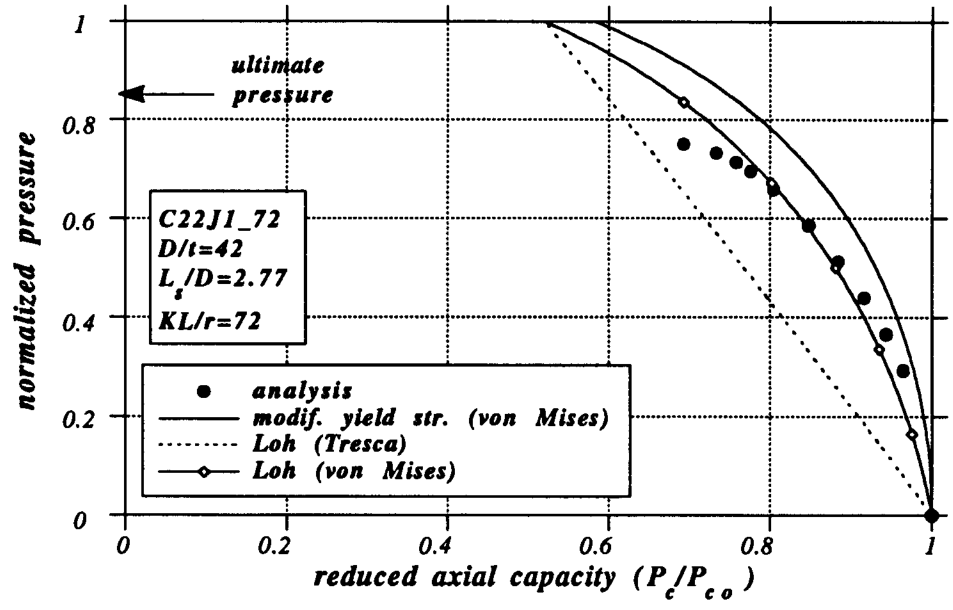

Figure 6.20: Effects of pressure on axial capacity for tube C22J1

with the present calculations and the analytical results begin to deviate from the simplified formulas as the pressure level approaches the collapse pressure of the tube.

6.3 Analysis of Stiffened Beam-Columns

In this section, the effects of external pressure on the beam-column stability of stiffened tubes are examined. The tubes are analyzed under the assumption of nonzero residual stresses and initial out-of-roundness equal to the API allowable value ($e = 0.01$). For the initial out-of-straightness a value of Δ equal to 1/4000 is used.

Before presenting the analytical results, it is necessary to summarize the API specification provisions for beam-column stability. For axial, bending and hoop loading interaction, three requirements must be satisfied. First, the global stability criterion expressed through the well-known stability equation with amplification factor as well as the cross-sectional strength criterion must be met:

$$\frac{P}{P_{cr}} + \frac{M}{(1 - P/P_e)M_n} = 1 \tag{6.39}$$

and

$$cos\left(\frac{\pi}{2}\frac{P}{P_{xc}}\right) = \frac{M}{M_n} \tag{6.40}$$

These two criteria can be found in API-LRFD rules as formulas D.3.2-1 and D.3.2-2 respectively. However, they concern only structural loads and are independent of external pressure. To account for pressure effects the specification requires that the applied external pressure be less than the ultimate pressure p_{hc} given by Equation 5.3.

In order to account for the interaction of pressure and structural loads, the following local interaction equation must be satisfied:

$$\left(\frac{\sigma_x - 0.5\sigma_{hc}}{\sigma_{xe} - 0.5\sigma_{hc}}\right) + \left(\frac{p}{p_{hc}}\right)^2 = 1 \tag{6.41}$$

where σ_x is the total axial compressive stress (including capped-end compression), and

$$\sigma_{xe} = 0.6\,E\left(\frac{t}{D}\right) \tag{6.42}$$

is the elastic local-buckling axial stress.

It is interesting to note that, for D/t less than 60, σ_{xe} is very large and Equation 6.41 may be neglected. In addition, P_{xc} is equal to the yield load P_y, whereas P_{cr} is always smaller than P_y. Therefore, Equation 6.40 may be neglected and, hence, the global criterion of Equation 6.39 together with the hydrostatic pressure requirement of Equation 5.3 govern design.

Consequently, according to the new API-LRFD rules, beam-column design is not affected by the presence of external pressure provided that the pressure is below the ultimate pressure of the member. However, it has been shown previously that, in the cases of pure compression and pure bending, the presence of pressure decreases the capacity. It is possible to account for pressure effects on beam-columns by replacing P_{cr} and M_n in Equation 6.39 by P_{cr1} and M_{n1} which depend on the level of pressure. The value of the reduced axial capacity P_{cr1} can be estimated using one of the reduction formulas presented in the previous section. On the other hand, the value of the interaction curve on the horizontal axis M_{n1} (i.e. the ultimate moment in the presence of pressure) can be calculated through Equation 6.1. Consequently, the beam-column equation becomes

$$\frac{P}{P_{cr1}} + \frac{M}{(1 - P/P_e)M_{n1}} = 1 \qquad (6.43)$$

In Figure 6.21, the beam-column interaction curve for the stiffened tube C22J1_50 is compared with the interaction curve presented in Chapter 3 for the unstiffened case. For both curves zero pressure is assumed and their only difference is the presence of stiffeners. The two curves show identical results, indicating that stiffeners do not have any significant effect on beam-column capacity for zero external pressure.

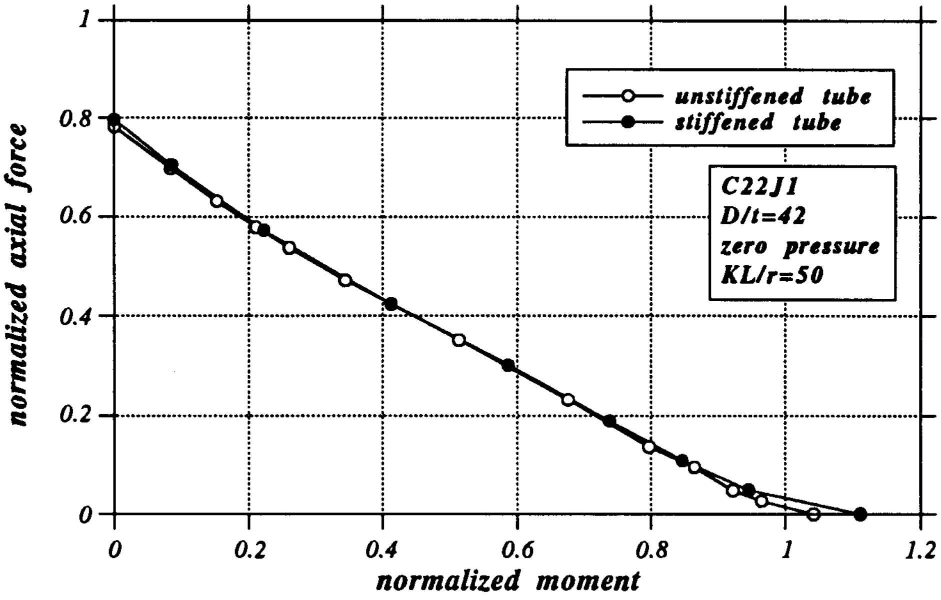

Figure 6.21: Effects of ring stiffeners on beam-column capacity for zero pressure (tube C22J1).

tube	max. press. (*psi*)	yield press. (*psi*)	analysis press. level (*psi*)
C22J1_50	2648.4	2730.6	1500.0
C22J1_72	2325.8	2730.6	1400.0

Table 6.7: Maximum pressure, yield pressure and analysis pressure level for tubes C22J1_50, C22J1_72.

In Figure 6.22, the effects of pressure on the response of beam-columns C22J1_50 and C22J1_72 are shown. For both tubes, the interaction curves for zero pressure are compared with the interaction curve for pressure equal to about 55% of the yield pressure. It is obvious that the presence of pressure reduces the ultimate capacity.

In the first graph of Figure 6.23, the analytical results for tube

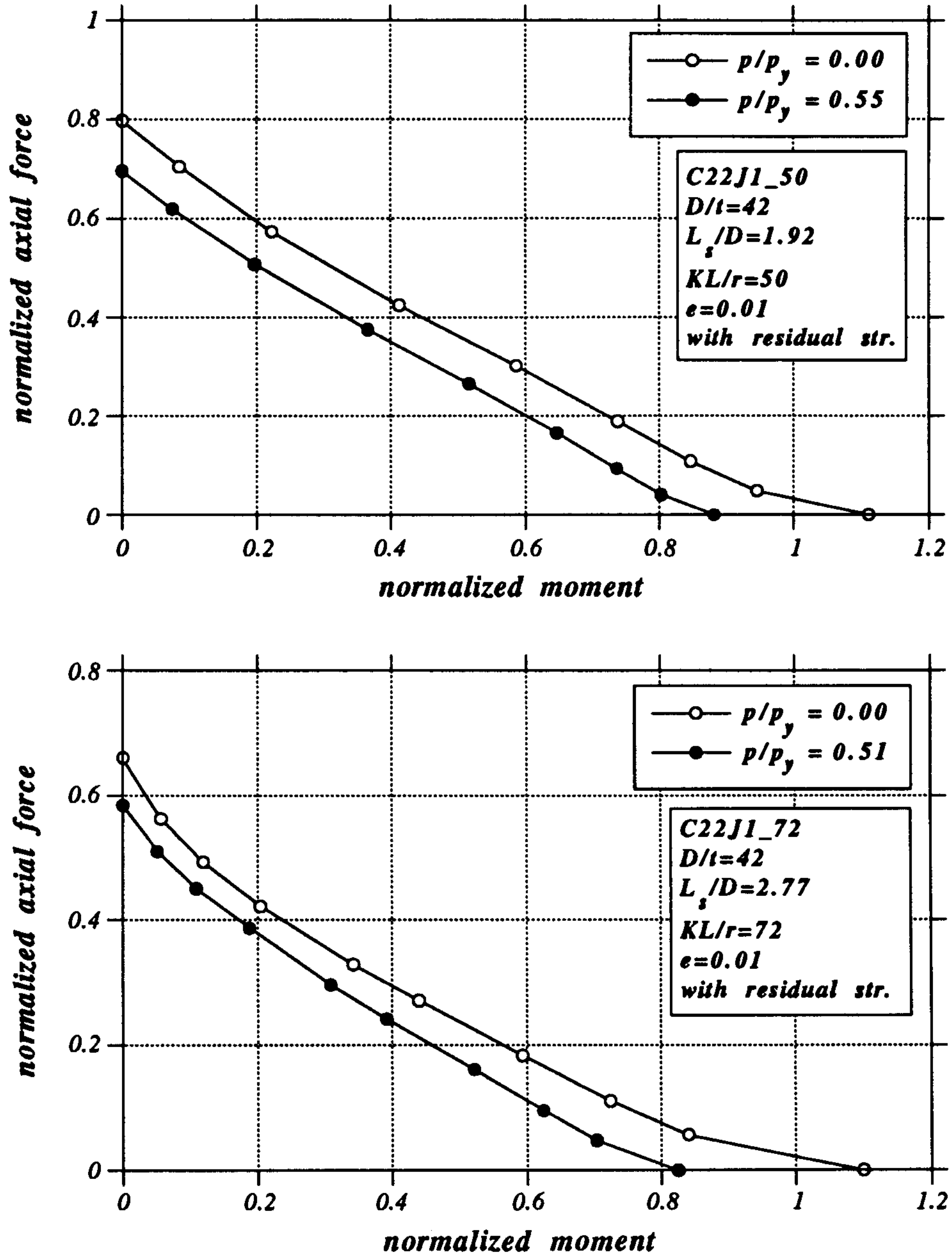

Figure 6.22: Effects of pressure on beam-column capacity of tubes C22J1_50 and C22J1_72.

C22J1_50 for zero pressure are seen to compare well with the AISC-LRFD formula 3.17. In the second graph of Figure 6.23, the interaction curve of tube C22J1_50 for pressure equal to 1500 *psi* ($p/p_y = 0.55$), is compared with Equation 6.43, where P_{cr1} is calculated through Equations 6.6 and 6.31 and M_{n1} from Equation 6.1. The comparison appears to be very good for axially dominant loading cases but very conservative for loading cases with substantial bending. The conservativeness of Equation 6.1 is responsible for the underestimation of bending capacity under high pressure levels. This phenomenon was also detected in Section 6.1. Figure 6.24 implies similar behavior for tube C22J1_72, which is a longer tube with a spacing parameter L_s/D equal to 2.77. This tube is analyzed for zero pressure as well for pressure equal to 1400 *psi* ($p/p_y = 0.51$). Again, note the conservative predictions of the specification formula for pressurized bending. Obviously, a better prediction of M_{n1} would result in a more accurate interaction curve.

For the sake of completeness, three slender tubes suggested by P. W. Marshall and C. D. Edwards [37] are also analyzed. The geometric characteristics of these tubes are given in Table 6.8.

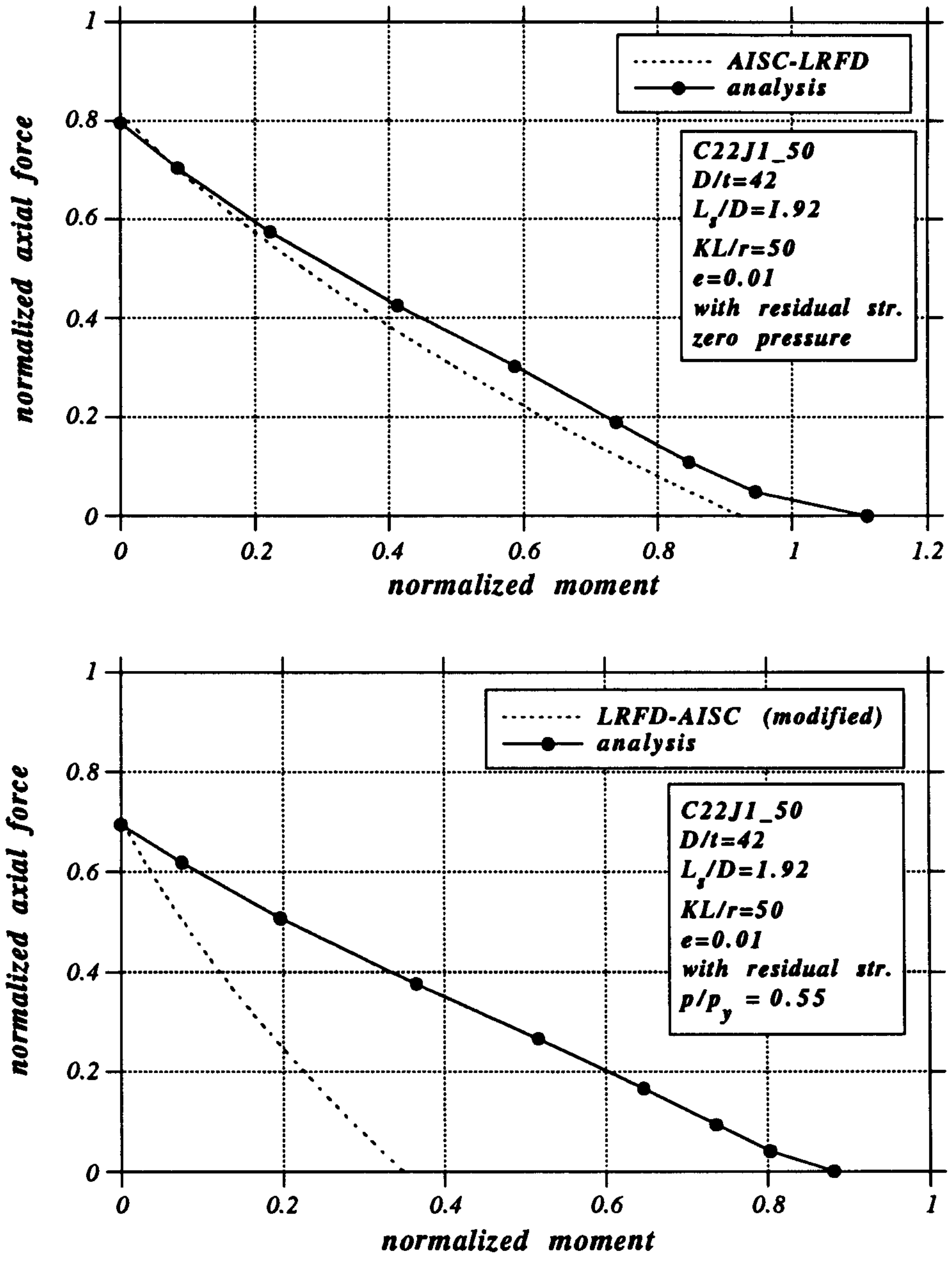

Figure 6.23: Analytical results for tube C22J1_50; comparison with design equations.

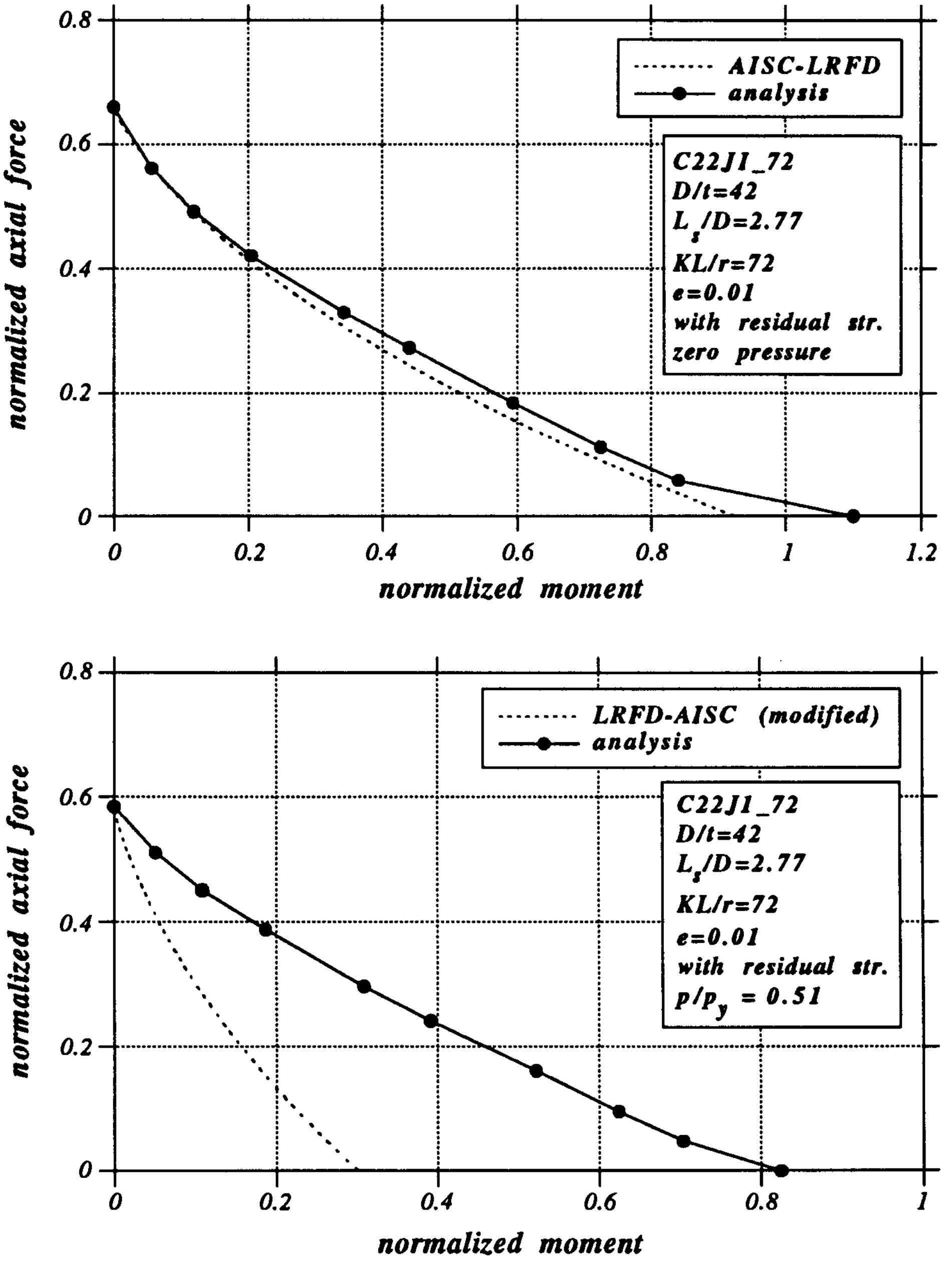

Figure 6.24: Analytical results for tube C22J1_72; comparison with design equations.

tube	SP1	SP2	SP3
$D\,(in)$	108.0	56.0	46.0
$t\,(in)$	2.375	1.625	1.125
$L\,(in)$	2040	1740	1020
$L_s\,(in)$	120	174	85
$t'\,(in)$	15.5	10.0	7.0
$h\,(in)$	1.125	0.625	0.500
L_s/D	1.11	3.11	1.85
KL/r	53.43	87.88	62.71
D/t	45.5	34.5	40.9

Table 6.8: Geometric properties of tubes SP1, SP2 and SP3.

tube	max. press.	yield press.	press. level
SP1	2890.0	2637.4	1180.0
SP2	3019.6	3478.3	1275.0
SP3	2975.3	2934.0	1222.0

Table 6.9: Maximum pressure, yield pressure and analytical pressure level for tubes SP1, SP2 and SP3.

In order to describe the material behavior of these tubes, a bilinear stress-strain curve is used, with yield stress of 60 ksi, Young's modulus of 29000 ksi and post-yielding modulus equal to $E/400$. This material curve does not have significant strain hardening and, therefore, results are expected to be somewhat conservative. All three tubes have residual stresses and initial out-of-roundness e equal to 0.01. The ultimate capacity of these tubes is determined for zero pressure and for a pressure level of about 1200 psi. The interaction curves are

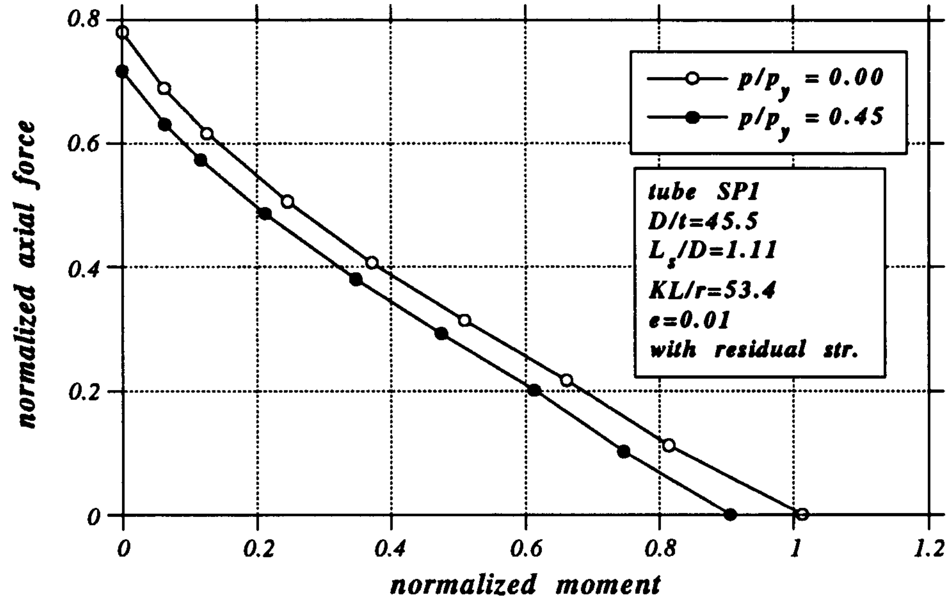

Figure 6.25: Effects of external pressure on beam-column capacity; tube SP1.

reported in Figures 6.25 - 6.30 and indicate the same trends observed in tubes C22J1_50 and C22J1_72.

It is interesting to mention that it was impossible to obtain a limit point for tubes SP1 and SP3 in the absence of axial force (i.e., the values of M_n and M_{n1}), due to convergence problems. In these cases, local buckling, rather than global instability, governs ultimate capacity. Tubes SP1 and SP3 have a very small spacing parameter ($L_s/D < 2$) and, apparently, this is the main reason for this phenomenon. Recall that convergence problems were encountered during the pure-pressure analysis of tube C22J1 for small values of L_s/D. An attempt was made to reanalyze these cases with more cross-sectional degrees of freedom and a finer mesh, without successful results. The "no axial force" points in Figures 6.25, 6.26, 6.29 and 6.30 (located on the

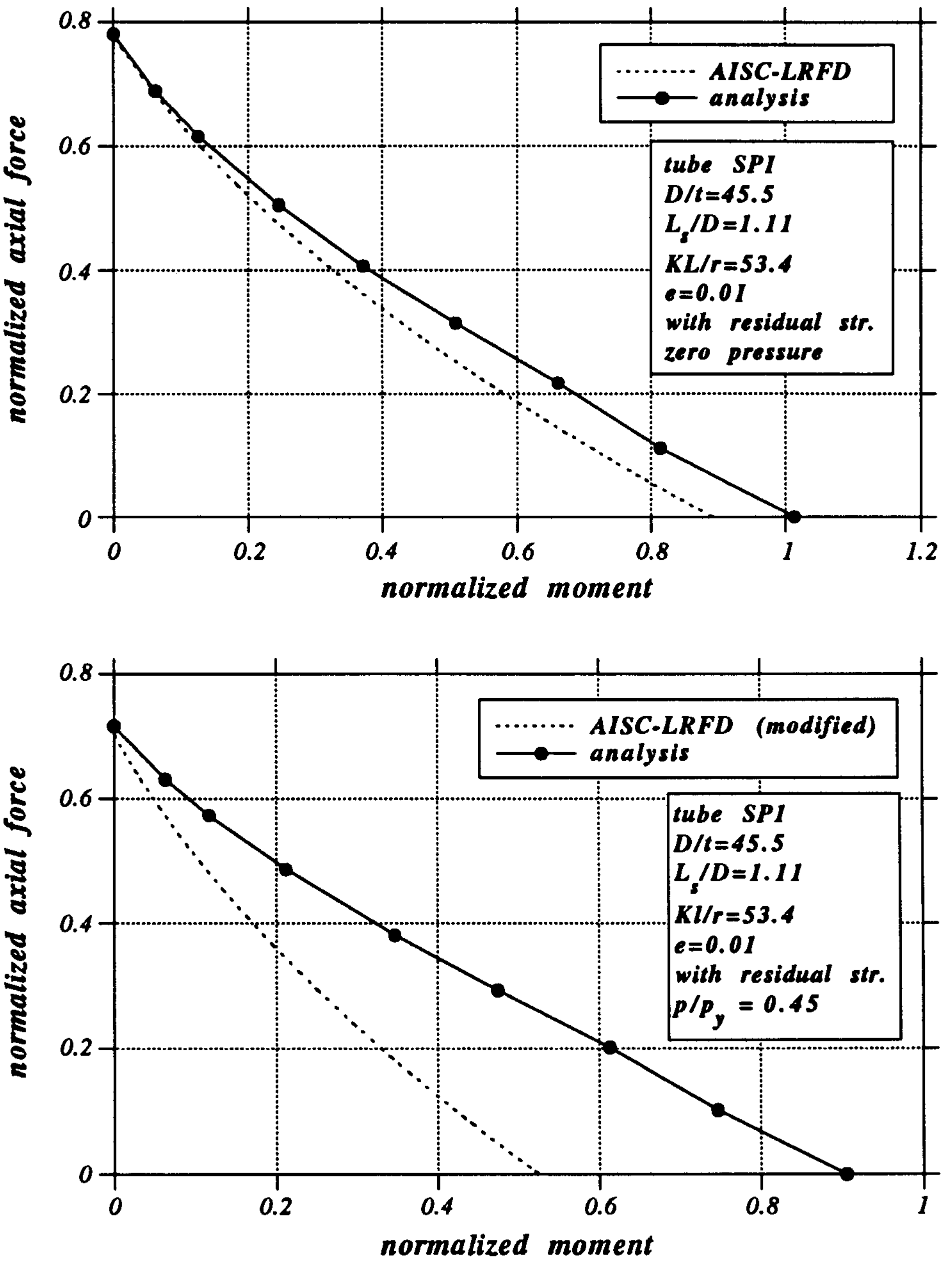

Figure 6.26: Analytical results for tube SP1; comparison with design equations.

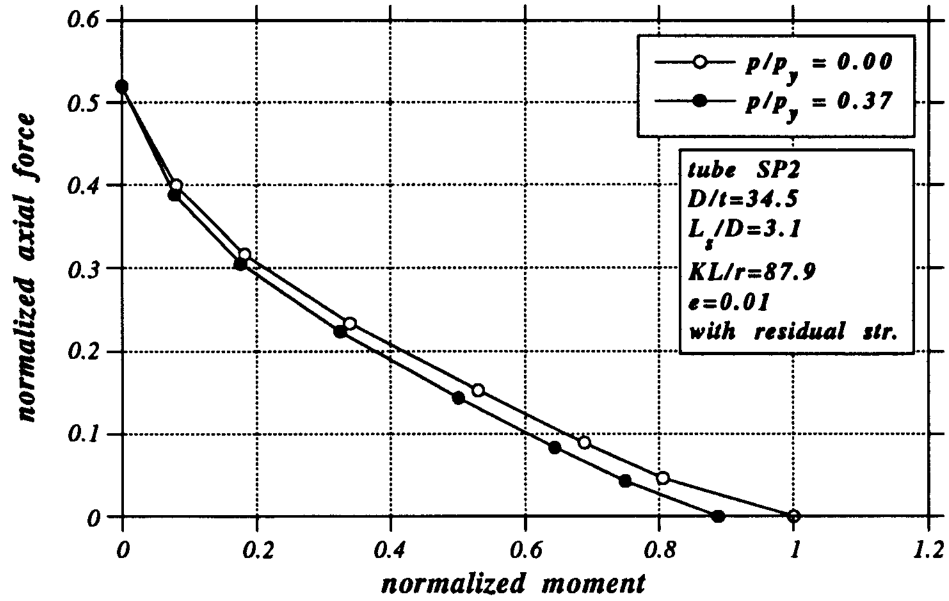

Figure 6.27: Effects of external pressure on beam-column capacity; tube SP2.

horizontal axis), correspond to the ultimate stage which the analysis reached and, clearly, they are on the conservative side. Figure 6.31 shows the moment-curvature curve for the pure bending case of tube SP1. The bending stiffness at point (1) has a very small value and, consequently, the moment at this point should be approximately equal to the actual ultimate moment. Nevertheless, these "no axial force" cases are not of primary interest for the present research and, therefore, no further effort was made to obtain the exact limit points.

Apparently, the axial capacity of tube SP2 is unaffected by the presence of pressure. A first reason for this phenomenon is the low D/t value of tube SP2. Recall that this is a relatively thick tube ($D/t = 34.5$) with a high yield pressure ($p_y = 3478\,psi$). In addition, the tube is very slender ($\lambda = 1.27$) and, consequently, fails elastically. Hence, when subjected to a relatively low

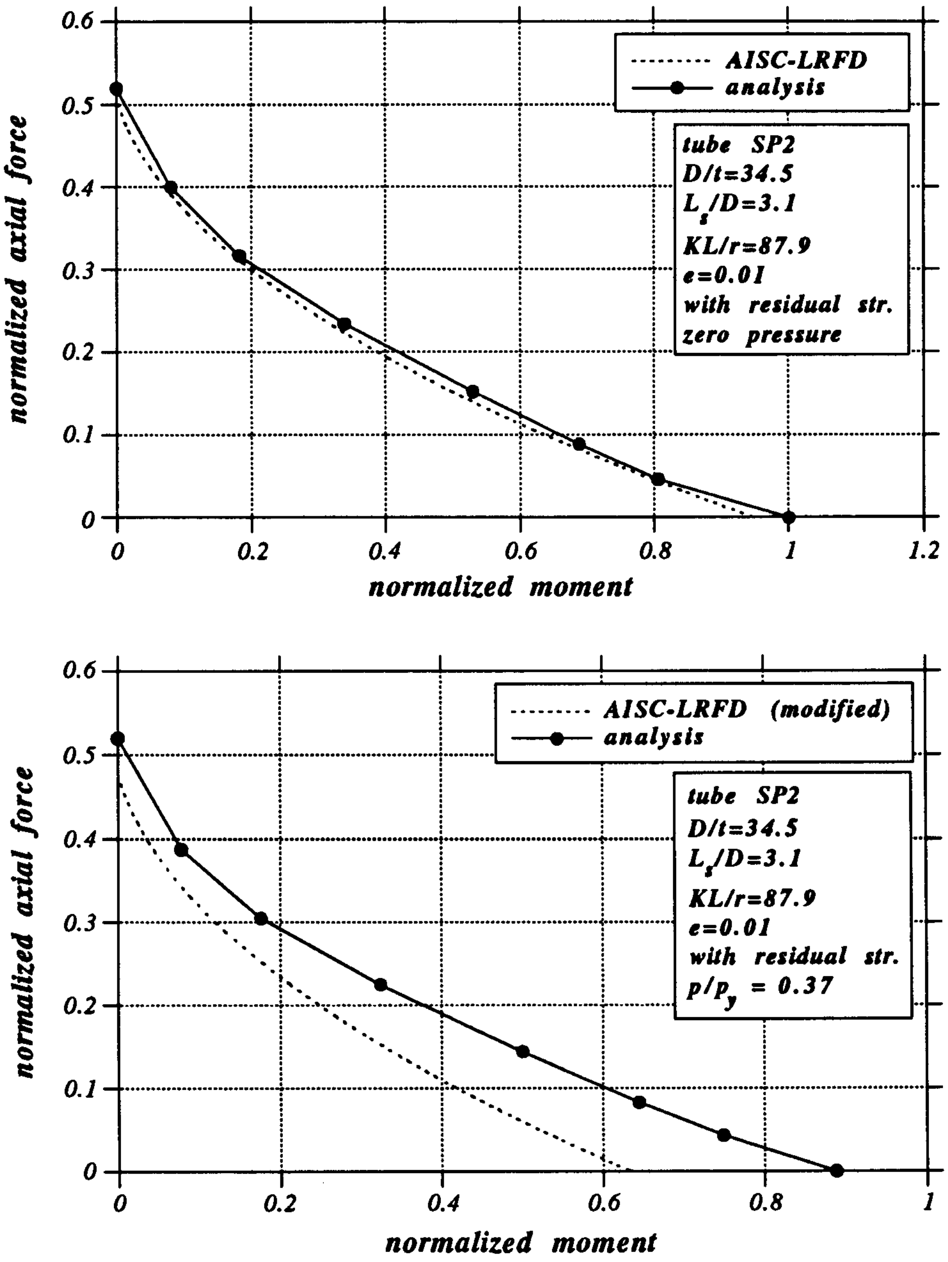

Figure 6.28: Analytical results for tube SP2; comparison with design equations.

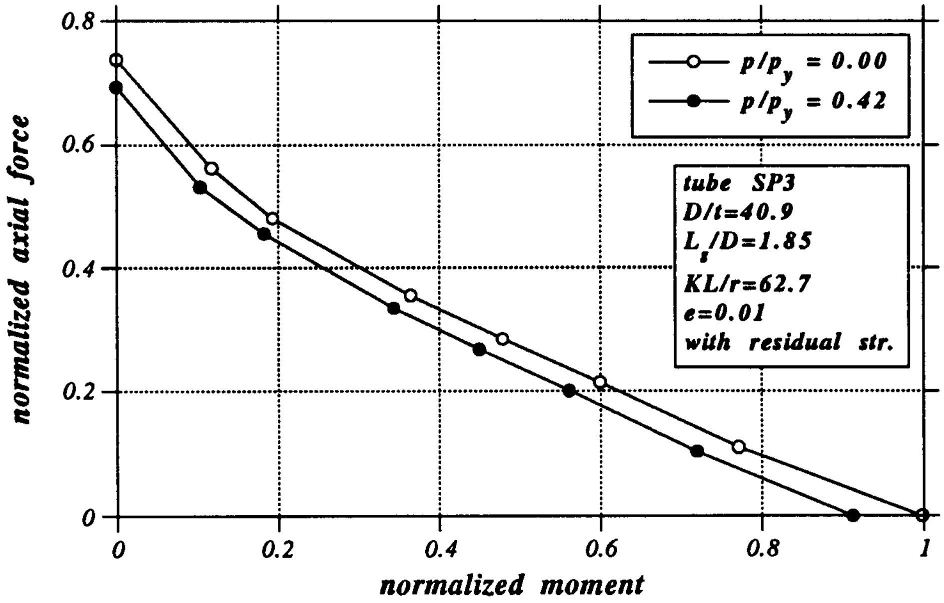

Figure 6.29: Effects of external pressure on beam-column capacity; tube SP3.

level of pressure ($p/p_y = 0.36$), no significant effects on the axial capacity are expected.

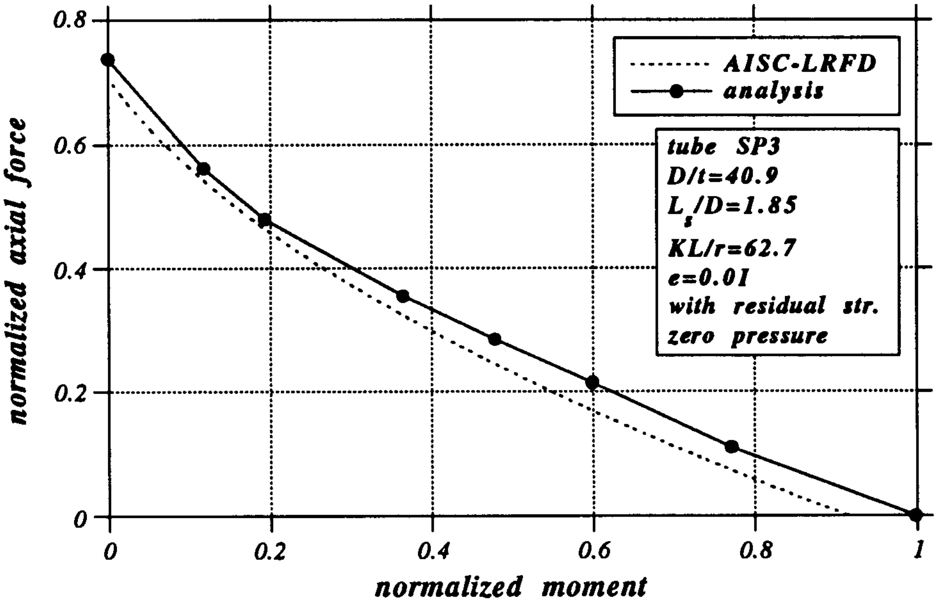

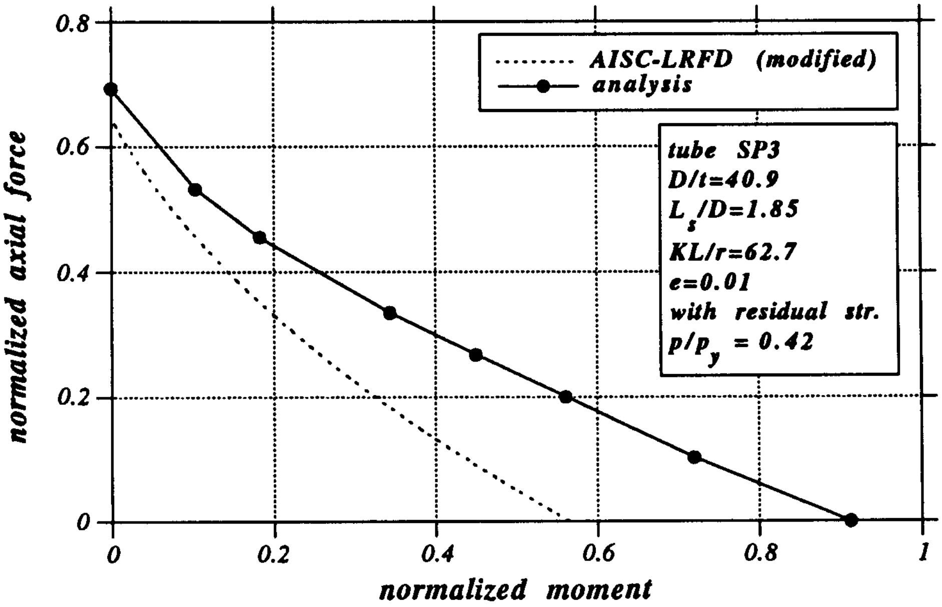

Figure 6.30: Analytical results for tube SP3; comparison with design equations.

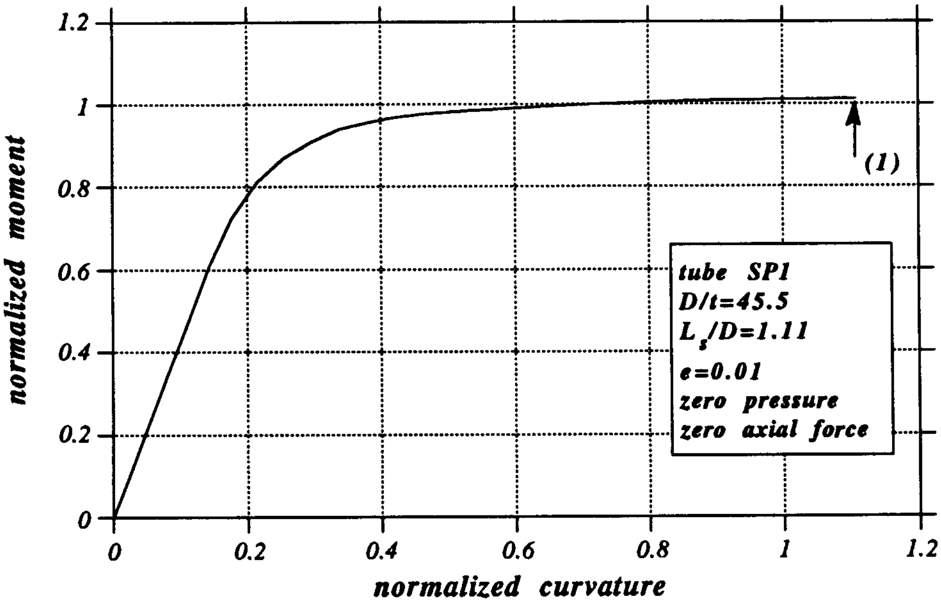

Figure 6.31: Pure bending of tube SP1.

Chapter 7

Conclusions

7.1 Summary

The present work was motivated by the desire for accurate analytical prediction of the ultimate capacity of inelastic tubular beam-columns. Such members are candidates for deep-water applications and must be designed to withstand high external pressure, as well as axial compression and bending.

A nonlinear finite element, referred to as a "tube element", which accounts for large deformations and plasticity effects, was developed for the purposes of this research. The element has a quadratic longitudinal interpolation, whereas a trigonometric series expansion is employed for cross-sectional deformation. Furthermore, the analytical formulation is capable of simulating rigorously the effects of ring stiffeners through a "stiffener element", which is a special case of the aforementioned tube element.

Extensive results were reported on the response of unstiffened tubes under bending and external pressure using a two-dimensional (cross-sectional) analysis, which accounts for cross-sectional ovalization (Brazier effect). The results were successfully compared with experimental data [15], [57], closed-form solutions, as well as with previous analytical results derived using shell elements [30]. Particular emphasis was given to the influence of residual stresses and initial imperfections on pressure capacity.

The effects of localized buckling on the ultimate capacity of tubes under bending and external pressure were examined using a three-dimensional analysis. Localization of deformation causes a sudden drop in moment capacity, reducing member ductility by a significant amount. However, for inelastic tubes of D/t ranging from 40 to 65, localized buckling does not affect the maximum moment capacity. Therefore, cross-sectional (two-dimensional) analysis can be used quite efficiently to obtain the pressure-moment interaction of inelastic tubes.

Results on unstiffened beam-columns were successfully compared with test data reported by CBI [15] and SwRI [57]. Special emphasis is given to the thrust-pressure interaction. It was found that the presence of pressure does not affect significantly the axial capacity of these tubes, provided that the pressure was below 85% of the collapse pressure.

Interesting results were obtained for stiffened tubes under external pressure. The influence of several parameters was examined: stiffener spacing, stiffener size and whether the stiffener is internal or external. As expected, the ultimate pressure value increases for increasing stiffener size and decreasing spacing. Moreover, internal stiffeners provide more stiffness against cross-sectional deformation than external stiffeners of the same size, thus increasing the pressure capacity. Another important factor is the presence of capped-end compression. Results show that the capped-end force has a beneficial effect on the member pressure capacity, because it increases the effective hoop yield stress. This is in agreement with the von Mises yield criterion. Analytical results were found to compare well with available experimental data reported in Refs. [15], [16], [38] and [39].

The bending capacity of pressurized stiffened tubes was also investigated in the work presented herein. The presence of stiffeners increases the ultimate capacity and permits the use of fabricated tubes in deep water. In the absence of experimental evidence, the data from stub column tests [15] were used to test the analytical technique. The comparison between experiments and analysis was very satisfactory.

In the final part of this study, the analytical technique was employed to analyze slender stiffened tubes under axial load and bending, in the presence of external pressure. First, the effects of external pressure on the axial capacity of stiffened members were investigated. Results show that the axial capacity reduction depends primarily on the level of external pressure with respect to the hoop yield pressure (i.e., the p/p_y ratio). Simplified methods proposed in earlier investigations were found to be in very good agreement with the numerical results. In addition, five slender stiffened beam-columns were analyzed with and without external pressure. Results were presented in the form of thrust-moment interaction diagrams and show a certain drop in ultimate capacity in the presence of pressure. It should be noted that, by the time that the present work was completed, there were no experimental results available for the case of slender beam-columns under combined loading.

7.2 Design Recommendations

Numerical as well as experimental results for all loading combinations examined in the present work were compared with the recent API rules [5]. The comparison showed that, in several cases, the specification formulas do not provide an accurate prediction of the ultimate capacity.

The prediction of ultimate bending moment capacity M_n is given by Equation 3.10 (specification equation D.2.3-2). It is notable that this formula, for high-strength steel and for D/t between 40 and 60, predicts a maximum moment below the plastic moment, contradicting both numerical and experimental results [15], [19]. Obviously, the effects of strain hardening are responsible for the specification conservativeness. In addition, Equation 3.10 does not account for the presence of ring stiffeners. On the other hand, it has been shown analytically and experimentally [17], that stiffeners prevent extensive cross-sectional ovalization and, therefore, increase maximum moment capacity.

The accurate prediction of the ultimate pressure p_{hc} of stiffened tubes is of major importance for the safe design of tubular members. Analytical results imply that the ultimate pressure of a stiffened tube depends on several parameters, some of which are not included in Equation 5.3 (specification equation D.2.5-4). More specifically, the design formula does not account for the beneficial effects of capped-end compression and the increase in ultimate capacity when internal stiffeners are used. In addition, both experimental and analytical results indicate that API rules underestimate the value of the maximum stiffener spacing which affects the ultimate pressure (Equation 5.2). The revision of Equation 5.2 would contribute to better estimation of the ultimate pressure p_{hc}.

Because of the aforementioned conservative specification estimation of the ultimate pressure p_{hc} and the maximum moment M_n of a stiffened tube, the pressure-bending interaction Equation 6.1 (API specification equation D.3.3-1) falls below the analytical and the experimental results [17], providing a conservative estimate of the ultimate moment under pressure M_{n1}. Clearly, a better prediction of p_{hc} and M_n would provide a more realistic interaction curve.

The parabolic curve given by Equation 6.5 has been adopted by API rules (specification equation D.2.2-2a) for the prediction of the ultimate inelastic compressive load in the absence of external pressure. On the other hand, analytical results seem to be in better agreement with the exponential curve, Equation 6.6, proposed by the recent AISC-LRFD specification.

For the prediction of thrust-moment interaction for slender columns, the API specification adopts the well-known beam-column equation with amplification factor (Equation 3.17, specification equation D.3.2-1). For the case of zero pressure, this formula is in excellent agreement with the numerical results.

In addition to the global stability equation 3.17, the specification requires the cross-sectional strength check suggested by Equation 3.18 (specification equation D.3.2-2). The recent API rules [5] adopt a cosine interaction curve which is less conservative than the straight-line equation proposed by the previous API specification [4]. The recent equation is closer to both analytical and experimental results. However, for D/t values below 60, the ultimate capacity predicted by Equation 3.18 is always greater than the one calculated through the global criterion of Equation 3.17 and, therefore, Equation 3.18 can be neglected.

The effects of pressure on axial capacity, as well as on the beam-column interaction for slender tubes are not considered in the API rules. This is, perhaps, explained by the lack of experimental evidence. However, numerical results show that stiffened tubes, pressurized to a level above 40% of the yield pressure, may exhibit a considerable drop in ultimate axial capacity. In addition, the conservative estimation of pressurized bending capacity under zero axial force M_{n1}, makes the specification beam-column interaction rather inaccurate at high pressure levels.

7.3 Synopsis

The present study was aimed at providing analytical support to the existing experimental database on tubular member capacity under combined loading, as well as exploring some features of tube response not investigated by previous researchers. In general, numerical results were found to be in good agreement with test data. However, further experimental and analytical efforts are necessary in the area of slender stiffened beam-columns in the presence of pressure.

It is hoped that the work reported herein has contributed towards better understanding of deep-water tubular member stability.

BIBLIOGRAPHY

[1] Ades, C. S., "Bending strength of tubing in the plastic range." *J. Aeronautical Sciences*, V.24, pp. 605–610, 1957.

[2] Ahmad, S., Irons, B. M. and Zienkiewicz, O. C., "Analysis of Thick and Thin Shell Structures by Curved Finite Elements," *International Journal for Numerical Methods in Engineering*, Vol. 2, pp. 419–451, 1970.

[3] American Institute of Steel Construction, "Manual of Steel Construction", *Load & Resistance Factor Design*, First Edition, 1986.

[4] American Petroleum Institute, "Recommended Practice for Planning, Designing and Constructing Fixed Offshore Platforms", API RP2A, 9th edition, August 1991.

[5] American Petroleum Institute, "Draft Recommended Practice for Planning, Designing and Constructing Fixed Offshore Platforms- Load and Resistance Factor Design", API RP2A-LRFD, 1st edition, December 1989.

[6] Bathe, K. J., *Finite Element Procedures in Engineering Analysis*, Prentice-Hall Inc., New Jersey, 1982.

[7] Bleich, F., *Buckling Strength of Metal Structures*, McGraw-Hill Book Co., 1952.

[8] Bouwkamp, J. G., "Buckling and post-buckling strength of circular tubular cross-sections", *Offshore Technology Conference*, OTC 2204, pp. 583–592, Houston, Texas, 1975.

[9] Brazier, L. G., "On the flexure of thin cylindrical shells and other thin sections." *Proceedings, Royal Society*, A, V. 166, pp. 104–114, 1927.

[10] Brush, D. O. and Almroth, B. O., *Buckling of Bars, Plates, and Shells*, McGraw-Hill, New York, 1975.

[11] Chen, W. F. and Atsuta, T., "Theory of beam-columns", *Vol. I – In-Plane Behavior and Design*, McGraw-Hill, New York, 1976.

[12] Chen, W. F. and Atsuta, T., "Theory of beam-columns", *Vol. II – Space Behavior and Design*, McGraw-Hill, New York, 1977.

[13] Chen, W. F. and Han, D. J., *Tubular Members in Offshore Structures*, Pitman, London, UK, 1985.

[14] Chen, W. F., and Ross, D. A., "Tests of fabricated tubular columns", *ASCE J. Str. Div.*, V.103, No. 3, pp. 619–633, 1977.

[15] Chicago Bridge & Iron, "Hydrostatic Beam-Column Tests (Phase II)", *Final Report - Contract Number C92731*, API Project Number 87-56 Plainfield, Illinois, 1989.

[16] Chicago Bridge & Iron, "Collapse Tests of Fabricated Cylinders Under Combined Axial Compression and External Pressure", *Final Report - Contract Number 21738*, API Project Number 82/83-46 Plainfield, Illinois, 1983.

[17] Chicago Bridge & Iron, "Collapse Tests of Short Tubular Columns Subjected to Combined Loads", *Final Report*, Pennzoil/Joint Industry Project, Plainfield, Illinois, 1985.

[18] Corona, E. and Kyriakides, S., "On the collapse of inelastic tubes under combined bending and pressure." *Int. J. Solids & Structures* V. 24, pp. 505–535, 1988.

[19] Corona, E. and Kyriakides, S., "Collapse of pipelines under combined bending and external pressure." *Proceedings, International Conference on the Behaviour of Offshore Structures*, V. 3, pp. 953–964, Trondheim, Norway, 1988.

[20] Crisfield, M. A., "An Arc-Length Method Including Line Searches and Accelerations.", *Int. J. Num. Meth. Eng.*, V. 19, pp. 1269–1289, 1983.

[21] Dorgant, P. L., "Titan Member Design Equations." *Interoffice Memorandum*, Shell Oil Co., November, 1990.

[22] Fiala, D. W. and Erzurumlu, H., "Moment-thrust-curvature of tubular members by iteration", *Offshore Technology Conference*, OTC 1668, pp. 480–486, Houston, Texas, 1972.

[23] Gurtin, M. E., *An Introduction to Continuum Mechanics*, ed. Academic Press, London 1981.

[24] Han, D. J. and Chen, W. F., "Buckling and Cyclic Inelastic Analysis of Steel Tubular Beam-columns", *Engineering Structures*, Vol. 5, No. 2, pp. 119-132, 1983.

[25] Hutchinson, J. W., "Finite Strain Analysis of Elastic-Plastic Solids and Structures," *Numerical Solutions of Nonlinear Structural Problems*, edited by R. F. Hartung, ASME, The Applied Mechanics Division, Vol. 6, pp. 17–29, 1973.

[26] Ikeda, I. Jr., "Dynamic Response of Tendons and Risers", *M.Sc. Thesis*, Dept. of Civil Engineering, The University of Texas, Austin, Texas, 1993.

[27] Jirsa, J. O., Lee, F.-H., Wilhoit Jr., J. C. and Merwin, J. E., "Ovaling of pipelines under pure bending", *Offshore Technology Conference*, OTC 1569, pp. 583–592, Houston, Texas, 1972.

[28] Johns, T. G. and McConnell, D. P., "Response and stability of elastoplastic circular pipes under combined bending and external pressure." *Proceedings, 11th Pipeline Technology Conference*, Houston, Texas, 1983.

[29] Ju, G. T. and Kyriakides, S., "Bifurcation and Localization Instabilities in Cylindrical Shells under Bending – II. Predictions", *International Journal of Solids and Structures*, Vol. 29, No. 9, pp. 1143–1171, 1992.

[30] Karamanos, S. A. and Tassoulas, J. L., "Stability of Deep-Water Pipelines Under Combined Loading", *Offshore Technology Research Center, Report No. 6/91-B-18-100*, The University of Texas, Austin, Texas, 1991.

[31] Katsounas, A. T. and Tassoulas, J. L., "Finite element analysis of propagating buckles in deep-water pipelines." *Offshore Technology Research Center, Report No. 1/90-B-1-100*, The University of Texas, Austin, Texas, 1989.

[32] Kyriakides, S. and Shaw, P. K., "Reponse and Stability of Elastoplastic Circular Pipes Under Combined Bending and External pressure," *International Journal of Solids and Structures*, Vol. 18, No. 11, pp. 957–973, 1982.

[33] Kyriakides, S. and Ju, G. T., "Bifurcation and Localization Instabilities in

Cylindrical Shells under Bending – I. Experiments", *International Journal of Solids and Structures*, Vol. 29, No. 9, pp. 1117–1142, 1992.

[34] Kyriakides, S., Corona, E., Madhavan, R. and Babcock, C. D., "Pipe Collapse Under Combined Pressure, Bending and Tension Loads", *Offshore Technology Conference*, OTC 6104, pp. 541–550, Houston, Texas, 1989.

[35] Loh, J. T., "A Unified Design Procedure for Tubular Members", *Offshore Technology Conference*, OTC 6310, pp. 365–378, Houston, Texas, 1990.

[36] Malvern, L. E., *Introduction to the Mechanics of a Continuous Medium*, Prentice-Hall, Englewood Cliffs, New Jersey, 1969.

[37] Marshall, P. W. and Edwards, C. D., *Private Communication*, 1992.

[38] Miller, C. D. and Kinra, R. K., "External Pressure Tests of Stiffened Fabricated Steel Tubes", *Offshore Technology Conference*, OTC 4107, pp. 371–386, Houston, Texas, 1981.

[39] Miller, C. D., Kinra, R. K. and Marlow R. S. , "Tension and Collapse Tests of Fabricated Steel Cylinders", *Offshore Technology Conference*, OTC 4218, pp. 635–659, Houston, Texas, 1982.

[40] Miller, C. D., *Private Communication*, 1993.

[41] Murphey, C. E. and Langner, C. G., "Ultimate strength under bending collapse and fatigue", 4th *International Offshore and Arctic Engineering Symposium*, V. 1, pp. 467–477, 1985.

[42] Needleman, A., "Finite Elements for Finite Strain Plasticity Problems", *Plasticity of Metals at Finite Strain: Theory, Experiment and Computa-*

tion, edited by E. H. Lee and R. L. Mallett, Rensselaer Polytechnic Institute, Troy, New York, pp. 387–436, 1982.

[43] Nogueira, A. C., "Steady-State Finite Element Analysis of Buckle Propagation in Pipelines", *Ph.D. Dissertation*, Dept. of Civil Engineering, The University of Texas, Austin, Texas, 1993.

[44] Prinja, N. K. and Clegg, R. A., "Assembly Benchmark Tests for 3-D Beams and Shells Exhibiting Geometric Nonlinear Behavior", *Benchmark, NAFEMS*, pp. 16–23, June, 1993.

[45] Prion, H. G. L. and Birkemoe, P. C., "Beam-Column Behavior of Fabricated Steel Tubular Members", *ASCE J. Str. Div.*, to appear.

[46] Reddy, B. D., "An Experimental Study of the Plastic Buckling of Circular Cylinders in Pure Bending", *Int. J. Solids and Structures*, V. 15, pp. 669–683, 1979.

[47] Riks, E., "Some Computational Aspects of the Stability Analysis of Nonlinear Structures", *Comp. Meth. Appl. Mech. Eng.*, V. 47, pp. 219–259, 1984.

[48] Reissner, E., "On finite bending of pressurized tubes", *ASME J. Applied Mech.* V. 26, pp. 386–392, 1959.

[49] Seide, P. and Weingarten, V. I., "On the Bending of Circular Cylindrical Shells Under Pure Bending", *ASME J. Applied Mech.* V. 28, No. 1, pp. 112–116, 1961.

[50] Sherman, D. R., "Test of circular steel tubes in bending." *ASCE J. Str. Div.*, V. 102, ST11, pp. 2181–2195, 1976.

[51] Sherman, D. R., Mueller, W. H. and Erzurumlu, H., "Behavioral study of circular tubular beam columns", *ASCE J. Str. Div.*, V.105, No. 6, pp. 1055–1068, 1979.

[52] Sherman, D. R. "Experimental Study of Post Local Buckling Behavior in Tubular Portal Type of Beam-Columns" *Report to Shell Oil Co.*, Univ. of Wisconsin-Milwaukee, 1979.

[53] Sherman, D. R. "Post Local Buckling Behavior in Tubular Strut Type Beam-Columns: an Experimental Study" *Report to Shell Oil Co.*, Univ. of Wisconsin-Milwaukee, 1980.

[54] Sohal, S. I. and Chen, W. F. "Local buckling and sectional behavior of fabricated tubes", *ASCE J. Str. Div.*, V.113, No. 3, pp. 519–533, 1987.

[55] Sohal, S. I. and Chen, W. F. "Moment-curvature expressions for fabricated tubes", *ASCE J. Str. Div.*, V.110, No. 11, pp. 2738–2757, 1984.

[56] Song, H.- W. and Tassoulas, J. L. "Dynamics of propagating buckles in deep-water pipelines", *Offshore Technology Research Center, Report No. 6/90-B-4-100*, The University of Texas, Austin, Texas, 1990.

[57] Southwest Research Institute "Effects of External Hydrostatic Pressure on Tubular Beam-Columns", *Final Report - Project Number 06-1184*, API Project Number 86/87-56, San Antonio, Texas, 1988.

[58] Structural Stability Research Council, *"Guide to Stability Design Criteria for Metal Structures."*, Edited by T. V. Galambos, John Wiley & Sons, 1988.

[59] Tassoulas, J. L., Katsounas, A. T. and Song, H-W. "Finite element analysis of propagating buckles in deepwater pipelines." *Proceedings, 22nd Offshore Technology Conference*, Houston, Texas, pp. 631–638, 1990.

[60] Timoshenko, S., *Theory of Elastic Stability*, McGraw-Hill, New York, 1961.

[61] Toma, S. and Chen, W. F. "Analysis of fabricated tubular columns", *ASCE J. Str. Div.*, V.105, No. 11, pp. 2343–2366, 1979.

[62] Toma, S. and Chen, W. F. "Post-buckling behavior of tubular beam-columns", *ASCE J. Str. Div.*, V.109, No. 8, pp. 1918–1932, 1983.

[63] Toma, S. and Chen, W. F. "Design of vertical chords in deepwater platforms", *ASCE J. Str. Div.*, V.109, No 11, pp. 2733–2746, 1983.

[64] Toma, S. and Chen, W. F. "External pressure and sectional behavior of fabricated tubes", *ASCE J. Str. Div.*, V.108, No 1, pp. 177–194, 1982.

[65] Wagner, A. L., Mueller, W. H. and Erzurumlu, H. "Design interaction curves for tubular steel beam-columns", *Offshore Technology Conference*, OTC 2684, pp. 755–764, Houston, Texas, 1976.

[66] Zienkiewicz, O. C., *The Finite Element Method*, Third Edition, McGraw-Hill, London, England, 1977.